

**OPTICAL STUDIES OF SOME RARE - EARTH DOPED  
NANO-COMPOSITES FOR PHOTONIC APPLICATIONS**

**A THESIS SUBMITTED IN PARTIAL FULFILLMENT OF  
THE REQUIREMENTS FOR THE DEGREE OF DOCTOR OF  
PHILOSOPHY**

**K.M.S. DAWNGLIANA**

**MZU REGISTRATION NO.: 1502661**

**Ph.D. REGISTRATION NO.: MZU/Ph.D./1525 OF 21.10.2020**



**DEPARTMENT OF PHYSICS  
SCHOOL OF PHYSICAL SCIENCES  
OCTOBER, 2024**

**OPTICAL STUDIES OF SOME RARE - EARTH DOPED NANO-  
COMPOSITES FOR PHOTONIC APPLICATIONS**

**By**

**K.M.S. DAWNGLIANA**

**Department of physics**

**Supervisor**

**Prof. SUMAN RAI**

**Submitted**

**In partial fulfillment of the requirement of the degree of Doctor of  
Philosophy in Physics in Mizoram University, Aizawl**



**Mizoram University (A Central University)**  
**Tanhril-796004, Aizawl, Mizoram**  
**Department of Physics**

**Prof. Suman Rai**  
**Dean, School of Physical Sciences**

Post Box No. 190  
Gram: MZU  
Phone: 8732853277(M)  
Email: [srai.rair677@gmail.com](mailto:srai.rair677@gmail.com)

---

Dt. 16<sup>th</sup> October, 2024

## ***Certificate***

*This is to certify that the thesis entitled ‘Optical studies of some rare-earth doped nano-composites for photonics applications’ submitted by K. M. S. Dawngliana for the degree of Doctor of Philosophy under the Mizoram University, Aizawl, embodies the record of original investigations carried out by him under my supervision. He has been duly registered and the thesis presented is worthy of being considered for the award of the Ph.D degree. This work has not been submitted for any degree of any other university.*

(Prof. SUMAN RAI)  
Supervisor  
&  
Dean,  
School of Physical Science

**DEAN**  
**SCHOOL OF PHYSICAL SCIENCE**  
**MIZORAM UNIVERSITY**

# Declaration

Mizoram University

October, 2024

I **K M S Dawngliana**, hereby declare that the subject matter of this thesis is the record of the work done by me, that the contents of this thesis did not form basis of the award of any previous degree to me or to the best of my knowledge to anybody else, and that the thesis has not been submitted by me for any research degree in any other University/Institute.

This thesis is being submitted to Mizoram University for the **Degree of Doctor of Philosophy in Physics.**



(Prof. SUMAN RAI)

Supervisor

&

Dean

School of Physical Science

**DEAN  
SCHOOL OF PHYSICAL SCIENCE  
MIZORAM UNIVERSITY**



(K M S DAWNGLIANA)

Candidate



(PROF. ZAITHANZAUVA PACHUAU)

Head

Department of Physics

**Head  
Department of Physics  
Mizoram University  
Tanhri : Aizawl**

## Acknowledgements

*Working as a research scholar for the past few years in the Department of Physics, Mizoram University has been a great experience for me. There were times of hardships and struggles as well as success and joy. I thank the God Almighty for his guidance all along the way.*

*First of all, I am deeply indebted to Prof. S. Rai, Department of Physics, Mizoram University, Aizawl for his valuable guidance, support and supervision, keen interest, support and continuous inspiration during the course of my research work. It was a very precious experience to work with Prof. S. Rai and learnt valuable academic skills from his instructions. Whenever I met problems, they were there to help me out. Without my supervisor guidance, it is impossible for me to finish this work smoothly.*

*I would like to thank the Head of the Department of Physics for allowing me to work as a registered scholar in the Department of Physics, Mizoram University. I thank the faculty members of the department for their valuable suggestions and directions regarding my research work. I also the Special thanks to V. Malsawma, non-teaching staff of the department for always being very helping whenever I needed.*

*Special thanks to Dr. A L Fanai, former scholar of Prof. S. Rai for his guidance especially during the early days of my research.*

*I would also like to acknowledge IIT-Guwahati, IIT-Dhanbad and IIT-BHU for providing necessary measurement facilities. The technical help received from C. Borgohain M. Borah, Prof. P.M. Sarun, and Dr. A.L. Fanai for XRD, SEM, EDX and TEM characterization is highly appreciated.*

*I am very grateful to my fellow research scholars of Physics and other departments, my friends elsewhere and my family for their constant encouragements*

*and for providing supports whenever I needed. I am very grateful to my fellow research scholars of physics and other departments, especially thanks to my fellow lab mates Lalruatpuia, Lalnunpuia Khiangte, C. Zothansanga, Beckham Lalthangkima Zathang.*

*Last but not the least, I would like to thank my family members, especially my wife, Ms Lalhriatzuali, for their immense understanding and support without which the thesis could not have been completed. I am grateful to Mr. Lalmalsawma and Mr. Lallungmuana for their constant support and blessings to grow personally and achieve what is more dearest as dream.*

*This work had been made possible by the financial support of National Fellowship for Higher Education of ST Students (NFST) and I would also like to thank University Grants Commission (UGC) for awarding fellowship (202122-NFST-MIZ-00237).*

Dated 16<sup>th</sup> October 2024  
Mizoram University



(K M S Dawngliana)

## **CONTENTS**

	Page No.
<b>Certificate</b>	i
<b>Declaration of the candidate</b>	ii
<b>Acknowledgement</b>	iii-iv
<b>Contents</b>	v-ix
<b>List of figures</b>	x-xiii
<b>List of tables</b>	xiv-xvii
<b>Chapter 1: Introduction</b>	1
1.1 Rare-earth ions/Lanthanide	2-6
1.2 Glasses as host for Rare Earth ions	6-9
1.3 Co doping	9-11
1.4 Sol-gel synthesis	11-14
1.5 Analysis of Optical Spectra	14
1.5.1. Nephelauxetic Effect-Bonding Parameter	14-15
1.6 Spectral Intensities and Judd-Ofelt theory	15
1.6.1. Oscillator strength-Judd-Ofelt analysis	15-16
1.6.2. Radiative properties	16-17
1.6.3. Concentration Quenching	18
1.6.4. CIE- Color Coordinates	18
References	19-28
 <b>Chapter 2: Experimental Techniques</b>	 29
2.1. Introduction	29
2.2. Preparation of Glass Samples	29-34
2.3. Refractive index measurement	34-36
2.4. Density and porosity	36-37
2.5. Fourier Transform Infrared Spectroscopy (FTIR)	37-38
2.6. X-Ray Diffraction (XRD)	38-39

2.7. Scanning electron microscopy (SEM)	39-40
2.8. Energy Dispersive X-ray (EDX) Spectroscopy	40-41
2.9. Transmission electron microscopy (TEM)	41-42
2.10. Optical spectroscopic measurements	42-45
References	46
 <b>Chapter 3: Investigation on Sm<sup>3+</sup> doped (Al<sub>2</sub>O<sub>3</sub>, TiO<sub>2</sub>, ZnS and ZnO) in silicate matrix</b>	 47
<b>3.1. Samarium doped Al glasses</b>	47
3.1.1. Introduction	47-48
3.1.2. Experimental Details	49
3.1.3. Results and Discussions	49
3.1.3.1. XRD analysis	49-50
3.1.3.2. ATR-FTIR spectra	50-52
3.1.3.3. Physical Properties	53-54
3.1.3.4. Absorption Spectra	54-55
3.1.3.5. Photoluminescence Spectra	55-57
3.1.3.6. Effect of Annealing	57-58
3.1.3.7. Judd-Ofelt and Radiative Parameters	58-62
3.1.3.8. Non-linear Properties	63
3.1.3.9. CIE Chromaticity	63-64
3.1.3.1. Conclusion	64
References	65-69
<b>3.2. Samarium doped TiO<sub>2</sub> glasses</b>	70
3.2.1. Introduction	70-71
3.2.2. Experimental Details	71
3.2.3. Results and Discussions	72
3.2.3.1. Physical Properties	72-73
3.2.3.2. XRD Spectra	73-74
3.2.3.3. TEM Analysis	74-75
3.2.3.4. FTIR Spectra	75-76
3.2.3.5. Absorption Spectra	76-77



3.2.3.6. Photoluminescence Spectra	77-78
3.2.3.7. Effect of Annealing	78-79
3.2.3.8. Judd-Ofelt and Radiative Parameters	80-81
3.2.3.9. CIE Chromaticity	81-82
3.2.3.10. Non-linear Properties	82
3.2.4. Conclusion	83
References	84-87
<b>3.3. Samarium doped ZnS glasses</b>	88
3.3.1. Introduction	88-91
3.3.2. Experimental Details	91
3.3.3. Results and Discussions	92
3.3.3.1. Physical Properties	92-93
3.3.3.2. XRD Spectra	94-95
3.3.3.3. FTIR spectra	95-96
3.3.3.4. SEM Analysis	96-97
3.3.3.5. TEM Analysis	97-98
3.3.3.6. Absorption Spectra	98-100
3.3.3.7. Photoluminescence Spectra	100-101
3.3.3.8. Effect of Annealing	102-103
3.3.3.9. Judd-Ofelt and Radiative Parameters	103-105
3.3.3.10. Non-linear Properties	106
3.3.3.11. CIE Chromaticity	106-107
3.3.4. Conclusion	107
References	108-113
<b>3.4. Samarium doped ZnO glasses</b>	114
3.4.1. Introduction	114-117
3.4.2. Experimental Details	117-118
3.4.3. Results and Discussions	118
3.4.3.1. Physical Properties	118
3.4.3.2. XRD spectra	119
3.4.3.3. SEM Analysis	120
3.4.3.4. TEM Analysis	120-121

3.4.3.5. FTIR spectra	121-122
3.4.3.6. Absorption Spectra	122-123
3.4.3.7. Photoluminescence Spectra	123-124
3.4.3.8. Judd-Ofelt and Radiative Parameters	124-127
3.4.3.9. Effect of Annealing	127-128
3.4.3.10. CIE Chromaticity	128-129
3.4.3.11. Non-linear Properties	129-130
3.4.4. Conclusion	131
References	132-136
<b>Chapter 4: Investigation on <math>\text{Eu}^{3+}</math> doped (<math>\text{Al}_2\text{O}_3</math> and <math>\text{TiO}_2</math>)</b>	137
in silicate matrix	
<b>4.1. Europium doped Al glasses</b>	137
4.1.1. Introduction	137-138
4.1.2. Experimental Details	138-139
4.1.3. Results and Discussions	139
4.1.3.1. XRD analysis	139
4.1.3.2. FTIR spectra	139-141
4.1.3.3. Physical Properties	142
4.1.3.4. Absorption Spectra	142-143
4.1.3.5. Photoluminescence Spectra	143-144
4.1.3.6. Effect of Annealing	144-145
4.1.3.7. Judd-Ofelt and Radiative Parameters	146-148
4.1.3.8. CIE Chromaticity	148-149
4.1.3.9. Non-linear Properties	149-150
4.1.4. Conclusion	150
References	151-155
<b>4.2. Europium doped <math>\text{TiO}_2</math> glasses</b>	156
4.2.1. Introduction	156-157
4.2.2. Experimental Details	157-158
4.2.3. Results and Discussions	158
4.2.3.1. Physical Properties	158-159
4.2.3.2. FTIR Spectra	159-162

4.2.3.3. XRD Spectra	162-163
4.2.3.4. SEM Analysis	163-164
4.2.3.5. TEM Analysis	164-165
4.2.3.6. Absorption Spectra	165-167
4.2.3.7. Photoluminescence Spectra	168-170
4.2.3.8. Effect of Annealing	171-172
4.2.3.9. Judd-Ofelt and Radiative Parameters	172-174
4.2.3.10. Non-linear Properties	175
4.2.3.10. CIE Chromaticity	175-176
4.2.4. Conclusion	176-177
References	178-184
<b>Chapter 5: Investigation on Nd<sup>3+</sup> doped Al in silicate matrix</b>	185
5.1. Introduction	185-187
5.2. Experimental Details	187
5.3. Results and Discussions	187
5.3.1. Physical Properties	187-189
5.3.2. XRD Spectra	190
5.3.3. FTIR Spectra	190-193
5.3.4. Absorption Spectra	193-194
5.3.5. Photoluminescence Spectra	194-195
5.3.6. Effect of Annealing	195-196
5.3.7. Judd-Ofelt and Radiative Parameters	197-200
5.3.8. Non-linear Properties	201
5.4. Conclusion	201-202
References	203-208
<b>Chapter 6: Conclusion cum Summary</b>	209
6.1. Introduction	209
6.2. Summary and conclusions	209-213

<b>Future Prospects</b>	214
<b>Bio-data</b>	215
<b>List of Paper Publications (Accepted)</b>	216
<b>List of Papers Presented in Conferences/ Seminars attended</b>	217-218
<b>Reprint of Publications</b>	

## List of Figures

Sl. No.	Fig. No.	Title	Page No.
1	1.1	Some applications of rare-earth elements.	2
2	1.2	Charge distributions of electrons in various orbitals for RE <sup>3+</sup> ions demonstrating how outer filled 5s <sup>2</sup> and 5p <sup>6</sup> shell electrons shelter unpaired 4f electrons.	4
3	1.3	Energy level diagram (Dieke diagram) for RE ions in LaCl <sub>3</sub> crystal	6
4	1.4	Sol-gel reaction scheme	15
5	2.1(a)	A magnetic stirrer is used to stir a mixture in the proper ratio	40
6	2.1(b)	Muffle furnace used for annealing	40
7	2.2(a)	Flow chart of sample preparation of alumino-silicate and titania-silicate host and	41
8	2.2(b)	Flow chart of sample preparation of Zinc oxide and Zins Sulphide host.	41
9	2.3	The working principle of an Abbe refractometer.	43
10	2.4	(a) Schematic diagrams and (b) Image of FTIR spectrophotometer	45
11	2.5	(a) Diffraction of radiation by crystal planes and (b) Image of X-Ray diffractometer.	46
12	2.6	(a) Schematic diagram (b) Image of FESEM.	47
13	2.7	(a) Schematic diagram (b) Image of FETEM	50
14	2.8	(a) iHR320 imaging spectrometer used for recording absorption and emission spectra, (b) block diagram showing arrangement for recording absorption spectrum and (c) block diagram showing arrangement for recording PL spectrum	52
15	3.1.1	XRD spectrum of Sm <sup>3+</sup> (1.2 mol %) and Al (4.2, 2.0 mol %) co-doped silicate sol-gel glasses annealed up to 800 °C	58
16	3.1.2	ATR-FTIR spectra of Sm <sup>3+</sup> (1.2 mol%) and Al (2.0 mol%) in dense sol-gel silicate glass at annealing at different temperatures.	60
17	3.1.3	Absorption spectra of Sm <sup>3+</sup> (1.2 mol %) and Al (2.0 mol %) co-doped in sol-gel silicate glass annealing at 1000 °C in UV-VIS and NIR range.	65

18	3.1.4	PL Spectra of fixed $\text{Sm}^{3+}$ (1.2 mol%) ion and different concentrations of Al (0.0-4.2 mol%) co-doped in sol-gel silicate glass annealing at 1000 °C.	66
19	3.1.5	Schematics energy diagram of $\text{Sm}^{3+}$ ions co-doped with Al in silica host.	67
20	3.1.6	PL Spectrum of $\text{Sm}^{3+}$ (1.2 mol%) and Al (2.0 mol%) co-doped in sol-gel silicate glass with various annealing temperatures	68
21	3.1.7	CIE 1931 chromaticity diagram of $\text{Sm}^{3+}$ (1.2 mol%) co-doped with Al (0.0, 1.2, 2.0, 4.2 mol%) in $\text{SiO}_2$ sol-gel glasses	75
22	3.2.1	XRD patterns of parent 33% $\text{TiO}_2$ –66% $\text{SiO}_2$ nanoparticles.	87
23	3.2.2	(a) TEM image of $\text{TiO}_2$ nanoparticles doped in silica glass-ceramic; (b) SAED pattern confirms the larger grain size and polycrystalline nature due to the presence of rings with discrete spots	88
24	3.2.3	<i>FTIR spectra of 2.0 mol% <math>\text{Sm}^{3+}</math> doped with 33% <math>\text{TiO}_2</math>–66% <math>\text{SiO}_2</math> with sol gel glass-ceramic at different annealing temperatures.</i>	89
25	3.2.4	Absorption spectrum: 33% $\text{TiO}_2$ –66% $\text{SiO}_2$ sol-gel glass-ceramic doped with (2.0 mol%) $\text{Sm}^{3+}$ ions.	90
26	3.2.5	<i>Photoluminescence Spectra of <math>\text{Sm}^{3+}</math> ion co-doped with 33% <math>\text{TiO}_2</math>: 66% <math>\text{SiO}_2</math> sol-gel glass-ceramic.</i>	92
27	3.2.6	<i>Effect of annealing temperature on PL intensity.</i>	93
28	3.2.7	<i>Different energy manifolds of <math>\text{Sm}^{3+}</math> ions doped in 33% <math>\text{TiO}_2</math>-66% <math>\text{SiO}_2</math> sol-gel glass are depicted schematically.</i>	93
29	3.2.8	CIE 1931 chromaticity diagram of $\text{Sm}^{3+}$ co-doped with $\text{TiO}_2$ in sol-gel silica glass at annealing temperatures.	96
30	3.3.1	Variation of density and molar volume of the dense glass samples	109
31	3.3.2	Variation of polaron radius and field strength of the dense glass samples.	110
32	3.3.3	X-Ray Diffraction Spectra of SSZ5 dense glass-ceramic annealed at 900 °C.	112
33	3.3.4	ATR-FTIR spectra of SSZ5 glass-ceramic annealed at different temperatures.	113
34	3.3.5	(a) SEM image of SZ0.5 dense glass-ceramic; (b) SEM image of SSZ5 dense glass-ceramic annealed at 900 °C.	114
35	3.3.6	(a) TEM image of SZ0.5 dense glass-ceramic; (b) TEM image of SSZ5 dense glass-ceramic; (c) SAED pattern with	115

		distinct spot rings verifies the increased particle size and polycrystalline nature.	
36	3.3.7(a)	Optical absorption spectra of prepared dense glass-ceramic annealed at 1000 °C.	117
37	3.3.7(b)	Shows the absorption spectra of SZ0.5 sol-gel glass at room temperature	117
38	3.3.8(a)	PL emission spectra of the prepared dense glass-ceramic annealed at 1000°C.	119
39	3.3.8(b)	Luminescence spectra of SZ0.5 dense glass-ceramic annealed at 1000°C.	119
40	3.3.9	Effect of annealing temperatures of PL spectra of SSZ3 dense glass-ceramic.	120
41	3.3.10	Energy level diagram Sm <sup>3+</sup> doped ZnS nanoparticles.	121
42	3.3.11	The color coordinates of the prepared glasses are displayed in the CIE chromaticity diagram.	125
43	3.4.1	XRD pattern of Sm <sup>3+</sup> doped ZnO NPs in the glass sample annealed at 900 °C.	142
44	3.4.2	SEM image of fixed Sm <sup>3+</sup> -doped ((a) 0.5, (b) 1.5 and (c) 2.5 mol%) ZnO NPs annealed at 900 °C.	143
45	3.4.3	(a) TEM image (b) SAED pattern (c) HRTEM of fixed Sm <sup>3+</sup> doped ZnO(2.5 mol%) in sol-gel silicate glass annealed at 900 °C.	144
46	3.4.4	FTIR spectrum of fixed Sm <sup>3+</sup> ions doped with (2.5 mol%)ZnO NPs in sol-gel silicate glasses at various temperatures.	146
47	3.4.5	Absorption spectra fixed Sm <sup>3+</sup> -doped (2.5 mol%) ZnO NPs in sol-gel silicate dense glass-ceramic annealed at 1030 °C.	147
48	3.4.6	PL spectra of fixed Sm <sup>3+</sup> doped with different concentrations of ZnO in sol-gel silicate glasses annealed at 1030 °C.	148
49	3.4.7	<i>Effect of annealing temperature on PL intensity of fixed Sm<sup>3+</sup> ions doped (2.5 mol%) ZnO NPs in sol-gel silicate glasses.</i>	153
50	3.4.8	Energy level diagram of Sm <sup>3+</sup> doped ZnO NPs in sol-gel silicate glasses.	154
51	3.4.9	CIE chromaticity diagram of fixed Sm <sup>3+</sup> ions doped with different concentrations of ZnO NPs in sol-gel silicate glasses.	155

52	4.1.1	XRD spectra of (2.0 mol%)Eu <sup>3+</sup> -doped Al in silicate glass annealed at 900 °C.	167
53	4.1.2	FTIR spectra of glass co-doped with Eu <sup>3+</sup> ions (2.0 mol%) at various annealing temperatures.	169
54	4.1.3	Absorption spectra of (2.0 mol%)Eu <sup>3+</sup> ions co-doped with Al sol-gel silica glasses.	172
55	4.1.4	PL spectra of Eu <sup>3+</sup> ions co-doped with Al sol-gel silica glasses.	174
56	4.1.5	Effect of annealing temperature on PL intensity.	175
57	4.1.6	Energy diagram of co-doped Eu <sup>3+</sup> and Al ions in a silica host schematic.	175
58	4.1.7	CIE chromaticity diagram.	179
59	4.2.1	ATR–FTIR spectra of SiTiEu1.5 glass annealed at different temperatures.	191
60	4.2.2	XRD diffractogram of (a) SiTi and (b) SiTiEu1.5 glasses annealed up to 700 °C.	194
61	4.2.3	(a) SEM image of SiTi (b) SEM image of SiTiEu1.5 binary glasses annealed up to 700 °C.	195
62	4.2.4	(a) TEM image of SiTi, (b) TEM image of SiTiEu1.5, (c) HR-TEM, (d) SAED pattern of SiTiEu1.5, and (e) EDX spectrum of SiTi of the binary glasses annealed up to 700 °C.	197
63	4.2.5	Absorption spectrum of SiTiEu1.5 glass annealed up to 700 °C.	199
64	4.2.6	(a) UV–vis absorption spectra of SiTi glass. (b) Kubelka–Munk plots and bandgap energy estimation of SiTi glass.	199
65	4.2.7	PL spectra of SiTiEu glasses ( $\lambda_{ex}$ =370 nm).	203
66	4.2.8	PL spectra of SiTi glasses ( $\lambda_{ex}$ =370 nm).	203
67	4.2.9	Effect of annealing temperatures of PL emission spectra.	205
68	4.2.10	Schematics energy diagram of SiTiEu glasses.	205
69	4.2.11	CIE 1931 chromaticity diagram of SiTiEu glasses.	210
70	5.1	(a) The variations in the refractive index and average molecular weight (g) characteristics in sol-gel glasses for SiNdAl0, SiNdAl.2, SiNdAl2, and SiNdAl3. (b) Inter ionic distance ( $10^{-7}$ ) and field strength ( $10^{13} \text{ cm}^{-2}$ ) parameter variations in sol-gel glasses as a function of SiNdAl0, SiNdAl.2, SiNdAl2, and SiNdAl3.	224
71	5.2	XRD spectrum of SiNdAl0 and SiNdAl3 in sol-gel glasses.	226
72	5.3	The Fourier Transmission Infrared spectra of SiNdAl3 in the glass samples after being annealed at various temperatures.	227
73	5.4(a)	Sol-gel glass at the porous gel stage (150 °C) absorption spectra with SiNdAl3.	230



74	5.4(b)	Sol-gel glass after densification (1060 °C) absorption spectra with SiNdAl3.	231
75	5.5	PL spectra of SiNdAl0, SiNdAl1.2, SiNdAl2 and SiNdAl3 in sol-gel glasses annealed at 1060 °C.	232
76	5.6	Effect of the PL spectrum of SiNdAl3 glass samples at annealing temperatures.	233
77	5.7	Schematics diagram of energy level of SiNdAl0, SiNdAl1.2, SiNdAl2 and SiNdAl3 in sol-gel glasses.	234

## List of Tables

Sl. No.	Table No.	Title	Page No.
1	1.1	The electronic configurations of lanthanides, including their ground states and valence states.	4
2	3.1.1	FTIR peak positions and their different assignments of the glass samples.	60
3	3.1.2	Various physical properties of $\text{Sm}^{3+}$ (1.2 mol%) and Al (2.0 mol%) co-doped in Sol-Gel silicate glass annealing at 1000 °C.	63
4	3.1.3	The Experimental ( $f_{\text{exp}}$ ) and Calculated ( $f_{\text{cal}}$ ) Oscillator Strengths with relative Absorption peak for $\text{Sm}^{3+}$ (1.2 mol%) and Al (2.0 mol%) co-doped in sol-gel silicate glass annealing at 1000 °C.	69
5	3.1.4	Judd–Ofelt parameters ( $\times 10^{-20} \text{ cm}^2$ ) and spectroscopic quality factor ( $X=\Omega_4/\Omega_6$ ) comparison of the $\text{Sm}^{3+}$ co-doped with Aluminium in silica glasses with other available literature.	71
6	3.1.5	Radiative parameters of $\text{Sm}^{3+}$ (1.2 mol%) co-doped with Al (2.0 mol%) in silicate glasses.	72
7	3.1.6	PL lines wavelength, energy, effective bandwidth, and stimulated cross-section for various peaks of $\text{Sm}^{3+}$ (1.2 mol%) co-doped with Al (2.0 mol%) in sol-gel silicate glasses.	73
8	3.1.7	Stark splitting in the spectrum $\text{Sm}^{3+}$ (1.2 mol%) co-doped with Al (2.0, 4.2 mol%) in sol-gel silicate glasses at different concentrations	73
9	3.1.8	Stark splitting in the spectrum of $\text{Sm}^{3+}$ (1.2 mol%) co-doped with Al (2.0 mol%) in sol-gel silicate glasses at different annealing temperatures.	74
10	3.1.9	Abbe number ( $v_A$ ), dispersive power ( $v_A^{-1}$ ), non-linear index of refraction ( $n_2$ ), coefficient of the index of refractions ( $\gamma_c$ ), and susceptibility ( $\chi_s$ ) of $\text{Sm}^{3+}$ (1.2 mol%) co-doped with Al (2.0 mol%) in sol-gel silicate glass.	75

11	3.1.10	CIE Chromaticity coordinates of the $\text{Sm}^{3+}$ (1.2 mol%) co-doped with Al (0.0, 1.2, 2.0, 4.2 mol%) in sol-gel silicate glasses.	76
12	3.2.1	Various physical properties of a sol-gel glass-ceramic containing 2 mol% $\text{Sm}^{3+}$ : 33% $\text{TiO}_2$ -66% $\text{SiO}_2$ .	85
	3.2.2	Oscillator strength cum J-O intensity parameters for prepared glass samples	95
	3.2.3	Judd–Ofelt parameters ( $\times 10^{-20} \text{ cm}^2$ ) and spectroscopic quality factor ( $X=\Omega_4/\Omega_6$ ) comparison of the $\text{Sm}^{3+}$ -doped with $\text{TiO}_2$ - $\text{SiO}_2$ in sol-gel glasses with other available literature.	95
	3.2.4	Estimated radiative parameters of synthesized glass-ceramic samples.	96
	3.2.5	Non-linear quantities of $\text{Sm}^{3+}$ -doped $\text{TiO}_2$ - $\text{SiO}_2$ by sol-gel process.	97
	3.3.1	Certain physical properties of ZnS and $\text{Sm}^{3+}$ -doped ZnS NPs in sol-gel $\text{SiO}_2$ glass-ceramic annealed at 1020 °C.	108
	3.3.2	The prepared glasses' root mean square deviation ( $\Delta\delta_{\text{rms}}$ ), experimental and oscillator strengths ( $\times 10^{-6}$ ) for Sm:ZnS were determined.	122
	3.3.3	JO intensity parameters ( $\times 10^{-20} \text{ cm}^2$ ) and the spectroscopic quality factor ( $\Omega_4/\Omega_6$ ) of $\text{Sm}^{3+}$ in the current work and also various other host glass materials.	123
	3.3.4	The peak wavelength ( $\lambda_P$ ), radiative transition probability ( $A_{\text{ed}}$ ), branching ratio ( $\beta_R$ ), total radiative transition probability ( $A_T$ ), effective bandwidth ( $\Delta\lambda_{\text{eff}}$ ) and radiative lifetime ( $\tau_R$ ) of the prepared glasses.	124
	3.3.5	Certain non-linear properties of SSZ5 glasses.	125
	3.3.6	Chromaticity coordinates of the prepared glasses	126
	3.4.1	The physical characteristics of fixed $\text{Sm}^{3+}$ ions doped with (2.5 mol%) ZnO NPs in sol-gel silicate dense glass-ceramic annealed at 1030 °C.	141
	3.4.2	The calculated ( $f_{\text{cal}}$ ) and experimental ( $f_{\text{exp}}$ ) oscillator	150

		strengths with esteem to the relative absorption peak for fixed $\text{Sm}^{3+}$ doped with (2.5 mol%)ZnO NPs in sol-gel silicate dense glass-ceramic annealed at 1030 °C.	
	3.4.3	Comparison of spectroscopic quality factors and J-O intensity characteristics for $\text{Sm}^{3+}$ across many well-known hosts.	151
	3.4.4	Estimated radiative characteristics of fabricated glass samples.	152
	3.4.5	CIE Chromaticity coordinates of fixed $\text{Sm}^{3+}$ -doped with different concentrations of ZnO NPs in sol-gel silicate dense glass-ceramic.	155
	3.4.6	Non-linear properties of fixed $\text{Sm}^{3+}$ ions doped (2.5 mol%) ZnO NPs in sol-gel silicate dense glass-ceramic annealed at 1030 °C.	156
	4.1.1	The glass sample's FTIR peak positions and various assignments.	169
	4.1.2	Certain physical properties of $\text{Eu}^{3+}$ co-doped with Al in sol-gel $\text{SiO}_2$ glasses.	171
	4.1.3	Judd-Ofelt intensity parameters and oscillator strengths of $\text{Eu}^{3+}$ ion.	177
	4.1.4	Comparison of calculated Judd-Ofelt intensity parameters.	178
	4.1.5	Radiative properties of $\text{Eu}^{3+}$ (2.0 mol%) co-doped with fixed aluminium in sol-gel $\text{SiO}_2$ glasses.	178
	4.1.6	CIE chromaticity coordinates of (0.75, 2.0, 4.0 mol%) $\text{Eu}^{3+}$ -doped Al in sol-gel silicate glasses.	179
	4.1.7	Sol-gel alumino-silicate glass was doped with different nonlinear levels of $\text{Eu}^{3+}$ (2.0 mol%) and annealed at 950 °C.	180
	4.2.1	Various physical properties of 1.5% $\text{Eu}^{3+}$ ions doped with 20% $\text{TiO}_2$ –80% $\text{SiO}_2$ binary glass-ceramic derived by sol-gel process.	190
	4.2.2	The glass-ceramic samples' ATR-FTIR peak locations and their various assignments.	192
	4.2.3	The values of bandgap energy of SiTi glass at different annealing temperatures.	200

4.2.4	The following absorption spectra were calculated ( $f_{cal}$ ) and experimentally ( $f_{exp}$ ) for SiTiEu1.5 glass during annealing at 700 °C.	207
4.2.5	Judd Ofelt intensity measurements for $Eu^{3+}$ doped in various hosts were compared.	208
4.2.6	Radiative parameters	208
4.2.7	Non-linear parameters (e.g. $\vartheta_d$ , $1/\vartheta_d$ , $n_2$ , $\gamma_c$ and $\chi$ ) of SiTiEu1.5 binary glass	209
4.2.8	CIE chromaticity coordinates of SiTiEu glasses.	209
5.1	Various physical properties of SiNdAl0, SiNdAl1.2, SiNdAl2 and SiNdAl3 in sol–gel glasses annealed at 1060 °C were observed.	223
5.2	The various assignments of the glass samples' FTIR peak positions.	228
5.3(a)	Oscillator strengths and $\Omega_\lambda$ parameters for SiNdAl3 samples in the porous gel stage.	236
5.3(b)	After densification, the oscillator strengths and $\Omega_\lambda$ parameters for SiNdAl3 samples in the dense glass.	237
5.4	Spectroscopic quality factor ( $X=\Omega_4/\Omega_6$ ) and JO parameters ( $x \cdot 10^{-20} \text{ cm}^2$ ) comparison of the $Nd^{3+}$ co-doped with aluminum in $SiO_2$ glasses with previous published works.	238
5.5	Radiative parameters.	239
5.6	Stark splitting in the spectrum of SiNdAl0, SiNdAl1.2, SiNdAl2 and SiNdAl3 in sol-gel glasses.	239
5.7	Compare stark-split energy levels of $Nd^{3+}$ in various crystalline lattices.	240
5.8	Non-linear parameters of co-doped with SiNdAl3 in sol-gel glasses annealing at 1060 °C, such as $\vartheta_d$ , $1/\vartheta_d$ , $n_2$ , $\gamma$ and $\chi$ . Non-linear parameters of co-doped with SiNdAl3 in sol-gel glasses annealing at 1060 °C, such as $\vartheta_d$ , $1/\vartheta_d$ , $n_2$ , $\gamma$ and $\chi$ .	241

## CHAPTER 1

### INTRODUCTION

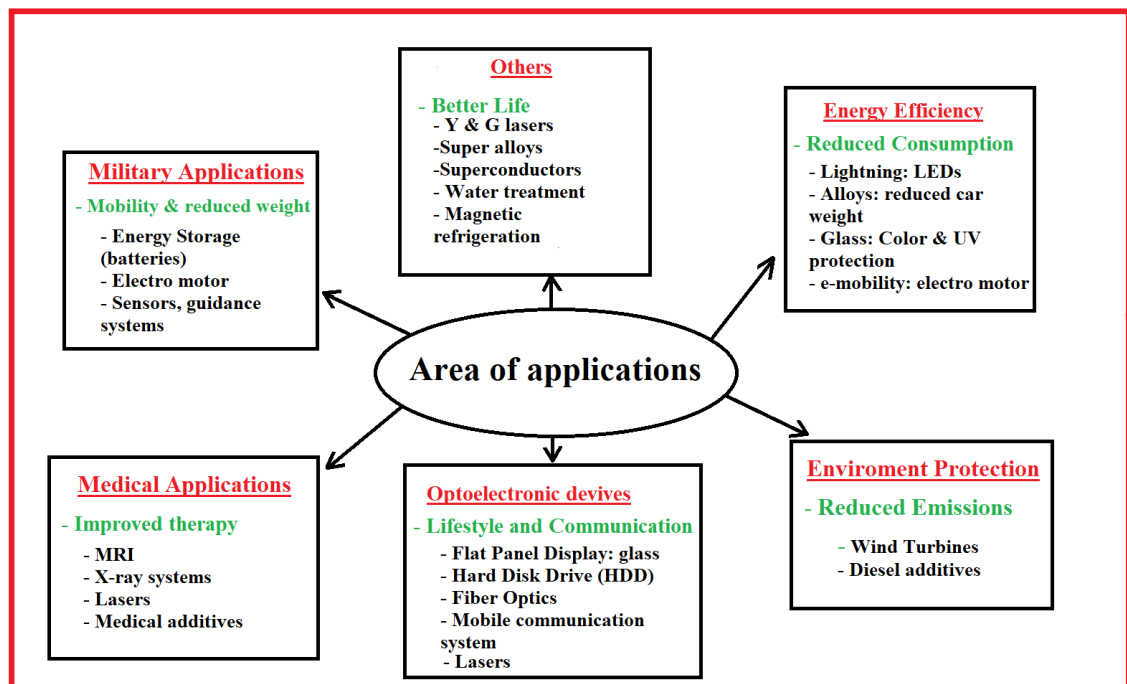
---

Rare Earth (RE) ions are excellent candidates for active ions in solid-state laser materials due to their numerous sharp fluorescent transitions, which cover nearly every part of the visible and near-infrared regions of the electromagnetic spectrum. A solid state laser is a material capable of emitting coherent radiation under specific conditions, consisting of RE ions or transition metals embedded in a solid host, which can be either crystalline or amorphous. The optical properties of the laser material are determined by the combination of the dopant and the host. The invention of the first solid state ruby laser by Maiman in 1960 sparked investigations into various materials for luminescence characteristics (Maiman, 1960); this was soon followed by the operation of  $\text{U}^{3+}:\text{CaF}_2$  by Sorokin and Stevenson (Sorokin *et al.*, 1960). In 1961, Snitzer operated the first Nd: glass laser (Snitzer, 1961). Today, there are numerous types of lasers covering a wide range of wavelengths, from UV to far IR, and offering a variety of output powers. Rare earth ions are also utilized as phosphors in various applications, ranging from fluorescent lighting to display devices like cathode ray tubes, etc. (Ronda *et al.*, 1998).

Significant advancements in the field of phosphors have been achieved by deliberately introducing trivalent rare earth (RE) ions as luminescent centers in various host matrices, resulting in rare earth-activated phosphors (Psuja *et al.*, 2007, Li *et al.*, 2009, Lakshminarayana *et al.*, 2009, Bosze *et al.*, 2003). Over the years, these rare-earth-based phosphors have been crucial to the operation and success of many lighting and display devices within the lighting industry (Ronda *et al.*, 1998, Minh *et al.*, 2007, Naarov *et al.*, 2005, Shea *et al.*, 1998). Cathode-ray tube (CRT) screens and liquid-crystal displays (LCDs) are the most common types of display devices. However, conventional CRTs are bulky and heavy, while LCDs suffer from limited viewing angles and slow response times (Lee *et al.*, 2008, Tannas *et al.*, 1995, Shionoya *et al.*, 1999, Talian *et al.*, 2001). Field emissive displays are seen as a promising next-generation flat panel display technology due to their anticipated high brightness, high contrast ratio, light weight, and low power consumption (Minh *et al.*, 2007, Talian *et al.*, 2001). Another example of flat panel display technology is

the plasma display panel (PDP), which, unlike LCDs, offers rapid response times and wide viewing angles, making them ideal for large TV displays (Minh *et al.*, 2007, Tannas *et al.*, 1995, Shionoya *et al.*, 1999, Talian *et al.*, 2001). In the past decade, plasma display panels have dominated the display market due to these advantages.

Due to their excellent properties, rare earth elements are widely used in various fields, including glass production, ceramics, and battery alloys (Shionoya *et al.*, 1999). The functional use of each element in the lanthanide series has led to the development of new high-tech products that address many of today's societal challenges, such as improving energy efficiency, reducing environmental hazards, and lowering costs (Talian *et al.*, 2001). Some of these applications are illustrated in Fig. 1.1, which clearly demonstrates that rare earth elements are indispensable to modern technology.



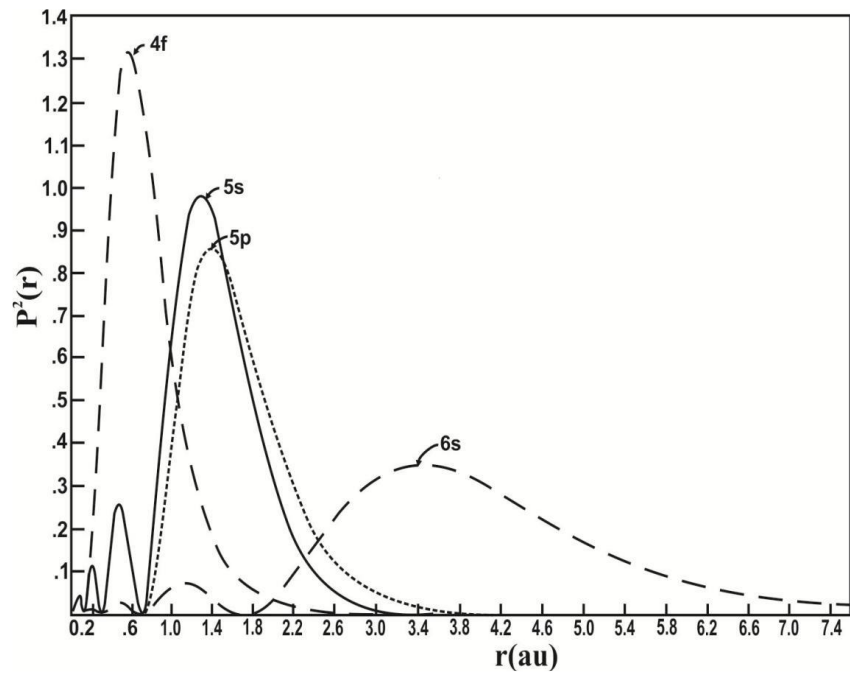
**Fig. 1.1:** Some applications of rare-earth elements.

### 1.1. Lanthanide/Rare earth ions

Rare earth (RE) ions have a long history of use in optical and magnetic applications. They play a significant role in modern optical technology as active species due to their unique luminescent properties, which arise from intra-configurational transitions within the partially filled 4f energy level structures. Rare

earth ions include the elements from Lanthanum ( $Z=57$ ) to Lutetium ( $Z=71$ ), typically referred to as the lanthanide series. These elements are characterized by their partially filled 4f shell, shielded by  $5s^2$  and  $5p^6$  electrons. All lanthanide elements form trivalent cations ( $3+$ ), with a common electronic configuration of  $[\text{Xe}]4f^n6s^2$  or  $[\text{Xe}]4f^{n-1}5d^16s^2$ , where  $[\text{Xe}]$  represents the electronic configuration of xenon and  $n$  ranges from 1 to 14 (Wybourne, 1965). Scandium and Yttrium are also regarded as RE elements due to their similar chemical properties with the lanthanides, leading to the interchangeable use of the terms. In 1937, J. H. Van Vleck (Vleck, 1937), highlighted the puzzle regarding the spectra of RE ions in a solid medium, noting the sharp spectral lines of REs which would be expected if transitions between levels within the 4f electronic shell were allowed. These transitions are forbidden by the Laporte selection rule, which states that an even parity state can only transition to an odd parity state via Electric Dipole (ED) transition and vice versa (Mukharjee *et al.*, 1978). However, when doped in a host, the distortion of electronic motion by the crystalline field of the host lattice overrides this selection rule for free atoms. It is now well-established that many of the spectral features arise from transitions among the 4f configurations (Walsh *et al.*, 2006). The 4f orbitals are shielded by the filled  $5s^2$  and  $5p^6$  orbitals, (see Fig. 1.2) causing the surrounding ligands to weakly perturb the 4f electrons. This shielding also contributes to the unique optical properties of RE ions. Their energy levels are relatively insensitive to the surrounding environment, meaning they do not vary much across different hosts and their electronic states can be easily identified by their energy. The energy levels of RE ions is well documented in many works (Carnall *et al.*, 1968, Carnall *et al.*, 1978, Peijzel *et al.*, 2005) one such being by Dieke (Dieke *et al.*, 1968) and the so called Dieke diagram presents the numerous energy levels of various RE ions and has been used extensively in identifying the electronic states of RE ions. Table 1.1 provides specifics on the ground state, valence state, and electronic configuration of these elements.





**Fig. 1.2:** Charge distributions of electrons in various orbitals for  $\text{RE}^{3+}$  ions demonstrating how outer filled  $5s^2$  and  $5p^6$  shell electrons shelter unpaired  $4f$  electrons (Dieke *et al.*, 1968).

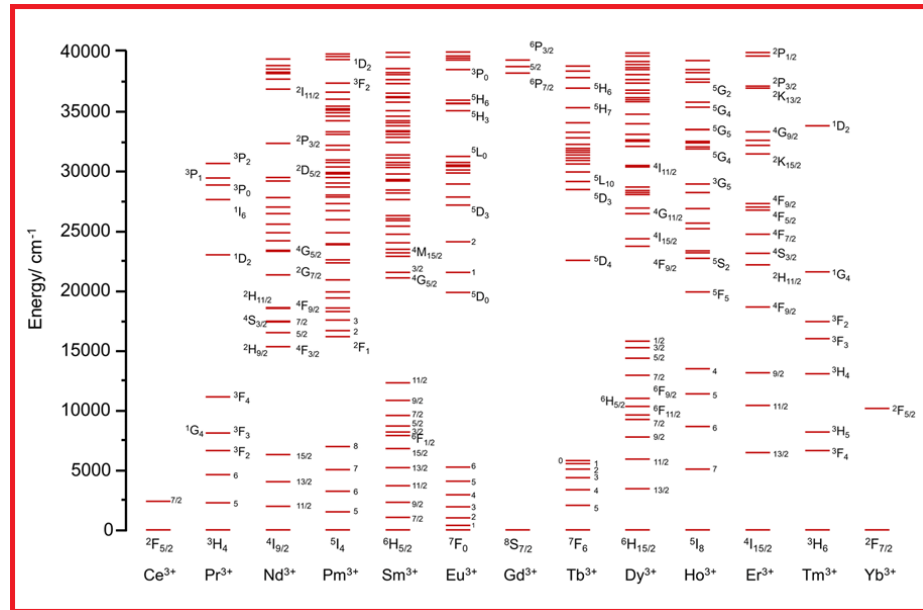
**Table 1.1:** The electronic configurations of lanthanides, including their ground states and valence states.

Element (Symbol)	Atomic Number	Neutral atom electronic configuration	Observed valence	Electronic configuration	Ground State
Lanthanum (La)	57	[Xe] 4f <sup>0</sup> 5d <sup>1</sup> 6s <sup>2</sup>	3	[Xe] 4f <sup>0</sup>	<sup>1</sup> S <sub>0</sub>
Cerium (Ce)	58	[Xe] 4f <sup>2</sup> 6s <sup>2</sup>	3,4	[Xe]4f <sup>1</sup> 5d <sup>1</sup> 6s <sup>2</sup>	<sup>2</sup> F <sub>5/2</sub>
Praseodymium (Pr)	59	[Xe] 4f <sup>3</sup> 6s <sup>2</sup>	3	[Xe]4f <sup>3</sup> 6s <sup>2</sup>	<sup>3</sup> H <sub>4</sub>
Neodymium (Nd)	60	[Xe] 4f <sup>4</sup> 6s <sup>2</sup>	3	[Xe]4f <sup>4</sup> 6s <sup>2</sup>	<sup>4</sup> I <sub>9/2</sub>
Promethium (Pm)	61	[Xe] 4f <sup>5</sup> 6s <sup>2</sup>	3	[Xe]4f <sup>5</sup> 6s <sup>2</sup>	<sup>5</sup> I <sub>4</sub>
Samarium (Sm)	62	[Xe] 4f <sup>6</sup> 6s <sup>2</sup>	2, 3	[Xe]4f <sup>6</sup> 6s <sup>2</sup>	<sup>6</sup> H <sub>5/2</sub>
Europium (Eu)	63	[Xe] 4f <sup>7</sup> 6s <sup>2</sup>	2, 3	[Xe]4f <sup>7</sup> 6s <sup>2</sup>	<sup>7</sup> F <sub>0</sub>
Gadolinium (Gd)	64	[Xe] 4f <sup>7</sup> 5d <sup>1</sup> 6s <sup>2</sup>	3	[Xe]4f <sup>7</sup> 5d <sup>1</sup> 6s <sup>2</sup>	<sup>8</sup> S <sub>7/2</sub>
Terbium (Tb)	65	[Xe] 4f <sup>9</sup> 6s <sup>2</sup>	3,4	[Xe]4f <sup>9</sup> 6s <sup>2</sup>	<sup>7</sup> F <sub>6</sub>
Dysprosium (Dy)	66	[Xe] 4f <sup>10</sup> 6s <sup>2</sup>	3	[Xe]4f <sup>10</sup> 6s <sup>2</sup>	<sup>6</sup> H <sub>15/2</sub>
Holmium (Ho)	67	[Xe] 4f <sup>11</sup> 6s <sup>2</sup>	3	[Xe]4f <sup>11</sup> 6s <sup>2</sup>	<sup>5</sup> I <sub>8</sub>
Erbium (Er)	68	[Xe] 4f <sup>12</sup> 6s <sup>2</sup>	3	[Xe]4f <sup>12</sup> 6s <sup>2</sup>	<sup>4</sup> I <sub>15/2</sub>
Thulium (Tm)	69	[Xe] 4f <sup>13</sup> 6s <sup>2</sup>	3	[Xe]4f <sup>13</sup> 6s <sup>2</sup>	<sup>3</sup> H <sub>6</sub>
Ytterbium (Yb)	70	[Xe] 4f <sup>14</sup> 6s <sup>2</sup>	2,3	[Xe]4f <sup>14</sup> 6s <sup>2</sup>	<sup>2</sup> F <sub>7/2</sub>
Lutetium (Lu)	71	[Xe] 4f <sup>14</sup> 5d <sup>1</sup> 6s <sup>2</sup>	3	[Xe] 4f 14	<sup>1</sup> S <sub>0</sub>

These emissions occur from the energy states with relatively long lifetimes i.e. metastable states. Of all the many different energy states of RE ions, efficient emissions are observed from only a small number of states. Though the positions of the energy levels of RE ions vary only to a small extent, the strengths of transitions between the electronic states and the luminescence emission efficiencies greatly depend on the host environment.

Under the direction of Dieke (Dieke *et al.*, 1968), Johns Hopkins group

generated the complete set of energy level assignments for all  $\text{RE}^{3+}$  ions in anhydrous trichlorides. Fig. 1.3 displays the locations of the various energy levels and transitions of  $\text{RE}^{3+}$  ions. Since the centers of gravity of J manifolds show tiny differences with the host, it aids in our understanding of the position of J states of  $\text{RE}^{3+}$  ions.



**Fig. 1.3:** Energy level diagram (Dieke diagram) for RE ions in  $\text{LaCl}_3$  crystal (Dieke, 1968).

Trivalent lanthanide ions such as rare earths are used extensively for the preparation of optically pumped solid-state lasers, because they have suitable absorption bands and numerous sharp emission lines with high quantum efficiency in different regions of the electromagnetic spectrum. The lanthanide ions employed in this investigation's absorption, emission, and specific laser-characteristic features are listed below.

**Neodymium:**  $\text{Nd}^{3+}$  ( $4f^3$ ) is the most extensively studied laser ion. Optical pumping efficiency is increased by the quick energy cascade from the visible absorption bands of  $\text{Nd}^{3+}$  ion to the  $^4\text{F}_{3/2}$  level. The Nd:  $\text{Y}_3\text{Al}_5\text{O}_{12}$  (YAG) solid state laser is the most often utilized kind. Nevertheless, the threshold for CW  $\text{Nd}^{3+}$  laser activity in anhydrous  $\text{CeCl}_3$  is 0.6 times larger than in YAG.  $\text{Nd}^{3+}$  - doped glasses are predominantly used for the laser action for the following reasons (a) the absorption spectrum of  $\text{Nd}^{3+}$  ions in glassy materials extends from ultraviolet ( $\approx 350$  nm) to

infrared (  $\approx 900$  nm) region and (b) owing to its favorable energy-level dynamics, the laser transition at  $1.06\text{ }\mu\text{m}$  is capable of large energy storage (Venkateswarlu *et al.*, 20015).

**Samarium:**  $\text{Sm}^{3+}$  ( $4f^5$ ) ions are very important in glassy hosts for various communication applications, storage and displays.  $^4\text{G}_{5/2}$  is the metastable state for this ion. The laser transitions take place from this level. In most of the hosts this ion emits orange red emission lines (Deun *et al.*, 1999).

In conclusion,  $\text{Sm}^{3+}$  ions hold potential for use in nuclear fusion lasers in the future. By using these glasses, the microchip laser's medium efficiency at high doping levels may be increased. They have the basic energy level system needed for a laser system. In contrast to the other  $\text{RE}^{3+}$  doped glasses,  $\text{Sm}^{3+}$  ions doped glasses offer a variety of uses, such as zero excited state absorption, low concentration quenching (CQ), low quantum defect (LQD), no up-conversion losses, and reduced thermal load due to the absence of high lying excited levels. According to a number of studies,  $\text{Sm}^{3+}$  has a longer effective lifespan ( $\tau$  ( $\sim\text{ms}$ )) than other  $\text{RE}^{3+}$  doped in the same host medium and produces high luminescence output, particularly in the near-infrared range (Farrires *et al.*, 1990, Filho *et al.*, 2000, Vijaya *et al.*, 2013, Praveena *et al.*, 2009, Rai *et al.*, 2008, Okada *et al.*, 2011, Kindrat *et al.*, 2019, Gao *et al.*, 2018).

**Europium:**  $\text{Eu}^{3+}$  ( $4f^6$ ) ion has widely been used in glasses, crystals, and phosphors etc., based on different applications because of strong dependence of these ions on environment. The two levels that are  $^7\text{F}_0$  level and  $^5\text{D}_0$  level are non-degenerate (Hussein *et al.*, 2018). The  $\text{Eu}^{3+}$  ions are most prominent in red emitting materials for the applications of fluorescent lamps and color televisions.

Of all the many different energy states of RE ions, efficient emissions are observed from only a small number of states. Though the positions of the energy levels of RE ions vary only to a small extent, the strengths of transitions between the electronic states and the luminescence emission efficiencies greatly depend on the host environment.

The phenomenon of photon upconversion, which is the conversion of long wavelength (low energy) radiation into shorter wavelength (high energy) radiation by

successively absorbing two or more pump photons and then emitting the output radiation at a shorter wavelength than the pump wavelength, is one of the intriguing characteristics of lanthanide ions. Auzel is one of the pioneers in upconversion of RE ions (Auzel *et al.*, 2004) and demonstrated the Auzel APTE (addition de photon par transferts d'énergie) effect later termed as energy transfer upconversion (ETU) [Auzel, 1973, Auzel 1980). Since then upconversion has been the subject of many studies and had been observed in a variety of RE-host combinations (Biswas *et al.*, 2003, Goldner *et al.*, 1993, Santos *et al.*, 2001, Bullock *et al.*, 1997). Upconversion lasers are among the most efficient sources of coherent visible and near-ultraviolet radiation and can provide practical solutions for diverse applications from medical diagnosis and treatment, underwater surveillance and full color (RGB) all-solid state displays (Schep, 1996).

## **1.2. Glasses as host for Rare Earth ions**

Since the pioneering works by Snitzer in 1961, RE doped glasses have been the subject of many studies and the versatility have led to many applications especially in solid state laser and optical amplifier devices. Glasses being amorphous lack the long range order and regularity in arrangement of atoms found in crystals (Zachariasen *et al.*, 1932). So RE ions doped in glasses are subjected to a more random and diverse environment. As a result there are small variations in the energy levels of the ions and this result in broader absorption and emission lines compared to crystal hosts (Weber *et al.*, 1979).

The development of RE-based optical materials heavily depends on the choice of appropriate host material for RE ions. There are different types of host media for lanthanides like liquids, crystals and glasses. A large no. of studies have been done on the spectroscopic behaviour of the RE ions in various hosts. Carnall *et al.* (Carnall *et al.*, 1968, Carnal *et al.*, 1978) investigated the electronic energy levels of the RE ions in different solution media. Hazarika *et al.* (Hazarika *et al.*, 2004) studied the structural, optical and non-linear investigation of  $\text{Eu}^{3+}$   $\text{Al}(\text{NO}_3)_3$ – $\text{SiO}_2$  sol–gel glass. Weber *et al.* (Weber, 1966) studied the probabilities of radiative and non-radiative decay of  $\text{Er}^{3+}$  in  $\text{LaF}_3$  crystals. Dutta *et al.* (Dutta *et al.*, 2011) Optical transitions and frequency up conversions of  $\text{Ho}^{3+}$  and  $\text{Ho}^{3+}/\text{Yb}^{3+}$  ions in

$\text{Al}(\text{NO}_3)_3\text{-SiO}_2$  sol-gel glasses. Rai *et al.* (Rai *et al.*, 2016) reported the effect of annealing and dopants concentration on the optical properties of  $\text{Nd}^{3+}:\text{Al}^{3+}$  co-doped sol-gel silica glass.

Over the years, many different types of glasses have been used and studied as the host for RE ions (Weber *et al.*, 1990, Cases *et al.*, 1991, Rakov *et al.*, 2002, Wang *et al.*, 2007). Different types of glasses have different optical and structural properties which affect the spectroscopic properties of the RE ions, making them more suitable to certain applications. Transparency is one important feature of glasses and the transparency range varies among different types (Yamane *et al.*, 2000). Oxides and fluoride glasses are generally transparent in the visible region owing to the large band gap between valence band and conduction band while chalcogenides with lower band gaps are translucent in the visible but transparent in the infrared region. Heavy metal fluoride glasses like fluorozirconate also has high transparency up to mid infrared wavelengths but their synthesis require very carefully controlled environment due to chemical reactivity of the raw materials. Among oxide glasses other than silica, phosphates, germanates, borates and tellurites are also used in various optoelectronic devices making use of their unique properties. But they are often costly to produce and have inferior chemical durability.

Generally different types of glass materials are considered as effective host for RE ions because of its numerous advantages viz. optical transparency in UV-Vis region, non-reactive nature, disordered environment for RE, possibility of fabrication of complex shapes including fibers, low fabrication cost, non-uniform environment for REs to undergo Stark splitting, convenience in fabricating homogeneous pieces having lower nonlinear refractive indices, possibility for large doping concentration etc. (Rao *et al.*, 2012). RE ion doped glasses have attracted considerable attention during the past few decades because of the potential applications in areas such as fluorescent display devices, optical detectors, bulk lasers, optical fibers, waveguide lasers etc. (Nguyen, 2007). The optical and spectroscopic behaviour of tri-positive RE ions doped in various crystals and glasses have already been studied extensively for their diverse applications (Kaminskii *et al.*, 1986, Yuen *et al.*, 2004, Zhang *et al.*, 2005, Koch *et al.*, 2002, Scholle *et al.*, 2004). There are two major components of a glass viz. network former and network modifier. The species which can form the

glass without the help of any other species is called a glass former. Typical examples of glass former are  $B_2O_3$ ,  $SiO_2$ ,  $P_2O_5$  etc. A modifier is a species which modifies the structure of the glass network and changes different properties of a glass. A modifier is sometimes very effective to improve the optical properties of a glass. Among the most popular glass hosts for trivalent RE ions, silica glass can be considered as a very effective host. It has drawn the attention of researchers because of its unique properties like non-toxic nature, superior chemical and thermal stability, better mechanical strength, low thermal expansion etc. (Rai *et al.*, 2016). Because of its technical benefits, silica matrix is widely researched and employed despite having a comparatively greater phonon energy. Therefore, there is a lot of promise for the investigation of improving RE ion emission efficiency in silica matrix. A lot of research work has been done on RE doped silica matrices. To mention a few are Locher *et al.* (Locher *et al.*, 2005) fabricated and studied the RE doped  $SiO_2$ - $AlO_2$  material for Optical waveguide. Rai *et al.* investigated the structural, optical and nonlinear properties of  $Eu^{3+}$  in  $Al(NO_3)_3$ - $SiO_2$  glass (Rai *et al.*, 2004). The fluorescence behaviour of  $Eu^{2+}$  and  $Eu^{3+}$  in silica glass was analyzed by Danping *et al.* (Danping *et al.*, 2006). The Optical properties of  $Ho^{3+}$  in sol-gel silica glass co-doped with Aluminium was investigated by Fanai *et al.* (Fanai *et al.*, 2016). Most of the RE doped silica glass hosts are prepared by sol-gel technique and hence they are also mentioned as sol-gel silica glass.

Silicate glass is an important class under the oxide family. With its remarkable optical transparency in the visible, near-infrared, and deep ultraviolet ranges, silicate glass is a highly advantageous host for RE ions. It has good thermo-mechanical and chemical properties. In addition, silicate glass is bestowed with some outstanding qualities, viz. thermal stability, high degree of homogeneity, excellent transparency in the optical region and cost-effectiveness etc. (Rejikumar *et al.*, 2010, Fanderlick, 1991). Moreover, the thermal expansion of silica glass is the lowest among all the conventional technical glass due to its exclusively stronger Si-O bonds. As a result, silicate glass has high resistance to thermal shock, which is very significant in high power lasers (Reisfeld *et al.*, 1987). One drawback of silicate is the relatively high phonon energy (Layne *et al.*, 1977) which leads to lower efficiency in the luminescence of RE ions, a process known as multi-phonon

relaxation (Arai *et al.*, 1986). The ion in an excited state can lose its energy to the vibration of the host lattice in the form of multiple phonons and the rate of the non-radiative multi-phonon relaxation increases for less number of phonons required to bridge the energy gap between an excited state and the next lower energy state. So in silicate glass, multi-phonon relaxation effectively quenches the luminescence from energy states that would have stronger emissions in hosts with lower phonon energy such as tellurites and fluorozirconates. Another disadvantage of silicate glass is the low solubility of RE ions which leads to clustering (Arai *et al.*, 1986). According to Almeida *et al.* (Almeida *et al.*, 1998) the RE ions have high coordination numbers and must share the limited number of non-network oxygen (NNO) atoms in the silicate glass matrix. Ions can be evenly dispersed and attached to NNO atoms in RE–Si–O bonds at low concentrations of RE; but, as concentrations rise, clusters are generated by RE–O–RE bonding. These formations of clusters can lead to energy transfer among the RE ions which can lead to concentration quenching resulting in luminescence reduction. The rate of energy transfer between RE ions strongly depends upon the interionic distance and so the clustered RE ions in close proximities promote energy migration among themselves and resulting in concentration quenching. An ion in the emitting level may lose its energy to a nearby ion through phonon assisted energy transfer or cross-relaxation (Auzel, 2004) resulting in quenching of the luminescence which would otherwise occur in the absence of the energy transfer. Cross-relaxation process is dependent on the energy level structure of RE ions and some are more prone to it. It is a major quenching mechanism for the  $^4F_{3/2}$  emissions of  $Nd^{3+}$  (Stokowski *et al.*, 1981). For integrated optics, silicate-based glasses that are activated by RE ions continue to be a desirable material. Finding ways of improving the luminescence efficiency of RE ions in silicate is one of the areas of interest in the field of optical materials and photonics. The prospect of creating optically limited structures has created new avenues for the creation of innovative optical components. This study aims to describe current developments in photonic systems based on RE-activated silicate and suitable manufacturing processes that allow tailoring and enhancement of optical and spectroscopic characteristics.



### 1.3. Co-doping

As mentioned in the previous section, pure silicate though it has many superior properties to other glasses, has few disadvantages that adversely affect its usability as efficient luminescent material. Over the years many works had been carried out and suitable co-doping has been found to improve the luminescence properties of RE doped silicate glass. To improve the clustering problem (Rai *et al.*, 2016) studied the effects of co-doping with Phosphorus and Aluminum. The effect of Phosphorus was found to be more subtle and Aluminum was more effective. There have been numerous works on the study of Aluminum effect on RE doped silica glass and the luminescence enhancement of Aluminum is well known but the exact mechanism is a subject of much debate. It has been claimed to reduce clustering of RE ions (Fujiyama *et al.*, 1990, Lockhead *et al.*, 1995, Thomas *et al.*, 1991), but through the use of numerical simulation suggested that the luminescence enhancement mechanism is due to the local modification of RE environment rather than physical dispersion (Monteil *et al.*, 2004).

In semi-conductor nanoparticles, quantum confinement effects can significantly change their optical and electrical properties as compared to the bulk material (Woggon *et al.*, 1997, Kayanuma *et al.*, 1988). Many studies have shown them to be attractive hosts for RE ions and have beneficial effects on the luminescence properties. ZnO nanoparticles doped with RE ions are reported to show white light emission (Huang *et al.*, 2014, Luo *et al.*, 2016) and have potential application in display devices. It also showed that the luminescence of Europium doped SiO<sub>2</sub> is enhanced 5-10 times in presence of ZnO nanoparticles (Bang *et al.*, 2005). The luminescence enhancement was also observed in Europium and Terbium doped in Zirconia films in presence of CdS nanoparticles by claiming the energy transfer from CdS to the RE ions to be the enhancement mechanism (Reisfeld *et al.*, 1987). The strong UV absorption of CdS allows more efficient absorption of the 337 nm excitation energy which is then transferred to the RE ions. Similar enhancement in presence of CdS nanoparticles was also reported in Europium doped sol-gel silica (Hayakawa *et al.*, 2000). More recent studies on effect of CdS nanoparticles on Terbium doped sol-gel silica suggested that the modification of the host silica network may also be a contributing factor in the luminescence enhancement (Jyothy

*et al.*, 84).  $\text{TiO}_2$  is another semi-conductor that has been extensively studied as host for RE ions. It has relatively low phonon energy which is favorable for efficient luminescence. It can be easily prepared by sol-gel technique which allows the synthesis in the form of thin films by dip coating. Works showed Erbium doped in  $\text{TiO}_2$  planar waveguide having 1.5 $\mu\text{m}$  fluorescence emission and also infrared to visible up-conversion in later work (Bahtat *et al.*, 1996, Bahtat *et al.*, 1994). Photoluminescence was also observed in  $\text{TiO}_2$  thin films doped with Europium (Palomino-Merino *et al.*, 2001). In studies of bulk  $\text{SiO}_2$ - $\text{TiO}_2$  composite glass doped with Europium, it observed energy transfer from Ti-O charge transfer band to the Eu ions, formation of RE-O-Ti bonds and increase in luminescence intensity (You *et al.*, 2004). It also recently reported green to violet up-conversion in Neodymium doped in  $\text{TiO}_2$ - $\text{SiO}_2$  composite glass (Dihingia *et al.*, 2012).

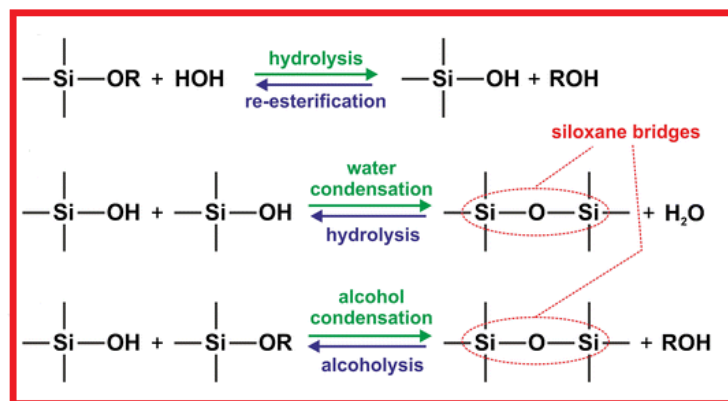
ZnS is a wide and direct band gap (3.7 eV) II-VI semiconductor which is non-toxic (Amirian *et al.*, 2018). It exists in both cubic (zinc blende) and hexagonal (wurtzite) crystalline structures (Synnott *et al.*, 2013, Aneesh *et al.*, 2014). ZnS NPs interacts very well with UV-light; it exhibits strong absorption and broad emission by relaxation from their several defect states (Thai *et al.*, 2016, Shahi *et al.*, 2017). In general, bulk ZnS shows absorption band at 335 nm. But, the absorption band is blue shifted with the variation of its size from bulk to nano, the amount of shifting is directly dependent on the particle size and shape. Hence the absorption and emission band can be tuned by controlling the nanostructure. ZnS crystal has various defect sites which create defect states for e.g. zinc vacancy, sulphur vacancy, zinc interstitial, sulphur interstitial, surface defect states, impurity defect etc. The formation and the recombination process of the electron hole pair between these defects states along with valence band and conduction band results the different possible transitions of ZnS (Kakoti *et al.*, 2019, Fang *et al.*, 2011). These transitions are essential characteristics of ZnS for its optical applications. It is one of the most attractive and extensively studied semiconductors due to its numerous applications in various areas like optical coating, electro-optic modulator, photoconductor, optical sensor, phosphor, reflector, dielectric filter, window material, the field emission displays and other light emitting materials (Pathak *et al.*, 2011, Hoa *et al.*, 2011, Mandal *et al.*, 2011, Klausch *et al.*, 2010, Wang *et al.*, 2010, Zhang *et al.*, 2007,

Taherian *et al.*, 2014). In the study of RE spectroscopy, ZnS NPs also acts as potential sensitizer and effective network modifier (Pathak *et al.*, 2013, Kakoti *et al.*, 2019). At present many research groups are shifting their attention to the applications of ZnS NPs because of its very fascinating properties. To mention a few are Arago *et al.* (Arago *et al.*, 2008) reported an enhancement in PL intensity of the  $\text{Eu}^{3+}$  ion due the energy transfer from Mn doped ZnS to  $\text{Eu}^{3+}$ , Wang *et al.* (Wang *et al.*, 2011) discussed the different types of defect luminescence of ZnS for the applications in optoelectronic devices, light emitting displays etc., Moos *et al.* (Moos *et al.*, 2017) studied the structural and optical properties of ZnS NPs produced by laser irradiation of micro-sized ZnS particles dispersed in water and isopropyl alcohol with and without the addition of Ag NPs, Amirian *et al.* (Amirian *et al.*, 2018) used UV-assisted approach for the synthesis of water soluble and transition metal doped ZnS NPs and investigated their optical and photocatalytic properties etc.

#### **1.4. Sol-gel synthesis**

Sol-gel (a low temperature method) and Melt quench (a high temperature method) are two traditional manufacturing techniques for glass. The melt quench glasses are produced by very rapid cooling of liquid melt mixture. This creates a difficulty in the uniform incorporation of the dopants like RE elements. As the melting point of silica glass is extremely high (1983 K), its synthesis by the melt quench technique is a difficult process (Yamane *et al.*, 2000). Being a low temperature technique, sol-gel technique in this aspect is a very convenient method for fabricating silica matrix. The technique is based on chemical reaction at room temperature (Huang *et al.*, 2010) commonly known as a Chimiedouce or soft chemistry. Chimiedouce is the branch of chemistry in which chemical reactions are maintained at room temperature in open reaction container. These are very similar to the reactions that occur in biological systems. The Chimiedouce based synthesis techniques for different solid materials have been developed in the last few decades (Rouxel *et al.*, 1994). The synthesis process includes both wet chemistry as well as sol-gel chemistry. The sol-gel method is related to polymerization of molecular precursors. These precursors are such that they can be easily mixed at molecular stage with other components due to which the fabrication of multicomponent

materials is possible at low temperatures in comparison to the melt quench technique (Livage *et al.*, 1997). In general sol-gel technique allows precursors of metal oxides  $M(OR)_Z$ . Here, R represents an alkyl group. The formation of an oxide network is purely dependent on the hydrolysis and condensation of these precursors. Fig. 1.4 shows the reaction scheme for the sol-gel process.



**Fig. 1.4:** Sol-gel reaction scheme (Locher *et al.*, 2005).

Glasses are traditionally produced by melt-quenching technique where the constituent raw materials are melted and fused, then formed into desired shape and then quenched to avoid crystallization (Cable, 1984). This technique is convenient for a wide variety of glasses with lower melting temperature, but melting of silicate requires temperatures in excess of 2000 °C. By exploiting a chemical interaction between liquid precursors, the sol-gel approach allows for the production of silica glass at lower temperatures. As the name suggests, in this process a colloidal suspension or sol is formed by reaction of a metal alkoxide with water. For synthesizing silica glass, tetraethyl orthosilicate (TEOS) and tertramethyl orthosilicate (TMOS) are commonly used. The sol, when left standing in a mould or substrate turns into gel due to coagulation of the colloidal particles. During gelation the colloidal particles aggregate and form clusters that link with each other. As the link grows across and throughout the containing mould the gel point is reached and the liquid sol turns into a solid network enclosing a liquid phase. Supercritical drying of the gel at this stage removes the liquid while maintaining the volume and produces aerogels which are extremely light solids with most of their volume being air. Under

normal condition, however, the gel shrinks with ageing (syneresis) and drying. The dried gels are called xerogels and have only a fraction of the original wet volume. Xerogels are highly porous with nanopores throughout the bulk (Brinker et al., 1990). The high porosity is one unique property of sol-gel synthesized silica which is unattainable by traditional methods. The refractive index and density of the porous gels are very low compared to melt glasses. On further heating to certain temperatures, the pores of the xerogel begin to collapse, a process called sintering. Sintering of the porous gel removes the pores and densified silica glass can be obtained. The great purity that may be achieved by sol-gel glass synthesis is one of its benefits. This is partly because the precursors are readily refined by repeated distillation because they are in the liquid condition. Additionally, contamination from the crucibles carrying the components is avoided because the procedure does not call for melting them in crucibles. Because the precursors are in a liquid state, the sol-gel technique also permits greater homogeneity because all of the elements may be fully combined and churned. Unwanted contaminants and inhomogeneities can have a negative impact on glasses, lowering their transparency and increasing the loss of scattered light. Additionally, a far greater range of forms and sizes, including thin films and fibers, may be synthesized using the sol-gel technique. Our research work focuses on the understanding the structure of sol-gel glasses and improving the luminescence properties through annealing and co-doping.

Some of major advantages of the sol-gel techniques are mentioned below (Rai *et al.*, 2016)

- i) It is a cost-effective technique. No high-power electricity is required during fabrication.
- ii) Being a low temperature (room temperature) process, the biological and organic species can be easily incorporated to the fabricated samples without damaging their inherent properties.
- iii) The host can bear considerably higher concentration of the dopants in comparison to melt-quench technique. The dopants are generally present in the form of some inorganic salts and can be mixed in the solution very easily.
- iv) As the precursor quality can be controlled, production of high quality glasses is

possible.

- v) Homogeneous distribution of dopants is possible as they are dissolved in the solution phase.
- vi) This technique allows the fabrication of host materials with versatile size and shape.

## 1.5. Analysis of Optical Spectra

When a  $\text{RE}^{3+}$  ion is doped into a solid matrix, the ligand environment has minimal effect on the 4f shell due to the effective shielding provided by the closed 5s and 5p shells. Despite being weak, this perturbation is crucial as it generates rich electronic spectra, offering detailed fingerprint information about the surrounding atomic arrangement and their interactions with the 4f electrons. Therefore, evaluating the electronic energy level structure of  $\text{RE}^{3+}$  ions in any solid matrix is essential to understanding their luminescence properties.

### 1.5.1. Nephelauxetic Effect-Bonding Parameter

The nephelauxetic effect measures the covalency of the rare earth-oxygen bond in a host matrix, stemming from the partially filled f-shell. When a rare earth ion is doped into a host matrix, the 4f electronic orbitals are deformed in the host ligand field due to this effect. The overlap between the oxygen and 4f orbitals contracts the energy level structure of the rare earth ions, leading to a wavelength shift. To understand the nature of the rare earth-ligand bond, nephelauxetic ratios ( $\beta$ ) and bonding parameters ( $\delta$ ) are evaluated using the following relations (Jiang *et al.*, 2003, Ozawa *et al.*, 1990).

$$\beta = \frac{\vartheta_a}{\vartheta_c} \quad (1.1)$$

Where  $\vartheta_c$  is the wave number (in  $\text{cm}^{-1}$ ) of a specific transition for the rare earth ion being studied, and  $\vartheta_a$  is the wave number (in  $\text{cm}^{-1}$ ) for the same transition of an aqua ion. The bonding parameter  $\delta$  is calculated using the following formula (Jiang *et al.*, 2003, Ozawa *et al.*, 1990).

$$\delta = \frac{1-\beta}{\beta} \times 100 \quad (1.2)$$

Here,  $\bar{\beta}$  represents the average value of  $\beta$ . Depending on the environmental field, the bonding parameter  $\beta$  can be positive or negative, indicating covalent or ionic bonding, respectively. Similarly, the value of  $\delta$  can also be positive or negative, suggesting that the RE-ligand bond is ionic or covalent, depending on the ligand field environment.

## 1.6. Spectral Intensities and Judd-Ofelt theory

In 1962, Judd and Ofelt (Judd, 1962, Ofelt, 1962) independently developed a theoretical formulation for the intensities of absorption bands of rare earth (RE) ions in solid hosts. The Judd-Ofelt (J-O) theory is based on a static, free-ion, and single-configuration approximation, where the central ion is influenced by the surrounding host ions via a static electric field, treated as a perturbation on the free-ion Hamiltonian. In a host medium, electric dipole transitions become allowed due to the admixture of states from configurations of opposite parity, and the transition probability depends on the extent of this admixture. The J-O theory requires the measurement of the absorption spectrum to calculate specific intensity parameters, which are then used to determine the radiative properties of the fluorescing levels from the fluorescence spectrum.

### 1.6.1 Oscillator strength-Judd-Ofelt analysis

According to J-O theory, the calculated oscillator strengths ( $f_{cal}$ ) from each absorption peak consequent to transitions  $|\Psi J\rangle \rightarrow |\Psi' J'\rangle$  relies on the three JO parameters  $[\Omega_\lambda; \lambda=2, 4, 6]$  and it can be expressed as:

$$f_{cal}^{ed} = \frac{8\pi^2 m_e c \bar{\nu} (n^2 + 2)^2}{3h(2J+1)9n} \sum_{\lambda=2,4,6} \Omega_\lambda (\Psi J \| U^\lambda \| \Psi' J')^2 \quad (1.3)$$

where  $m_e$  is the electron mass,  $c$  stands for velocity of light in vacuum,  $h$  is Planck's constant,  $n$  is the index of refraction,  $J$  stands for the initial state's total angular momentum and  $\|U^{(\lambda)}\|$  stands for estimated reduced matrix elements [RME] within the approximation of intermediate coupling for  $|\Psi J\rangle \rightarrow |\Psi' J'\rangle$  transition at energy  $\bar{\nu}$

[in  $\text{cm}^{-1}$ ]. The host independent RME values,  $\|U^\lambda\|$  are used in this calculation as obtained by Carnal *et al.* (Carnal *et al.*, 1968).

The absorption spectrum is used to estimate the experimental oscillator strengths ( $f_{exp}$ ) from the area under transition peaks from the GS ( $\Psi J$ ) to respective the ES ( $\Psi' J'$ ) using the following relation;

$$f_{exp} = 4.319 \times 10^{-9} \int \varepsilon(\bar{\nu}) d\bar{\nu} \quad (1.4)$$

Here  $\varepsilon(\bar{\nu})$  stands for molar absorptivity with wavenumber  $\bar{\nu}$  (in  $\text{cm}^{-1}$ ). The JO parameters are estimated using the least square fitting of correlation between  $f_{exp}$  and  $f_{cal}$  obtained from above Eq. (1.4) and from Eq. (1.3) where the forced electronic dipole transitions {solution to the correlation matrix} are calculated with the help of MATLAB (MATLABR12) commands at a suitable step. The J-O parameters ( $\Omega_i$ ) are estimated from absorption spectra for a particular  $\text{RE}^{3+}$  ion-doped host. The dependence of  $\Omega_2$  parameter is observed on the local neighborhood around the  $\text{RE}^{3+}$  ion as well as the covalence among  $\text{RE}^{3+}$  and ligand anions. The RE-O bonding is a hint of the asymmetry of the local neighborhood around  $\text{RE}^{3+}$  ions. Thus  $\Omega_2$  has a small value for ionic host material (fluoride glasses) while it is huge for covalent host materials. The  $\Omega_4$  is relatable to the viscosity and rigidity of the host material.

It is possible to find the JO intensity parameters  $\Omega_2$ ,  $\Omega_4$ , and  $\Omega_6$  by using a conventional least-square fitting method between the theoretical oscillator strengths  $f_{cal}$  and the experimental  $f_{exp}$  (Rai *et al.*, 2016). To ascertain the precision of the acquired intensity parameters, the equation (Manasa *et al.*, 2016) computes the root mean square (rms) deviation between  $f_{exp}$  and  $f_{cal}$ .

$$rms \Delta f = \sqrt{\frac{\sum_{i=1}^L (f_{exp} - f_{cal})^2}{L}} \quad (1.5)$$

where L is the total amount of bands that were employed in the absorption fit.

### 1.6.2. Radiative properties

The J-O parameters obtained from the absorption measurements can be used to describe the radiative properties of different excited fluorescent levels. The spontaneous emission probability for an electric dipole transition is expressed as (Rai



et al., 2016, Scholle *et al.*, 2004).

(i) Radiative transition probability  $A(aJ, bJ')$ : The radiative transition probability between an initial  $(|(S, L)J\rangle)$  and final  $(|(S', L')J'\rangle)$  manifold, assuming an electric-dipole allowed transition, can be computed from (Yang *et al.*, 2003):

$$A(aJ, bJ') = \frac{64\pi^4 e^2 n(n^2+2)^2}{3h\lambda^3 (2J+1)9} \sum_{\lambda=2,4,6} \Omega_{\lambda} \langle (S, L)J | U^{\lambda} | (S', L')J' \rangle^2 \quad (1.6)$$

Here  $\lambda$  stands for the average wavelength of transition.

(ii) Total radiative emission probability  $A_T$ : It is represented by the expression (Yang *et al.*, 2003) and represents the total radiative transition probability from a given energy level to all potential terminal states.

$$A_T(aJ) = \sum_{bJ'} A(aJ, bJ') \quad (1.7)$$

(iii) Fluorescence branching ratio  $\beta_R$ : This forecasts the intensity of fluorescence at any lasing transition and is represented as (Yang *et al.*, 2003):

$$\beta_R = \frac{A(aJ, bJ')}{A_T(aJ)} \quad (1.8)$$

(iv) Radiative lifetime  $\tau_R$ : It is expressed as (Yang *et al.*, 2003) and indicates how long the system remains in the excited condition.

$$\tau_R = \frac{1}{A_T(aJ)} \quad (1.9)$$

(v) Stimulated emission cross-section  $\sigma_P(\lambda_P)$ : The energy extraction efficiency from optical materials is evaluated by this crucial metric, which is provided by (Yang *et al.*, 2003):

$$\sigma_P(\lambda_P) = \frac{\lambda_P^4}{8\pi c n^2 \Delta \lambda_{eff}} A(aJ, bJ') \quad (1.10)$$

(vi) Figure of Merit (FOM): It is defined as follows and is utilized to assess the

bandwidth characteristics of optical fiber amplifiers (Yang *et al.*, 2003):

$$FOM = \Delta\lambda_{eff} X \sigma_P \quad (1.11)$$

### 1.6.3. Concentration Quenching

According to Dexter, when the concentration of the activator (acceptor) exceeds a critical threshold, the distance between activator ions becomes so small that energy transfer between them becomes possible. This allows the excitation energy to migrate through the lattice to sites where it is lost non-radiatively, known as killer sites, which may include impurities, defects, and surface sites. As a result, the fluorescence intensity is significantly reduced. Measurements of concentration-dependent lifetime and fluorescence intensity reveal the energy transfer mechanisms responsible for concentration quenching (Huang *et al.*, 2014) The fluorescence yield of rare earth (RE) ions exhibits such quenching above a certain concentration.

### 1.6.4 CIE- Color Coordinates

The chromaticity coordinates can be calculated from PL spectra of the samples by using Commission International de l'Eclairage (CIE) system (Vimal *et al.*, 2004). And their specific color appearance can be evaluated by CCT with Kelvin degree (K) (Vimal *et al.*, 2004). McCamy empirical expression was used to calculate the CCT values (Vimal *et al.*, 2004),

$$CCT = -449n^3 + 3525n^2 - 6823.3n + 5520.33 \quad (1.12)$$

where  $n = (x - 0.332)/(y - 0.186)$ .

All the multi chromatic wavelengths will fall within the area of chromaticity diagram. The color purity emitted by a source is obtained by taking the distance in the chromaticity diagram between the emission color coordinates and the coordinates of equal energy point, divided by the distance of separation between the equal energy point and the dominant wavelength point. Thus the color purity can be calculated with the following equation (Vimal *et al.*, 2004):

$$CP = \frac{\sqrt{(x-x_{ee})^2 + (y-y_{ee})^2}}{\sqrt{(x_d-x_{ee})^2 + (y_d-y_{ee})^2}} \quad (1.13)$$

where  $(x, y)$ ,  $(x_{ee}, y_{ee})$  and  $(x_d, y_d)$  are the chromaticity coordinates of the emission light, equal energy point and the dominant wavelength points respectively.

## Reference

- A. Bahtat, M. Bouazaoui, M. Bahtat, C. Garapon, B. Jacquier, J. Mugnier (1996), Up-conversion fluorescence spectroscopy in  $\text{Er}^{3+}:\text{TiO}_2$  planar waveguides prepared by a sol-gel process, *J. Non-Cryst. Solids*, **202**: 16-22.
- A. Bahtat, M. Bouazaoui, M. Bahtat, J. Mugnier (1994), Fluorescence of  $\text{Er}^{3+}$  ions in  $\text{TiO}_2$  planar waveguides prepared by sol-gel process, *Opt. Comm.* **111**: 55-60.
- A. Biswas, G.S. Maciel, C.S. Friend, P.N. Prasad (2003), Upconversion properties of a transparent  $\text{Er}^{3+}\text{-Yb}^{3+}$  co-doped  $\text{LaF}_3\text{-SiO}_2$  glass-ceramics prepared by sol-gel method, *J. Non-Cryst. Sol.* **316**: 393-397.
- A. Klausch, H. Althues, C. Schrage, P. Simon, A. Szatkowski, M. Bredol, D. Adam and S. Kaskel (2010), Preparation of luminescent  $\text{ZnS}:\text{Cu}$  nanoparticles for the functionalization of transparent acrylate polymers, *J. Lumin.* **130**: 692-697.
- A. Monteil, S. Chaussedent, G. Alombert-Goget, N. Gaumer, J. Obriot, S.J.L. Ribeiro, Y. Messaddeq, A. Chiasera, M.J. Ferrari (2004), Clustering of rare earth in glasses, aluminum effect: experiments and modeling, *J. Non-Cryst. Solids*, **348**: 44-50.
- A.A Talian, K.A. Dean, J.E. Jaskie (2001), Field emission displays: a critical review, *Solid State Electron*, **45**: 963-976.
- A.A. Kaminskii, L.K. Aminov, L. Ermolaev and E.B. Sveshnikova (1986), Physics and Spectroscopy of Laser Crystals, *Moskva Nauka, Russia*, 272.
- A.G.S. Filho, J. M. Filho, F. E. A. Melo, M. C. C. Custodio, R. Lebullenger and A. C. Hernandez (2000), Optical properties of  $\text{Sm}^{3+}$  doped lead fluoroborate glasses, *J. Phys. Chem. Solids*, **61**: 1535.
- A.K. Shahi, B.K. Pandey, B.P. Singh, B.K. Gupta, S. Singh and R. Gopal (2017), Photo physical studies of PVP arrested  $\text{ZnS}$  quantum dots, *Electron. Mater. Lett.* **13**: 160-167.
- B.G. Wybourne (1965), Spectroscopic Properties of Rare Earths, *John Wiley and Sons*, 220.

- B.M. Walsh (2006), Judd-Ofelt theory: Principles and practices, (Eds.) Di Bartolo B and Forte O., In: *Advances in spectroscopy for laser and sensing*, Springer, 403-433.
- B.R. Judd (1962), Optical absorption intensities of rare-earth ions, *Phys. Rev.* **197**: 750.
- C. Danping, Y. Luyun, P. Mingying, W. Chen, D. Ning, Q. Yanbo, Z. Quinling, Z. Congshan and T. Akai (2006), *J Rare Earth*, **24**: 191-195.
- C.B. Layne, W.H. Lowdermilk, M.J. Weber (1977), Multiphonon relaxation of rare earth ions in oxide glasses, *Phys. Rev. B*, **16**: 10–20.
- C.H. Huang, Rare Earth Coordination Chemistry: Fundamentals and Applications, 1st ed. Wiley, Asia 2010.
- C.J. Brinker, G.W. Scherer (1990), *Sol-Gel Science: The Physics and Chemistry of Sol-Gel Processing*, Academic Press, New York, 870.
- C.R. Ronda, T. Justel, H. Nikol (1998), Rare earth phosphors: fundamentals and applications, *J. Alloys Comp.* **275-277**: 669-676.
- C.S. Pathak and M.K. Mandal (2011), Optical properties of  $\text{Mn}^{2+}$  doped ZnS nanoparticles, *Asian J. Chem.* **23(10)**: 4655-4658.
- C.S. Pathak and M.K. Mandal (2011), Yellow light emission from  $\text{Mn}^{2+}$  doped ZnS nanoparticles, *Optoelectronic Adv. Mater. Rapid Comm.* **5(3)**: 211-214.
- C.S. Pathak, M.K. Mandal and V. Agarwala (2013), Synthesis and characterization of zinc sulphide nanoparticles prepared by mechanochemical route, *Superlattices Micros.* **58**: 135-143.
- C.S. Rao, K. Upendra Kumar, P. Babu and C.K. Jayasankar (2012), Optical properties of  $\text{Ho}^{3+}$  ions in lead phosphate glasses, *Opt Mater.* **35**: 102-107.
- D. Kakoti, P. Dutta, P. Gogoi, N. Dehingia, N. Rajkonwar, A. Boruah, A.T.T. Mostako, P.K. Saikia, P.K. Gogoi (2019), Effect of ZnS nanoparticles on the Judd-Ofelt and radiative parameters of  $\text{Sm}^{3+}$  ions in sol-gel silica matrix, *J. Lumin.* **211**: 401-412.
- D.V. Thai, P.V. Ben, T.M. Thi, N.V. Truong and H.H. Thu (2016), The photoluminescence enhancement of  $\text{Mn}^{2+}$  ions and the crystal field in ZnS:Mn nanoparticles covered by polyvinyl alcohol, *Opt. Quant. Electron.* **48**: 1-15.

- D.W. Synnott, M.K. Seery, S.J. Hinder, J. Colreavy and S.C. Pillai (2013), Novel microwave assisted synthesis of ZnS nanomaterials, *Nanotech.* **24**: 1-6.
- E. J Bosze, G.A. Hirata, L.E. Shea-Rohwer, J. McKittrick (2003), Improving the efficiency of a blue-emitting phosphor by an energy transfer from  $Gd^{3+}$  to  $Ce^{3+}$ , *J. Lumin.* **104**: 47-54.
- E. Snitzer (1961), Optical maser action of  $Nd^{3+}$  in a barium crown glass, *Phys. Rev. Lett.* **7**: 444-446.
- F. Amirian, M. Molaei, M. Karimipour and A. R. Bahador (2018), A new and simple UV-assisted approach for synthesis of water soluble ZnS and transition metals doped ZnS nanoparticles (NPs) and investigating optical and photocatalyst properties, *J. Lumin.* **196**: 174-180.
- F. Amirian, M. Molaei, M. Karimipour and A.R. Bahador (2018), Improvement of the optical and photocatalytic properties of ZnSe QDs by growth of ZnS shell using a new approach, *Materials Chemistry and Physics*, **206**: 76-84
- F. Auzel (1973), Materials and devices using double-pumped-phosphors with energy transfer, *Proc. IEEE*, **61**: 758-786.
- F. Auzel (1980), Multiphonon processes, cross-relaxation and upconversion in ion activated solids, exemplified by minilaser materials. (Eds.) Di Bartolo B., Goldberg V., In: *Radiation less Processes*, Plenum Publishing Co., New York, 213-286.
- F. Auzel (2004), Upconversion and Anti-Stokes Processes with f and d Ions in Solids, *Chem. Rev.*, **104**: 139-173.
- G. Lakshminarayana, J. Qiu (2009), Photoluminescence of  $Pr^{3+}$ ,  $Sm^{3+}$  and  $Dy^{3+}$ -doped  $SiO_2-Al_2O_3-BaF_2-GdF_3$  glasses, *J. Alloys Compd.* **476**: 470-476.
- G. Okada, B. Morrell, C. Koughia, A. Edgar, C. Varoy, G. Belev, T. Wysokinski, D. Chapman and S. Kasap (2011), *Appl. Phys. Lett.* **99**: 1211051.
- G. Vimal, Kamal P. Mani, P.R. Biju, Cyriac Joseph, N.V. Unnikrishnan, M.A. Ittyachen (2014), Synthesis, structural and spectroscopic investigations of nanostructured samarium oxalate crystals, *Spectro. Acta Part A: Molecular*

*and Biomolecular Spectroscopy*, **122**: 624–630.

G.H. Dieke (1968), Spectra and energy levels of rare earth ions in crystals, *Interscience Publishers*, 401.

G.J. Koch, M. Petros, J. Yu and U.N. Singh (2002), Precise wavelength control of a single-frequency pulsed Ho:Tm:YLF laser, *Appl. Opt.* **41**: 1718-1721.

G.S. Ofelt (1962), Intensities of crystal spectra of rare earth ions, *J. Chem. Phys.* **37**: 511.

H. L. Li, Z.L. Zhang, and J.H. Hao (2009), Red, green and blue low-voltage cathodoluminescence of rare-earth doped BaWO<sub>4</sub> phosphors, *Mater. Sci. Eng.* **1**: 012010.

H. You, M. Nogami (2004), Optical Properties and Local Structure of Eu<sup>3+</sup> Ions in Sol-Gel TiO<sub>2</sub>-SiO<sub>2</sub> Glasses, *J. Phys. Chem. B*, **108**: 12003-12008.

H.T. Yuen, J.C. Daniel and A.K. Terence (2004), H.T. Yuen, J.C. Daniel, A.K. Terence, High power 1.9  $\mu\text{m}$  Tm<sup>3+</sup>-silica fibre laser pumped at 1.09  $\mu\text{m}$  by a Yb<sup>3+</sup>-silica fibre laser, *Opt. Commun.* **231**: 357-364.

Hussein Fneich, Nathalie Gaumer, Stephane Chaussedent, Wilfried Blanc, Ahmad Mehdi (2018), Europium-Doped Sol-Gel SiO<sub>2</sub>-Based Glasses: Effect of the Europium Source and Content, Magnesium Addition and Thermal Treatment on Their Photoluminescence Properties, *Molecules*, **23(7)**: 1768.

I. Fanderlick (1991), Silica Glass and Its Applications, *Elsevier*, Amsterdam, 95.

I.I. Kindrat, B. V. Padlyak, B. Kuklinski, A. Drzewiecki and V. T. Adamiv (2019), Effect of silver co-doping on enhancement of the Sm<sup>3+</sup> luminescence in lithium tetraborate glass, *J. Lumin.* **213**: 290.

I.M. Thomas, S.A. Payne, G.D. Wilke (1991), Optical properties and laser demonstrations of Nd-doped sol-gel silica glasses, *J. Non-Cryst. Solids*, **151**: 183-194.

J. Bang, H. Yang, P.H. Holloway (2005), Enhanced luminescence of SiO<sub>2</sub>:Eu<sup>3+</sup> by energy transfer from ZnO nanoparticles, *J. Chem. Phys.* **123**: 084709-1-5.

J. Huang, S. Liu, B. Gao, T. Jiang, Y. Zhao, S. Liu, L. Kuang, X. Xu (2014), Synthesis and optical properties of Eu<sup>3+</sup> doped ZnO nanoparticles used for white light emitting diodes, *J. Nanosci. Nano.* **14**: 3052-3055.

- J. Livage, C. Opin (1997), Sol-gel processes, *Solid State Mater Sci.* **2**: 132-138.
- J. Rouxel and M. Tournoux, R. Brec (1994) Soft chemistry routes to new materials, *Trans Tech Publications in Aedermannsdorf, Switzerland*.
- J.H. Lee, D.N. Liu, S.T. Wu (2008), Introduction to Flat Panel Displays, *John Wiley & Sons: Chichester*.
- J.H. Van Vleck (1937), The Puzzle of Rare-earth Spectra in Solids, *J. Phys. Chem.* **41**: 67-80.
- J.P. Arago, B.J. Lopez, E.C.P. Escribano, F. Pelle, B. Vianab and C. Sanchezb (2008), Lanthanide doped ZnS quantum dots dispersed in silica glasses: an easy one pot sol-gel synthesis for obtaining novel photonic materials, *J. Mater. Chem.* **18**: 5193-5199.
- K. Arai, H. Namikawa, K. Kumata, T. Honda, Y. Ishii, T. Handa (1986), Aluminum or phosphorus co-doping effects on the fluorescence and structural properties of neodymium doped silica glass, *J. Appl. Phys.* **59**: 3430-3436.
- K. Scholle, E. Heumann and G. Huber (2004), Single mode Tm and Tm, Ho: LuAG lasers for LIDAR applications, *Laser Phys. Lett.* **1**: 285-290.
- K.K.R. Mukharjee (1978), Principles of Photochemistry, revised 2nd ed., *New Age International (P) limited, India*.
- L. Luo, F.Y. Huang, G.S. Dong, Y.H. Wang, Z.F. Hu, J. Chen (2016), White light emission and luminescence dynamics in  $\text{Eu}^{3+}/\text{Dy}^{3+}$  codoped ZnO nanocrystals, *J. Nanosci. Nano.* **16**: 619-625.
- L. Ozawa, Cathodoluminescence: Theory and Applications, Kodansha, VCH, Tokyo, Weinheim (1990) *Phosphor Handbook*, ed. S. Shionoya and W. M. Yen, CRC, Boca Raton, FL, 1999.
- L. Wang, X. Xu, X. Yuan (2010), Preparation and photoluminescent properties of doped nanoparticles of ZnS by solid-state reaction, *J. Lumin.* **130**: 137-140.
- L.E. Shea (1998), Low-Voltage Cathodoluminescent Phosphors, *Electrochem. Soc. Interface-Summer*, **7**: 24.
- L.E. Tannas, W. E. Glenn, and J.W. Doane (1995), Flat-Panel Display Technologies, *Noyes Publications: New Jersey*.



- L.Q. Minh, W. Streck, T.K. Anh, and K. Yu (2007), Luminescent Nanomaterials, *J. Nanomater.* **4**: 1.
- M. Cable (1984), Principles of Glass Melting, (Eds.) Uhlmann D.R., Kreidl N.J., In: *Glass Science and Technology*, **2**: 1-44.
- M. Chang, H. Zou, Y. Song, Y. Sheng, K. Zheng and X. Zhou (2016), Luminescence properties and Judd–Ofelt analysis of  $\text{TiO}_2\text{:Eu}^{3+}$  nanofibers via polymer-based electrospinning method, *RSC Adv.* **6**: 52113-52121.
- M. Locher, V. Romano, H. P. Weber (2005), Rare-earth doped sol–gel materials for optical waveguides, *Opt Lasers Eng.* **43**: 341-347.
- M. Nazarov, J.H. Kang, D.Y. Jeon, S. Bukesov, T. Akmaeva (2005), Synthesis and luminescent performances of some europium activated yttrium oxide based systems, *Opt. Mater.* **27**: 1587–1592.
- M. Taherian, A.A.S. Alvani, M.A. Shokrgozar, R. Salimi, S. Moosakhani H. Sameie and F. Tabatabaee (2014), *Electron. Mater. Lett.* **10**: 393-400.
- M. Yamane, Y. Asahara (2000), Glasses for Photonics, *Cambridge University Press*, 284.
- M. Venkateswarlu, Sk. Mahamuda, K. Swapna, M.V.V.K.S. Prasad, A. Srinivasa Rao, A. Mohan Babu, Suman Shakya, G. Vijaya Prakash (2015), Spectroscopic studies of  $\text{Nd}^{3+}$  doped lead tungsten tellurite glasses for the NIR emission at 1062 nm, *Optical Mater.* **39**: 8-15.
- M.C. Farries, P. R. Morkel and J. E. Townsend (1990), Spectroscopic and lasing characteristics of samarium doped glass fibre, *IEEE Proceedings*, **137**: 318.
- M.J. Lockhead, K.L. Bray (1995), Rare-earth clustering and aluminum co-doping in sol-gel silica: investigation using europium (III) fluorescence spectroscopy, *Chem. Mater.* **7**: 572-577.
- M.J. Weber (1966), Probabilities for Radiative and Non-radiative Decay of  $\text{Er}^{3+}$  in  $\text{LaF}_3$ , *Phys. Rev.* **157**: 262.
- M.J. Weber (1979), Solid State Lasers, *Methods of Experimental Physics*, **15**: 167-207.

- M.J. Weber (1990), Science and technology of laser glass, *J. Non-Cryst. Sol.* **123**: 208-222.
- M.T. Anderson, R.J. Walko, and M.L.F. Phillips (1995), Phosphors for flat panel emissive displays, *97<sup>th</sup> Annual Meeting of the American Ceramic Society*, 1-14.
- N. Rakov, G.S. Maciel, C.B. de Araujo, Y. Messaddeq (2002), Energy transfer assisted frequency upconversion in  $\text{Ho}^{3+}$  doped fluorindate glass, *J. Appl. Phys.*, **91**: 1272-1276.
- P. Dutta, S. Rai (2011), Optical transitions and frequency up-conversions of  $\text{Ho}^{3+}$  and  $\text{Ho}^{3+}/\text{Yb}^{3+}$  ions in  $\text{Al}(\text{NO}_3)_3\text{-SiO}_2$  sol-gel glasses, *Optik*, **122**: 858–863
- P. Manasa, C.K. Jayasankar (2016), Luminescence and phonon side band analysis of  $\text{Eu}^{3+}$  doped lead fluorosilicate glasses, *Opt. Mater.* **62**: 139–145.
- P. Psuja, D. Hreniak, and W. Strek (2007), Rare-Earth Doped Nanocrystalline Phosphors for Field Emission Displays, *J. Nanomater.* **81350**: 1-7.
- P. Yang, M.K. Lu, D.R. Yuan, C.F. Song, S.W. Liu and X.F. Cheng (2003), Luminescence characteristics of ZnS nanoparticles co-doped with  $\text{Ni}^{2+}$  and  $\text{Mn}^{2+}$ , *Opt. Mater.* **24**: 497.
- P.J. Dishingia, S. Rai (2012), Synthesis of  $\text{TiO}_2$  nanoparticles and spectroscopic upconversion luminescence of  $\text{Nd}^{3+}$ -doped  $\text{TiO}_2\text{-SiO}_2$  composite glass, *J. Lumin.*, **132**: 1243-1251.
- P.M. Aneesh, M.R. Shijeesh, A. Aravind and M.K. Jayaraj (2014), Highly luminescent undoped and Mn-doped ZnS nanoparticles by liquid phase pulsed laser ablation, *Appl. Phys. A*, **116(3)**: 1085-1089.
- P.P. Sorokin, M.J. Stevenson (1960), Stimulated infrared emission from trivalent uranium, *Phys. Rev. Lett.* **5**: 557-559.
- P.R. Rejikumar, P.V. Jyothy, S. Mathew, V. Thomas and N.V. Unnikrishnan (2010), Effect of silver nanoparticles on the dielectric properties of holmium doped silica glass, *Physica B*, **405**: 1513-1517.
- P.S. Peijzel, Meijerink A., Wegh R.T., Reid M.F., Burdick G.W. (2005), A complete  $4f^n$  energy level diagram for all trivalent lanthanide ions, *J. Solid State*

*Chem.*, **178**: 448-453.

- P.V. Jyothy, K.A. Amrutha, J. Gijo, N.V. Unnikrishnan (2009), Fluorescence Enhancement in Tb<sup>3+</sup>/CdS Nanoparticles Doped Silica Xerogels, *J. Fluor.* **19**: 165-168.
- P.V. Santos, M.V.D Vermelho, E.A. Gouveia, M.T. de Araujo, F.C. Cassanjes, S.J.L. Ribeiro, Y. Messaddeq (2001), Efficient energy upconversion emission in Tm<sup>3+</sup>/Yb<sup>3+</sup>-co-doped TeO<sub>2</sub>-based optical glasses excited at 1.064  $\mu$ m, *J. Appl. Phys.* **90**: 6550-6552.
- Ph. Goldner, and F. Pelle (1993), Site Selection and Upconversion Studies in Erbium and Ytterbium doped CsCdBr<sub>3</sub>, *J. Lumin.* **55**:197-207.
- R. Cases, M.A. Chamarro (1991), Judd-Ofelt analysis and multiphonon relaxations of rare earth ions in fluorohafnate glasses, *J. Solid State Chem.* **90**: 313-319.
- R. Moos, I.L. Graff, V.S. de Oliveira, W.H. Schreiner and A.G.B. Jr (2017), Influence of plasmon coupling on the photoluminescence of ZnS/Ag nanoparticles obtained by laser irradiation in liquid, *Opt. Mater.* **72**: 98-105.
- R. Palomino-Merino, A. Conde-Gallardo, M. Garcia-Rocha, I. Hernandez-Calderon, V. Castano, R. Rodriguez (2001), Photoluminescence of TiO<sub>2</sub>:Eu<sup>3+</sup> thin films obtained by sol-gel on Si and Corning glass substrate, *Thin Film Solids*, **401**: 118-123.
- R. Praveena, R. Vijaya, C.K. Jayasankar (2008), Photoluminescence and energy transfer studies of Dy<sup>3+</sup>-doped fluorophosphate glasses, *Spectrochimica Acta Part A: Molecular and Biomolecular Spectroscopy*, **70**: 577-586.
- R. Reisfeld, C.K. Jorgensen (1987), Excited State Phenomena in Vitreous Materials, *Elsevier Science Publishers*, **8**: 1-84.
- R. Scheps (1996), Upconversion laser processes, *Prog. Quant. Electr.* **20**: 271-358.
- R. Vijaya, V. Venkatramu, P. Babu, C. K. Jayasankar, U. R. Rodriguez-Mendoza and V. Lavin (2013), Spectroscopic properties of Sm<sup>3+</sup> ions in phosphate and fluorophosphate glasses, *J. Non. Cryst. Solids*, **365**: 85.
- R.M. Almeida, H.C. Vasconcelos, M.C. Goncalves, L.F. Santos (1998), XPS and NEXAFS studies of rare-earth doped amorphous sol-gel films, *J. Non-Cryst. Solids*, **232**: 65-71.
- R.V. Deun, K. Binnemans, C. Gorller-Walrand and J. L. Adam (1999), Judd-Ofelt

- intensity parameters of trivalent lanthanide ions in a  $\text{NaPO}_3\text{--BaF}_2$  based fluorophosphate glass, *Journal of Alloys and Compounds*, **283**: 59-65.
- S. Hazarika and S. Rai (2004), Structural, optical and non-linear investigation of  $\text{Eu}^{3+}$  ions in sol–gel silicate glass, *Opt. Mater.* **27**: 173-179.
- S. Rai and A.L. Fanai (2016), Optical properties of  $\text{Ho}^{3+}$  in sol-gel silica glass co-doped with Aluminium, *J. Non-Cryst. Sol.* **449**: 113-118.
- S. Hazarika, S. Rai (2004), Structural, optical and non-linear investigation of  $\text{Eu}^{3+}$  ions in sol–gel silicate glass, *Optical Materials*, **27**: 173-179.
- S. Rai, A.L. Fanai (2016), Effect of annealing and dopants concentration on the optical properties of  $\text{Nd}^{3+}:\text{Al}^{3+}$  co-doped sol–gel silica glass, *Journal of Luminescence*, **170**: 325-329.
- S.E. Stokowski, R.A. Saroyan, M.J. Weber (1981), Nd-doped Laser Glass Spectroscopic and Physical Properties, *Lawrence Livermore National Laboratory, University of California*, 15011789.
- S.R. Bullock, B.R. Reddy and P. Venkateswarlu (1997), Energy Upconversion and Spectroscopic Studies of  $\text{ZBLAN}:\text{Er}^{3+}$ , *Opt. & Quant. Electron.* **29**: 83-92.
- S.Y. Shionoya, W.M. Yen (1999), Phosphor Handbook, *CRC Press LLC: Boca Raton, Florida*.
- T. Fujiyama, M. Hori, M. Sasaki (1990), Preparation of Nd-doped silica glass by the sol-gel method, *J. Non-Cryst. Solids*, **121**: 273-278.
- T. Hayakawa, S.T. Selvan and M. Nogami (2000) Energy Transfer Between  $\text{Eu}^{3+}$  Ions and CdS Quantum Dots in Sol-Gel Derived  $\text{CdS}/\text{SiO}_2:\text{Eu}^{3+}$  Gel, *J. Sol-Gel Sci. & Technol.* **19**: 779-783.
- T.H. Maiman (1960), Stimulated optical radiation in ruby, *Natur.* **187**: 493-494.
- T.T. Nguyen (2007), The role of aluminium in rare earth-doped sol-gel silicate glasses Phd thesis, Department of Physics, Hamilton College, Clinton, NY 13323, U.S.A.
- T.T.Q. Hoa, N.D. The, S. McVitie, N.H. Nam, L.V. Vu, T.D. Canh and N.N. Long (2011), *Opt. Mater.* **33**: 308-314.
- U. Woggon (1997), Optical properties of Semiconductor Quantum Dots, Springer-Verlag, Berlin.
- V.K. Rai and C. B. D. Araujo (2008), Fluorescence intensity ratio technique for

- $\text{Sm}^{3+}$  doped calibo glass, *Spectrochim. Acta A*, **69**: 509.
- W.H. Zachariasen (1932), The atomic arrangement in glass, *J. Am. Ceram. Soc.* **54**: 3841-3851.
- W.T. Carnall, H. Crosswhite, H.M. Crosswhite (1978), Energy level structure and transition probabilities in the spectra of the trivalent lanthanides in  $\text{LaF}_3$ , Argonne National Laboratory Report no. ANL-78-XX-95.
- W.T. Carnall, P.R. Fields, K. Rajnak (1968), Electronic energy levels in the trivalent lanthanide aquo ions. I.  $\text{Pr}^{3+}$ ,  $\text{Nd}^{3+}$ ,  $\text{Pm}^{3+}$ ,  $\text{Sm}^{3+}$ ,  $\text{Dy}^{3+}$ ,  $\text{Ho}^{3+}$ ,  $\text{Er}^{3+}$ , and  $\text{Tm}^{3+}$ , *J. Chem. Phys.*, **49**: 4425-4442.
- X. Wang, H. Lin, D. Yang, L. Lin, E. Pun (2007), Optical transitions and upconversion fluorescence in  $\text{Ho}^{3+}/\text{Yb}^{3+}$  doped bismuth tellurite glasses, *J. Appl. Phys.* **101**: 113535-1-6.
- X. Wang, J. Shi, Z. Feng, M. Li and C. Li (2011), Visible emission characteristics from different defects of ZnS nanocrystals, *Phys. Chem. Chem. Phys.* **13**: 4715-4723.
- Xiaosheng Fang, Tianyou Zhai, Ujjal K. Gautam, Liang Li, Limin Wu, Yoshio Bando and Dmitri Golberg (2011), ZnS nanostructures: From synthesis to applications, *Prog. Mater. Sci.* **56**: 175-287.
- Y. Gao, S. Murai, K. Fujita and K. Tanaka (2018), Visible and near-infrared photoluminescence enhanced by Ag nanoparticles in  $\text{Sm}^{3+}$ -doped aluminoborate glass, *Opt. Mater.* **86**: 611.
- Y. Jiang, X.M. Meng, J. Liu, Z.Y. Xie, C.S. Lee and S.T. Lee (2003), *Adv. Mater.* **15**: 323; C. Ma, D. Moore, J. Li and Z.L. Wang (2003), *Adv. Mater.* **15**: 228; Z. W. Wang, L.L. Daemen, Y.S. Zhao, C.S. Zha, R.T. Downs, X.D. Wang, Z.L. Wang and R.J. Hemley (2005), *Nat. Mater.* **4**: 922; Y.F. Hao, G.W. Meng, Z.L. Wang, C.H. Ye and L.D. Zhang (2006), *Nano Lett.* **6**: 1650.
- Y. Kayanuma (1988), Quantum-size effects of interacting electrons and holes in semiconductor microcrystals with spherical shape, *Phys. Rev. B*, **38**: 9797-9805.
- Y. Zhang, F. Lu, Z. Wang, H. Wang, M. Kong, X. Zhu, L. Zhang (2007), ZnS Nanoparticle-Assisted Synthesis and Optical Properties of ZnS Nanotowers,

*Cryst. Growth Des.* **7(8)**: 1459-1462.

Y.J. Zhang, Y.Z. Wang, Y.L. Ju and B.Q. Yao (2005), *Laser Optoelectron. Prog.* **42**:

34.

## CHAPTER 2

### EXPERIMENTAL TECHNIQUES

---

#### 2.1. Introduction

This chapter is embodied with the experimental process relevant to the present work. Here sol-gel synthesis method is discussed in detail for understanding crucial point considered for material synthesis along with different precursor and useful instruments.

The experimental procedure pertinent to the current work is represented in this chapter. It has many parts and subsections that deal with the structural characteristics of the solid sample that was made using the sol-gel process as well as the UV-Vis and IR spectra of absorption or fluorescence of a solid or liquid sample. In this chapter we study briefly the experimental details of the work while providing sufficient information for the work to be replicated. The structural characterization of the samples is discussed with X-Ray Diffraction (XRD), and Fourier-transform infrared spectroscopy (FTIR). The morphology of the samples is studied with Transmission Electron Microscopy (TEM) and Scanning Electron Microscopy (SEM). A brief theoretical background and working procedure of each technique is discussed in detail with image of each instrument. The optical characterizations are performed with recording Absorption spectra and Photoluminescence spectra. Due to limitation of availability of facilities recording of XRD, SEM and TEM were done in other institution while sample preparation, FTIR, refractive index measurements and optical spectroscopy were done in our own laboratory.

#### 2.2. Preparation of glass samples

##### 2.2.1. Precursors and starting material

Following precursors and materials are used in sol-gel synthesis of pair of  $\text{RE}^{3+}$  ions codoping in Alumino-silicate, Titania-Silicate, Zinc-Silicate and Zinc sulphide host.

### 2.2.1.1. Precursor

All of the compounds employed in this investigation were analytical grade, and no additional purification was required. Tetraethyl orthosilicate (TEOS; Sigma-Aldrich 99%),  $RE^{3+}$  (i.e. Neodymium chloride hexahydrate ( $NdCl_3 \cdot 6H_2O$ ; Sigma Aldrich, 99.9%), Samarium oxide ( $Sm_2O_3$ , Sigma-Aldrich 99.9%)), methanol (MeOH; Merck, 99.8%), Europium (III) chloride hexahydrate ( $EuCl_3 \cdot 6H_2O$ ; Sigma Aldrich, 99.9%), Aluminum Nitrate nitrate-hydrate ( $Al(NO_3)_3 \cdot 9H_2O$ , Merak), Titanium isopropoxide (TIPO; Sigma Aldrich, 99%), Zinc sulphide ( $ZnS$ ; Sigma Aldrich, 99.5%), Zinc acetate dehydrate ( $Zn(CH_3COO)_2 \cdot 2H_2O$ ) Sigma Aldrich, 97%), nitric acid ( $HNO_3$ ; Sigma-Aldrich 70%), N, N-dimethyl formamide (DMF; Merck 99.5%) and banana trunk sap were purchased and used as such.

### 2.2.1.2. Materials

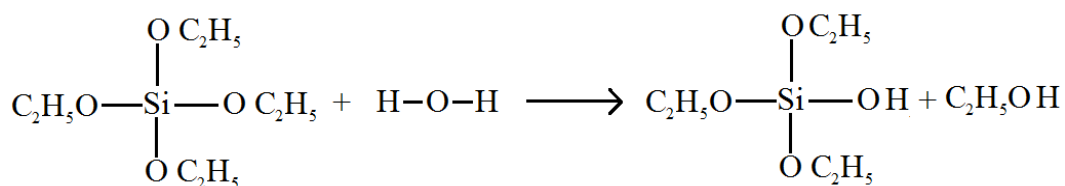
Glass vessel (10 ml), Dropper (2.5 ml), Electric muffle furnace, Magnetic stirrer cum hot plate, Polypropylene container, Spin Coater, Substrate (Si wafer, Quartz plate, Borosilicate glass etc.) and Plastic Container.

### 2.2.2. Synthesis process

#### 2.2.2.1. Alumino-silicate and Titania-silicate binary host for $RE^{3+}$ ion doping

For the preparation of the glass samples, sol-gel technique is followed in which the silica host is formed as a result of hydrolysis of tetraethyl orthosilicate (TEOS). The formation of the silica network can be explained in the following simplified reaction steps.

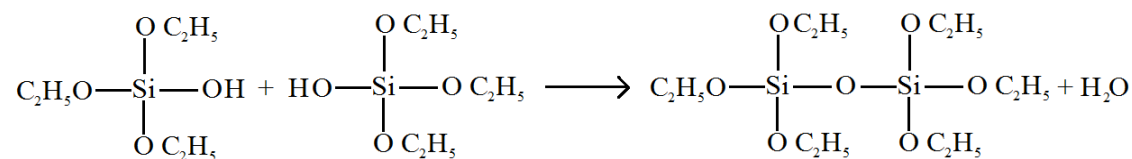
First is the hydrolysis in which the TEOS reacts with water where the ethoxy group in the TEOS is replaced by Hydroxyl group thereby producing its silanol and ethyl alcohol as the by-product.



When two such silanols come together, a Si-O-Si bond is formed with water



as the by-product, the process of condensation.



When the hydrolysis and condensation occurs at various ethoxy sites, a long three dimensional network of Si-O-Si is formed and causes increase in the viscosity resulting in the gelation and solidification.

For synthesizing the RE doped samples, required amount of the RE compound (oxides, fluorides, chlorides or nitrates), depending on the concentration desired is dissolved in deionized water by stirring in a magnetic stirrer for 20 minutes. Samarium oxide ( $\text{Sm}_2\text{O}_3$ ) is also hard to dissolve, and requires heating in the presence of Aluminium Nitrate ( $\text{Al}(\text{NO}_3)_3 \cdot 9\text{H}_2\text{O}$ ) for dissolving completely. Other RE compounds are in the form of their chloride or nitrate salts which dissolve readily.

After dissolving, TEOS,  $\text{C}_2\text{H}_5\text{OH}$ , and a little quantity of  $\text{HNO}_3$  are added to reduce the pH and speed up hydrolysis. Using a magnetic stirrer, the combination of TEOS, banana trunk sap,  $\text{C}_2\text{H}_5\text{OH}$ , and  $\text{HNO}_3$  in the molar ratio 1:5.5:3.5:0.1 with the dissolved dopants is stirred for one hour to produce a sol (Fig. 2.1(a)). In most cases, 3 ml of TEOS is used per sample while maintaining the mentioned molar ratio between the constituents. For samples co-doped with Aluminum, required amount of  $\text{Al}(\text{NO}_3)_3 \cdot 9\text{H}_2\text{O}$  is added along with the RE compound in the initial dissolving process. For samples containing  $\text{TiO}_2$  nanoparticles titanium isopropoxide (TIPO) is added dropwise while stirring vigorously after 10 minutes of adding TEOS. Continuous stirring while adding TIPO is necessary to avoid agglomeration.

The sol is stirred, then transferred into tiny plastic containers, sealed to prevent evaporation, and kept undisturbed. After a few days, the sol begins to solidify and forms a gel which takes the shape of the container. Slow evaporation of the residual ethanol, water etc. is allowed during the ageing process, resulting in the shrinkage of the gel. Slow evaporation is necessary to prevent non-uniform shrinkage from causing the sample to become broken and distorted. After two weeks of ageing in room temperature, highly porous stiff gels are obtained which are then

heated/annealed in muffle furnace (Fig. 2.1(b)), initially very gradually in the room temperature to 100 °C range, and then at the rate of 1 °Cmin<sup>-1</sup> afterwards. After 900 °C the pores begin to collapse and further shrinkage occurs so the rate of heating is reduced to 0.5 Cmin<sup>-1</sup> to avoid uneven shrinking. Heating is done upto 1050 °C after which densified glass samples are obtained. Simplified flow chart of the synthesis process is shown in Fig. 2.2.

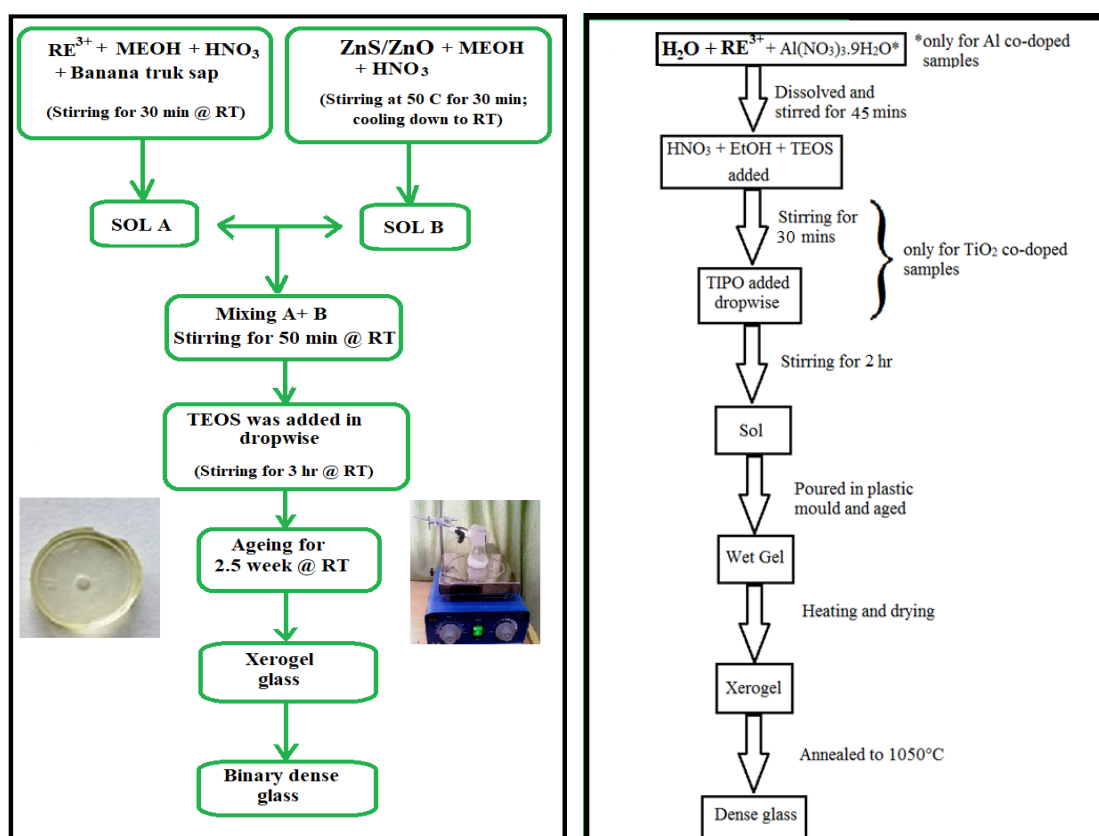
#### **2.2.2.2. ZnS/ZnO-SiO<sub>2</sub> binary host for RE<sup>3+</sup> ions doping**

The sol-gel technique was used to manufacture ZnS/ZnO and RE<sup>3+</sup> ions doped ZnS/ZnO in silicate dense glass-ceramic integrated with different modifiers.

Starting materials *i.e.* pure zinc sulphide (ZnS) or zinc oxide (ZnO), and RE<sup>3+</sup> ions were precisely weighed in accordance with the composition of each glass. To fabricate RE<sup>3+</sup> doped silica matrices, we used tetraethyl orthosilicate (TEOS) as the precursor, methanol as the mutual solvent, nitric acid as the catalyst, and N,N-dimethyl formamide (DMF) as the drying control chemical additive (DCCA). These components were combined with banana trunk sap in a volumetric ratio of 8:10:2:5:20 (Puia *et al.*, 2024). The prepared samples contain both RE<sup>3+</sup> and ZnS/ZnO in sol-gel silicate glasses respectively. First, methanol and nitric acid, were combined with the dopants (ZnS/ZnO) and stirring at 50 °C for 50 minutes and cooling down to room temperature. Secondly, methanol, nitric acid and banana trunk sap and stirring for 40 minutes at room temperature. And then the two solution were mixing together and stirring for 30 minutes. After that adding TEOS was added in dropwise and stirred for an additional 50 minutes. The mixture was stirred for 40 minutes, or until the gelation began, after adding the DMF. After 20 days at room temperature, the final solution was converted into the xerogel samples in a sealed container. Initially, a hot air oven was used to gradually dry the xerogel samples from room temperature to 150 °C (Puia *et al.*, 2024). The samples were then annealed in an electric muffle furnace at a controlled rate of 1 °C/min to a final temperature of 1030 °C (Bharadwaj *et al.*, 2023).



**Fig. 2.1:** (a) A magnetic stirrer is used to stir a mixture in the proper ratio and (b): Muffle furnace used for annealing.



**Fig. 2.2:** (a) Flow chart of sample preparation of alumino-silicate and titania-silicate host and (b) Flow chart of sample preparation of Zinc oxide and Zinc Sulphide host.

For samples co-doped with Aluminum, required amount of  $\text{Al}(\text{NO}_3)_3 \cdot 9\text{H}_2\text{O}$  is added along with the RE compound in the initial dissolving process. For samples containing  $\text{TiO}_2$  nanoparticles titanium isopropoxide (TIPO) is added dropwise while stirring vigorously after 10 minutes of adding TEOS. Continuous stirring while adding TIPO is necessary to avoid agglomeration.

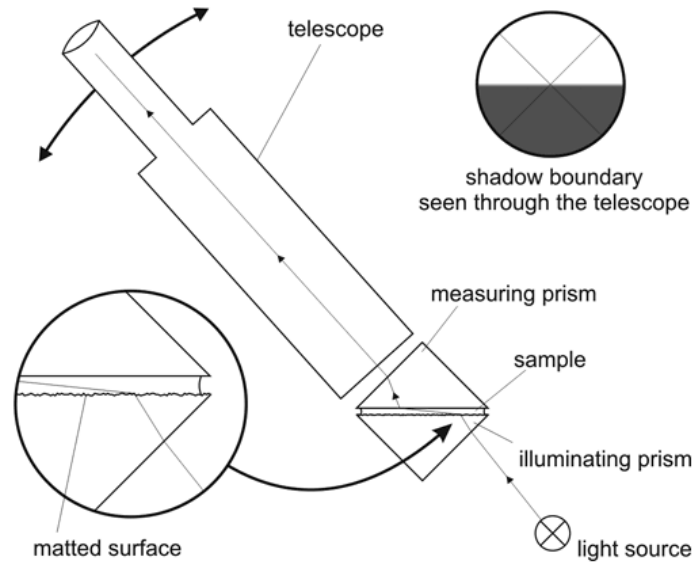
After stirring, the sol is poured into small plastic containers and then sealed to control evaporation and is left undisturbed (Rai *et al.*, 2014). After a few days, the sol begins to solidify and forms a gel which takes the shape of the container. Slow evaporation of the residual ethanol, water etc. is allowed during the ageing process, resulting in the shrinkage of the gel. Evaporation has to be very slow; otherwise non-uniform shrinkage can lead to deformed and cracked sample (Rai *et al.*, 2014). After two weeks of ageing in room temperature, highly porous stiff gels are obtained which are then heated/annealed in muffle furnace (Fig. 2.1), initially very gradually in the room temperature to 100 °C range, and then at the rate of 1 °C/min afterwards. After 900 °C the pores begin to collapse and further shrinkage occurs so the rate of heating is reduced to 0.5 °C/min to avoid uneven shrinking. Heating is done upto 1060 °C after which densified glass samples are obtained. Simplified flow chart of the synthesis process is shown in Fig. 2.2.

### **2.3. Measurement of refractive index**

The Abbe refractometer, invented by Ernst Abbe (1840-1905), was the first laboratory instrument designed for the precise measurement of the refractive index of liquids and solids. This device operates based on the principle of total reflection. In an Abbe refractometer, reference media glasses (prisms) with high refractive indices can be selected. To perform a measurement, light from a radiation source is directed by a mirror onto a double prism. A few drops of the sample are placed between the two prisms. The incident light passes through the double prism and sample only if its angle of incidence at the interface is less than the critical angle for total reflection. The light/dark boundary line, or shadow line, is then determined using a microscope and a mirror equipped with an appropriate mechanism.

The Abbe refractometer is the easiest-to-use and most popular type. Fig. 2.3

shows a schematic diagram of its optical system. In this device, the sample is enclosed in a thin layer ( $\sim 0.1$  mm) between two prisms. A side arm (indicated by dotted lines) allows the upper prism to rotate, as it is securely attached to a bearing. The hinge connecting the bottom and top prisms enables them to be separated for easy sample insertion and cleaning. The lower prism face is rough-ground, making it an effective source for an infinite number of rays when light is reflected into the prism. These rays pass through the sample at various angles. The radiation is refracted at the interface between the sample and the smooth-ground face of the upper prism before passing into the fixed telescope. Two Amici prisms, which can be rotated relative to each other, collect the divergent critical angle rays of different colors into a single white beam, corresponding to the sodium D line. The telescope's eyepiece is equipped with crosshairs. During measurement, the prism angle is adjusted until the light-dark interface coincides with the crosshairs. The prism's position is then read from a fixed scale, typically graduated in units of  $n_d$ . Temperature control is achieved by circulating water through jackets surrounding the prisms. The Abbe refractometer is highly popular due to its convenience, wide measurement range ( $n_d = 1.3$  to  $1.7$ ), and minimal sample requirement (Meeteen *et al.*, 1999). The instrument's accuracy is approximately  $\pm 0.0002$ , with a precision of half this value (Meeteen *et al.*, 1999). The most significant error in the Abbe instrument arises from nearly grazing rays being cut off by the prism arrangement, resulting in a less sharp boundary than desirable. A precision Abbe refractometer, which reduces the uncertainties of the standard instrument by a factor of three, is also available. This enhanced accuracy is achieved by replacing the compensator with a monochromatic light source and utilizing larger, more precise prism mounts. The monochromatic light source provides a much sharper critical boundary, while the precise mounts enable more accurate determination of the prism position.



**Fig. 2.3:** The working principle of an Abbe refractometer.

#### 2.4. Density and porosity

The Archimedes principle may be used to calculate a sample's density. According to this principle “the upward buoyant force that is exerted on a body immersed in a fluid, whether fully or partially, is equal to the weight of the fluid that the body displaces”. The weight and volume of the sample in the air may be measured using the following relation to get the experimental density (Rai *et al.*, 2015):

$$\rho \left( \frac{g}{cm^3} \right) = \left[ \frac{W_a}{W_{Va} - W_{Vb}} \right] \quad (2.1)$$

Where  $W_a$  is the glass sample's weight in air,  $W_{Va}$  is the glass sample's volume after immersion in xylene, and  $W_{Vb}$  is the volume prior to immersion.

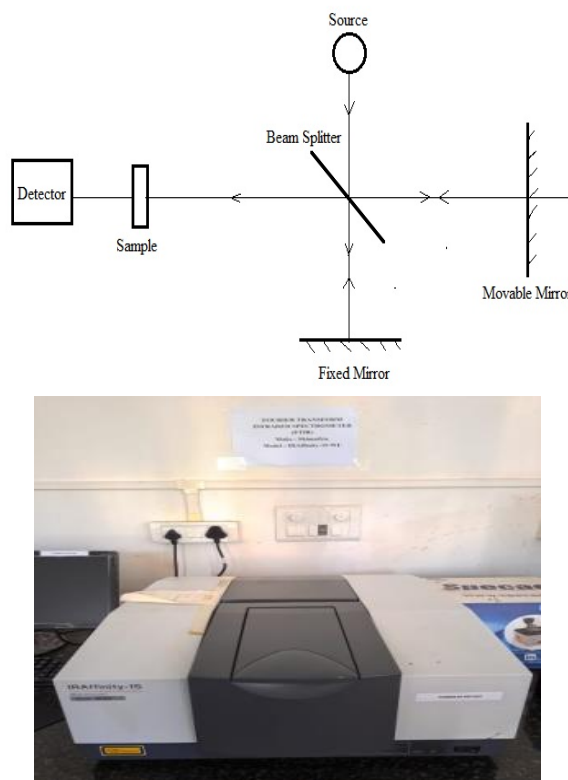
The relative volume of the pores that are present in the material is known as its porosity. For the sample, the porosity is computed as,

$$p = \frac{\rho_x - \rho}{\rho_x} \times 100 \% \quad (2.2)$$

Where  $\rho$  is the sample's experimental density and  $\rho_x$  is its relative density.

## 2.5. Fourier Transform Infrared Spectroscopy (FTIR)

Fourier transform infrared (FTIR) spectroscopy is a powerful technique for identifying both organic and inorganic compounds. It can quantify unknown mixtures and analyze both solid and liquid samples. FTIR works by transforming data collected from an interference pattern into a spectrum. This method is especially useful for identifying chemical bonds, such as hydrogen bonds. In FTIR spectra, infrared absorption is displayed as a function of vibrational frequency, expressed in  $\text{cm}^{-1}$ . Fig. 2.4(a) shows the experimental setup of a Michelson Interferometer used in FTIR spectroscopy. This setup includes a fixed mirror, a beam splitter, and a movable mirror. A beam of light from an infrared source hit the beam splitter, which directs one part of the beam to the fixed mirror and the other part to the movable mirror. Both mirrors then reflect the beams back through the beam splitter, through the sample, and finally to the detector. The movable mirror creates a path difference between the two split beams, resulting in constructive and destructive interference. Fig. 2.4(b) shows the FTIR spectra recorded by the IRAffinity-1S (SHIMADZU) in the Department of Chemistry at MZU (Rai *et al.*, 2015).

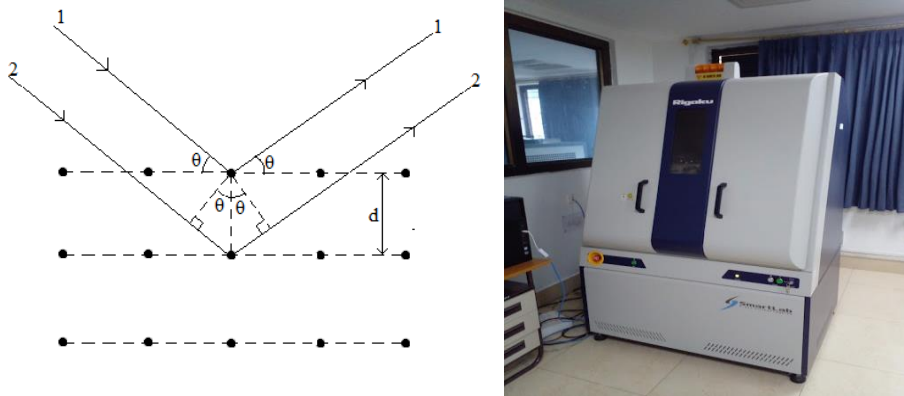


**Fig. 2.4:** (a) Schematic diagrams and (b) Image of FTIR spectrophotometer

## 2.6. X-Ray Diffraction (XRD) analysis

XRD analysis is one of the most extensively used techniques for structural study of materials. Its working principle is based on Bragg's law which gives the relation for the condition of constructive interference of the X-ray beams diffracted by the crystal lattice. If two parallel X-ray beams 1 and 2 are diffracted by the first and second lattice planes of a crystal (Fig. 2.5) having spacing 'd' between the lattice planes, then for constructive interference to occur between the diffracted beams, the path difference should be a whole number multiple of the wavelength of the X-ray. If  $\lambda$  is the wavelength of the X-ray and  $\theta$  is the angle between the X-ray beams and the lattice plane, then the condition for constructive interference is given by Bragg's law expressed mathematically as (Connolly *et al.*, 2007):

$$2d \sin \theta = n\lambda \quad (2.3)$$



**Fig. 2.5:** (a) Diffraction of radiation by crystal planes and (b) Image of X-Ray diffractometer.

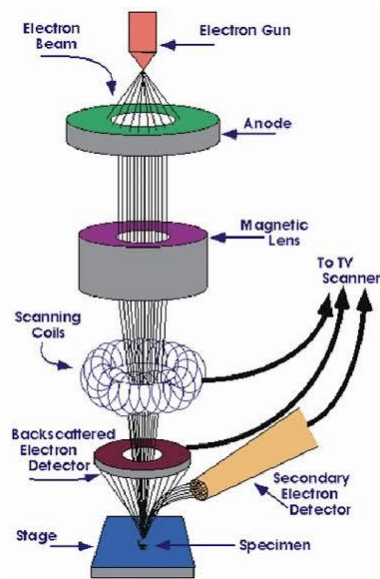
Since the Bragg angles in XRD analysis can be determined from the wavelength of the X-ray, it is possible to determine the distance between the crystalline planes. Crystals may be used to determine the composition of materials since they exhibit distinctive XRD patterns. Amorphous materials however lack the sharp peaks of crystals due to the irregular arrangement. In case of silica glass for example, the sharp peaks of crystalline  $\text{SiO}_2$  (quartz) are merged into a broad peak. The peaks of crystalline samples can also be broadened as the crystallite size decreases and this broadening can be used to estimate the crystallite size using Scherrer formula.



In this study, finely powdered samples were analyzed using an X-ray diffractometer (Model: INEL C120) at the Department of Physics, BHU, Varanasi. The X-ray source is  $\text{CuK}\alpha$  radiation having wavelength ( $\lambda_{\text{ex}}=1.5406 \text{ \AA}$ ).

## **2.7. Scanning electron microscopy (SEM)**

Scanning electron microscopy (SEM) is an invaluable tool for imaging the surfaces of nearly any material, providing high magnification and resolution through the use of an electron beam. The resolution achieved by SEM depends on both the properties of the electron probe and its interaction with the specimen. When the electron beam interacts with the specimen, it generates secondary or backscattered electrons, typically with energies less than 50 eV (Kirk *et al.*, 2009). Additionally, x-rays are emitted when the electron beam strikes the sample, providing information characteristic of the sample's atomic composition. If an x-ray spectrometer is attached, these x-rays can be analyzed using energy dispersive x-ray spectroscopy (EDX). Field Emission SEM offers high-resolution images ideal for examining defects, surface morphology, stains, grain size, particle distribution, and porosity in materials and coatings. This technique provides outstanding image resolution, distinctive image contrast, and a significant depth of field. In this study, SEM images of phosphor powders were acquired using the JEOL-JSM 7500F Field Emission Scanning Electron Microscope (FESEM). Fig. 2.6 illustrates a schematic diagram of the scanning electron microscope.



**Fig. 2.6:** (a) Schematic diagram (b) Image of FESEM.

## 2.8. Energy Dispersive X-ray (EDX) Spectroscopy

Energy dispersive X-ray analysis is a crucial technique for determining the composition of a sample. It characterizes the sample by analyzing the X-rays emitted and scattered during interactions with electromagnetic radiation. Each element in the periodic table has a unique electronic configuration, leading to specific responses to electromagnetic waves, which are utilized in this analysis.

In this technique, a beam of electrons or photons is directed onto the sample under investigation. This energy excites electrons initially at rest within the sample, particularly those in inner shells. This excitation forms electron holes within the atom's electronic structure, which can subsequently be filled by electrons from outer shells. The energy difference between these electron transitions is emitted as X-rays. These X-rays produce highly specific spectral lines unique to each element. The emitted X-ray data are plotted as a graph of counts versus energy and their analysis leads to characterization of the sample.

The electron gun includes a tungsten cathode filament, a Whnelt electrode, and an anode. It emits an electron beam thermionically from the tungsten filament cathode. The whnelt cylinder which is negatively biased against the cathode causes a cross-over of the primary electron beam. The cross-over acts as a virtual electron source with a diameter between 25  $\mu\text{m}$  and 100  $\mu\text{m}$ , depending on the geometry and

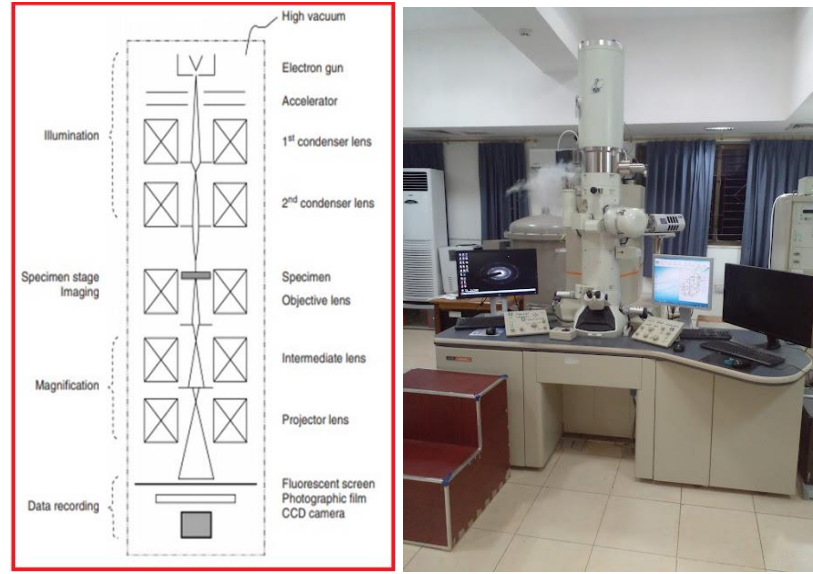
the applied electric field. The emitted electrons are accelerated from cathode to anode. The electron beam, usually ranging in energy from 0.2 keV to 40 keV, is focused by one or two condenser lenses to achieve a spot size of approximately 0.4 nm to 5 nm in diameter. As the beam reaches the final lens, it passes through pairs of scanning coils or deflector plates in the electron column, which deflect it along the x and y axes. Therefore, the scan coils allow a line-by-line scan of the sample surface by the electron beam. The beam finally hits the sample surface and secondary electrons are generated.

A scintillator-photomultiplier combination detects secondary electrons generated, producing a voltage signal of specific intensity. This voltage is carried out of the microscope column to an electronic console where it is processed and amplified, generating a bright spot on a cathode ray tube (CRT) screen. Each spot on the CRT corresponds to the beam's position on the specimen in the microscope, creating a distribution map of emitted signals from the scanned area. The image can also be captured using standard photography.

## **2.9. Transmission electron microscopy (TEM)**

TEM is used to obtain the micro structural images of materials at much higher resolution than optical microscope. This is possible as a result of the much shorter wavelength (about four orders of magnitude) of electrons in electron microscope compared to visible light. The working of TEM is analogous to that of optical microscope. In TEM electron rays replace visible light rays, and glass lenses are substituted with electromagnetic lenses. A schematic diagram of TEM is shown in Fig. 2.7. For TEM analysis, the samples should be very thin to allow the transmission of electrons i.e. electronically transparent.

Furthermore, the particle nanostructure and selected area electron diffraction (SAED) patterns of the nano-composites were analyzed using FEI Tecnai high-resolution transmission electron microscopy (HR-TEM) with an acceleration voltage of 300 kV at Banaras Hindu University, Varanasi.



**Fig. 2.7:** (a) Schematic diagram (b) Image of FETEM.

## 2.10. Optical spectroscopic measurements and Instrumentation

### 2.10.1. Ultraviolet-Visible (UV-VIS) absorption spectroscopy

In UV-VIS absorption spectroscopy, electrons are excited from the valence band to the conduction band by absorbing photons within the UV-VIS range. This technique is employed to determine the optical bandgap, where the absorption coefficient ( $\alpha$ ) is calculated using the following relation:

$$\alpha = \frac{2.303 \times \log(\text{absorption})}{\text{thickness of the sample}} \quad (2.4)$$

### Tauc Plot

The relationship between the absorption coefficient ( $\alpha$ ) and the incident photon energy ( $h\nu$ ) can be expressed as follows:

$$\alpha h\nu = A(h\nu - E_g)^n \quad (2.5)$$

Here,  $A$  is a constant and  $E_g$  represents the bandgap energy of the material. For materials with direct band gaps ( $n = \frac{1}{2}$ ) and indirect band gaps ( $n = 2$ ), the value of  $n$  differs. The optical bandgap is determined by extrapolating the linear portion of the Tauc plot specific to each type of band gap.

### **2.10.2. Photoluminescence (PL) Spectra**

PL spectra represent the emission from luminescent materials, where electrons are excited from the valence band to the conduction band upon absorbing photons from a laser with energy greater than the material's band gap. This non-destructive technique is used to study the electronic structure of semiconductor materials, including the nature of structural and compositional defects such as unintentional dopants and surface-related defects. The presence of impurity level and its position also identified from PL spectra. The light sources are aligned at  $90^\circ$  geometry to the sample as in Fig. 2.8(a).

In direct band gap semiconductors like  $\text{TiO}_2$ , electrons in the conduction band quickly relax by emitting photons that correspond to the material's band gap. Similarly, in direct band gap semiconductors such as  $\text{ZnS/ZnO}$ , electrons in the conduction band also relax rapidly by emitting photons corresponding to the semiconductor's band gap. Electrons may also recombine with defects and perturbations within the lattice structure of the material, such as valence band holes. These additional energy states affect the energy of the emitted photons.

### **2.10.3. CIE diagram**

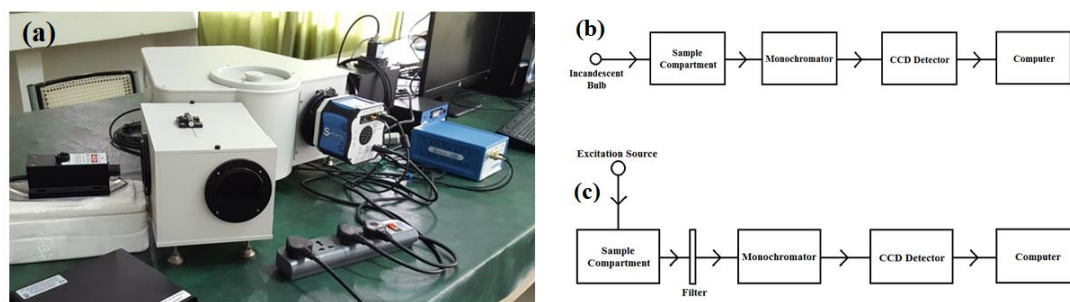
The CIE 1931 color spaces established the initial quantitative connections between the distribution of wavelengths in the visible spectrum and the physiological perception of colors in human vision. These mathematical relationships are fundamental tools in color management, crucial for applications involving illuminated displays, color inks, and recording devices like digital cameras.

The CIE diagram is representing each possible color with a pair of numerical

co-ordinates (x, y) hue and saturation (also called colorfulness) respectively. The mixing of different colors of light can be observed. The purity of the resultant color from luminescent material are geometrically from the CIE diagram.

#### 2.10.4. Instrumentation

For recording the optical spectra of the prepared samples iHR320 imaging spectrometer (Horiba) is used which is fitted with CCD detector (Fig. 2.8). The spectrometer has a separate sample compartment which is highly customizable for diverse sample types. It does not have an inbuilt light source, so appropriate external sources have to be used.



**Fig. 2.8:** (a) iHR320 imaging spectrometer used for recording absorption and emission spectra, (b) block diagram showing arrangement for recording absorption spectrum and (c) block diagram showing arrangement for recording PL spectrum.

To record absorption spectra, an incandescent light bulb is typically used as the light source due to its broad continuous spectral range from visible to near-infrared regions. However, its emission in the ultraviolet (UV) region is very weak, making it unsuitable for UV absorption spectra recording. Therefore, absorption measurements are limited to the visible and near-infrared regions. In the setup, the sample is positioned in the sample compartment so that external light falls on it and passes to monochromator (see Fig. 2.8). The entrance slit of the monochromator is adjusted to optimize the amount of light entering and reaching the detector. The monochromator then separates the incident light into different wavelength components, and a CCD detector records the intensity of each wavelength within the

desired range. The same procedure is followed again, but with an un-doped reference sample in place of the doped glass sample. The reference sample is pure silica glass prepared in a similar way to the RE doped samples, but without any dopants added. The reading for the reference and the sample is then compared and analyzed using the computer software to obtain the absorption spectrum.

To measure the photoluminescence (PL) spectrum, the sample in the sample compartment is excited by appropriate light source at  $90^\circ$  angle to minimize the amount of excitation light rays entering the monochromator (Fig. 2.8). Filters may also be used for this purpose to remove lights of unwanted wavelengths. The intensities of the various wavelength components of the photoluminescence emission from the sample are then recorded as mentioned above. The sensitivity of the CCD detector falls sharply beyond 1100 nm and so the spectra recorded are limited to this wavelength range.

## Reference

- G.H. Meeteen (1999), Refractive index measurement, *Schlubger Cambridge Research*, CRC press LLC.
- J. Rheims, J. Koser and T. Wriedt (1997), Refractive-index measurements in the near-IR using an Abbe refractometer, *Meas. Sci. Technol.* **8**: 601–605.
- J.R. Connolly (2007), for EPS400-002, Introduction to X-Ray Powder Diffraction, *Springer*,
- K. Schmidt and A. Penzkofer (1983), Refractive-index measurements with a Pellin–Broca prism apparatus, *Appl. Opt.* **22**: 1824–1827.
- L. Puia, S. Rai (2024), Structural and Spectroscopic Studies of  $\text{Sm}^{3+}$  Ions Doped ZnS Nanoparticle in Silica Glass Matrix, *Indian Journal of Science and Technology*, **17(9)**: 773-779.
- Mrigankadeep Bharadwaj, S. Rai, Ankita Gaur (2023), Structural and morphological characterizations of *ex-situ* sol-gel derived luminescent  $\text{Nd}^{3+}$ - $\text{Yb}^{3+}$  ion co-doped zinc-silicate dense glass-ceramic, *Journal of Non-Crystalline Solids*, **619**: 122552
- S. Rai and A.L. Fanai (2014), Spectroscopic studies of  $\text{Ho}^{3+}$  doped  $\text{SiO}_2$ - $\text{TiO}_2$  nanoparticle for photonic applications, *Sci. Vis.* **14**: 112-117.
- S. Rai and A.L. Fanai (2015), Structural and spectroscopic studies of sol gel silica doped with  $\text{Er}^{3+}$  and  $\text{TiO}_2$  nanoparticle for photonic applications, *Science and Technology Journal*, **3**: 68-72.
- T.L. Kirk, U. Ramsperger, L.G. De Pietro, H. Cabrera, T. Bahler (2009), Near field emission scanning electron microscopy, *Journal of Vacuum Science & Technology B Microelectronics Processing and Phenomena*, 1600-1607.



## CHAPTER 3

### INVESTIGATION ON Sm<sup>3+</sup> DOPED (Al<sub>2</sub>O<sub>3</sub>, TiO<sub>2</sub>, ZnS and ZnO) IN SILICATE MATRIX

---

#### **3.1. Linear, nonlinear and Optical properties of Sm<sup>3+</sup> co-doped alumino-silicate glass prepared by sol-gel method**

##### **Overview**

In this paper, we report the investigations of Sm<sup>3+</sup> co-doped alumino-silicate glass synthesized, by the sol-gel method for the linear and nonlinear optical characteristics. The structural characterization is performed with the XRD and FTIR techniques. The result of XRD shows that the amorphous even after heating at 800 °C. The functional groups of the prepared sol-gel silica glass have been identified by FTIR. The absorption spectra exhibit seventeen peaks in UV-VIS & NIR region from ground state <sup>6</sup>H<sub>5/2</sub>. The Judd-Ofelt intensity parameters were estimated from the absorption spectra of Sm<sup>3+</sup> co-doped alumino-silicate glass. Photoluminescence emissions in the visible region were observed under 450 nm excitations along with **Stark splitting with different aluminum (Al) concentrations and annealing temperatures**. The CIE Chromaticity diagram is presented to show the color tunability of the Sm<sup>3+</sup>/Al doped silica glass.

##### **3.1.1. Introduction**

Recently glasses doped with rare earth (RE) ions have been extensively studied because of their potential applications in photonic devices. In the light of the rapid growth of photonics devices based applications such as optical fiber communication, sensor, optical memory devices, optical amplifier, bio-photonics, and other optoelectronic devices (Nathalie Kunkel *et al.*, 2018, Jack Fong Chuen Loo *et al.*, 2019, Meiqi Chang *et al.*, 2017). In the quest for novel materials, nanoparticles of semiconductors demonstrate an interest in their physical and chemical properties (Alivisatos *et al.*, 1996, Peng *et al.*, 2000). With these scientifically interesting applications, numerous attention has been devoted to the study of various optical properties of RE<sup>3+</sup> ions surrounded by nanoparticles (NPs) dispersed in a dense glass host (Brus *et al.*, 1991, Yang *et al.*, 2006). Glasses are considered to be more favorable than crystals because almost every element can be embedded into glasses,

which makes it easier to control the quantities and energy level of electrons, and holes trap glasses more than crystals. The sol-gel technique which works at a low temperature is used here for the synthesis, this technique is quite suitable for the preparation of Sm-doped Al silica glass. Silica glass has many favorable properties as a host for  $\text{RE}^{3+}$  ions as it has good thermal stability, low thermal expansion, and good mechanical strength. However, their effective use as optical material is limited for different reasons. The sol-gel silica glass is high residual hydroxyl content due to precursors. Annealing to high temperatures is an effective way to use reduce the hydroxyl content of sol-gel glasses. Another drawback is the natural tendency for  $\text{RE}^{3+}$  ions to form a cluster in the sol-gel preparation. Our earlier work (Rai *et al.*, 2016) showed that the addition of aluminum as a dopant disperses the  $\text{RE}^{3+}$  cluster, thus reducing the NR relaxations it is likely that the lower coordination number of Al increases the probability that Al-O-RE bonds form. Modification of the glass composition with the addition of aluminum decreased the phonon energy and thereby increased the excited state lifetime as well as the photoluminescence efficiency of  $\text{RE}^{3+}$  ions.

Spectroscopic studies of Samarium have received much interest because of good luminescence efficiency in visible and IR regions. Understanding the optical properties of  $\text{Sm}^{3+}$  its great importance due to its potential technological applications such as optical memory (Swapna *et al.*, 2014), Here, we are investigating the effect of  $\text{Al}_2\text{O}_3$  on enhancing luminescence emission from  $\text{Sm}^{3+}$  ions.  $\text{Sm}^{3+}$  ion doped in silica host is extensively studied by various researchers (Vijaya *et al.*, 2013, Bernd Ahrens, 2009). Modification of the glass composition with the addition of nanoparticles further decreases the phonon energy (Alombert-Goget *et al.*, 2005) and thereby increased the excited state lifetimes as well as the quantum efficiency of the emissions from  $\text{RE}^{3+}$  ions. Aluminum co-doping is useful for scattering  $\text{RE}^{3+}$  ions in silica xerogel and glass networks.  $\text{RE}^{3+}$  ions will be rather detached by aluminium, as the esterification of  $\text{RE}^{3+}$  ions through RE-O-RE bonds is hindered by the formation of Al-O-RE bonds (Munehiro Tada *et al.*, 1998). These nanocomposite form non-bringing oxygen (NBO, e.g. Al-O-Si (Yan Jiao *et al.*, 2021), etc.) which in turn enhance the optical properties of the hosts by decreasing phonon energy.

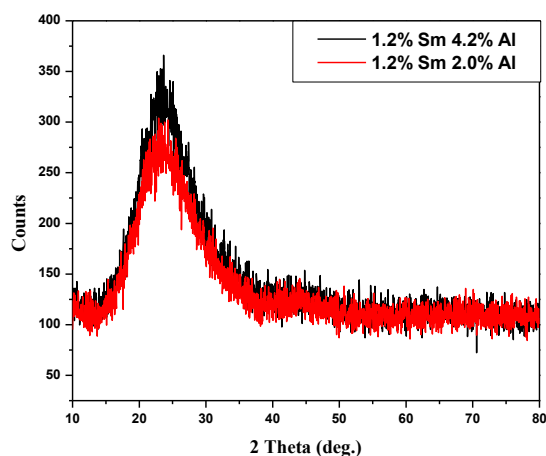
### 3.1.2. Experimental Details

The dense glass samples were synthesized with the Sol-Gel process, where hydrolysis and condensation of Tetraethyl-Orthosilicate (TEOS, Merak, 99.9%) were performed in the presence of distilled water ( $H_2O$ ) to structure the network of  $SiO_2$ . For specific concentrations of  $Sm^{3+}$  and aluminium dopant on a particular sample, the required amounts of Samarium Nitrate Hexa- hydrate [ $Sm(NO_3)_3 \cdot 6H_2O$ , Merak] and Aluminum Nitrate nitrate-hydrate [ $Al(NO_3)_3 \cdot 9H_2O$ , Merak] are dissolved in deionized water, after that ethanol [ $EtOH$ ,  $C_2H_5OH$ , Merak] and TEOS are added. The addition of an insignificant amount of Nitric Acid [ $HNO_3$ , Merak] helps to decrease the pH value and amplify the rate of hydrolysis. The final solutions of TEOS, de-ionized water, EtOH, and  $HNO_3$  have molar ratio 1:5.5:3.5:0.1 respectively. This final in-situ mixed solution with various dopants is stirred with a magnetic stirrer for ca. 2 h to convert into a sol of high viscosity. The sol is poured into a plastic container of a volume of 15ml to allow aging at RT few days which converts the sample into a solid gel. The container is sealed to avoid fast evaporation. The shrinking of the volume of the initial sol after 2-3 weeks is termed as xerogel as it is allowed to evaporate slowly through some pinhole on the polythene cover of the container. The xerogel is initially dried slowly up to 60 °C and then annealed to form dense glass with an electric muffle furnace by further heating up to 1050 °C at the rate of 1 °C per min.

### 3.1.3. Results and Discussion

#### 3.1.3.1. XRD spectral measurements

Fig. 3.1.1 showed the powdered XRD spectrum of silica glasses annealing at 800 °C with two different concentrations of  $Sm^{3+}$  (1.2 mol%) and Al (4.2, 2.0 mol%) co-doping respectively. The distinct broad hollow peaks are observed rather than intense crystalline peaks with a crystallinity index of more than 37% which established the glassy amorphous nature of the glass samples. The broad peak around  $2\theta = 21.12^\circ$  is attributed to the amorphous nature of silica glass (Swapna *et al.*, 2014).

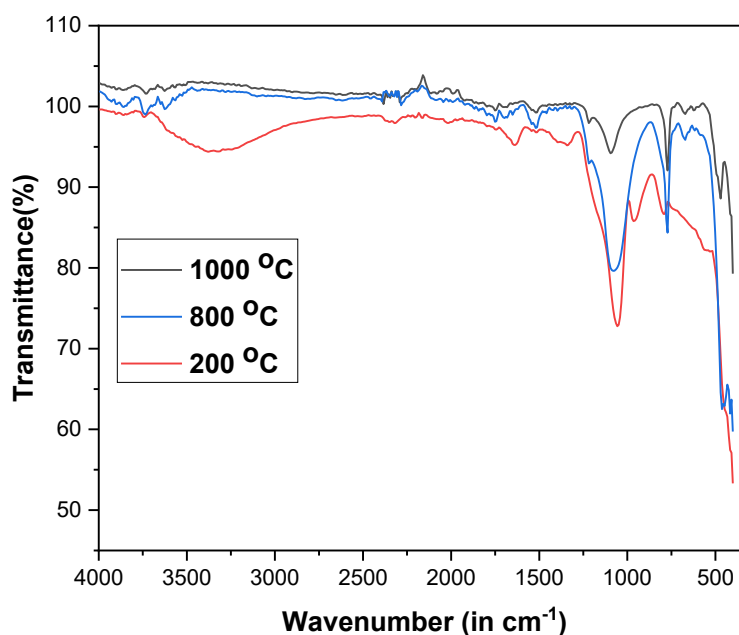


**Fig. 3.1.1:** XRD spectrum of  $\text{Sm}^{3+}$  (1.2 mol %) and Al (4.2, 2.0 mol %) co-doped silicate sol-gel glasses annealed up to 800 °C.

### 3.1.3.2. FTIR analysis

The ATR-FTIR spectrum due to the vibration of different bonds presence in the  $\text{Sm}^{3+}$  (1.2 mol%) and Al (2.0 mol%) co-doped sol-gel silicate glass annealing at different temperatures (200, 800, 1000 °C) is recorded in the wave number range 400 to 4000  $\text{cm}^{-1}$  as presented in Fig. 3.1.2. It is observed various peaks at approximately 416, 447, 470, 586, 671, 771, 980, 1064, 1080, 1095, 1219, 1365, 1651 and 3500  $\text{cm}^{-1}$ . The water and alcohol-assisted hydrolysis and condensation reaction of TEOS produce Si-OH groups which give a 3-D silica network. The sol-gel glass has primarily water and other organic species present in its gel stage. The broad peak around 3700-3500  $\text{cm}^{-1}$  is removed with the increase in sintering temperature due to the removal of  $\text{OH}^-$  and a water molecule ( $\text{H}_2\text{O}$ ) which contribute to O-H stretching vibration in the sample. The intensity of the band is highest for glass at 200 °C, progressively diminishes the band intensity at higher temperatures. The peak due to stretching of Si-OH bands and the occurrence of absorbed water diminished in intensity with rising temperatures as evidenced by the FTIR spectra. The reduction of phonon energy is indicated by the broadening and shift of the peak towards the low-frequency side. The aluminum ion as a network modifier ruptures the silica structure producing a non-bridging Al-O group (e.g. Si-O-Al), which can also be coordinated

with  $\text{Sm}^{3+}$  ions. The NBO of Sm-O-Si also may arise with the breaking of the bond Si-O-Si (Bokatial *et al.*, 2012). The peak around  $470\text{-}586\text{ cm}^{-1}$  are assigned to the bending mode of Al-O in the octahedral coordination state. The band at  $1365\text{ cm}^{-1}$  and  $1064\text{ cm}^{-1}$  are allocated to the polymerization of Si-OH groups leading to Si-O-Si bands. In the gels annealed at  $200\text{ }^{\circ}\text{C}$ , the existence of a Si-O free broadened peak at  $980\text{ cm}^{-1}$  has been observed. The peak at  $1651\text{ cm}^{-1}$  was caused by -OH bending vibration mode of water showing decreased and shifted to  $1527\text{ cm}^{-1}$  at  $800\text{ }^{\circ}\text{C}$  and  $1000\text{ }^{\circ}\text{C}$ . Thus annealing of the glass sample leads to the gradual disappearance of the constituents from the glass host matrix and finally rigid glassy network is evolved, which is obvious from the FTIR spectra. The assignment of the bands is shown in Table 3.1.1.



**Fig. 3.1.2:** ATR-FTIR spectra of  $\text{Sm}^{3+}$  (1.2 mol%) and Al (2.0 mol%) in dense sol-gel silicate glass at annealing at different temperatures.

**Table 3.1.1**

FTIR peak positions and their different assignments of the glass samples.

Wavenumber (cm <sup>-1</sup> )	Assignment	Observed Intensity	Intensity change during heating
416-447	Si-O, asymmetric stretching vibrations, O-Si-O stretching (Wang <i>et al.</i> , 1997)	Strong, broad	Peak around 470 arise at 800 °C and In three peaks arise 416, 447, 462 at 1000 °C
470-586	Si-O-Al asymmetric bending, NBO (Non-bridging oxygen) (Yan Jiao <i>et al.</i> , 2021)	No peak	An intense peak arises at 800 °C and slightly decreases at 1000 °C
671	Si-O of SiO <sub>4</sub> symmetric bending (Yan Jiao <i>et al.</i> , 2021)	No peak	A minor peak at 800 °C and decrease with rising temperature
771	Si-OH stretching (Wang <i>et al.</i> , 1997)	Strong	Decrease with increasing temperature
980	Si-O-H stretch vibrational mode	Sharp peaks	Remove in higher temperatures
1080-1095	Si-O-Al, asymmetric stretching (Wang <i>et al.</i> , 1997)	Intense peak	Redshift, decrease in intensity
1219	C-O-C stretching	Minor peak	Remove in T > 800

	vibration (Naveen Kumar <i>et al.</i> , 2015)		°C
1365	Si-O-Si	Diffuse	Remove in T > 800 °C
1527-1651	–OH bending vibration mode of water	Minor peak	Shifted when annealed at 800- 1000 C
3500-3700	O-H stretching (Wang <i>et al.</i> , 1997)	Broad, strong	It is completely removed in T > 800 °C

---

### 3.1.3.3. Physical Properties

The density of Sm<sup>3+</sup> (1.2 mol%) and Al (2.0 mol%) co-doped in sol-gel silicate glass annealing at ca. 1000 °C, was measured by using the principle of Archimedes, where the sample is immersed in xylene. The index of refraction of glass was estimated by an Abbe refractometer based on the principle of total reflection with bromonaphthalene (C<sub>10</sub>H<sub>7</sub>Br) as contact liquid. These two practically measured values of densities ( $\rho$ ) and index of refraction ( $n$ ) are used to calculate other related properties such as average molecular weight ( $M_T$ ), molar refractivity ( $R_M$ ), molecular electronic polarizability ( $\alpha_e$ ), concentration of Sm<sup>3+</sup> ion ( $N$ ), dielectric constant ( $\epsilon$ ), optical dielectric constant ( $\epsilon-1$ ), losses due to reflection ( $R_L$ ), molar refraction ( $R_m$ ), polaron radius ( $R_p$ ) and inter atomic distance ( $R_i$ ) have been computed by using the appropriate expressions (Annapurna *et al.*, 2019) and a represented in Table 3.1.2. The non-linear dynamics of the materials are governed by the electronic polarizability of the sample. This electronic polarization is initiated as the material is exposed to intense light. In theory Volf and Lorentz–Lorentz (Yasi *et al.*, 1982, Haralampieva *et al.*, 2012), are used to derive the polarizability ( $\alpha_e$ ) with the refractive index ( $n$ ) as follows,

$$\frac{(n^2-1)}{(n^2+1)} V_m = \frac{4}{3\pi} N \alpha_e \quad (3.1)$$

**Table 3.1.2**

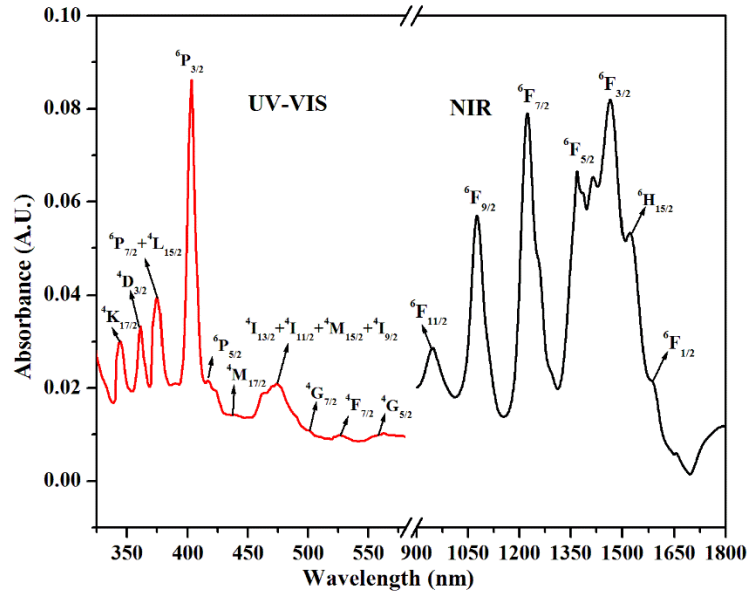
Various physical properties of  $\text{Sm}^{3+}$  (1.2 mol%) and Al (2.0 mol%) co-doped in Sol-Gel silicate glass annealing at 1000 °C.

Physical properties	Value
Weight of the sample (gm)	1.96
Density ( $\rho$ ) (gm/cm <sup>3</sup> )	2.2
Index of Refraction ( $n$ )	1.66
Thickness	0.18
Average molecular weight ( $M_T$ )	61.86
Molar volume ( $V_m$ ) (cm <sup>-3</sup> )	28.12
Reflection losses ( $R_L$ )	0.06
Molar refractivity ( $R_m$ ) (cm <sup>-3</sup> )	10.40
Energy gap ( $E_g$ )	7.94
Molar electronic polarizability ( $\alpha_m$ )	4.13
Dielectric constant ( $\epsilon_c$ )	2.76
Optical dielectric constant ( $\epsilon_c-I$ )	1.76
Electronic polarizability( $\alpha_e$ ) (x 10 <sup>-21</sup> cm <sup>-3</sup> )	1.47
$\text{Sm}^{3+}$ ion concentration ( $N$ ) (x 10 <sup>20</sup> ions/cm <sup>3</sup> )	1.18
Polaron radius ( $R_p$ ) (x 10 <sup>-8</sup> )	8.20
Inter-ionic distance ( $R_i$ ) (x 10 <sup>-7</sup> )	2.91
Field Strength ( $F_s$ X 10 <sup>10</sup> )	2.20
Optical Basicity ( $\Lambda$ )	0.49
Metallization criterion ( $M_C$ )	0.63



#### 3.1.3.4. Absorption Spectra

The absorption spectra of  $\text{Sm}^{3+}$  (1.2 mol%) and Al (2.0 mol%) co-doped in Sol-Gel silica glass annealing at 1000 °C is recorded in UV–VIS & NIR [325–580 & 900–1800 nm at RT] regions as in Fig. 3.1.3. It consists of numerous intense peaks assigned to  $4f^N-4f^N$  transitions from the ground state [GS,  $^6\text{H}_{5/2}$ ] to different excited states [ES] of  $\text{Sm}^{3+}$  ions in this host glass. These absorption bands are recorded at 345, 362, 376, 402, 418, 436, 475, 502, 526, 560, 946, 1079, 1226, 1370, 1466, 1521, 1586 nm and are assigned as  $^6\text{H}_{5/2} \rightarrow ^4\text{K}_{17/2}; ^4\text{D}_{3/2}; ^6\text{P}_{7/2} + ^4\text{L}_{15/2}; ^6\text{P}_{3/2}, ^6\text{P}_{5/2}$ , (Fig. 5);  $^6\text{P}_{3/2} \rightarrow ^4\text{M}_{17/2}; ^4\text{I}_{13/2} + ^4\text{I}_{11/2} + ^4\text{M}_{15/2} + ^4\text{I}_{9/2}$ ,  $^6\text{H}_{5/2} \rightarrow ^4\text{G}_{7/2}, ^4\text{F}_{3/2}, ^4\text{G}_{5/2}$ , (Fig. 5);  $^6\text{H}_{5/2} \rightarrow ^6\text{F}_{11/2}, ^6\text{F}_{9/2}, ^6\text{F}_{7/2}, ^6\text{F}_{5/2}, ^6\text{F}_{3/2}, ^6\text{H}_{15/2}, ^6\text{F}_{1/2}$  transitions respectively. Due to the location of  $\text{RE}^{3+}$  ions in a low symmetry crystal field, the fine structure is moderately well resolved so that absorption bands of  $^{2S+1}\text{L}_J$  manifolds are observed which can be concluded from inhomogeneous line broadening. The data of Carnal et al. is used to assign all the above peaks (Carnall *et al.*, 1968). The ED-induced interactions are responsible for the majority of observed transitions with  $\Delta J \leq 6$  selection rules. A few transitions also originated due to the contribution of the magnetic dipole with selection rule  $\Delta J = 0, \pm 1$  (Katarina Vukovic *et al.*, 2015). The weak absorption peaks are emerged due to spin forbidden MD transition in the visible region which becomes laborious to assign due to the overlap of different  $^{2S+1}\text{L}_J$  levels in the UV-VIS range. The sharp and intense peaks observed in the IR range with energies below 11000  $\text{cm}^{-1}$  possibly benefited from the effective shielding around 4f electrons due to 5s and 5p shells. These spin-allowed transitions from the GS ( $^6\text{H}_{5/2}$ ) to  $^6\text{F}_J$  terms with selection rule ( $\Delta S=0$ ) are assigned to  $^6\text{H}_{5/2} \rightarrow ^6\text{F}_J$  [ $J = 1/2, \dots, 11/2$ ] manifolds (Mahamuda *et al.*, 2014). The schematic transition from the absorption spectrum of  $\text{Sm}^{3+}$  (1.2 mol%) and Al (2.0 mol%) co-doped in sol-gel silica glass annealed at 1000 °C is presented as (solid line) in Fig. 3.1.5.

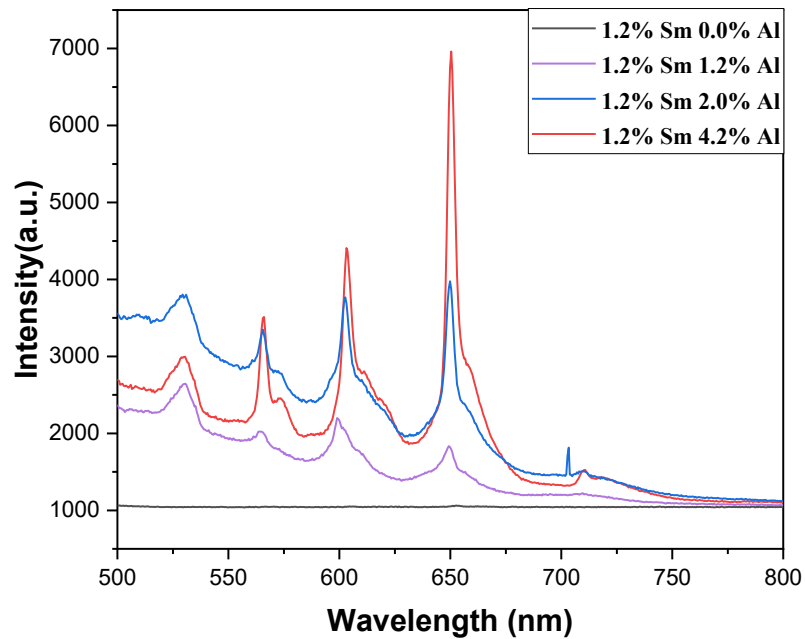


**Fig. 3.1.3:** Absorption spectra of  $\text{Sm}^{3+}$  (1.2 mol %) and Al (2.0 mol %) co-doped in sol-gel silicate glass annealing at 1000 °C in UV-VIS and NIR range

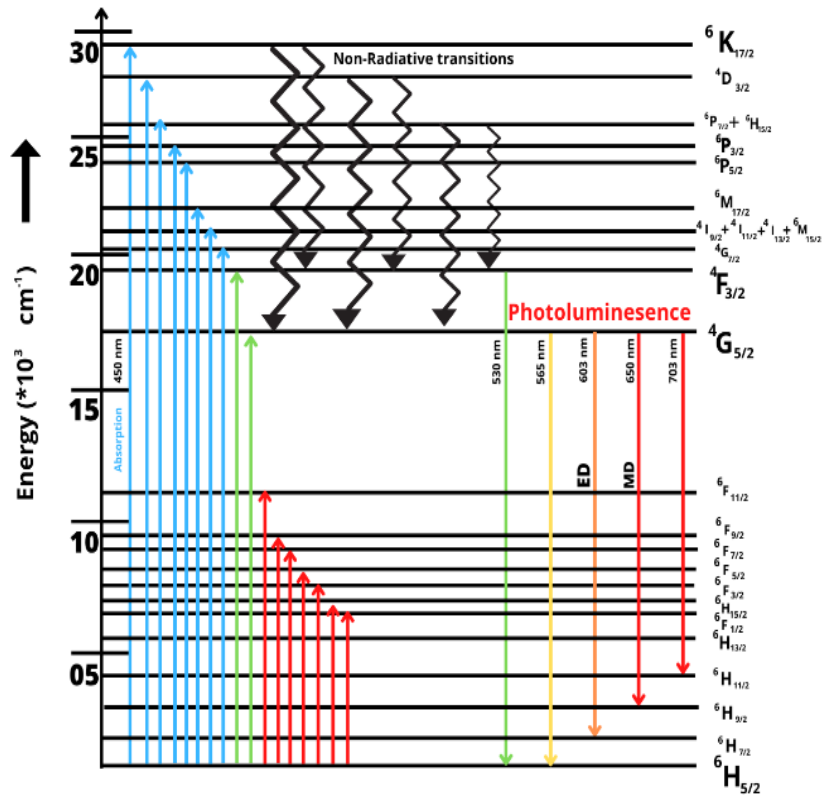
### 3.1.3.5. Photoluminescence spectra

The PL spectrum with five peaks of fixed  $\text{Sm}^{3+}$  (1.2 mol%) ion and different concentrations of Al(0.0-4.2 mol%) co-doped in sol-gel silicate glass annealed at 1000 °C is recorded in UV–VIS [500–800 nm] range as in Fig. 3.1.4. The peaks are assigned to the transition of  $^4\text{F}_{3/2} \rightarrow ^6\text{H}_{5/2}$  (530 nm);  $^4\text{G}_{5/2} \rightarrow ^6\text{H}_{5/2}$  (565 nm);  $^6\text{H}_{7/2}$  (603 nm);  $^6\text{H}_{9/2}$  (650 nm);  $^6\text{H}_{11/2}$  (709 nm) respectively. The highest emission peak is observed in the orange region [ $^4\text{G}_{5/2} \rightarrow ^6\text{H}_{9/2}$ ] compared to the rest transitions for all glass samples. With a rise in the concentrations of aluminium ions, the reduction of concentration quenching effects is evident along with a red color peak which appeared at around 712 nm and convert into a sharp from broad one with further increased concentrations. The strong enhancement of PL indicates the modification of the local environment around  $\text{Sm}^{3+}$  ions due to the presence of aluminium ions (Swapna *et al.*, 2014). The works published with  $\text{Sm}^{3+}$  doped glasses reported intense peaks around 600 nm and 545 nm (Goyal *et al.*, 2017, Shamshad *et al.*, 2018, Khan *et al.*, 2019, Campos-Zuniga *et al.*, 2019). In the present work, transition with a peak

of 650 nm is most intense. The peaks are intense with rising concentrations of aluminium as the electronic structure of glasses is modified due to the rise of NBO and thus promotes transitions of lower energy which is also confirmed from FTIR spectra (Rai *et al.*, 2016, Brahmachary *et al.*, 2015). The schematic diagram of fixed  $\text{Sm}^{3+}$  (1.2 mol%) ion and different concentrations of Al (0.0-4.2 mol%) co-doped in sol-gel silicate glass annealed at 1000 °C with PL (solid line) and possible non-radiative relaxation (wavy arrow) transitions as in Fig. 3.1.5. The PL spectra with Stark splitting is observed for  $\text{Sm}^{3+}$  (1.2 mol%) and Al (2.0, 4.2 mol%) co-doped in silicate sol-gel glasses annealing at 1000 °C which is consistent with the fact of modification of host with Al concentration Rai *et al.*, 2016).



**Fig. 3.1.4:** PL Spectra of fixed  $\text{Sm}^{3+}$  (1.2 mol%) ion and different concentrations of Al (0.0-4.2 mol%) co-doped in sol-gel silicate glass annealing at 1000 °C.

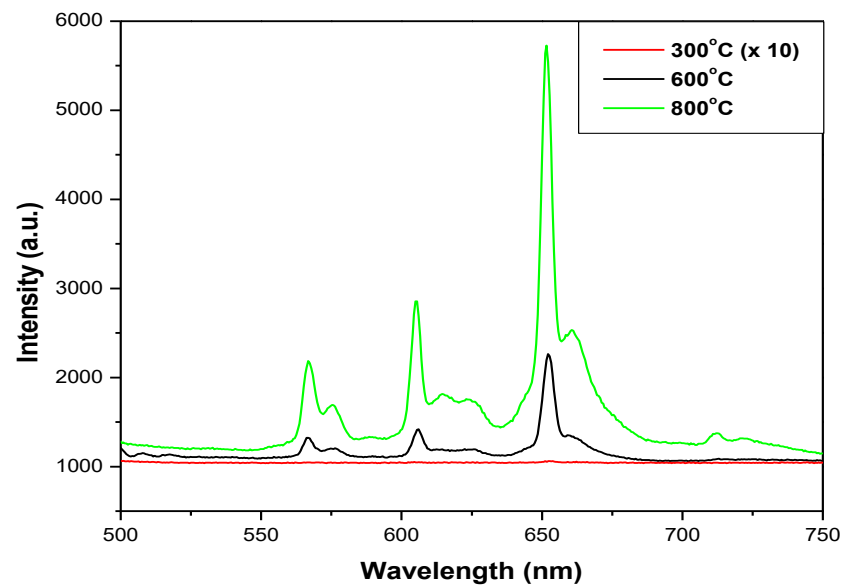


**Fig 3.1.5:** Schematics energy diagram of  $\text{Sm}^{3+}$  ions co-doped with Al in silica host.

### 3.1.3.6. Dependence of annealing temperature on PL spectra

The PL spectra of  $\text{Sm}^{3+}$  (1.2 mol%) and Al (2.0 mol%) co-doped in sol-gel silicate glasses with different annealing temperatures were recorded by the excitation wavelength ( $\lambda_{\text{ex}} = 450 \text{ nm}$ ) as shown in Fig. 3.1.6. The asymmetry arises due to development of NBO (Si-O-Al) with smaller phonon energy compared to the vibration of Si-O-Si bond, which also confirms from recorded FTIR spectra. The sample annealed at  $300^\circ\text{C}$  shows very minor intensity which is due to the quenching due to the hydroxyl (OH) group. The OH group with high phonon energy has a quenching effect on the PL of  $\text{Sm}^{3+}$  ions. With the creation of electrons and holes from recombination of defects, energy release and transfer to the  $\text{Sm}^{3+}$  ions in silica xerogel is quenched. Thus PL intensity is increased for the dense glasses which are annealed at higher temperature with the removal of the OH group (Fig. 3.1.6). Thus asymmetry of host matrix and removal of OH group at high annealing temperature are effective in PL enhancement. For PL spectra for  $\text{Sm}^{3+}$  (1.2 mol%) and different

Al (2.0, 4.2 mol%) concentrations (Tables 3.1.7) are observed to show Stark splitting at transitions  ${}^6H_{5/2}$ ,  ${}^6H_{7/2}$  and  ${}^6H_{9/2}$  in  $Sm^{3+}$  in silica glass when annealed at 1000 °C which is consistent with the fact of modification of host at the higher temperature. Similarly, the variation of annealing temperature of  $Sm^{3+}$  (1.2 mol%) and Al (2.0 mol%) co-doped in sol-gel silica glass also shows Stark splitting at transitions  ${}^6H_{5/2}$ ,  ${}^6H_{7/2}$ ,  ${}^6H_{9/2}$  and  ${}^6H_{11/2}$  as presented in (Tables 3.1.8).



**Fig. 3.1.6:** PL Spectrum of  $Sm^{3+}$  (1.2 mol%) and Al (2.0 mol%) co-doped in sol-gel silicate glass with various annealing temperatures (Note: Curve with red color is magnified to 10 times for clarity).

### 3.1.3.7. Judd-Ofelt and Radiative parameters

Judd-Ofelt (JO) theory is used to estimate the oscillator strength of numerous  $4f-4f$  transitions of  $Sm^{3+}$  (1.2 mol%) co-doped with Al (2.0 mol%) in sol-gel silicate glasses as seen in absorption spectra (Fig. 3.1.3). The JO parameters (Judd, 1962, Ofelt, 1962) are estimated to extract practical information regarding the different optical properties and the  $Sm^{3+}$  ion's neighborhood in the aluminium co-doped silica host. Here  $\Omega_2$  is extremely structured and sensitive and associated with the symmetry and covalency of the  $Sm^{3+}$  ions neighborhood (Carnal *et al.*, 1968, Vijayakumar *et al.*, 2015). The values of  $\Omega_4$  and  $\Omega_6$  are decided by the viscosity and

dielectric properties of the media (glass) and induce vibronic transition due to the bond between  $\text{Sm}^{3+}$  ions and the ligand atoms (Uzair Khan *et al.*, 2018). The spectroscopic quality ( $\Omega_4/\Omega_6$ ) is significant in foreseeing the stimulation of emission for the laser active host (Rai *et al.*, 2011, Hazarika *et al.*, 2004, Agarwal *et al.*, 2009). The J-O intensity parameters ( $\Omega_\lambda$ ) of  $\text{Sm}^{3+}$  doped glasses are compared in Table 3.1.4.

To estimate various radiative quantities, phenomenological JO parameters calculated from absorption spectra are combined with observed PL spectra of the fluorescence level  $^4\text{G}_{5/2}$  of the of  $\text{Sm}^{3+}$  (1.2 mol%) co-doped with Al (2.0 mol%) in  $\text{SiO}_2$  sol-gel glasses. The estimation of radiative properties such as spontaneous emission probabilities ( $A_{\text{rad}}$ ), luminescence branching ratios ( $\beta_r$ ), and radiative lifetime ( $\tau_{\text{rad}}$ ) for the optical transitions of  $\text{Sm}^{3+}$  (1.2 mol%) co-doped with Al (2.0 mol%) in  $\text{SiO}_2$  glasses have been estimated using J-O intensity parameters in 3.1.5.

**Table 3.1.3** The Experimental ( $f_{\text{exp}}$ ) and Calculated ( $f_{\text{cal}}$ ) Oscillator Strengths with relative Absorption peak for  $\text{Sm}^{3+}$  (1.2 mol%) and Al (2.0 mol%) co-doped in sol-gel silicate glass annealing at 1000 °C.

Transitions	Energy	Wavelength	f <sub>exp</sub>	f <sub>cal</sub>
<sup>6</sup> H <sub>5/2</sub> →ES	(in cm <sup>-1</sup> )	(in nm)	(x 10 <sup>-6</sup> )	(x 10 <sup>-6</sup> )
<sup>6</sup> F <sub>1/2</sub>	6297	1588	0.236	0.141
<sup>6</sup> H <sub>15/2</sub>	6575	1521	0.044	0.033
<sup>6</sup> F <sub>3/2</sub>	6825	1465	0.198	0.225
<sup>6</sup> F <sub>5/2</sub>	7309	1368	0.249	0.168
<sup>6</sup> F <sub>7/2</sub>	8149	1224	1.378	1.178
<sup>6</sup> F <sub>9/2</sub>	9293	1076	0.978	0.639
<sup>6</sup> F <sub>11/2</sub>	10548	948	0.273	0.239
<sup>4</sup> G <sub>5/2</sub>	17762	563	0.314	0.225
<sup>4</sup> F <sub>3/2</sub>	19011	526	0.269	0.056
<sup>4</sup> G <sub>7/2</sub>	20243	494	0.377	1.029
<sup>4</sup> I <sub>13/2</sub> + <sup>4</sup> I <sub>11/2</sub>	21097	474	0.450	0.356
+ <sup>6</sup> M <sub>15/2</sub> + <sup>4</sup> I <sub>9/2</sub>				
<sup>6</sup> M <sub>17/2</sub>	22624	442	0.219	0.072
<sup>6</sup> P <sub>5/2</sub>	24096	415	0.353	0.742
<sup>6</sup> P <sub>3/2</sub>	24814	403	2.093	0.971
<sup>6</sup> P <sub>7/2</sub> + <sup>4</sup> L <sub>15/2</sub>	26666	375	0.686	1.054
<sup>4</sup> D <sub>3/2</sub>	27700	361	0.384	0.134
<sup>4</sup> K <sub>17/2</sub>	29069	344	0.433	0.096
δ <sub>rms</sub> ( x 10 <sup>-6</sup> )			±0.429	
	Ω <sub>2</sub> =0.47±0.016	Ω <sub>4</sub> =0.24±0.009	Ω <sub>6</sub> =2.28±0.0	
	( x 10 <sup>-20</sup> cm <sup>2</sup> )	(x 10 <sup>-20</sup> cm <sup>2</sup> )	38	
			(x 10 <sup>-20</sup> cm <sup>2</sup> )	
	Ω <sub>4</sub> /Ω <sub>6</sub> =0.105±0.006			
	(x 10 <sup>-20</sup> )			

**Table 3.1.4**

Judd–Ofelt parameters ( $\times 10^{-20} \text{ cm}^2$ ) and spectroscopic quality factor ( $X=\Omega_4/\Omega_6$ ) comparison of the  $\text{Sm}^{3+}$  co-doped with Aluminium in silica glasses with other available literature.

$\Omega_2$	$\Omega_4$	$\Omega_6$	$\Omega_4/\Omega_6$	References
$0.47 \pm 0.016$	$0.24 \pm 0.009$	$2.28 \pm 0.038$	$0.105 \pm 0.006$	Present work
24.87	1.44	2.56	0.563	$\text{SiO}_2\text{-CdS:Sm}^{3+}$ (Rai <i>et al.</i> , 2011)
1.029	2.511	2.866	0.876	$\text{ZnAlBiB:Sm}^{3+}$ (Swapna <i>et al.</i> , 2014)
4.31	4.28	5.78	0.74	Phosphate (Vijaya <i>et al.</i> , 2013)
0.55	9.68	9.77	0.99	NaZnBS (Set A) (Jayasankar <i>et al.</i> , 1997)
0.18	11.37	11.45	0.99	KZnBS (Set A) (Jayasankar <i>et al.</i> , 1997)
0.930	10.97	11.41	0.96	KZnBS (Set B) (Jayasankar <i>et al.</i> , 1997)
0.19	2.81	2.78	1.01	TeWLiSm (Annapurna <i>et al.</i> , 2019)
0.042	3.496	2.368	1.476	LiTFP (Jayasimhadri <i>et al.</i> , 2006)



**Table 3.1.5**

Radiative parameters of  $\text{Sm}^{3+}$  (1.2 mol%) co-doped with Al (2.0 mol%) in silicate glasses.

Transitions $^4\text{G}_{5/2} \rightarrow \text{GS}$	Energy (in $\text{cm}^{-1}$ )	$A_{\text{ed}}$ (in $\text{s}^{-1}$ )	$\beta_{\text{r}}$ (in %)
$^6\text{F}_{11/2}$	7258.2	3.61	4.07
$^6\text{F}_{9/2}$	8568.6	2.76	3.11
$^6\text{F}_{7/2}$	9856.5	1.70	1.92
$^6\text{F}_{5/2}$	10626.3	1.94	2.19
$^6\text{F}_{3/2}$	11052.2	1.14	1.28
$^6\text{H}_{15/2}$	11096.7	0.51	0.57
$^6\text{F}_{1/2}$	11382.4	0.03	0.03
$^6\text{H}_{13/2}$	12642.3	1.52	1.71
$^6\text{H}_{11/2}$	14135.1	17.49	19.70
$^6\text{H}_{9/2}$	15485.3	37.51	42.26
$^6\text{H}_{7/2}$	16768.5	2.18	2.46
$A_{\text{T}} (\text{s}^{-1}) = 88.77 \pm 0.674$		$\tau_{\text{R}} = 11.27 \pm 0.047$ (ms)	

**Table 3.1.6**

PL lines wavelength, energy, effective bandwidth, and stimulated cross-section for various peaks of  $\text{Sm}^{3+}$  (1.2 mol%) co-doped with Al (2.0 mol%) in sol-gel silicate glasses.

Transitions	Wavelength( $\lambda_p$ ) (nm)	Energy ( $\text{cm}^{-1}$ )	$\lambda_{\text{eff}}$ (nm)	$\sigma_p$ ( $\times 10^{-23} \text{cm}^2$ )
$^4\text{F}_{3/2} \rightarrow ^6\text{H}_{5/2}$	530	18867.92	9.75	$20.47 \pm 0.451$
$^4\text{G}_{5/2} \rightarrow ^6\text{H}_{5/2}$	565	17699.12	6.06	$5.17 \pm 0.175$
$^4\text{G}_{5/2} \rightarrow ^6\text{H}_{7/2}$	603	16583.75	5.29	$2.42 \pm 0.098$
$^4\text{G}_{5/2} \rightarrow ^6\text{H}_{9/2}$	650	15384.62	7.59	$7.47 \pm 0.182$
$^4\text{G}_{5/2} \rightarrow ^6\text{H}_{11/2}$	709	14104.37	4.77	$12.77 \pm 0.217$

**Table 3.1.7**

Stark splitting in the spectrum  $\text{Sm}^{3+}$  (1.2 mol%) co-doped with Al (2.0, 4.2 mol%) in sol-gel silicate glasses at different concentrations.

Transitions	Wavelength ( $\lambda_p$ )	Energy	Assignment
$^4\text{G}_{5/2} \rightarrow \text{GS}$			
$^6\text{H}_{5/2}$	565	17699.12	0
	574	17421.60	278
$^6\text{H}_{7/2}$	603	16583.75	1116
	611	16366.61	1332
	621	16366.61	1596
$^6\text{H}_{9/2}$	650	15384.62	2315
	659	15174.51	2525

**Table 3.1.8**

Stark splitting in the spectrum of  $\text{Sm}^{3+}$  (1.2 mol%) co-doped with Al (2.0 mol%) in sol-gel silicate glasses at different annealing temperatures.

Transitions	Wavelength ( $\lambda_p$ )	Energy	Assignment
$^4\text{G}_{5/2} \rightarrow \text{GS}$			
$^6\text{H}_{5/2}$	566.75	17644.46	0
	575.74	17368.95	276
$^6\text{H}_{7/2}$	605.62	16512	1132
	615.06	16258.58	1386
	624.50	16012.81	1632
$^6\text{H}_{9/2}$	651.82	15341.66	2303
	661.26	15122.64	2522
$^6\text{H}_{11/2}$	711.68	14051.26	3593
	721.12	13867.32	3777

### 3.1.3.8. Non-Linear Properties

Certain non-linear characteristics, ascertained from optical parameters, such as the non-linear refractive index ( $n_2$ ), non-linear refractive index susceptibility ( $\chi^{(3)}$ ), co-efficient ( $\gamma_{ce}$ ), and relatively high Abbe number ( $v_{Ab}$ ), suggest the good optical quality of the sol-gel silicate dense glass-ceramic (Hazarika *et al.*, 2004). Table 5 shows these values.

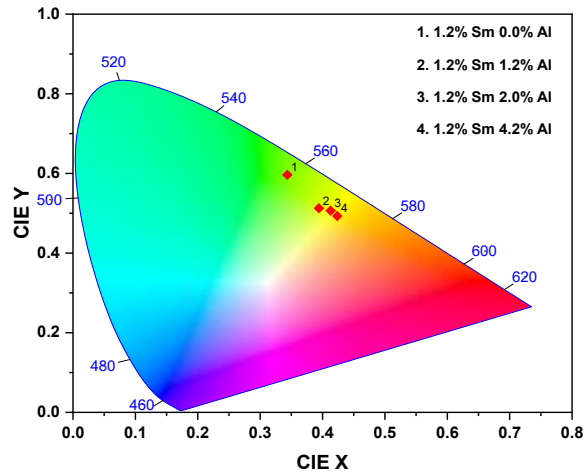
**Table 3.1.9**

Abbe number ( $v_A$ ), dispersive power ( $v_A^{-1}$ ), non-linear index of refraction ( $n_2$ ), coefficient of the index of refractions ( $\gamma_c$ ), and susceptibility ( $\chi_s$ ) of  $\text{Sm}^{3+}$  (1.2 mol%) co-doped with Al (2.0 mol%) in sol-gel silicate glass.

$n_g$	$n_r$	$(n_g - n_r)$	$n_b$	$v_A$	$v_A^{-1}$	$n_2$ (*10 <sup>-13</sup> esu)	$\gamma_c$ (*cm <sup>2</sup> /W)	$\omega_o$ (*10 <sup>-13</sup> )	N (*10 <sup>-16</sup> )	$\chi^{e(3)}$
1.54	1.53	0.010	1.54	54.	0.018	1.595	0.434	102.73	671.33	26.3
7	7		1	1				7	6	4

### 3.1.3.9. Chromaticity diagram (CIE-1931)

The color tunability of the PL emission of  $\text{Sm}^{3+}$  (1.2 mol%) co-doped with Al (0.0, 1.2, 2.0, 4.2 mol%) in  $\text{SiO}_2$  sol-gel glasses have been exemplified using the chromaticity figure. The CIE color coordinates X and Y at different Aluminium concentrations have been cited in Table 3.1.10. PL color is tuned from green to red with the increase in Aluminium concentrations as in Fig. 3.1.7.



**Fig. 3.1.7:** CIE 1931 chromaticity diagram of  $\text{Sm}^{3+}$  (1.2 mol%) co-doped with Al (0.0, 1.2, 2.0, 4.2 mol%) in  $\text{SiO}_2$  sol-gel glasses.

**Table 3.1.10**

CIE Chromaticity coordinates of the  $\text{Sm}^{3+}$  (1.2 mol%) co-doped with Al (0.0, 1.2, 2.0, 4.2 mol%) in sol-gel silicate glasses.

Color Coordinates	0.0% Al	1.2% Al	2.0% Al	4.2% Al
X	0.344	0.394	0.418	0.424
Y	0.596	0.513	0.507	0.493

#### 3.1.4. Conclusions

Enhanced PL intensity of  $\text{Sm}^{3+}$  can be attributed to the presence of Al co-dopant and annealing conditions. Al co-doping prevents RE clustering, RE ions are subjected to a modified vibrational coupling, and RE are located in the aluminum-rich regions because there is a greater quantity of non-bridging Al-O groups with which to coordinate. Al-O-Si bonds vibrate with lower phonon energy than Si-O-Si bonds. The amorphous nature of the prepared sample is confirmed by XRD spectra. In ATR-FTIR spectra, it is confirmed that NBO on the low phonon energy side evolves for the sample annealed at higher temperatures along with the removal of the OH group. The intensity parameters were estimated. From the result, it can be concluded that the rise in the concentration of Al positively influences the enhancement of PL property. From the chromaticity diagram, it is evident that the color of emission is tunable with different aluminum concentrations.

## References

- Nathalie Kunkel, Philippe Goldner (2018), Recent Advances in Rare Earth Doped Inorganic Crystalline Materials for Quantum Information Processing, *J. Inorg. Gen. Chem.* **644(2)**: 66–76.
- A. Agarwal, I. Pal, S. Sanghi, M.P. Aggarwal (2009), Judd–Ofelt parameters and radiative properties of  $\text{Sm}^{3+}$  ions doped zinc bismuth borate glasses, *Optical Materials*, **32**: 339–344.
- A. Haralampieva, I.S. Lozanova and V. Dimitrov (2012), Optical properties and structure of  $\text{BaO-V}_2\text{O}_5$  and  $\text{Fe}_2\text{O}_3\text{-BaO-V}_2\text{O}_5$  glasses, *J. Chemical Technology and Metallurgy*, **47**: 392.
- A.P. Alivisatos (1996), Perspectives on the Physical Chemistry of Semiconductor Nanocrystals, *Journal of Physical Chemi.* **100**: 13226-13239.
- B.R. Judd (1962), Optical absorption intensities of rare-earth ions, *Phys. Rev.* **127**: 750.
- Bernd Ahrens (2009), Down and Up-Conversion in Fluorozirconate-Based Glasses and Glass Ceramics for Photovoltaic Application.
- C.K. Jayasankar, E. Rukmini (1997), Optical properties of  $\text{Sm}^{3+}$  ions in Zinc and Alkali zinc borosulphate glasses, *Optical Mat.* **8**: 193–205.
- C.K. Mahamuda, K. Swapma, M. Venkateswarlu, Srinivasa Rao, Suman Shakya, G. Vijaya Prakash (2014), Spectral characterization of  $\text{Sm}^{3+}$  ions doped Oxy-fluoroborate glasses for visible orange luminescent applications, *Journal of Luminescence*, **154**: 410-424.
- Ch. B. Annapurna Devi, K. Swapna, S.K. Mahamuda, M. Venkateswarlu, M.V.V.K.S. Prasad, K. Siva Rama Krishna Reddy, Nisha Deopa, A.S. Rao (2019), Spectroscopic studies and lasing potentialities of  $\text{Sm}^{3+}$  ions doped single alkali and mixed alkali fluoro tungstentellurite glasses, *Optics and Laser Technology*, **111**: 176–183.
- E.E. Campos-Zuniga, I.L. Alonso-Lemus, V. Agarwal, J. Escorcia-Garcia (2019), Sol-gel synthesis for stable green emission in samarium doped borosilicate glasses, *Ceramics international*, **45(18)**: 23857-24954.
- G. Alombert-Goget, N. Gaumer, J. Obriot, A. Rammal, S. Chaussedent, A. Monteil, H. Portales, A. Chiasera, M. Ferrari (2005), Aluminum effect on

photoluminescence properties of sol–gel-derived  $\text{Eu}^{3+}$ -activated silicate glasses, *Journal of Non-Crystalline Solids*, **351**: 1754–1758.

G.S. Ofelt (1962), Intensities of crystal spectra of rare-earth ions, *J. Chem. Phys.* **37**: 511.

I. Khan, G. Rooh, R. Rajaramakrishna, N. Srisittipokakun, H.J. Kim, K. Kirdsiri, J. Kaewkhao (2019), Luminescence characteristics of  $\text{Sm}^{3+}$ -doped lithium barium gadolinium silicate glasses for Orange LED's, *Spectrochim. Acta A Mol. Biomol. Spectrosc.* **214**: 14–20.

J. Yasi, J. Fusong, and G. Fuxi (1982), Optical and other physical properties of  $\text{Al}(\text{PO}_3)_3$ -containing fluorophosphate glasses, *J. Phys.* **43**: 315.

Jack Fong Chuen Loo, Yi Hsin Chien, Feng Yin, Siu Kai Kong, Ho Pui Ho, Ken Tye Yong (2019), Upconversion and downconversion nanoparticles for biophotonics and nanomedicine, *Co-ord. Chem. Rev.* **400**: 213042.

K. Brahmachary, D. Rajesh, Y.C. Ratnakaram (2015), Radiative properties and luminescence spectra of  $\text{Sm}^{3+}$  ion in zinc–aluminum–sodium-phosphate (ZANP) glasses, *Journal of Luminescence*, **161**: 202–208.

K. Naveen Kumar, L. Vijayalakshmi, Y.C. Ratnakaram (2015), Energy transfer based photoluminescence properties of  $(\text{Sm}^{3+} + \text{Eu}^{3+})$ :PEO + PVP polymer films for Red luminescent display device applications, *Optical Materials*, **45**: 148–155.

K. Swapna, Sk. Mahamuda, A. Srinivasa Rao, T. Sasikala, L. Rama Moorthy (2014), Visible luminescence characteristics of  $\text{Sm}^{3+}$  doped Zinc Alumino Bismuth Borate glasses, *Journal of Luminescence*, **146**: 288-294

Katarina Vukovic, Sanja Culubrk, Milica Sekulic, and D.D. Miroslav (2015), Analysis of luminescence of  $\text{Eu}^{3+}$  doped  $\text{Lu}_2\text{Ti}_2\text{O}_7$  powders with Judd-Ofelt theory, *Journal of Research in Physics*, **38**: 23-32.

L. Shamshad, N. Ali, Ataullah, J. Kaewkhao, G. Rooh, T. Ahmad, F. Zaman (2018), Luminescence characterization of  $\text{Sm}^{3+}$ -doped sodium potassium borate glasses for laser application, *J. Alloy. Comp.* **766**: 828–840.

- L. Yang, Q. Shen, J. Zhou, K. Jiang (2006), Biomimetic synthesis of CdS nanocrystals in aqueous solution of pepsin, *Mater. Chem. Phys.* **98(1)**: 125-130.
- L.E. Brus (1991), Quantum crystallites and nonlinear optics, *Appl. Phys. A*, **53**: 465-474.
- M. Jayasimhadri, L.R. Moorthy, S.A. Saleem, R.V.S.S.N. Ravikumar (2006), Spectroscopic characteristics of  $\text{Sm}^{3+}$ -doped alkali fluorophosphate glasses, *Spectro. Acta Part A*, **64**: 939–944
- M. Vijayakumar, K. Marimuthu, V. Sudarsan (2015), Concentration dependent spectroscopic behavior of  $\text{Sm}^{3+}$  doped leadfluoro-borophosphate glasses for laser and LED applications, *Journal of Alloys and Compounds*, **647**: 209-220.
- Meiqi Chang, Yanhua Song, Jie Chen, Lei Cui, Zhan Shi, Ye Sheng and Haifeng Zou (2017), Photocatalytic and photoluminescence properties of core-shell  $\text{SiO}_2@\text{TiO}_2:\text{Eu}^{3+}, \text{Sm}^{3+}$  and its etching products, *ACS Sustain. Chem. Eng. Photocatalytic*, **6**: 223–236.
- Munehiro Tada, Shinobu Fujihara and Toshio Kimura (1998), Sol-gel processing and characterization of alkaline earth and rare-earth fluoride thin films, *Journal of materials research*, **14**: 1610-1616.
- P. Goyal, Y.K. Sharma, S. Pal, U.C. Bind, S.C. Huang, S.L. Chung (2017), Structural, optical and physical analysis of  $\text{B}_2\text{O}_3\text{-SiO}_2\text{-Na}_2\text{O-PbO-ZnO}$  glass with  $\text{Sm}^{3+}$  ions for reddish-orange laser emission, *J. Lumin.* **192**: 1227–1234.
- R. Vijaya, V.V. Enkatramu, P. Babu, C.K. Jayasankar (2013), Spectroscopic properties of  $\text{Sm}^{3+}$  ions in phosphate and fluorophosphate glasses, *Journal of Non-crystalline solids*, **365**: 85-92.
- S. Hazarika and S. Rai (2004), Structural, optical and non-linear investigation of  $\text{Eu}^{3+}:\text{Al}(\text{NO}_3)_3\text{-SiO}_2$  sol-gel glass, *Bulletin of Materials Science*, **27**: 273-279



- . Rai, A.L. Fanai (2014), Spectroscopic studies of  $\text{Ho}^{3+}$  doped  $\text{SiO}_2$  - $\text{TiO}_2$  nanoparticle for photonic applications, *Science Vision*, **14(3)**: 112–117.
- S. Rai, A.L. Fanai (2016), Effect of annealing and dopants concentration on the optical properties of  $\text{Nd}^{3+}:\text{Al}^{3+}$  co-doped sol–gel silica glass, *Journal of Luminescence*, **170**: 325-329
- S. Rai, A.L. Fanai (2016), Optical properties of  $\text{Ho}^{3+}$  in sol-gel silica glass co-doped with Aluminium, *Journal of Non-Crystalline Solids*, **449**: 113–118.
- S. Rai, L. Bokatial and P.J. Dihingia (2011), Effect of CdS nanoparticles on fluorescence from  $\text{Sm}^{3+}$  doped  $\text{SiO}_2$  glass, *J. Luminescence*, **131(5)**: 978-983.
- S.S. Wang, Y. Zhou, Y.L. Lam, C.H. Kam, Y.C. Chan, X. Tao (1997), Fabrication and characterization of neodymium-doped silica glass by sol-gel process, *Mat. Res. Inn*, **1**: 92-96.
- W.T. Carnal, P.R. Fields, K. Rajnak (1968), *J. Chem. Phys.* **49**: 4424.
- W.T. Carnall, P.R. Fields and K.J. Rajnak (1968), Electronic Energy Levels in the Trivalent Lanthanide Aquo Ions. I.  $\text{Pr}^{3+}$ ,  $\text{Nd}^{3+}$ ,  $\text{Pm}^{3+}$ ,  $\text{Sm}^{3+}$ ,  $\text{Dy}^{3+}$ ,  $\text{Ho}^{3+}$ ,  $\text{Er}^{3+}$ , and  $\text{Tm}^{3+}$ , *Chem. Phys.* **59**: 4424.
- X. Peng, L. Manna, W. Yang, J. Wickham, E. Scher, A. Kadavanich, A.P. Alivisators (2000), Shape control of CdSe nanocrystals, *Nature*, **404**: 59-61.
- Yan Jiao, Mengting Guo, Renle Wang, Chongyun Shao, and Lili Hu (2021), Influence of Al/Er ratio on the optical properties and structures of  $\text{Er}^{3+}/\text{Al}^{3+}$  co- doped silica glasses, *J. Appl. Phys.* **129**: 053104.

### **3.2. Structural and Optical Studies of Sm<sup>3+</sup>-doped Silica Glass along with TiO<sub>2</sub> Nanoparticles for Photonic Applications**

#### **Overview**

The physical, structural, and optical properties of the Sm<sup>3+</sup> ion in TiO<sub>2</sub>–SiO<sub>2</sub> sol-gel have been investigated. Different physical properties like refractive index, density, polarizability, etc. are measured and listed for prepared glass material. X-ray diffraction, Fourier transform infrared spectroscopy (ATR-FTIR), and transmission electron microscopy (TEM) are utilized to study the structure of the prepared material. The XRD and TEM measurements confirmed that our glass sample is a nanocrystal. From absorption spectra, the Judd-Ofelt (J-O) intensity parameters ( $\Omega_\lambda$ ) of the transition are determined by least square fit analysis. Photoluminescence (PL) spectra for the sample were recorded by employing a laser at 450 nm. PL spectra along with J-O intensity parameters, different radiative parameters, for example, radiative transition probabilities ( $A_T$ ), radiative lifetimes ( $\tau_r$ ), measured and calculated branching ratios ( $\beta_r$ ), effective bandwidths ( $\Delta\lambda_{\text{eff}}$ ), and cross-sections of stimulated emission ( $\sigma_p$ ) were estimated for recorded emission transitions. The CIE 1931 chromaticity diagram is evidence of the color purity of the synthesized materials, which is slightly amplified by the appropriate Sm<sup>3+</sup> ion addition.

#### **3.2.1. Introduction**

Rare-Earth (RE) doped glasses have gained much interest due to their excellent optical and physical properties. RE ions have been doped in a variety of host materials for applications such as phosphor (Kumar *et al.*, 2007, Chen *et al.*, 2012), bio-photonics (Loo *et al.*, 2019, Kunkel *et al.*, 2018), quantum memory (Liang *et al.*, 2019, Xiaoqi *et al.*, 2014), and others. Silica based Rare Earth doped glasses (RED) show excellent durability and optical quality. It is to be noted that it is difficult to prepare RED glasses by conventional melt quench technique because of high melting temperature of silica. Sol-gel process offer an attractive method for preparing RED silica glasses at relatively low temperature without melting. However the optimum performance of these materials is hindered by various factors such as

concentration quenching, rare earth clustering, and high phonon energy various relaxation processes reduced the fluorescence efficiency due to high phonon energy ( $1100\text{ cm}^{-1}$ ). Co-doping of aluminium (Rai *et al.*, 2016) and nanoparticles in sol gel glasses doped RE has been shown to increase the fluorescence efficiency (Rai *et al.*, 2016). Researchers employ different methods to overcome these shortcomings. Silica glass host suffers from its high phonon energy, which is considered a negative attribute for efficient RE doped material. Optical properties of RE imbedded in semiconductor nanomaterial are very attractive for fabricating optoelectronic devices for technological applications.  $\text{TiO}_2$  is wide band gap semiconductor are good candidate to be used as glass modifier of RE doped glasses because of good mechanical, thermal, wide range of good transparency and optical properties.  $\text{TiO}_2$  has been used as photo catalyst for decomposition and solar conversion because of its high photo reactivity (Kamat *et al.*, 2007). It as also been used for optical coating in beam splitter and anti-reflection coating because of its high dielectric constant (Hai *et al.*, 2012, Chen *et al.*, 2007).  $\text{TiO}_2$  nanocrystals (NCs) have wide band limits and a tendency to transform to rutile from anatase, which reduces photocatalytic activity (Asahi *et al.*, 2001, Li *et al.*, 2009). An appropriate amount of  $\text{TiO}_2$  is co-doped with the RE host to enhance sensitization (Dihingia *et al.*, 2012). Many researchers have looked into  $\text{TiO}_2$  photonic applications like wave guides and thin films (Rai *et al.*, 2014, Bahtat *et al.*, 1994).

### 3.2.2. Experimental Details

The glass sample is manufactured by the sol-gel process where tetraethyl orthosilicate (TEOS) is utilized as the glass precursor, ethanol (EtOH) as the solvent, nitric acid ( $\text{HNO}_3$ ) as the catalyst, samarium chloride and titanium isopropoxide (TIPO) as the sources for the  $\text{Sm}^{3+}$  and  $\text{TiO}_2$  dopants, respectively. The dopants were mixed with EtOH,  $\text{HNO}_3$ , and banana trunk sap (a natural product containing more than 90% water) and stirred for 45 minutes. Into this solution, TEOS was poured such that the molar ratio of TEOS, ethanol, banana trunk sap, and nitric acid was maintained at a molar ratio of 1:4:4:0.00165, respectively. The final solution with these dissolved dopants is stirred for 2 hours with the help of a magnetic stirrer to form a sol. In a plastic container, this sol is poured and left to form stiff gels. To

allow slow evaporation, small miniature holes are created in the lid of the plastic container and left stranded for 2-3 weeks. After that, the gels are dried gradually up to 60 °C and then annealed by an electric furnace at a heating rate of 1 °C/min up to 1000 °C. The refractive index was calculated with the help of the Abbe Refractometer method. The thickness of the disc-shaped sample is 0.226 cm along with a density of 2.12 gm/cm<sup>3</sup> and a refractive index of 1.748.

### 3.2.3. Results and Discussion

#### 3.2.3.1. Various physical properties

The density of Sm<sup>3+</sup> ions doped with TiO<sub>2</sub> in silica glass-ceramic by the sol-gel method was estimated by using the Archimedes principle. Here, xylene is used as the immersion liquid. The refractive index of glass was measured by the use of the Abbe Refractometer method. From the practically computed values of densities and refractive index, the additional associated properties like molecular electronic polarizability ( $\alpha_e$ ), average molecular weight ( $M_T$ ), molar refractivity ( $R_M$ ), the concentration of Sm<sup>3+</sup> ion ( $N$ ), dielectric constant ( $\epsilon$ ), optical dielectric constant ( $\epsilon-1$ ), reflection losses ( $R_L$ ), molar refraction ( $R_m$ ), polaron radius ( $R_p$ ) and interatomic distance ( $R_i$ ) have been computed by using the appropriate expressions (Annapurna *et al.*, 2019) and listed in Table 3.2.1. Electronic polarizability is considered a significant property that decides the non-linear response of the materials. The intense light exposed to the material initiates this electronic polarization, which in turn leads to optical nonlinearity. The theoretical expressions of Volf and Lorentz–Lorentz (Yasi *et al.*, 1982, Haralampieve *et al.*, 2012), relate the refractive index ( $n$ ), to the polarizability ( $\alpha_e$ ), as follows:

$$\frac{(n^2-1)}{(n^2+1)} V_m = \frac{4}{3\pi} N \alpha_e \quad (3.2)$$

**Table 3.2.1**

Various physical properties of a sol-gel glass-ceramic containing 2 mol%  $\text{Sm}^{3+}$ : 33%  $\text{TiO}_2$ -66%  $\text{SiO}_2$ .

Physical properties	Value
Density ( $\rho$ ) ( $\text{gm/cm}^3$ )	2.12
Thickness	0.266
Average molecular weight ( $M_T$ )	62.92
Refractive index ( $n$ )	1.748
Loss due to Reflection ( $R_L$ )	0.074
Molar Refractivity ( $R_m$ )	12.069
Energy gap ( $E_g$ )	7.04
Molar electronic polarizability ( $\alpha_m$ )	4.789
Dielectric constant ( $\epsilon_c$ )	3.056
Optical dielectric constant ( $\epsilon_c-1$ )	2.056
Electronic polarizability ( $\alpha_e \times 10^{-20}$ )	1.613
$\text{Sm}^{3+}$ ion concentration ( $N \times 10^{19}$ )	2.441
Molar volume ( $V_m$ )	29.679
Radius of Polaron ( $R_p \times 10^{-8}$ )	6.45
Inter-ionic distance ( $R_i \times 10^{-7}$ )	1.6
Metallization Criterion ( $M_C$ )	0.593

### 3.2.3.2. XRD Spectra Analysis

The X-ray diffraction (XRD) technique is the most convenient method for the gross characterization of materials. This technique has been widely employed to examine the microstructure, phase formation, and texture as well as the lattice parameters.

Diffraction peak positions can be accurately measured with XRD, which makes it the best method for analyzing homogeneous and inhomogeneous strains. Homogeneous or uniform elastic strain shifts the diffraction peak positions. From the

shift in peak positions, one can calculate the change in d-spacing, which is the result of the change of lattice constants under a strain. Inhomogeneous strain varies from crystallite to crystallite or within a single crystallite, causing the diffraction peaks to broaden as  $\sin \theta$  increases. Peak broadening is also caused by the finite size of crystallites, but here the broadening is independent of  $\sin \theta$ . When both crystallite size and inhomogeneous strain contribute to the peak width, these can be separately determined by careful analysis of peak shapes.

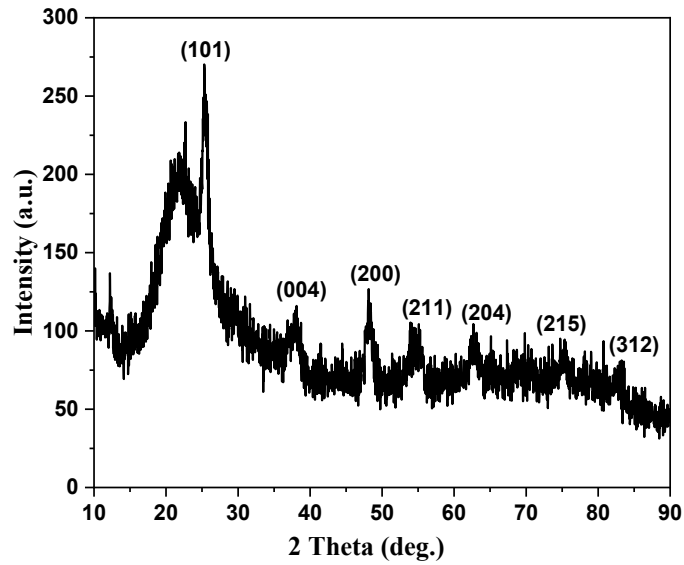
If there is no inhomogeneous strain, the crystallite size,  $D$ , can be estimated from the peak width with the Scherrer formula (Toney *et al.*, 2007).

$$D = \frac{0.9\lambda}{\beta \cos \theta_B} \quad (3.3)$$

Where  $\lambda$  is the X-ray wavelength,  $\beta$  is the full width of half maximum (FWHM) of a diffraction peak  $\theta_B$  is the diffraction angle.

However, one should keep in mind that nanoparticles often form twinned structures; therefore, the Scherrer formula may produce a result different from that of the true particle size (Brik *et al.*, 2015). In addition, X-ray diffraction only provides the collective information of the particle sizes and usually requires a sizable amount of powder.

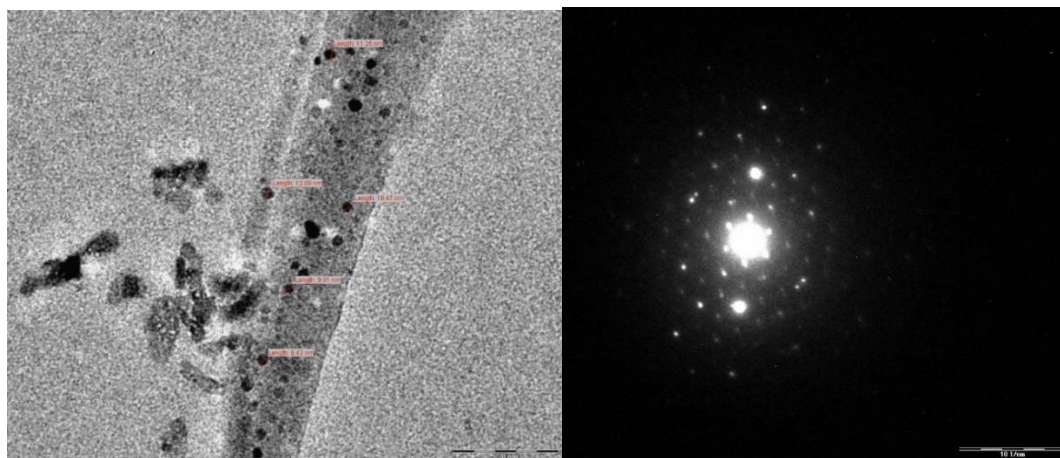
The dominant diffraction peaks in the  $2\theta$  range of  $10^\circ$ – $90^\circ$  corresponded to the presence of anatase  $\text{TiO}_2$  phases (101), (004), (200), (211), (204), (215), and (312) respectively. The  $\text{TiO}_2$  crystalline size calculated with the help of the Debye-Scherrer formula (Theivasanthi *et al.*, 2013) using the anatase (101), (004), (200), (211), (204), (215) and (312) peaks of  $\text{TiO}_2$  nanoparticles (Fig. 3.2.1) is 8.3 nm.



**Fig. 3.2.1:** XRD patterns of parent 33% TiO<sub>2</sub>–66% SiO<sub>2</sub> nanoparticles.

### 3.2.3.3. Transmission Electron Microscopy (TEM)

The TEM image with selective area electron diffraction (SAED) is shown in Fig. 3.2.2(a) & (b), respectively. The TEM image shows that the average particle size is around 10 nm, which is consistent with the crystallite size of 8.3 nm calculated by the Scherrer equation. A SAED pattern is used to learn about the crystal properties of a particular region, i.e., whether the material is single crystalline, polycrystalline, polycrystalline textured, or amorphous (Arasi *et al.*, 2018). Single-crystalline materials' SAED patterns are only spot patterns, whereas polycrystalline materials have ring pattern form. The SAED pattern shows a ring-like pattern, which means the prepared TiO<sub>2</sub> doped sample is a polycrystalline material.



**Fig. 3.2.2:** (a) TEM image of TiO<sub>2</sub> nanoparticles doped in silica glass-ceramic; (b) SAED pattern confirms the larger grain size and polycrystalline nature due to the presence of rings with discrete spots.

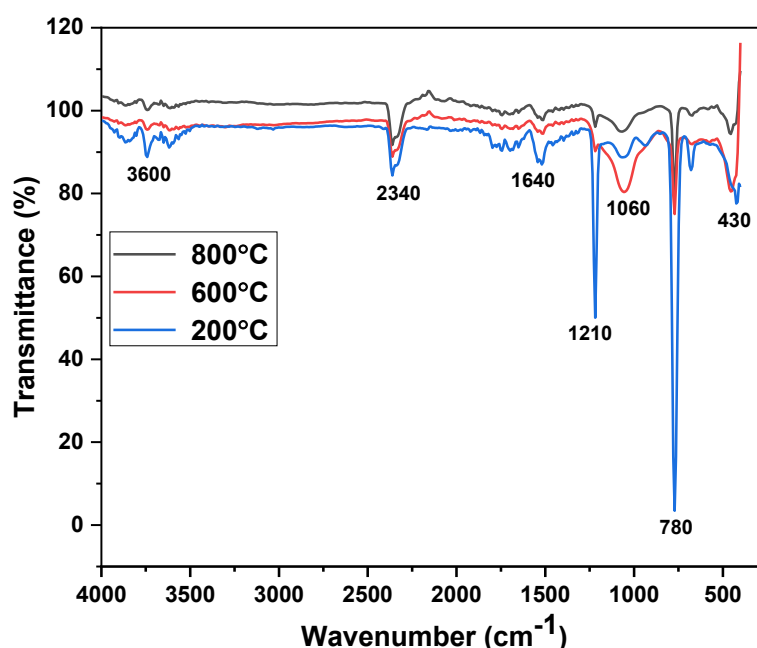
#### 3.2.3.4. FTIR Spectrum Analysis

The FTIR spectra of the 2 mol% Sm<sup>3+</sup> ion doped in 33% TiO<sub>2</sub>–66% SiO<sub>2</sub> sol-gel glass-ceramic are presented in Fig. 3.2.3. The samples are sintered at (a) 200 °C, (b) 600 °C, and (c) 800 °C. The FTIR spectra indicates peaks at about 458, 552, 670, 768, 856, 954, 1053, 1327, 1530, 1631, 2347, and 3744 cm<sup>-1</sup> for the samples at different sintering temperatures. Although a variation in the peak intensity is observed for an increase in sintering temperature.

The hydrolysis of TEOS contributes to the Si-OH group through a polycondensation reaction. These sol-gel samples at the gel phase have a large amount of H<sub>2</sub>O with additional organics. These compounds steadily escape from the matrix as we heat the prepared sample inside a muffle furnace and convert it into a rigid glassy network. The band at 430 cm<sup>-1</sup> is due to Ti-O bond in TiO<sub>2</sub> crystalline structure (Hazarika *et al.*, 2004). The weak band around 940 cm<sup>-1</sup> is also due to Si-O-Ti bond which implies that the bond could be formed in the TiO<sub>2</sub>/SiO<sub>2</sub> samples prepared by an inorganic synthesis route from TiO<sub>2</sub> and SiO<sub>2</sub> sol. This is evidence of Si assimilating into titania's framework. Strong sharp band around 780cm<sup>-1</sup> is assigned to symmetrical stretching of Si-O bond (Vijayakumar *et al.*, 2015) and the broad band around 1060 cm<sup>-1</sup> is assigned to asymmetrical stretching of Si-O-Si bond



(Hazarika *et al.*, 2004). The sharp band around  $1210\text{ cm}^{-1}$  is attributed to Si-O-Si asymmetrical stretching in cyclic structure (Swapna *et al.*, 2014). The band around  $1640\text{ cm}^{-1}$  and  $3600\text{ cm}^{-1}$  are due to the presence of residual hydroxyls and the strength reduce with higher temperature treatment.



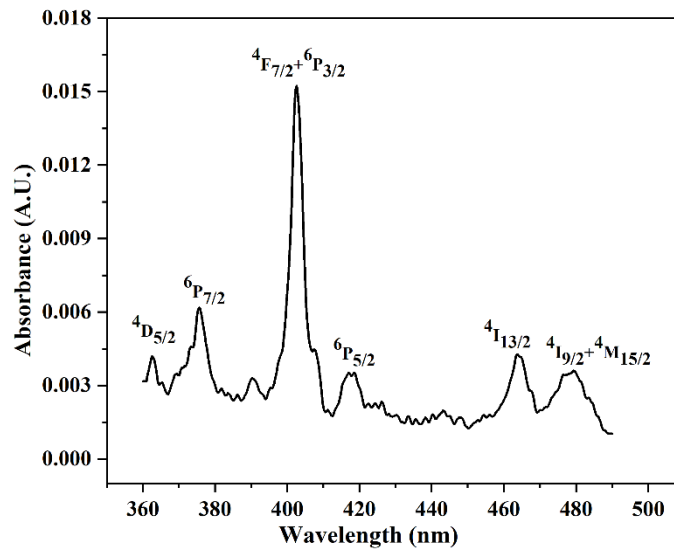
**Fig. 3.2.3:** FTIR spectra of 2.0 mol%  $\text{Sm}^{3+}$  doped with 33%  $\text{TiO}_2$ –66%  $\text{SiO}_2$  with sol gel glass-ceramic at different annealing temperatures are presented.

### 3.2.3.5. Absorption spectra

The absorption spectrum of the synthesized glass material is presented in Fig. 3.2.4. The absorption peaks are observed around 363, 376, 402, 418, 463, and 480 nm resulting from the transitions to  $^4\text{D}_{5/2}$ ;  $^6\text{P}_{7/2}$ ;  $^4\text{F}_{7/2} + ^6\text{P}_{3/2}$ ;  $^6\text{P}_{5/2}$ ;  $^4\text{I}_{13/2}$  and  $^4\text{I}_{9/2} + ^4\text{M}_{15/2}$  respectively, originating from the ground state  $^6\text{H}_{5/2}$ . The oscillator strengths were estimated using data from  $\text{Sm}^{3+}$  ion absorption in  $\text{SiO}_2$ - $\text{TiO}_2$  glass samples, and J-O intensity parameters were calculated for various transitions from the  $^6\text{H}_{5/2}$  ground state [24-26]. The outcomes of these J-O intensity parameters are useful to understand

the local configuration as well as bonding in the neighborhood of the RE ions (Rai *et al.*, 2011).

A wide variation in band intensity is observed for the electric-dipole initiated  ${}^6\text{H}_{5/2} \rightarrow {}^4\text{D}_{5/2}$  transition, which is also hypersensitive. The most intense  ${}^6\text{H}_{5/2} \rightarrow {}^4\text{F}_{7/2} + {}^6\text{P}_{3/2}$  transition is observed for the prepared sample among all the absorption bands (Pisarska *et al.*, 2006). The symmetry of the local neighborhood around the  $\text{RE}^{3+}$  ions is decided by the ratio of intensity among electric dipole (ED) transitions and magnetic dipole (MD) transitions. Here, the enhanced intensity of the ED transition indicates the higher asymmetry around ions.

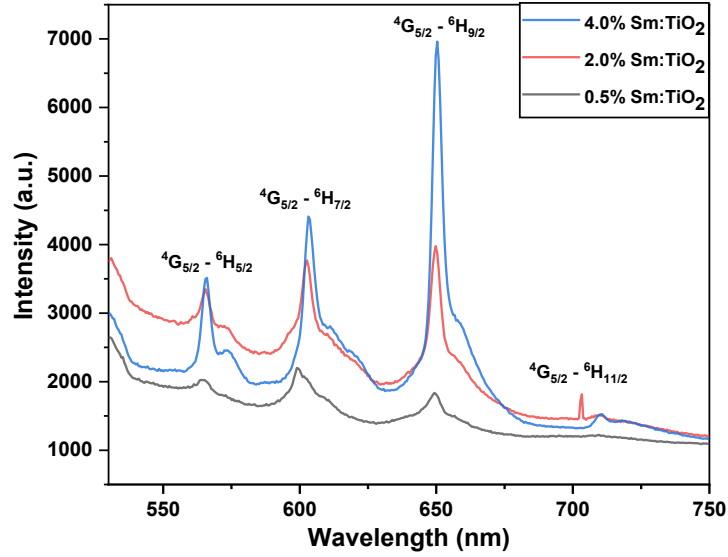


**Fig. 3.2.4:** Absorption spectrum: 33%  $\text{TiO}_2$ –66%  $\text{SiO}_2$  sol-gel glass-ceramic doped with (2.0 mol%)  $\text{Sm}^{3+}$  ions.

### 3.2.3.6. Photoluminescence spectra

The PL spectra of the  $\text{Sm}^{3+}$  ions of different concentrations (4.0 mol%, 2.0 mol%, 0.5 mol%) doped in 33%  $\text{TiO}_2$ –66%  $\text{SiO}_2$  sol-gel glass-ceramics heated to 1000 °C are shown in Fig. 3.2.5. The PL spectra of  $\text{TiO}_2$ - $\text{SiO}_2$  glasses doped with the  $\text{Sm}^{3+}$  ions have been recorded within the spectral range 750-530 nm, and it shows evidence of emission bands around 566 nm, 605 nm, 652 nm, and 709 nm. Here, the highest peak of emission spectra is 652 nm. All the spectra show four transitions that are from the initial state  $^4\text{G}_{5/2}$  to the terminal state  $^6\text{H}_{5/2}$ ;  $^6\text{H}_{7/2}$ ;  $^6\text{H}_{9/2}$ ;  $^6\text{H}_{11/2}$ , respectively of the  $\text{Sm}^{3+}$  ions. The transition from states  $^4\text{G}_{5/2}$  to  $^6\text{H}_{9/2}$  (652 nm, red) and  $^6\text{H}_{11/2}$  (709 nm, deep red) states are the most and least intense, respectively, in the present study.

The transition  $^4\text{G}_{5/2} \rightarrow ^6\text{H}_{9/2}$  is significant because it allows for partial MD and partial ED with the  $\Delta J = \pm 2$  selection rule. This makes it appropriate for laser emission. The transition  $^4\text{G}_{5/2} \rightarrow ^6\text{H}_{5/2}$  (566 nm, yellow green) is a prohibited MD transition ( $\Delta J = 0$  i.e.,  $J \neq 0 \leftrightarrow 0$  values),  $^4\text{G}_{5/2} \rightarrow ^6\text{H}_{7/2}$  (605 nm, orange) is purely ED transition with  $\Delta J = \pm 1$  having reasonable intensity, and the transition  $^4\text{G}_{5/2} \rightarrow ^6\text{H}_{11/2}$  (709 nm, deep red) is prohibited with  $\Delta J = \pm 3$  having faint intensity (Reddy *et al.*, 2014). The asymmetry around the  $\text{Sm}^{3+}$  ion doped in the titania-silicate host is evident from the higher intensity ED transition compared to the MD transition in this present work. A rise in the intensity of yellow green, orange, red and deep red colors with an increase in the  $\text{Sm}^{3+}$  ion concentration is also evident in Fig 3.2.5.

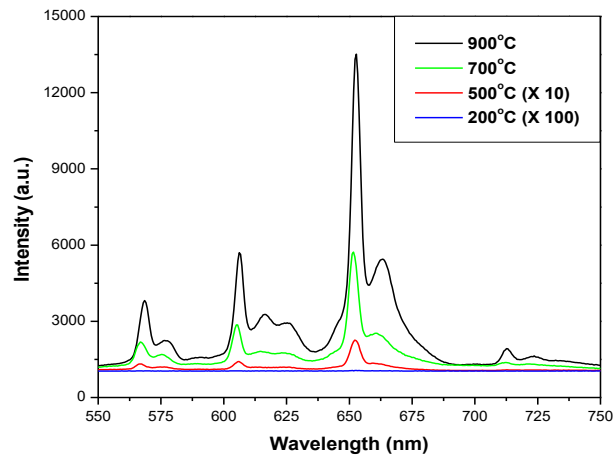


**Fig. 3.2.5:** Photoluminescence Spectra of  $\text{Sm}^{3+}$  ion co-doped with 33%  $\text{TiO}_2$ : 66%  $\text{SiO}_2$  sol-gel glass-ceramic.

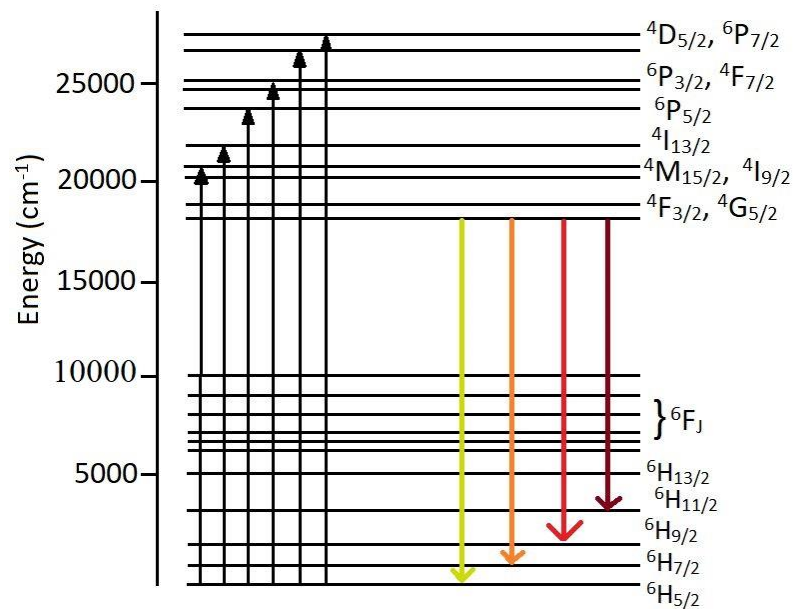
### 3.2.3.7. Dependence of annealing temperature on PL spectra

The PL spectra of (2 mol%)  $\text{Sm}^{3+}$  doped in 33%  $\text{TiO}_2$ : 66%  $\text{SiO}_2$  in sol-gel glass-ceramic at various annealing temperatures were recorded by the excitation wavelength ( $\lambda_{\text{ex}} = 450 \text{ nm}$ ) as shown in Fig. 3.2.6. The relation between PL intensity and annealing temperature is plotted for 2 mol%  $\text{Sm}^{3+}$  doped in 33%  $\text{TiO}_2$ : 66%  $\text{SiO}_2$  sol-gel glasses as in Fig. 3.2.6. It is observed that PL peak intensity increases with a rise in annealing temperature of 200 °C–900 °C. The formation of  $\text{TiO}_2$  at high annealing temperatures is the reason behind it.

A schematic diagram illustrating the possible mechanism of absorption and photoluminescence is presented in Fig. 3.2.7.



**Fig. 3.2.6:** Effect of annealing temperature on PL intensity. (Note: PL intensities of samples annealed to 200 °C and 500 °C are magnified 100 and 10 times for clarification).



**Fig. 3.2.7:** Different energy manifolds of  $\text{Sm}^{3+}$  ions doped in 33%  $\text{TiO}_2$ -66%  $\text{SiO}_2$  sol-gel glass are depicted schematically.

### 3.2.3.8. Judd-Ofelt and Radiative parameters

The oscillator strength of numerous  $4f-4f$  transitions in rare-earth is provided by the J-O theory. A study of the J-O parameter (Judd, 1962, Ofelt, 1962), is performed on the absorption spectra of the synthesized materials (Fig. 3.2.4) to extract valuable data about the optical properties as well as the neighborhood of  $\text{Sm}^{3+}$  ions in the host matrix. In Table 3.2.2 three different J-O intensity parameters ( $\Omega_\lambda$ ) as well as the experimental ( $f_{\text{exp}}$ ) and calculated oscillator strength ( $f_{\text{cal}}$ ) of the  $\text{Sm}^{3+}$  ions co-doped with  $\text{TiO}_2$  in silica glass are tabulated. The covalent bonding among glass host and  $\text{RE}^{3+}$  ions is evident from the large value of  $\Omega_2$ . Here  $\Omega_2$  is extremely sensitive to configuration. It is linked with the symmetry cum covalency of the  $\text{RE}^{3+}$  sites. The other two parameters,  $\Omega_4$  and  $\Omega_6$ , are influenced by the bulk properties of the medium, such as viscosity and dielectric, as well as the vibronic transition of the RE ions bonding to the ligand atoms. The spectroscopic quality ( $\Omega_4/\Omega_6$ ) is significantly important in forecasting the stimulated emission for the laser active medium, which can also be derived from J-O parameters. The J-O intensity parameters ( $\Omega_\lambda$ ) of  $\text{Sm}^{3+}$  doped glasses are compared in Table 3.2.3.

To estimate various radiative quantities, phenomenological JO parameters calculated from absorption spectra are combined with observed PL spectra of the fluorescence level  $^4\text{G}_{5/2}$  of the of (2 mol%) $\text{Sm}^{3+}$  ions doped in  $\text{TiO}_2\text{-SiO}_2$  glass. The estimation of radiative properties such as spontaneous emission probabilities ( $A_{\text{rad}}$ ), luminescence branching ratios ( $\beta_r$ ), and radiative lifetime ( $\tau_{\text{rad}}$ ) for the optical transitions of (2 mol%) $\text{Sm}^{3+}$  ions doped in  $\text{TiO}_2\text{-SiO}_2$  glass have been estimated using J-O intensity parameters in 3.2.4.

**Table 3.2.2**

Oscillator strength cum J-O intensity parameters for prepared glass samples

Transitions	Energy( in $\text{cm}^{-1}$ )	$f_{\text{exp}} (* 10^{-6})$	$f_{\text{cal}} (* 10^{-6})$	$\Omega_{\lambda} (10^{-20} \text{ cm}^2)$
${}^6\text{H}_{5/2} \rightarrow {}^4\text{D}_{5/2}$	27548	0.013	0.030	$\Omega_2 = 6.179 \pm 0.023$
${}^6\text{P}_{7/2}$	26596	0.145	0.125	
${}^4\text{F}_{7/2} + {}^6\text{P}_{3/2}$	24876	0.377	0.012	$\Omega_4 = 0.215 \pm 0.016$
${}^6\text{P}_{5/2}$	23924	0.041	0.040	
${}^4\text{I}_{13/2}$	21598	0.061	0.009	$\Omega_6 = 0.208 \pm 0.045$
${}^4\text{I}_{9/2} + {}^4\text{M}_{15/2}$	20833	0.057	0.085	
				$\Omega_4/\Omega_6 = 1.034 \pm 0.299$

**Table 3.2.3**

Judd–Ofelt parameters ( $\times 10^{-20} \text{ cm}^2$ ) and spectroscopic quality factor ( $X=\Omega_4/\Omega_6$ ) comparison of the  $\text{Sm}^{3+}$ -doped with  $\text{TiO}_2\text{-SiO}_2$  in sol-gel glasses with other available literature.

$\Omega_2$	$\Omega_4$	$\Omega_6$	$\Omega_4/\Omega_6$	References
6.179	0.215	0.208	1.034	Present work
9.28	8.03	5.46	1.47	LFB(Mg) (Balakrishna <i>et al.</i> , 2012)
7.34	5.09	3.70	1.38	LFB(Cd) (Balakrishna <i>et al.</i> , 2012)
8.87	8.36	6.34	1.32	LFB(Mg-Ca) (Balakrishna <i>et al.</i> , 2012)
6.36	6.02	3.51	1.72	Borate glass (Reisfeld <i>et al.</i> , 1974)
8.56	3.02	2.37	1.27	Lead fluoro germinate (Klimesz <i>et al.</i> , 2005)
0.19	2.81	2.78	1.01	TeWLiSm (Annapurna <i>et al.</i> , 2019)
0.68	3.77	2.15	1.75	Fluorozincate (Arul Rayappan <i>et al.</i> , 2011)
0.04	3.50	2.367	1.479	LiTFP (Jayasimhadri <i>et al.</i> , 2006)

**Table 3.2.4**

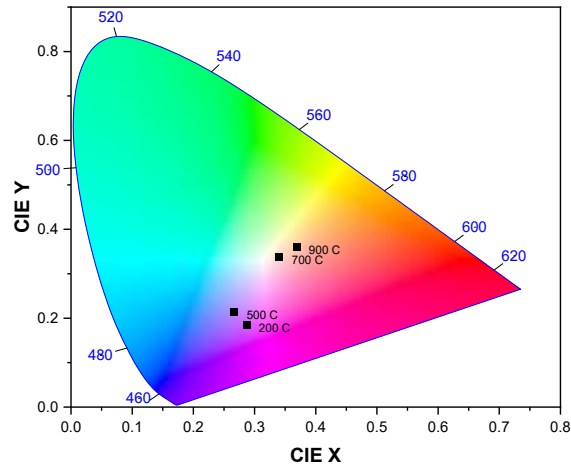
Estimated radiative parameters of synthesized glass-ceramic samples.

Transitions	Wavelength ( $\lambda_p$ ) (nm)	Energy ( $\text{cm}^{-1}$ )	$A_{\text{ed}}(\text{s}^{-1})$	$\beta_r$ (%)	$\lambda_{\text{eff}}$ (nm)	$\sigma_p (\times 10^{-21} \text{ cm}^2)$
$^4\text{G}_{5/2} \rightarrow ^6\text{H}_{5/2}$	566	17667.84	12.03	23.93	8.62	$7.08 \pm 0.372$
$^6\text{H}_{7/2}$	605	16528.93	32.22	63.19	8.78	$20.52 \pm 0.148$
$^6\text{H}_{9/2}$	652	15337.43	2.02	3.96	8.87	$2.16 \pm 0.109$
$^6\text{H}_{11/2}$	709	14104.37	4.72	9.22	8.98	$5.72 \pm 0.237$
$A_T (\text{s}^{-1}) = 50.99 \pm 0.237$			$\tau_R(\text{ms}) = 19.61 \pm 0.057$			



### 3.2.3.9. CIE-1931 chromaticity diagram

The intensity of the PL emission from optical measurements of the source has been exemplified using the CIE 1931 chromaticity Fig. 8. However, they affect the annealing temperature as the color emitted by the glass material changes from blue to red regions.



**Fig. 3.2.8:** CIE 1931 chromaticity diagram of  $\text{Sm}^{3+}$  co-doped with  $\text{TiO}_2$  in sol-gel silica glass at annealing temperatures.

### 3.2.3.10. Non-Linear Properties

Certain non-linear characteristics, ascertained from optical parameters, such as the non-linear refractive index ( $n_2$ ), non-linear refractive index susceptibility ( $\chi^{(3)}$ ), co-efficient ( $\gamma_{ce}$ ), and relatively high Abbe number ( $v_{Ab}$ ), suggest the good optical quality of the sol-gel silicate dense glass-ceramic (Hazarika *et al.*, 2004). Table 3.2.5 shows these values. These values are estimated using the approach outlined by (Dihingia *et al.*, 2012).

**Table 3.2.5**

Non-linear quantities of  $\text{Sm}^{3+}$ -doped  $\text{TiO}_2$ - $\text{SiO}_2$  by sol-gel process.

$n_G$	$n_R$	$n_{G-R}$	$n_B$	$\vartheta_A$	$1/\vartheta_A$	$n_2(10^{-13} \text{ esu})$	$\gamma_c$ ( $\text{cm}^2/\text{W}$ )	$\omega_o \times 10^{-13}$	$N \times 10^{-16}$	$\chi^{e(3)} \times 10^{-6}$
1.633	1.621	0.012	1.627	52.25	0.019	1.009	0.686	105.32	965.907	3.200

### 3.2.4. Conclusions

$\text{Sm}^{3+}$  was co-doped with  $\text{TiO}_2$  in sol-gel silica glass synthesized via the sol-gel process. The XRD and TEM measurements confirmed that our glass-ceramic sample contains nanocrystals of  $\text{TiO}_2$  in anatase phase. The structural properties of the prepared sample are studied using FTIR spectra. The optical properties of  $\text{Sm}^{3+}$ -doped with  $\text{TiO}_2$ - $\text{SiO}_2$  glass-ceramic have been observed through absorption and photoluminescence spectra. The Judd-Ofelt intensities and various radiative properties are also estimated. The optical quality of the  $\text{SiO}_2$  sol-gel glass is determined with the calculation of linear refractive index ( $n_2$ ), non-linear refractive index co-efficient ( $\gamma_c$ ), and Abbe number ( $\vartheta_A$ ).

## Reference

- A. Bahtat. M. Bouazaoui, and J. Mugnier (1994), Fluorescence of  $\text{Er}^{3+}$  ions in  $\text{TiO}_2$  planar waveguides prepared by a sol-gel process, *Opt. Commun.*, **111**: 55-60.
- A. Haralampieva, I.S. Lozanova, and V. Dimitrov (2012), Optical properties and structure of  $\text{BaO-V}_2\text{O}_5$  and  $\text{Fe}_2\text{O}_3\text{-BaO-V}_2\text{O}_5$  glasses, *J. Chemical Technology and Metallurgy*, **47**: 392.
- B. Klimesz, G. Dominiak, P. Solarz, M. Zelechower, W. Ryba-Romanowski (2005), Optical study of  $\text{GeO}_2\text{-PbO-PbF}_2$  oxyfluoride glass singly doped with  $\text{Pr}^{3+}$ ,  $\text{Nd}^{3+}$ ,  $\text{Sm}^{3+}$  and  $\text{Eu}^{3+}$ , *J. Alloys Compd.* **403**: 76-85.
- B.R. Judd (1962), Optical absorption intensities of rare-earth ions, *Phys. Rev.* **127**: 750.
- C.P. Reddy, V. Naresh, B.C. Babu, and Srinivasa (2014), Photoluminescence and Energy Transfer Process in  $\text{Bi}^{3+}/\text{Sm}^{3+}$  Co-Doped Phosphate Zinc Lithium Glasses, *Advances in Materials Physics and Chemistry*, **4**: 165-171.
- Ch. B. Annapurna Devi, K. Swapna, Sk. Mahamuda, M. Venkateswarlu, M.V.V.K.S. Prasad, K. Siva Rama Krishna Reddy, Nisha Deopa, A.S. Rao (2019), Spectroscopic studies and lasing potentialities of  $\text{Sm}^{3+}$  ions doped single alkali and mixed alkali fluoro tungsten tellurite glasses, *Optics and Laser Technology*, **111**: 176–183.
- Chen and S. S. Mao (2007), Titanium dioxide nanomaterials: synthesis, properties, modifications and applications, *Chemical Reviews*, **107**: 2891–2959.
- D. Milam and M.J. Weber (1976), Measurement of nonlinear refractive-index coefficients using time-resolved interferometry: Application to optical materials for high-power neodymium lasers, *J. Appl. Phys.* **47**: 2497-2499.
- G. Chen, T.Y. Ohulchansky, S. Liu, W. Law, F. Wu, M.T. Swihart and C.E.T. Al (2012), Nanocrystals with Efficient Near- Infrared to Near-Infrared Downconversion Photoluminescence for Bioimaging Applications, *ACS Nano*. **6**: 2969–2977.

- G.S. Ofelt (1962), Intensities of crystal spectra of rare-earth ion, *J. Chem. Phys.* **37**: 511.
- H. Li, D. Wang, P. Wang, H. Fan, and T. Xie (2009), Synthesis and studies of the visible-light photocatalytic properties of near- monodisperse Bi-doped TiO<sub>2</sub> nano-spheres, *Chemistry-A European Journal*, **15**: 12521–12527.
- Hai Liu, Lixin Yu, Weifan Chen, and Yingyi Li (2012), The Progress of TiO<sub>2</sub> Nanocrystals Doped with Rare Earth Ions, *Journal of Nanomaterials*, **2012**: 1-9.
- I. Arul Rayappan, K. Selvaraju, K. Marimuthu (2011), Structural and luminescence investigations on Sm<sup>3+</sup> doped sodium fluoroborate glasses containing alkali/alkaline earth metal oxides, *Phys. B*, **406**: 548–555.
- J. Yasi, J. Fusong, and G. Fuxi (1982), Optical and other physical properties of Al(PO<sub>3</sub>)<sub>3</sub>-containing fluorophosphates glasses, *J. Phys. Colloque*, **43**: 315.
- J.F. Loo, Y. Chien, F. Yin, S. Kong, H. Ho and K. Yong (2019), Upconversion and downconversion nanoparticles for biophotonics and nanomedicine, *Coord. Chem. Rev.* **400**: 213042.
- K. Swapna, Sk. Mahamuda, AS. Rao, T. Sasikala, LR. Moorthy (2014), Visible luminescence characteristics of Sm<sup>3+</sup> doped Zinc Alumino Bismuth Borate glasses, *Journal of Luminescence*, **146**: 288–294.
- L. Liang, D.B.L. Teh, N.D. Dinh, W. Chen, Q. Chen, Y. Wu, S. Chowdhury, A. Yamanaka, T.C. Sum, C.H. Chen, N. V. Thakor, A.H. All and X. Liu (2019), Upconversion amplification through dielectric superlensing modulation, *Nat. Commun.* **10**: 1–9.
- M. Jayasimhadri, L.R. Moorthy, S.A. Saleem, R.V.S.S.N. Ravikumar (2006), Spectroscopic characteristics of Sm<sup>3+</sup>-doped alkali fluorophosphate glasses, *Spectrochimica Acta Part A*, **64**: 939–944
- M. Vijayakumar, K. Marimuthu, V. Sudarsan (2015), Concentration dependent spectroscopic behavior of Sm<sup>3+</sup> doped leadfluoro-borophosphate glasses for laser and LED applications, *Journal of Alloys and Compounds*, **647**: 209-220.

- M. Xiaoqi, L. Lianqiang, Z. Kaishun and L. Juncheng (2014), The effect of SiO<sub>2</sub> on TiO<sub>2</sub> up-conversion photoluminescence film, *Opt. Mater.* **37**: 367–370.
- M.G. Brik, Z.M. Antic, K. Vukovic, and M.D. Dramicanin (2015), Judd-Ofelt Analysis of Eu<sup>3+</sup> Emission in TiO<sub>2</sub> Anatase Nanoparticles, *Materials Transactions*, **56**: 1416-1418.
- N. Kunkel and P. Goldner (2018), Recent Advances in Rare Earth Doped Inorganic Crystalline Materials for Quantum Information Processing, *Zeitschrift Fur Anorg. Und Allg. Chemie.* **644**: 66–76.
- P. V. Kamat (2007), Meeting the clean energy demand: nanostructure architectures for solar energy conversion, *Journal of Physical Chemistry C*, **111**: 2834–2860.
- P.J. Didingia and S. Rai (2012), Synthesis of TiO<sub>2</sub> nanoparticles and spectroscopic upconversion luminescence of Nd<sup>3+</sup>-doped TiO<sub>2</sub>-SiO<sub>2</sub> composite glass, *J. Lumin.* **132**: 1243–1251.
- R. Asahi, T. Morikawa, T. Ohwaki, K. Aoki, and Y. Taga (2001), Visible-light photocatalysis in nitrogen-doped titanium oxides, *Science*, **293**: 269–271.
- R. Reisfeld, E. Greenberg, E. Biron (1974), Energy transfer between Gd<sup>3+</sup> and Sm<sup>3+</sup> the effect of Gd<sup>3+</sup> on quenching of Sm<sup>3+</sup> and intensity parameters of Sm<sup>3+</sup> in borate glasses, *J. Solid State Chem.* **9**: 224-233.
- S. Hazarika and S. Rai (2004), Structural, optical and non-linear investigation of Eu<sup>3+</sup> ions in sol-gel silicate glass, *Optical Materials*, **27**: 173-179.
- S. Hazarika and S. Rai (2004), Structural, optical and non-linear investigation of Eu<sup>3+</sup>: Al(NO<sub>3</sub>)<sub>3</sub>-SiO<sub>2</sub> sol-gel glass, *Bulletin of Materials Science*, **27**: 273-279.
- S. Rai and A.L. Fanai (2004), Spectroscopic studies of Ho<sup>3+</sup> doped SiO<sub>2</sub>-TiO<sub>2</sub> nanoparticle for photonic applications, *Sci. Vis.* **14**: 112–117.
- S. Rai, AL. Fanai (2016), Effect of annealing and dopants concentration on the

- optical properties of  $\text{Nd}^{3+}:\text{Al}^{3+}$  co-doped sol-gel silica glass, *Journal of Luminescence*, **170**: 325–329.
- S. Rai, L. Bokatial and P. J. Dihingia (2011), Effect of CdS nanoparticles on fluorescence from  $\text{Sm}^{3+}$  doped  $\text{SiO}_2$  glass, *Journal of Luminescence*, **131**: 978–983.
- S.E. Arasi, J. Madhavan and M.V.A. Raj (2018), Effect of  $\text{Sm}^{3+}$  doping on structural, optical properties and photocatalytic activity of titanium dioxide nanoparticles, *J Taibah University of Science*, **12**: 1-5.
- T. Theivasanthi, and M. Alagar (2013), Titanium dioxide ( $\text{TiO}_2$ ) Nanoparticles - XRD Analyses – An Insight, *Chemical Physics*, **15**: 1-10.
- Toney Fernandez, Gijo Jose, Siby Mathew, P.R. Rejikumar, N.V. Unnikrishnan (2007), An ultra-low hydrolysis sol-gel route for titanosilicate xerogels and their characterization, *J Sol-Gel Sci. Tech.* **41**: 163–168.
- V. Kumar, O.M. Ntwaeaborwa, T. Soga, V. Dutta and H.C. Swart (2007), Rare Earth Doped Zinc Oxide Nanophosphor Power: A Future Material for Solid State Lighting and Solar Cells, *ACS Photonics*, **4**: 2613-2637.
- W.A. Pisarski, J. Pisarska, M. Maczka and W.R. Romanowski (2006), Europium-doped lead fluoroborate glasses: structural, thermal and optical investigations, *J. Mol. Structure*, **792**: 207–211.
- Y.C.R, A. Balakrishna, D. Rajesh, M. Seshadri (2012), Influence of modifier oxides on spectroscopic properties of  $\text{Sm}^{3+}$  doped lithium fluoroborate glass, *Journal of Molecular Structure*, **1028**: 141–147.

### **3.3. Effect of ZnS nanoparticles on the optical properties of Sm<sup>3+</sup> ions in silicate matrix**

#### **Overview**

ZnS and Sm<sup>3+</sup>-doped ZnS nanoparticles (NPs) in silicate glasses were prepared by sol-gel technique. X-ray diffractometer (XRD), scanning electron microscopy (SEM), transmission electron microscopy (TEM), and photoluminescence (PL) emission spectra were used to analyze the sample's morphology and crystal structure. UV-visible absorption spectra and PL emission spectra were used to look at the sample's optical characteristics. The formation of NBO and the elimination of the OH-group are confirmed by the FTIR spectra analysis. The XRD, SEM and TEM measurements confirmed that our glass sample is a nano-crystal. Optical absorption spectra have been used to evaluate three phenomenological Judd-Ofelt (JO) parameters  $\Omega_\lambda$  ( $\lambda = 2, 4, 6$ ) to determine the local structure and bonding surrounding Sm<sup>3+</sup> ions. Glasses containing SSZ5 are found to have the highest parameter  $\Omega_2$ , which shows the covalency of the Sm-O bond, followed in decreasing order by glasses containing SSZ3 and SSZ1. This result implies that the coordination environment surrounding the Sm<sup>3+</sup> ions site is less centro-symmetric and more asymmetric in glass containing ZnS. For the glasses under investigation, the covalent character of the Sm-O bond is shown by the positive values of the bonding parameter  $\delta$ . Four emission bands were seen in the PL spectra obtained at an excitation wavelength of 450 nm. Glass samples containing SSZ5 are shown to have greater radiative characteristics, such as branching ratio ( $\beta_R$ ) and stimulated emission cross-section ( $\sigma$ ), as well as potential emission band intensity. However all other prepared glasses, however, have been shown to be efficient lasing materials, indicating their appropriateness for the development of photonic materials that emit radiations in the range of blue to white regions. The Figure of Merit (FOM) results suggest that the prepared glasses might be used as optical amplifiers.

### 3.3.1. Introduction

Glasses doped with rare earth (RE) are particularly interesting because of their outstanding optical, spectroscopic, and luminescence characteristics (Rayappan *et al.*, 2011, Mahato *et al.*, 1998). These many potential applications are made possible by the versatility of RE-doped glasses as well as their broader emission and absorption spectra (Reisfeld *et al.*, 1975, Steudel *et al.*, 2016, Praveena *et al.*, 2008, Adams, 2002). They have been found to have potential applications in the fields of solid-state lasers, optoelectronic and photonic devices, sensors, solid-state lighting systems, light emitting diodes, optical amplifiers, energy up-converters, optical data storage devices, and high-power laser gain medium, among others (Adams, 2002, Rao *et al.*, 2017, Kaur *et al.*, 2017, Mugoni *et al.*, 2017). They are also crucial to the development of a number of technologically significant devices (Tanko *et al.*, 2016, Kaur *et al.*, 2016, Kaur *et al.*, 2016). A thorough analysis of several rare earth doped glass compositions has been provided by Gorller-Walrand and Binnemans (Walrand *et al.*, 1998). The host matrix's composition has a highly sensitive effect on how rare earth ion optical and spectroscopic characteristics are altered. Glass has shown to be an excellent host for rare earth doping due to its random network structure and capacity to accept a broad variety of dopants. It also offers a substantial amount of space for active functioning (Rao *et al.*, 2017, Kaur *et al.*, 2017, Mugoni *et al.*, 2017). We may transfer a passive glass into a laser glass, a non-linear optical glass, a magneto-optic glass, etc. by properly doping it (Decorby 2006).

Samarium ion ( $\text{Sm}^{3+}$ ), one of the several rare earth ions, has drawn a lot of interest as it may be found in many different applications such as memory devices, phosphor materials, display panels, UV sensors, and visible lasers (Boehm *et al.*, 1979, Rajesh *et al.*, 2012, Jayasankar *et al.*, 2000, Kaur *et al.*, 2013, Vijayakumar *et al.*, 2015, Ramachari *et al.*, 2013, NayabRasool *et al.*, 2013). The transitions  $^4\text{G}_{5/2} \rightarrow ^6\text{H}_J$  ( $J = 5/2, 7/2, 9/2, 11/2$ ) of  $\text{Sm}^{3+}$ , an essential activator ion, create bright luminescence in the visible range (Rajesh *et al.*, 2012). Numerous hosts, including borate (Boehm *et al.*, 1979), bismuth borate (Rajesh *et al.*, 2012), lithium borate and lithium fluoroborate (Jayasankar *et al.*, 2000), lithium aluminoborate (Kaur *et al.*, 2013), lead fluoro-borophosphate (Vijayakumar *et al.*, 2015), oxyfluorosilicate (Ramachari *et al.*, 2013), phosphate (NayabRasool *et al.*, 2013), sodium tellurite



(Mawlud *et al.*, 2017), lead oxyfluoroborate (Ahmadi *et al.*, 2016), and magnesium zinc sulpho-phosphate glasses, etc. (Rukmini *et al.*, 1995), have been reported in the literature regarding the spectroscopic and luminescent properties of  $\text{Sm}^{3+}$  ions.

Melt-quench and sol-gel methods, the latter of which relies on chemical reactions at room temperature (RT), can be used to create silica matrices (Jayasankar *et al.*, 2000). Benefits of the sol-gel process include cost-effectiveness, simplicity of controlling precursor quality, and product shape and size diversity (Rukmini *et al.*, 1995). Nevertheless, a substantial portion of the residual hydroxyl group (-OH) component from the precursors is still present in the silica matrix made via the sol-gel process. The PL intensities from RE ions are quenched by these -OH components. It is possible to lessen this quenching by annealing at high temperatures. Another quenching, referred to as concentration quenching, takes place as a result of RE ions clustering together due to their low solubility in a silicate matrix (Kakotia *et al.*, 2019). Therefore, to enhance the PL intensities displayed in the RE doped in silicate the host, some kind of structural modification is necessary. This can be accomplished through the incorporation of particular species known as modifiers, which inhibit cross-relaxation, or the RE-RE interactions, (Kakotia *et al.*, 2019) and simultaneously fine-tuning ligand field environment around the RE ions (Rukmini *et al.*, 1995). Thus, the modifiers can sensitize the ED transitions of RE ions and their radiative characteristics (Rukmini *et al.*, 1995). Various kinds of modifiers, such as oxides (Rukmini *et al.*, 1995, Jorgensen *et al.*, 1983, Satyanarayana *et al.*, 2010, Rai *et al.*, 2002) or nanoparticles (Reddy *et al.*, 2000, Sharma *et al.*, 2018, Manam *et al.*, 2010), have been reported for RE-doped glass materials. Metal and semiconductor nanoparticles have been reported in several studies as a well-known sensitizer for RE-based luminescent materials (Kole, 2012, Amirian *et al.*, 2018, Dehingia *et al.*, 2020, Rajkonwar *et al.*, 2022).

Zinc sulphide (ZnS) is a semiconductor that has been explored extensively due to its exceptional optical characteristics. UV light-emitting diodes and injection lasers have made use of zinc sulphide (ZnS), a significant wide-band gap (3.6 eV) semiconductor (Yamamoto *et al.*, 2001). Infrared windows, electroluminescent devices, and flat-panel displays (Bredol *et al.*, 1998, Vacassy *et al.*, 1998). The variety of uses for ZnS nanocrystals has expanded recently due to their special

properties that set them apart from bulk crystals. Due to its substantial exciton binding energy (40 meV) and tiny Bohr radius (2.4 nm), zinc sulphide (ZnS) is one of the best wide-bandgap semiconductors for studying intrinsic recombination mechanisms in dense excitonic systems (Vacassy *et al.*, 1998). Moreover, because of the well-known quantum confinement phenomena, ZnS nanocrystals, also known as quantum dots, with diameters similar to the bulk Bohr exciton radius, display discrete electron energy levels with bright luminescence and high oscillator strength (Bredol *et al.*, 1998). As a result, research on this nanoscale semiconductor is very important, with a lot of work going into understanding its production and physical characteristics (Jiang *et al.*, 2003). Zinc sulphide (ZnS), one of the most significant semiconductors, has long been recognized as a flexible and superior phosphor host material. Various photoluminescent, cathodoluminescent (Ozawa *et al.*, 1990), electroluminescent (Valenta *et al.*, 1996), and thermo-luminescent (Chen *et al.*, 1997) properties can be obtained when doped with appropriate ions. The luminescence properties of bulk ZnS and impurity-activated ZnS nanocrystals are quite different (Yang *et al.*, 2003). The high degree of dispersion in the Nano crystalline system and the size-dependent characteristics of semiconductor nanoparticles are the two explanations offered by Yang et al. (Yang *et al.*, 2003) for this behaviour. Because the excitation of the RE ions may occur through the recombination of photo-generated carriers localized in the semiconductor and subsequent energy transfer to the RE ions, it is well known that RE elements are effective luminescent centers for RE-doped semiconductors (Bhargava *et al.*, 1994). Numerous studies have documented enhancements in the luminous characteristics of numerous metal-semiconductor nanoparticles (Kakotia *et al.*, 2019, Dehingia *et al.*, 2020).

### 3.3.2. Experimental Details

ZnS and Samarium doped ZnS in silicate dense glass-ceramic incorporated with various modifiers were prepared by sol-gel method. The composition of the glasses that were created and the corresponding glass code are shown below:

SZ0.5: 99.5SiO<sub>2</sub> - 0.5ZnS

SSZ1: 94SiO<sub>2</sub> - 5Sm<sub>2</sub>O<sub>3</sub> - 1ZnS

SSZ3: 92SiO<sub>2</sub> - 5Sm<sub>2</sub>O<sub>3</sub> - 3ZnS

SSZ5: 90SiO<sub>2</sub> - 5Sm<sub>2</sub>O<sub>3</sub> - 5ZnS

Starting materials *i.e.* pure zinc sulphide (ZnS), and samarium oxide (Sm<sub>2</sub>O<sub>3</sub>) were precisely weighed in accordance with the composition of each glass. To fabricate Sm<sup>3+</sup> doped silica matrices, tetraethyl orthosilicate (TEOS) as precursor, methanol as mutual solvent, nitric acid as catalyst, N, N-dimethyl formamide (DMF) as drying control chemical additive (DCCA) were used together with banana trunk sap in the volumetric ratio 8:10:2:5:20 (Kole, 2012). The prepared sample contains only SZ0.5 in sol-gel silicate glass whereas the samples contain both Sm<sup>3+</sup> and ZnS in sol-gel silicate glasses with molar concentration of SSZ1, SSZ3 and SSZ5 respectively. First, methanol, nitric acid, and banana trunk sap were combined with the dopants (ZnS and/or Samarium) and magnetically stirred for 45 minutes. TEOS was added to the mixture drop-by-drop and stirred for an additional 50 minutes. After adding DMF, the mixture was agitated once more for 40 minutes, or until the gelation started. The final solution was transformed into the SZ0.5, SSZ1, SSZ3 and SSZ5-xerogel samples in a sealed container after 20 days at room temperature. First, the xerogel samples were progressively dried in a hot air oven from room temperature to 150 °C (Puia *et al.*, 2023). After that, they were further annealed in an electric muffle furnace to 1030 °C at a rate of 1 °C per minute (Puia *et al.*, 2023).

### 3.3.3. Result and Discussion

#### 3.3.3.1. Physical properties

From the observed glass densities and refractive indices, certain physical parameters of all these ZnS and Sm<sup>3+</sup>-doped ZnS NPs in sol-gel silicate glass-ceramic have been calculated (Puia *et al.*, 2023). These values are shown in Table 2. We estimate these values by applying the technique from our previous work (Puia *et al.*, 2023).

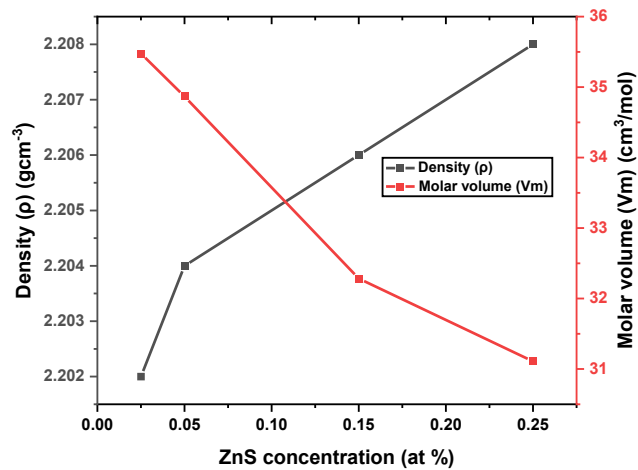
**Table 3.3.1.**

Certain physical properties of ZnS and Sm<sup>3+</sup>-doped ZnS NPs in sol-gel SiO<sub>2</sub> glass-ceramic annealed at 1020 °C.

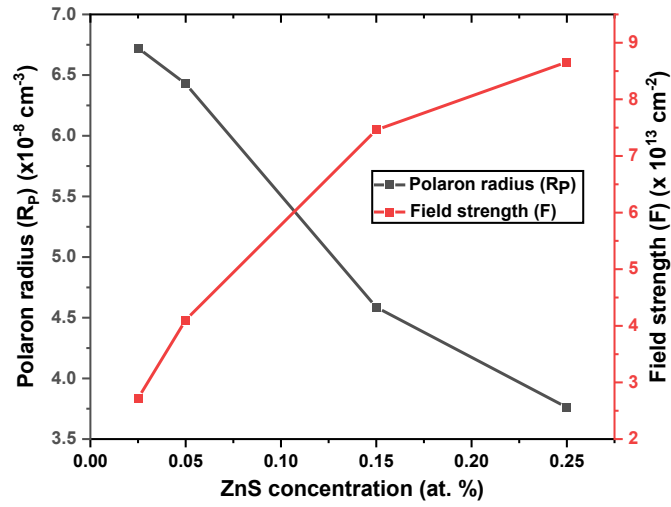
Physical properties	SZ0.5	SSZ1	SSZ3	SSZ5
Refractive index (n)	2.321	2.219	2.211	2.203
Density (ρ) (gcm <sup>-3</sup> )	2.202	2.204	2.206	2.208
Thickness (Z)	0.215	0.216	0.217	0.218
Average molecular weight M <sub>T</sub> (g)	69.31	72.44	75.63	77.52
RE ions concentration (N <sub>i</sub> ) (x 10 <sup>18</sup> )	4.790	4.958	7.531	9.873
Dielectric constant (ε)	5.387	4.924	4.889	4.853
Optical dielectric constant (P dt/dp)	4.387	3.924	3.889	3.853
Molar volume (V <sub>m</sub> ) (cm <sup>3</sup> /mol)	35.476	34.868	32.284	31.109
Reflection loss (R <sub>L</sub> )	0.158	0.144	0.142	0.141
Molar refraction (R <sub>M</sub> )	18.693	18.727	19.354	19.740
Energy gap (E <sub>g</sub> )	3.3	3.74	3.78	4.22
Polaron radius (R <sub>p</sub> ) (x10 <sup>-8</sup> Å)	6.723	6.428	4.587	3.761
Inter nuclear distance (R <sub>i</sub> ) (x10 <sup>-7</sup> Å)	1.758	1.641	1.439	1.229
Electronic polarizability (α <sub>e</sub> ) (x 10 <sup>-21</sup> )	2.364	2.247	2.239	2.229
Field strength (F) (x 10 <sup>13</sup> cm <sup>-2</sup> )	2.718	4.103	7.461	8.659
Molar polarizability (α <sub>m</sub> )	7.419	7.431	7.680	7.833
Oxygen packing density (OPD)	41.523	42.934	45.931	48.472
Metallization criterion (M)	0.416	0.430	0.435	0.438

Table 3.3.1 displayed the molar volume and density of glass samples with varying ZnS concentrations. Fig. 3.3.1 displays the density and molar volume with ZnS concentration. When added ZnS into sol-gel silicate glass network, the density of the glass samples increase because of the substitution molecular weight of ZnS (Mw. = 97.47 g/mol) higher molecular weight of SiO<sub>2</sub> (Mw. = 60.08 g/mol) (Puia *et al.*, 2023). There is a linear relationship between density and ZnS content. The molar volume of the glass sample were decrease with ZnS concentration increase due to the shorter bond length of ZnS compared to that of SiO<sub>2</sub> (Puia *et al.*, 2023). The Zn-S and Si-O distance is 2.54 Å and 1.62 Å respectively (Dehingia *et al.*, 2020). These distances are ionic radii (Dehingia *et al.*, 2020). This indicates that the network of the glass samples were compressed because of the substitution of ZnS in the place of SiO<sub>2</sub> (Dehingia *et al.*, 2020).

Fig. 3.3.2, demonstrates variation of polaron radius and field strength of ZnS nanoparticles doped Sm<sup>3+</sup> in sol-gel silicate glasses. It was observed that the polaron radius decreases proportionally with increase in ZnS nanoparticles content. This decrease may be due to the increase in Sm<sup>3+</sup> ion concentration (N<sub>i</sub>) which gives rise to high field strength.



**Fig. 3.3.1:** Variation of density and molar volume of the dense glass samples.



**Fig. 3.3.2:** Variation of polaron radius and field strength of the dense glass samples.

### 3.3.3.2. XRD spectra

The powder X-ray diffraction (XRD) patterns of the SSZ5 glass sample are displayed in Fig. 3.3.3. XRD technique is the most practicable method for the gross characterization of materials. This method has been extensively used to investigate the lattice parameters, microstructure, texturing, and phase formation.

XRD provides the most exact measurements of diffraction peak locations, making it the most helpful technique for analyzing homogeneous and inhomogeneous strains (Dehingia *et al.*, 2020).

The diffraction peak locations are shifted by homogeneous or uniform elastic strain (Dehingia *et al.*, 2020). The shift in peak locations may be used to compute the change in d-spacing, which is the outcome of the strain-induced variation in lattice constants (Dehingia *et al.*, 2020). When  $\sin\theta$  rises, the diffraction peaks expand due to inhomogeneous strain that changes between crystallites or within a single crystallite (Yang *et al.*, 2003). The limited size of crystallites also contributes to peak widening, however in this case, the broadening is not dependent on  $\sin\theta$  (Dawngliana *et al.*, 2023). Through careful examination of peak forms, it is possible to

independently ascertain the contribution of both crystallite size and inhomogeneous strain to the peak width (Yang *et al.*, 2003).

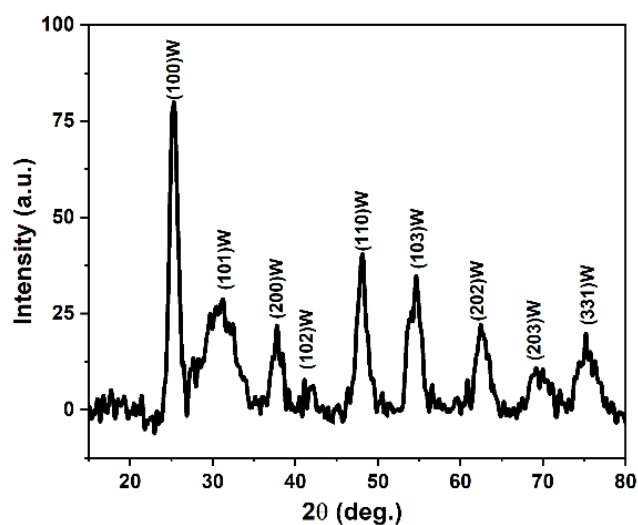
The Scherrer formula may be used to estimate the crystallite size,  $D$ , from the peak width in the absence of any inhomogeneous strain (Dehingia *et al.*, 2020).

$$D = \frac{0.9\lambda}{\beta \cos \theta_B} \quad (3.4)$$

Where the diffraction angle is  $\theta_B$ , the full width of half maximum (FWHM) of a diffraction peak is denoted by  $\beta$ , and the X-ray wavelength is represented by  $\lambda$  (Dehingia *et al.*, 2020).

It is important to remember that nanoparticles frequently form twinned structures, which means that the results of the Scherrer formula could differ from the actual particle size (Dehingia *et al.*, 2020). Furthermore, X-ray diffraction often needs a significant volume of powder and only yields the aggregate information about the particle sizes.

The dominant diffraction peaks in the  $2\theta$  range of  $15^\circ$ – $80^\circ$  corresponded to the presence of  $\text{Sm}^{3+}$ -doped ZnS wurtzite phases (100), (101), (200), (102), (110), (103), (202), (203) and (331) respectively ) (Puia *et al.*, 2023). The  $\text{Sm}^{3+}$ -doped ZnS crystalline size calculated with the help of the Debye-Scherrer formula ) (Puia *et al.*, 2023) using the wurtzite (101), (004), (200), (211), (204), (215) and (312) peaks of  $\text{Sm}^{3+}$ -doped ZnS NPs (Fig. 3) is 9.7 nm.



**Fig. 3.3.3:** X-Ray Diffraction Spectra of SSZ5 dense glass-ceramic annealed at 900 °C.

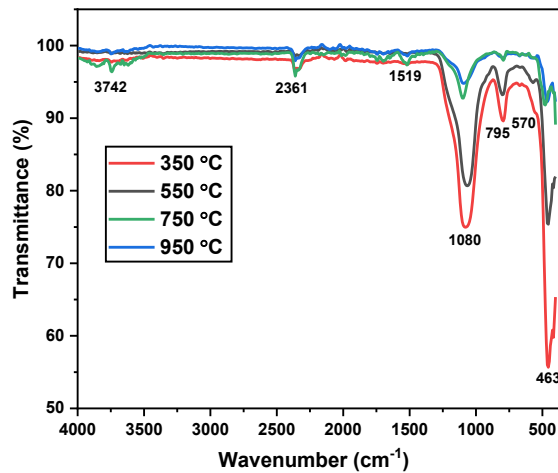
#### 3.3.3.3. Attenuated total reflectance Fourier transforms infrared spectroscopy (ATR-FTIR)

ATR-FTIR spectra of SSZ5 are recorded in the range 400–4000  $\text{cm}^{-1}$  and are shown in Fig. 3.3.4. The samples are sintered at 350 °C, 600 °C, 750 and 950 °C. The spectra display several peaks located at 3742, 2361, 1519, 1080, 795, 570 and 463  $\text{cm}^{-1}$ . Additionally, when sintering temperatures rise, there is a fluctuation in the peak intensity.

Through a poly-condensation process, the Si-OH group is produced by the hydrolysis of TEOS. These sol-gel samples contain extra organics and a significant quantity of  $\text{H}_2\text{O}$  during the gel phase (Dehingia *et al.*, 2020). As we heat the prepared samples inside a muffle furnace and transform them into a stiff glassy network, these chemicals gradually escape from the matrix (Puia *et al.*, 2023). The presence of adsorbed water at the glass sample is indicated by the weak bands at 3741  $\text{cm}^{-1}$  and 2361  $\text{cm}^{-1}$ , which are attributable to the O–H stretching and bending frequencies of water, respectively (Ashwini *et al.*, 2014). The stretching vibration of C=O in the acetate group is represented by the band detected at 1519  $\text{cm}^{-1}$  (Ashwini *et al.*, 2014), whereas the stretching vibration of the C-O group is



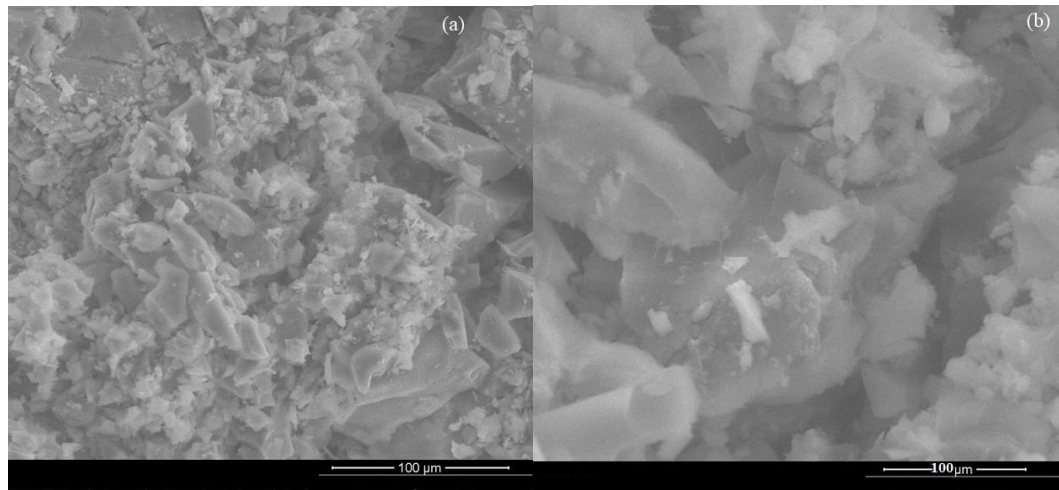
represented by the band located at  $1080\text{ cm}^{-1}$  (Reddy *et al.*, 2015). The distinctive bands at  $795\text{--}463\text{ cm}^{-1}$ , which are attributed to the stretching vibrations and the vibration bond of Zn–S, respectively, verify the creation of the ZnS complex (Gomez *et al.*, 2003, Shanmugam *et al.*, 2014).



**Fig. 3.3.4:** ATR-FTIR spectra of SSZ5 glass-ceramic annealed at different temperatures.

#### 3.3.3.4. SEM Analysis

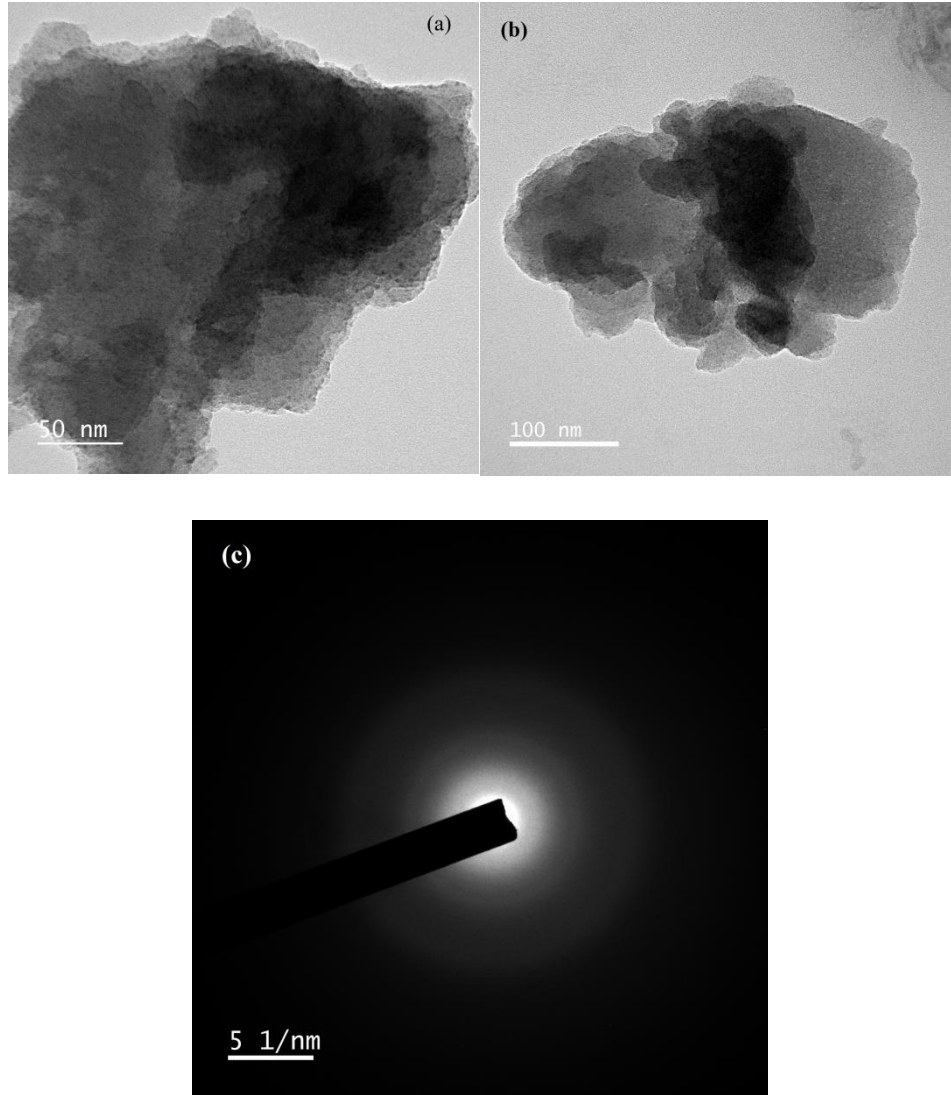
The SEM image of SZ0.5 and SSZ5 glasses are shown in [Fig. 3.3.5\(a\)](#) and [5\(b\)](#). The synthetic zinc sulphide (ZnS) is mostly composed of regular-shaped ZnS particle grains, according to the SEM microstructural investigation. It is obvious that nearly spherical nanoparticles have an almost homogenous size distribution with mean sizes of 18.5 and 16.8 nm respectively for SZ0.5 and SSZ5 glasses.



**Fig. 3.3.5:** (a) SEM image of SZ0.5 dense glass-ceramic; (b) SEM image of SSZ5 dense glass-ceramic annealed at 900 °C.

#### 3.3.3.5. TEM Analysis

Figs. 3.3.6 (a) and 3.3.6 (b) show the TEM images of SZ0.5 and SSZ5 glasses annealing at 900 °C. The TEM image shows that the average particle sizes is around 10 nm for glasses respectively, which is similar with the crystallite sizes calculated by the Scherrer equation. The SAED pattern is employed in Fig. 3.3.6(c) to determine the crystal properties at a particular region, i.e., whether the material is amorphous, single crystalline, polycrystalline, or polycrystalline textured (Kakotia *et al.*, 2019). Polycrystalline materials feature ring-shaped SAED patterns, whereas single-crystalline materials only have spot patterns. A ring-like pattern in the SAED pattern indicates that the synthesized ZnS and Sm<sup>3+</sup>-doped ZnS NPs samples are polycrystalline.



**Fig. 3.3.6:** (a) TEM image of SZ0.5 dense glass-ceramic; (b) TEM image of SSZ5 dense glass-ceramic; (c) SAED pattern with distinct spot rings verifies the increased particle size and polycrystalline nature.

### 3.3.3.6. Optical absorption spectra

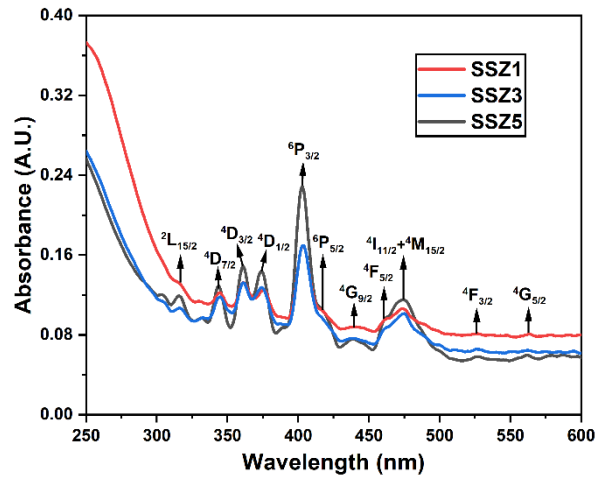
Fig. 3.3.7(a) shows the absorption spectra in the UV-Visible region of SSZ1, SSZ3 and SSZ5 glasses. Within the absorption spectra of  $\text{Sm}^{3+}$  doped ZnS glass, there are intra-configurational transitions from the ground state  $^6\text{H}_{5/2}$  to several excited states. The bands are assigned at  $^6\text{H}_{5/2} \rightarrow ^2\text{L}_{15/2}$  (316 nm),  $^6\text{H}_{5/2} \rightarrow ^4\text{D}_{7/2}$  (344 nm),  $^6\text{H}_{5/2} \rightarrow ^4\text{D}_{3/2}$  (361 nm),  $^6\text{H}_{5/2} \rightarrow ^4\text{D}_{1/2}$  (374 nm),  $^6\text{H}_{5/2} \rightarrow ^6\text{P}_{3/2}$  (404 nm),

${}^6\text{H}_{5/2} \rightarrow {}^6\text{P}_{5/2}$  (419 nm),  ${}^6\text{H}_{5/2} \rightarrow {}^4\text{G}_{9/2}$  (441 nm),  ${}^6\text{H}_{5/2} \rightarrow {}^4\text{F}_{5/2}$  (463 nm),  ${}^6\text{H}_{5/2} \rightarrow {}^4\text{I}_{11/2} + {}^4\text{M}_{15/2}$  (474 nm),  ${}^6\text{H}_{5/2} \rightarrow {}^4\text{F}_{3/2}$  (526 nm) and  ${}^6\text{H}_{5/2} \rightarrow {}^4\text{G}_{5/2}$  (562 nm) respectively (Herrmann *et al.*, 2014, Dillip *et al.*, 2013, Deun *et al.*, 1999, Reddy *et al.*, 2014, Suhasini *et al.*, 2009). The data presented by Shaweta Mohan *et al.* (Mohan *et al.*, 2018) and Carnal *et al.* (Carnall *et al.*, 1968) were used while assigning bands. Based on the selection rules  $|\Delta L| \geq 0$ ,  $|\Delta J| \geq 0$  and  $|\Delta S| = 0$  the majority of the absorption transitions of  $\text{Sm}^{3+}$  arise (Rajesh *et al.*, 2012). While the visible region's transitions are spin-forbidden, the infrared region's high intensity transitions are spin permitted ( $\Delta S = 0$ ). Some of these transitions such as  ${}^6\text{H}_{5/2} \rightarrow {}^6\text{F}$ ,  ${}^6\text{H}$  and  ${}^6\text{P}$  obey the selection rule  $\Delta S = 0$  and are spin allowed and therefore possess higher intensity than the spin forbidden transitions which include  ${}^6\text{H}_{5/2} \rightarrow {}^4\text{I}$ ,  ${}^4\text{M}$ ,  ${}^4\text{G}$ ,  ${}^4\text{L}$  and  ${}^4\text{D}$  (Rajesh *et al.*, 2012). Furthermore, the majority of the spectra's observed transitions are of the induced electric dipole type, which follow the selection criteria  $\Delta J \leq 6$  (Dillip *et al.*, 2013). A few transitions follow the selection criterion  $\Delta J = 0, \pm 1$ , and are of the magnetic dipole type. A prime example is the transition from  ${}^6\text{H}_{5/2} \rightarrow {}^4\text{G}_{5/2}$ , which is detected at around 562 nm and has a relatively low intensity in the current study.

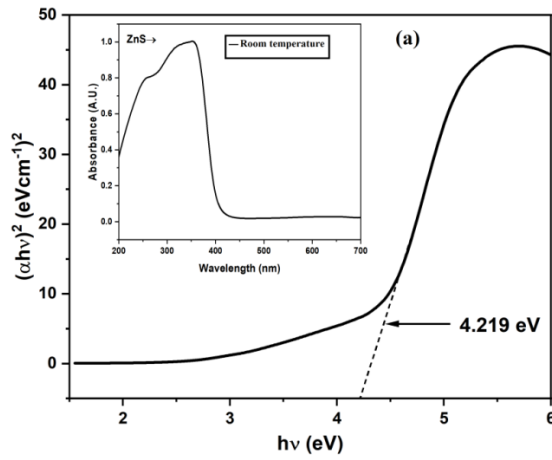
By using the Tauc plot of  $(h\nu\alpha)^2$  against  $(h\nu)$  and extrapolating the linear parts of the curves to the energy axis, one may determine the band gap energy ( $E_g$ ) of ZnS nanoparticles from the UV-Vis spectra as per reference (Soltani *et al.*, 2012).

$$ah\nu = B(h\nu - E_g)^{1/2} \quad (3.5)$$

Where B is a constant,  $h\nu$  is the photon energy,  $E_g$  is the direct band gap energy, and  $\alpha$  is the absorption coefficient (Soltani *et al.*, 2012). The absorption coefficient ( $\alpha$ ) can be calculated using the well-known relation derived from Beer-Lambert's relation,  $\alpha = 2.303A/d$ , where d is the quartz cuvette's path length and A is the absorbance found from the UV-visible spectrum (Seoudi *et al.*, 2010). Alternatively, the absorption coefficient ( $\alpha$ ) can be found from the relation  $A = I/I_0 = e^{(-\alpha d)}$  (Seoudi *et al.*, 2010). UV-Vis absorption spectra and the Tauc plot of ZnS nanoparticles at different temperatures are shown Fig. 3.3.7(b). The estimated optical band gap of ZnS nanoparticles are about 4.219 eV respectively. The observed size of the nanoparticles agrees with the change in the band gap energy (Soo *et al.*, 2013). The phenomenon of quantum confinement is responsible for this size-dependent fluctuation in the band gap energy.



**Fig. 3.3.7(a):** Optical absorption spectra of prepared dense glass-ceramic annealed at 1000 °C.

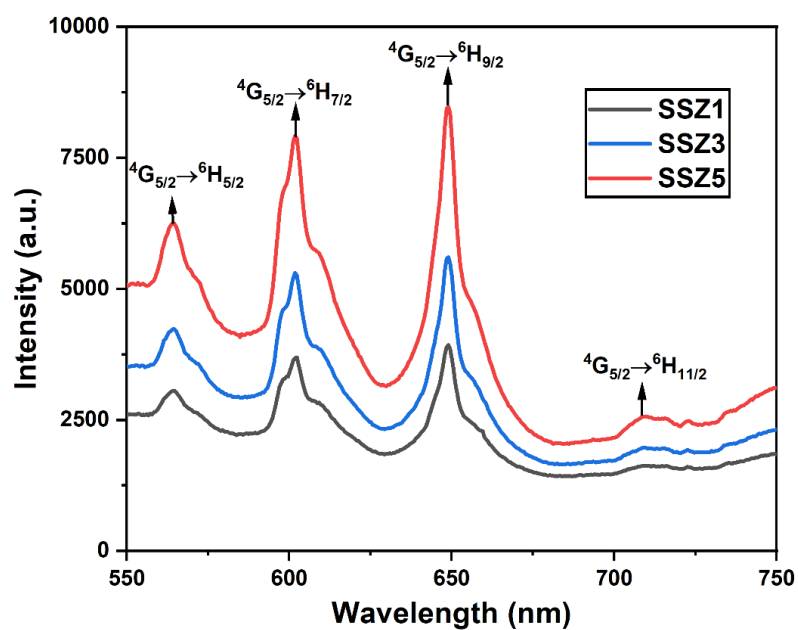


**Fig. 3.3.7(b):** Shows the absorption spectra of SZ0.5 sol-gel glass at room temperature.

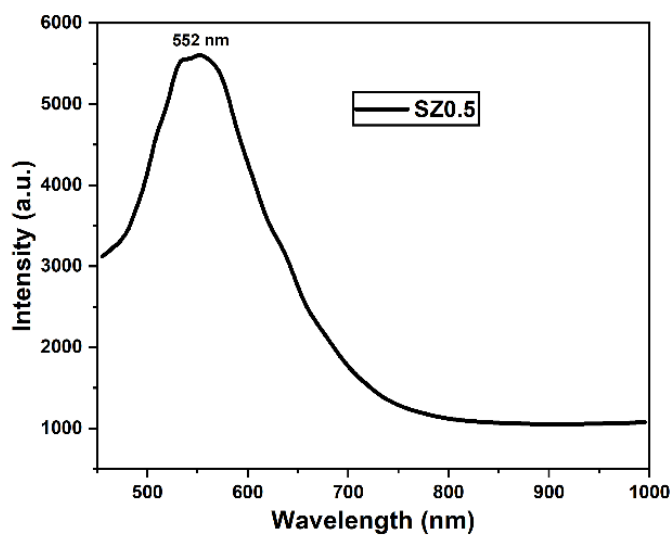
### 3.3.3.7. PL emission spectra

PL emission spectra of the fixed  $\text{Sm}^{3+}$  ions-doped with various concentrations of ZnS NPs in sol-gel silicates glasses, at an excitation wavelength of 450 nm are presented in Fig. 3.3.8(a). Based on the transitions  $^4\text{G}_{5/2} \rightarrow ^6\text{H}_{5/2}$ ,  $^6\text{H}_{7/2}$ ,  $^6\text{H}_{9/2}$ , and  $^6\text{H}_{11/2}$ , respectively, each spectrum has four strong emission bands, which are centered at around 564 nm (yellow), 602 nm (intense reddish orange), 648 nm (moderate red), and 708 nm (weak red) (Rao *et al.*, 2017, Kaur *et al.*, 2013). Color displays, medical diagnostics, and high-density optical data storage are among the potential applications for these emissions (NayabRasool *et al.*, 2013). The observed peaks exhibit intensity in the following order:  $^4\text{G}_{5/2} \rightarrow ^6\text{H}_{9/2} > ^6\text{H}_{7/2} > ^6\text{H}_{5/2} > ^6\text{H}_{11/2}$ , with the most apparent and intense transition occurring in  $^4\text{G}_{5/2} \rightarrow ^6\text{H}_{9/2}$ . Among the emission bands, the transitions  $^4\text{G}_{5/2} \rightarrow ^6\text{H}_{5/2}$  and  $^4\text{G}_{5/2} \rightarrow ^6\text{H}_{11/2}$  are purely electric dipoles (ED) and follow the selection rule  $\Delta J \leq 6$ , whereas the transitions  $^4\text{G}_{5/2} \rightarrow ^6\text{H}_{7/2}$  and  $^4\text{G}_{5/2} \rightarrow ^6\text{H}_{9/2}$  obey the selection rule  $\Delta J = \pm 1$  and have both electric and magnetic dipole character (Gomez *et al.*, 2013). Fig. 3.3.8(a) further shows that an increase in ZnS NP concentrations is correlated with an increase in the intensity of yellow, intense reddish orange, moderated red, and weak red colors (Mawlud *et al.*, 2017).

Fig. 3.3.8(b) displays the PL spectra of ZnS nanoparticle doped sol-gel silicate glass samples triggered by a 25 W UV light source with a wavelength of 370 nm in the 450–1000 nm wavelength range. For persistent luminous applications, ZnS doped sol-gel silicate glass samples were the most commonly employed material (Koen *et al.*, 2016). The wavelength of its wide, greenish emission is 552 nm. It was conventional to include radioactive ions in the compound to maintain the luminescence because the afterglow is rather weak (Nayab Rasool *et al.*, 2013).



**Fig. 3.3.8(a):** PL emission spectra of the prepared dense glass-ceramic annealed at 1000°C.

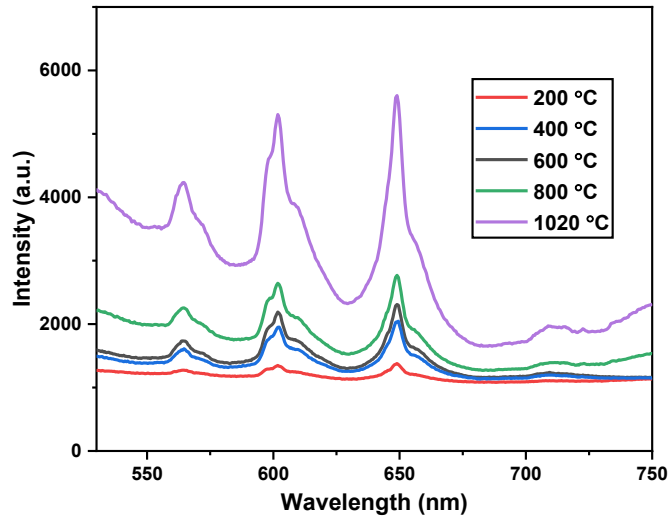


**Fig. 3.3.8(b):** Luminescence spectra of SZ0.5 dense glass-ceramic annealed at 1000°C.

### 3.3.3.8. Effect of annealing temperatures

Using an excitation wavelength of  $\lambda_{\text{ex}} = 450$  nm, the PL spectra of dense glass-ceramic SSZ3 were recorded at different annealing temperatures, as seen in Fig. 3.3.9. For SSZ3 glasses, the relationship between PL intensity and annealing temperature is depicted as a graph in Fig. 3.3.9. An increase in annealing temperature between 200 – 1020 °C is seen to lead to an increase in PL peak intensity. The cause of this is the creation of ZnS at high annealing temperatures.

Schematic diagram of fixed  $\text{Sm}^{3+}$  ion co-doped with different ZnS concentrations in sol-gel silicate glass annealed at 1000 °C, showing possible non-radiative relaxation transitions (wavy arrow) and PL (solid line), as shown in Fig. 3.3.10.



**Fig. 3.3.9:** Effect of annealing temperatures of PL spectra of SSZ3 dense glass-ceramic.



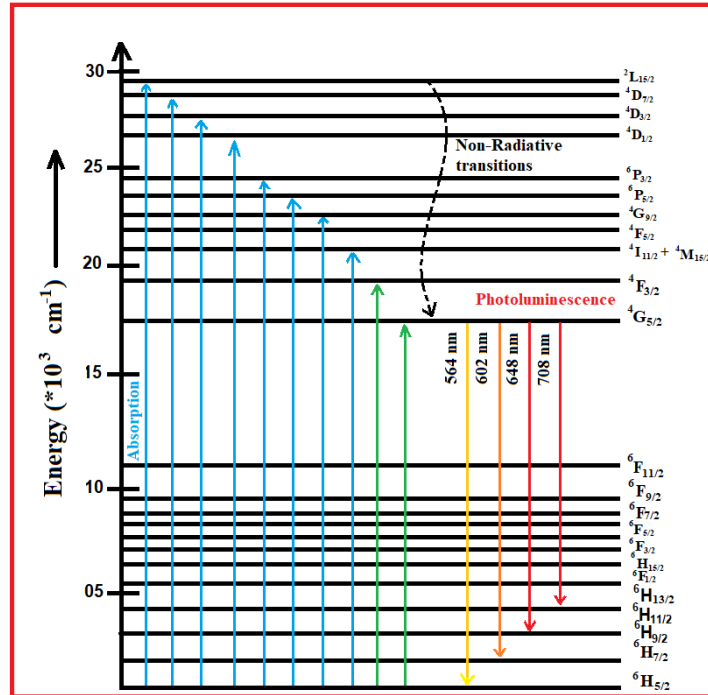


Fig. 3.3.10: Energy level diagram  $\text{Sm}^{3+}$  doped ZnS nanoparticles.

### 3.3.3.9. Judd-Ofelt and Radiative Parameters

The spectrum characteristics of RE ions doped in different glasses and crystals are often examined using the semi-empirical Judd-Ofelt (JO) theory [Judd, 1962, Ofelt 1962). The theory assists in the determination of the so-called JO parameters, a set of three phenomenological intensity parameters:  $\Omega_2$ ,  $\Omega_4$ , and  $\Omega_6$  (Bhargava *et al.*, 2005). These parameters are then used to determine other significant radiative parameters, including the branching ratio, radiative lifetime, and probability of radiative transition, as well as the stimulated emission cross-section of different emission transitions corresponding to the RE ion (Dehingia *et al.*, 2020). The FOM values for the current glass system suggest that these glasses may find application in optical amplifier devices.

**Table 3.3.2**

The prepared glasses' root mean square deviation ( $\Delta\delta_{rms}$ ), experimental and oscillator strengths ( $\times 10^{-6}$ ) for Sm:ZnS were determined.

<b>Transitions from <math>^6H_{5/2} \rightarrow</math></b>	<b>SSZ1</b>		<b>SSZ3</b>		<b>SSZ5</b>	
	<b>f<sub>exp</sub></b>	<b>f<sub>cal</sub></b>	<b>f<sub>exp</sub></b>	<b>f<sub>cal</sub></b>	<b>f<sub>exp</sub></b>	<b>f<sub>cal</sub></b>
$^2L_{15/2}$	0.157	0.089	0.507	0.314	0.713	0.423
$^4D_{7/2}$	0.758	0.437	0.961	0.782	1.507	0.989
$^4D_{3/2}$	0.731	0.409	0.907	0.738	1.493	0.946
$^4D_{1/2}$	0.703	0.398	0.958	0.792	0.129	0.921
$^6P_{3/2}$	5.263	5.053	5.683	5.471	5.924	5.709
$^6P_{5/2}$	0.203	0.097	0.358	0.146	0.473	0.314
$^4G_{9/2}$	0.094	0.073	0.138	0.096	0.251	0.098
$^4F_{5/2}$	0.071	0.054	0.089	0.062	0.097	0.075
$^4I_{11/2} + ^4M_{15/2}$	0.807	0.572	0.932	0.741	1.152	0.835
$^4F_{3/2}$	0.052	0.035	0.079	0.053	0.093	0.072
$^4G_{5/2}$	0.047	0.021	0.035	0.019	0.069	0.043
( $\Delta\delta_{rms}$ )	$\pm 0.402$		$\pm 0.432$		$\pm 0.446$	

**Table 3.3.3**

JO intensity parameters ( $\times 10^{-20} \text{ cm}^2$ ) and the spectroscopic quality factor ( $\Omega_4/\Omega_6$ ) of  $\text{Sm}^{3+}$  in the current work and also various other host glass materials.

Glass Composition	$\Omega_2$	$\Omega_4$	$\Omega_6$	$\Omega_4/\Omega_6$	Trend of $\Omega_\lambda$	Ref.
SSZ1: 94SiO <sub>2</sub> - 5Sm <sub>2</sub> O <sub>3</sub> - 1ZnS	2.841±0.009	0.374±0.021	0.263±0.032	1.442±0.257	$\Omega_2 > \Omega_4 > \Omega_6$	Present work
SSZ3: 92SiO <sub>2</sub> - 5Sm <sub>2</sub> O <sub>3</sub> - 3ZnS	3.107±0.014	0.692±0.018	0.473±0.022	1.463±0.107	$\Omega_2 > \Omega_4 > \Omega_6$	Present work
SSZ5: 90SiO <sub>2</sub> - 5Sm <sub>2</sub> O <sub>3</sub> - 5ZnS	5.309±0.011	1.968±0.025	1.209±0.031	1.628±0.060	$\Omega_2 > \Omega_4 > \Omega_6$	Present work
Sm: ZnS	45.53±2.45	3.52±0.14	3.15 (±0.14)	1.12	$\Omega_2 > \Omega_4 > \Omega_6$	(Kakoti et al., 2019)
PKSASm10	9.00	8.36	4.47	1.87	$\Omega_2 > \Omega_4 > \Omega_6$	(Vijaya et al., 2013)
PKMASm	6.83	2.97	2.03		$\Omega_2 > \Omega_4 > \Omega_6$	(Vijaya et al., 2013)
PPNSm10	3.42	2.80	1.85		$\Omega_2 > \Omega_4 > \Omega_6$	(Vijaya et al., 2013)
B <sub>2</sub> O <sub>3</sub>	6.36	6.02	3.51		$\Omega_2 > \Omega_4 > \Omega_6$	(Soo et al., 2013)
LKBBT	4.73	2.78	1.77		$\Omega_2 > \Omega_4 > \Omega_6$	(Rao et al., 2013)
Oxyfluoride	8.56	3.02	2.37		$\Omega_2 > \Omega_4 > \Omega_6$	(Praveena et al., 2008)

**Table 3.3.4**

The peak wavelength ( $\lambda_P$ ), radiative transition probability (A), branching ratio ( $\beta_R$ ), total radiative transition probability ( $A_T$ ), effective bandwidth ( $\Delta\lambda_{\text{eff}}$ ) and radiative lifetime ( $\tau_R$ ) of the prepared glasses

Sample	Transition	$\lambda_P$ (nm)	$\Delta\lambda_{\text{eff}}$ (nm)	A (s <sup>-1</sup> )	$\beta_R$ (%)	$A_T$ (s <sup>-1</sup> )	$\tau_R$ ( $\mu$ s)	$\sigma_P$ (10 <sup>-22</sup> cm <sup>2</sup> )	FOM
<b>SSZ1</b>	$^4G_{5/2} \rightarrow ^6H_{5/2}$	564	8.73	12.98	2.94	441.77	226	6.37	5.56
	$^4G_{5/2} \rightarrow ^6H_{7/2}$	602	10.09	206.22	46.68			18.13	18.29
	$^4G_{5/2} \rightarrow ^6H_{9/2}$	648	13.18	168.71	38.19			2.05	2.70
	$^4G_{5/2} \rightarrow ^6H_{11/2}$	708	15.35	53.86	12.19			4.52	6.94
<b>SSZ3</b>	$^4G_{5/2} \rightarrow ^6H_{5/2}$	564	9.03	13.63	2.97	458.75	218	6.94	6.27
	$^4G_{5/2} \rightarrow ^6H_{7/2}$	602	11.52	214.07	46.66			19.62	22.60
	$^4G_{5/2} \rightarrow ^6H_{9/2}$	648	13.37	172.72	37.65			2.89	3.86
	$^4G_{5/2} \rightarrow ^6H_{11/2}$	708	15.74	58.33	12.71			5.03	7.92
<b>SSZ5</b>	$^4G_{5/2} \rightarrow ^6H_{5/2}$	564	9.81	15.28	3.01	507.36	197	7.08	6.95
	$^4G_{5/2} \rightarrow ^6H_{7/2}$	602	11.94	229.17	45.17			21.84	26.08
	$^4G_{5/2} \rightarrow ^6H_{9/2}$	648	13.85	193.65	38.17			3.93	5.44
	$^4G_{5/2} \rightarrow ^6H_{11/2}$	708	16.27	69.26	13.65			5.87	9.55

### 3.3.3.10. Non-Linear Properties

Certain non-linear characteristics, ascertained from optical parameters, such as the non-linear refractive index ( $n_2$ ), non-linear refractive index susceptibility ( $\chi^{(3)}$ ), co-efficient ( $\gamma_{ce}$ ), and relatively high Abbe number ( $v_{Ab}$ ), suggest the good optical quality of the sol-gel silicate dense glass-ceramic (Dehingia *et al.*, 2020). Table 3.3.5 shows these values. We estimate these values following the procedure described by (Dihingia *et al.*, 2020).

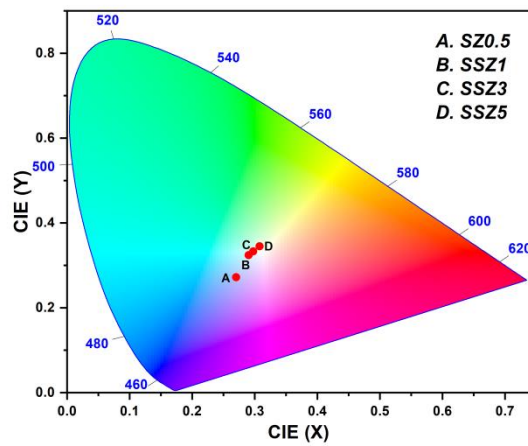
**Table 3.3.5**

Certain non-linear properties of SSZ5 glasses.

$n_f$	$n_r$	$n_f - n_r$	$n_b$	$v_{Ab}$	$1/v_{Ab}$	$n_2$ (in $10^{-13}$ esu)	$\gamma_{ce}$ (in $\text{cm}^2/\text{W}$ )	$\omega_0 \times 10^{-13}$	$N \times 10^{-16}$	$\chi^{(3)} \times 10^{-6}$
1.723	1.709	0.011	1.718	51.286	0.020	3.571	0.695	109.582	997.105	4.801

### 3.3.3.11. CIE Chromaticity

The fluorescence emission spectra generated by excitation at 450 nm were used to determine the monochromatic (x, y) color coordinates for the CIE1931 chromaticity diagram. The findings presented in Fig. 3.3.11 and the computations presented in Table 3.3.6 demonstrate that the light emitted by the glass is almost entirely white. This sample emitted a bright amount of blue-white regions, similar to that of daylight. A strong bluish color of light is produced by sample with SZ0.5, which is frequently seen in commercial settings and is ideal for bright work lighting [Rao *et al.*, 2017, Chen *et al.*, 1997] (Fig. 3.3.11).



**Fig. 3.3.11:** The color coordinates of the prepared glasses are displayed in the CIE chromaticity diagram.

**Table 3.3.6**

Chromaticity coordinates of the prepared glasses

SAMPLE	X	Y	CCT	
<b>SZ0.5</b>	0.271	0.273	12152	Day light
<b>SSZ1</b>	0.291	0.324	10562	Day light
<b>SSZ3</b>	0.297	0.334	7972	Day light
<b>SSZ5</b>	0.308	0.345	5736	Day light

**3.3.4. Conclusion**

In this research work, the structural and luminescence properties of  $\text{Sm}^{3+}$  ion co-doped with different concentration of ZnS NPs in sol-gel silicate glasses were investigated. Both the density and molar volume of with samarium doped ZnS NPs samples were higher than those of ZnS glass sample. Our glass-ceramic sample contains ZnS nanocrystals in a wurtzite structure, as evaluated by XRD and TEM investigations. The formation of NBO and the elimination of the OH-group are confirmed by the FTIR spectra analysis. Based on the measured absorption and PL spectra, ZnS estimated the J-O intensity parameters and other radiative parameters. The trend of the J-O intensity parameters for these studied samples is found to be  $\Omega_2 > \Omega_4 > \Omega_6$ . When comparing the current matrix to other well-known hosts, the  $\Omega_2$  parameter value is much greater, indicating a higher level of asymmetry around the  $\text{Sm}^{3+}$  ions in the ZnS co-doped  $\text{SiO}_2$  matrix (Dihingia *et al.*, 2020). The ZnS NPs' ability to affect the network is indicated by an increase in the  $\Omega_2$  parameter with ZnS concentration. When ZnS NPs are added, an improvement in the radiative parameters is shown for each of the three PL bands. The color tunability at various ZnS concentrations is demonstrated by the CIE chromaticity diagram. According to the study, ZnS in a sol-gel silica matrix has the potential to be a sensitizer and network modifier for  $\text{Sm}^{3+}$  ions. Furthermore,  $\text{Sm}^{3+}$  doped with ZnS has a great deal of promise for use in optical devices such as red lasers. The results suggest that the

samarium doped ZnS can be effectively utilized as an active material for producing strong white emission. Our research could be useful in the development of solid-state lasers.

## Reference

- A. Herrmann, S. Kuhn, M. Tiegel, C. Russel, J. Korner, D. Klopfel, J. Hein and M. Kaluza (2014), Structure and fluorescence properties of ternary aluminosilicate glasses doped with samarium and europium, *J. Mater. Chem. C*, **2**: 4328.
- A. Kaur, A. Khanna, L. I. Aleksandrov (2017), Structural, thermal, optical and photoluminescent properties of barium tellurite glasses doped with rare-earth ions, *J. Non-Crys. Solids*, **476**: 67-74
- A.K. Kole (2012), Cubic-to-hexagonal phase transition and optical properties of chemically synthesized ZnS nanocrystals. *Results Phys.* **2**: 150-155.
- B.R. Judd (1962), Optical absorption intensities of rare-earth ions, *Phys. Rev.* **127**: 750.
- C. Gorller-Walrand, K.A. Binnemans, in: K.A. Gschneidner Jr., L. Eyring (Eds.) (1998), *Hand book on the Physics and Chemistry of Rare Earths*, **25**: 101-264.
- C. K. Jayasankar, P. Babu (2000), Optical properties of  $\text{Sm}^{3+}$  ions in lithium borate and lithium fluoroborate glasses, *J. Alloys Compd.* **307**: 82-95.
- C. Mugoni, C. Gatto, A. Pla-Dalmau, C. Siligardi (2017), Structure and luminescence properties of  $\text{Dy}_2\text{O}_3$  doped bismuth-borate glasses, *J. Non-Cryst. Solids*, **471**: 295-300.
- C.K. Jorgensen (1983), Judd-Ofelt parameters and chemical bonding, *J. Less Common. Met.* **93**: 107-112.
- Ch. Srinivasa Rao, C.K. Jayasankar (2013), Spectroscopic and radiative properties of  $\text{Sm}^{3+}$ -doped K–Mg–Al phosphate glasses, *Opt. Commun.* **286**: 204–210.
- D Rajesh, A. Balakrishna, Y.C. Ratnakaram (2012), Luminescence, structural and dielectric properties of  $\text{Sm}^{3+}$  impurities in strontium lithium bismuth borate glasses, *Opt. Mater.* **35**: 108-116.
- D. Kakotia, P. Duttaa, P. Gogoib, N. Dehingiaa, N. Rajkonwara, A. Boruaha, A.T.T. Mostakoa, P.K. Saikiaa, P.K. Gogoi (2019), Effect of ZnS nanoparticles on the Judd-Ofelt and radiative parameters of  $\text{Sm}^{3+}$  ions in sol-gel silica matrix, *Journal of Luminescence*, **211**: 401–404.
- D. Rajesh, A. Balakrishna, Y.C. Ratnakaram (2012), Luminescence, structural and



- dielectric properties of  $\text{Sm}^{3+}$  impurities in strontium lithium bismuth borate glasses, *Opt. Mater.* **35**: 108.
- D. Ramachari, L. Rama Moorthy, C. K. Jayasankar (2013), Spectral investigations of  $\text{Sm}^{3+}$  doped oxyfluorosilicate glasses, *Mater. Research Bull.* **48** 3607-3613.
- Deun R., Binnemans K., Warrand C. and Adam J. (1999), Rare-Earth-Doped Materials and Devices III, *Proc. SPIE* 3622, 175.
- Dillip G., Kumar P. and Raju B (2013), Synthesis and luminescence properties of a novel  $\text{Na}_6\text{CaP}_2\text{O}_9\text{:Sm}^{3+}$  phosphor, *J. Lumin.* **134**: 333.
- E. Gomez-Barojas, E. Sanchez-Mora, C. Castillo-Abriz, E. Flores-Rodriguez, R. Silva-Gonzalez (2013), Synthesis and Study of Optical and Photocatalytic Properties of Mn and Sm Doped ZnS Grown by Sol-Gel, *J. Supercond Nov. Mag.* **26**: 2337–2340.
- E. Rukmini (1995), Spectroscopic properties of  $\text{Ho}^{3+}$  ions in zinc borosulphate glasses and comparative energy level analyses of  $\text{Ho}^{3+}$  ions in various glasses, *Opt. Mater.* **4**: 529-546.
- E. Rukmini, C.K. Jayasankar (1995), Spectroscopic properties of  $\text{Ho}^{3+}$  ions in zinc borosulphate glasses and comparative energy level analyses of  $\text{Ho}^{3+}$  ions in various glasses, *Optical Materials*, **4**: 529-546.
- F. Ahmadi, R. Hussin, S. K. Ghoshal (2016), Judd-Ofelt intensity parameters of samarium-doped magnesium zinc sulfophosphate glass, *J. Non-Cryst. Solids*, **448**: 43-51.
- F. Steudel, S. Loos, B. Ahrens, S. Schweizer (2016), Quantum efficiency and energy transfer processes in rare-earth doped borate glass for solid-state lighting, *J. Lumin.* **170**: 770-777.
- F. Amirian, M. Molaei, A.R. Bahador (2018), A new and simple UV-assisted approach for synthesis of water soluble ZnS and transition metals doped ZnS nanoparticles (NPs) and investigating optical and photocatalyst properties, *J. Lumin.* **196**: 174-180.
- G.S. Ofelt (1962), Intensities of crystal spectra of rare-earth ion, *J. Chem. Phys.* **37**: 511.

- H. A. Othman H. S. Elkholy, I. Z. Hager (2017), Structural and optical investigation of undoped and  $\text{Sm}^{3+}$  doped lead oxyfluoroborate glasses, *Mater. Research Bull.* **89**: 210-216.
- I. Arul Rayappan, K. Selvaraju, K. Marimuthu (2011), Structural and luminescence investigations on  $\text{Sm}^{3+}$  doped sodium fluoroborate glasses containing alkali/alkaline earth metal oxides, *Physica B*, **406**: 548-555.
- J. Valenta, D. Guennani, A. Manar, B. Honerlage, T. Cloitre and R. L. Aulombard (1996), *Solid State Commun.* **98**: 695; Y. Yamada, T. Yamamoto, S. Nakamura, T. Taguchi, F. Sasaki, S. Kobayashi and T. Tani (1996), *Appl. Phys. Lett.* **69**: 88.
- J. Manam (2010), Preparation, characterization and study of optical properties of ZnS nanophosphor, *J. Lumin.* **130**: 292-297.
- J.L. Adams (2002), Lanthanides in non-oxide glasses, *Chem. Rev.* **102**: 2461-2476.
- K. Ashwini, Y. Yashaswini, C. Pandurangappa (2014), Solvothermal Synth. *Opt. Mater.* **37**: 537–542.
- K.K. Mahato, D.K. Rai, S. B. Rai (1998), Optical studies of  $\text{Sm}^{3+}$  doped oxyfluoroborate glass, *Solid State Commun.* **108**: 671-676.
- Ki-Soo Lim, N. Vijaya, C.R. Kesavulu, C.K. Jayasankar (2013), Structural and luminescence properties of  $\text{Sm}^{3+}$  ions in zinc fluorophosphate glasses, *Opt. Mater.* **35**: 1557- 1563.
- Koen Van den Eeckhout (2016), Persistent luminescence: kinetics and compounds, 127-152.
- L Boehm, R. Reisfield, N. Spector (1979), Optical transitions of  $\text{Sm}^{3+}$  in oxide glasses, *J. Solid State Chem.* **28**: 75-78.
- L. Ozawa, Cathodoluminescence: Theory and Applications, Kodansha, VCH, Tokyo, Weinheim (1990); Phosphor Handbook, ed. S. Shionoya and W. M. Yen, CRC, Boca Raton, FL, 1999.
- M. Bredol and J. Merikhi (1998), ZnS precipitation: morphology control, *J. Mater. Sci.* **33**: 471.
- M. Vijayakumar, K. Marimuthu, V. Sudarsan (2015), Concentration dependent spectroscopic behavior of  $\text{Sm}^{3+}$  doped lead fluoro-borophosphate glasses for

- laser and LED applications, *J. Alloys Compds.* **647**: 209-220.
- M.R. Reddy (2000), Optical absorption and fluorescence spectral studies of  $\text{Ho}^{3+}$  ions in  $\text{PbO-Al}_2\text{O}_3\text{-B}_2\text{O}_3$  glass system, *J. Phys. Chem. Solid.* **61**: 1567-1571.
- N. Shanmugam, S. Cholan, N. Kannadasan, K. Sathishkumar, G. Viruthagiri (2014), Luminance behavior of  $\text{Ce}^{3+}$  doped ZnS nanostructures, *Spectrochim. Acta Part A: Mol. Biomol. Spectrosc.* **118**: 557–563.
- N. Dehingia, P. Gogoi, P. Dutta (2020), Effect of Ag nanoparticles on the Judd-Ofelt and radiative parameters of  $\text{Sm}^{3+}$  ions in sol-gel silica matrix, *J. Lumin.* **226**: 117414.
- N. Rajkonwar, P. Dutta (2022), Effect of ligands PPIA and TOPO on radiative behaviour of  $\text{Eu}^{3+}$  ions in sol-gel silica matrix, *J. Lumin.* **244**: 118677.
- Nayereh Soltani, Elias Saion, Mohd Zobir Hussein, Maryam Erfani, Alam Abedini, Ghazaleh Bahmanrokh, Manizheh Navasery and Parisa Vaziri (2012), Visible Light-Induced Degradation of Methylene Blue in the Presence of Photocatalytic ZnS and CdS Nanoparticles, *Int. J. Mol. Sci.*, **13**: 12242-12258.
- P. Kaur, D. Singh, T. Singh (2016), Optical, photoluminescence and physical properties of  $\text{Sm}^{3+}$  doped lead alumino phosphate glasses, *J. Non-Cryst. Solids*, **452**: 87-92.
- P. Kaur, S. Kaur, G. P. Singh, D. P. Singh (2013),  $\text{Sm}^{3+}$  doped lithium aluminoborate glasses for orange coloured visible laser host material, *Solid State Commun.* **171**: 22-25.
- P. Manasa, C.K. Jayasankar (2016), Luminescence and phonon side band analysis of  $\text{Eu}^{3+}$  doped lead fluorosilicate glasses, *Opt. Mater.* **62**: 139–145.
- P. Yang, M. K. Lu, D. R. Yuan, C. F. Song, S. W. Liu and X. F. Cheng (2003), *Opt. Mater.* **24** 497.
- R. Praveena, R. Vijaya, C. K. Jayasankar (2008), Photoluminescence and energy transfer studies of  $\text{Dy}^{3+}$ -doped fluorophosphate glasses, *Spectro. Acta Part A*, **70** 577-586.
- R. Bhargava and R. Gallagher (1994), *Phys. Rev. Lett.* **72** 416; W. Q. Peng, S. C. Qu, G. W. Cong, X. Q. Zhang and Z. G. Wang (2005), *J. Cryst. Growth*, **282**

- 179; S. Arora and S. Sundar (2007), *Solid State Commun.* **144** 319; G. Ehrhart, B. Capoen, O. Robbe, F. Beclin, Ph. Boy, S. Turrell and M. Bouazaoui (2008), *Opt. Mater.* **30** 1595.
- R. Decorby (2006), Glasses for Photonic Integration in: S. Kasap, P. Capper (eds) Springer *Handbook of Electronic and Photonic Materials*. 1041-1061.
- R. Praveena, V. Venkatramu, P. Babu, C.K. Jayasankar (2008), *Physica B*, **403** 3527–3534.
- R. Reisfeld (1975), Radiative and Non-radiative Transitions of Rare-Earth Ions in Glasses, in: Rare Earths. Structure and Bonding, *Springer, Berlin, Heidelberg*, **22** 123-175.
- R. Seoudi, A. Shabaka, W.H. Eisa, B. Anies, N.M. Farage (2010), Effect of the prepared temperature on the size of CdS and ZnS nanoparticle. *Physica B*, **405** 919–924.
- R. Vacassy, S. M. Scholz, J. Dutta, H. Hofmann, C. J. G. Plummer, G. Carrot, J. Hilborn and M. Akine (1998), *Mater. Res. Soc. Symp. Proc.* **501** 369; P. Calandra, M. Goffredi and V. T. Liveri (1999), *Colloids Surf. A*, **160** 1-9.
- R. Vijaya, V. Venkatramu, P. Babu, C.K. Jayasankar, U.R. Rodriguez-Mendoza, V. Lavin (2013), Spectroscopic properties of  $\text{Sm}^{3+}$  ions in phosphate and fluorophosphate glasses, *Journal of Non-Crystalline Solids*, **365** 85–92.
- R. Sharma (2018), Photoluminescence study of  $\text{Sm}^{3+}$  doped Zinc Lead Tungsten Tellurite glasses for reddish-orange photonic device applications, *Opt. Mater.* **84** 375-382.
- R.D.A. Reddy, R. Ma, M.Y. Choi, T.K. Kim (2015), *Appl. Surf. Sci.* **324** 725–735.
- Reddy C., Naresh V., Babu B. and S. Buddhudu (2014), *Adv. Mater. Phys. Chem.* **4** 165.
- Lalruatpuia, KMS Dawngliana, AL Fanai, S Rai (2023), Effect of ZnS nanoparticles in photoluminescence properties of  $\text{Tb}^{3+}$  ion doped silica glass for photonic applications, *Applied Physics A*, **29**: 751.
- S. Kaur, P. Kaur, G. P. Singh, D. Arora, S. Kumar, D.P. Singh (2016), White light emission of  $\text{Ce}^{3+}$  sensitized  $\text{Sm}^{3+}$  doped lead alumino borate glasses, *J. of Lumin.* **180** 190-197.

- S. Q. Mawlud, M. M. Ameen, Md. R. Sahar, Z. A. S. Mahraz, K. F. Ahmed (2017), Spectroscopic properties of  $\text{Sm}^{3+}$  doped sodium-tellurite glasses: Judd-Ofelt analysis, *Optical materials*, **69** 318-327,
- S.B. Rai (2002), Optical properties of  $\text{Ho}^{3+}$  doped oxyfluoroborate glass, *Spec. Act. Part A*, **58** 1599-1566.
- Shaweta Mohan, Simranpreet Kaurb, Puneet Kaurc, D. P. Singh (2018), Spectroscopic Investigations of  $\text{Sm}^{3+}$ -doped Lead Alumino-Borate glasses containing Zinc, Lithium and Barium oxides, *J. Alloys and Comp.* **763** 486-495,
- Sk. Nayab Rasool, L. Rama Moorthy, C. K. Jayasankar (2013), Spectroscopic Investigation of  $\text{Sm}^{3+}$  doped phosphate based glasses for reddish-orange emission, *Optics. Comm.* **311** 156-162.
- T. Suhasini, J. Kumar, T. Sasikala, K. Jang, H. Lee, M. Jayasimhadri, J. Jeong, S. Yi and L. Moorthy (2009), *Opt. Mater.* **3** 1167.
- T. Yamamoto, S. Kishimoto and S. Iida (2001), Control of valence states for ZnS by triple-codoping method, *Physica B: Condensed Matter*, **308** 916-919.
- T. Satyanarayana (2010), Role of Al coordination in barium phosphate glasses on the emission features of  $\text{Ho}^{3+}$  ion in the visible and IR spectral ranges, *J. Lum.* **130** 498-506.
- V. H. Rao, P. S. Prasad, M. M. Babu, P. V. Rao, L. F. Santos, G. N. Raju, N. Veeraiah (2017), Luminescence properties of  $\text{Sm}^{3+}$  ions doped heavy metal oxide tellurite tungstate antimonate glasses, *Ceramics International*, **43** 16467–16473.
- W. Chen, Z. G. Wang, Z. J. Yin and L. Y. Lin (1997), Thermoluminescence of ZnS nanoparticles, *Appl. Phys. Lett.* **70** 1465.
- Y. A. Tanko, S. K. Ghoshal, M. R. Sahar (2016), Ligand field and Judd-Ofelt intensity parameters of samarium doped tellurite glass, *J. Mol. Struc.* **1117** 64-68.
- Y. Jiang, X. M. Meng, J. Liu, Z. Y. Xie, C. S. Lee and S. T. Lee (2003), *Adv. Mater.* **15** 323; C. Ma, D. Moore, J. Li and Z. L. Wang (2003), *Adv. Mater.* **15** 228; Z. W. Wang, L. L. Daemen, Y. S. Zhao, C. S. Zha, R. T. Downs, X. D.

Wang, Z. L. Wang and R. J. Hemley (2005), *Nat. Mater.* **4** 922; Y. F. Hao, G. W. Meng, Z. L. Wang, C. H. Ye and L. D. Zhang (2006), *Nano Lett.* **6** 1650.

### **3.4. Effect of ZnO nanoparticles on the Judd-Ofelt and radiative parameters of Sm<sup>3+</sup> ions in sol-gel silica matrix**

#### **Overview**

The trivalent samarium ions doped with different concentrations of ZnO NPs in silicate glasses were prepared by the sol-gel technique. The structural and optical properties were characterized by using X-ray diffraction, Fourier transform infrared, scanning electron microscope, transmission electron microscope, optical absorption, and photoluminescence measurements at room temperature respectively. The structural analysis from X-ray diffraction, scanning electron microscope, and transmission electron microscope results confirmed the hexagonal wurtzite ZnO structure of all the nanoparticle samples. The evaluation has been made for the dependence of various radiative parameters along with the Judd-Ofelt of Sm<sup>3+</sup> on the concentration of ZnO NPs. The effective network changing the nature of ZnO NPs has been revealed by the high value of  $\Omega_2$  obtained in this system matrix. In the current investigation, the silica matrix's emission transition  $^4G_{5/2} \rightarrow ^6H_{9/2}$  of Sm<sup>3+</sup>, which corresponds to the red color observed at 653 nm, demonstrated excellent radiative behavior compared to other commonly used glass hosts. These results suggest that Sm<sup>3+</sup> ions doped with ZnO NPs in sol-gel silicate glasses can be more efficient luminescent materials in the field of lasers and optical devices in the visible region. CIE Chromaticity diagram observed that these coordinates fall in the bluish-purple to yellowish-orange region.

### 3.4.1. Introduction

Optical telecommunication has become a crucial communication platform with the rapid development of information technology (Takahashi *et al.*, 2011, Kakkar *et al.*, 2014, Berneschi *et al.*, 2011, Vinh *et al.*, 2009). A large amount of information can be transmitted through this system owing to the intrinsic nature of light. The transmission media attenuates long-distance photon transmission through absorption and scattering. In this case, the optical amplifiers and gain media play a vital role. Compact optical devices are required for high-speed signal transfers. The development of integrated optical circuits continues to provide novel advanced optical functional materials (Chiasera *et al.*, 2019). The improvement in material properties leads to versatility for application in various fields. This enhancement can be met by employing different methods. Among these methods, doping of appropriate elements is one of the methods that improves the material properties.

The nanostructured metal oxides show unique properties like semiconducting, insulating behavior, etc., over their same bulk materials (Meenatchi *et al.*, 2017, Manikandan *et al.*, 2015, Manikandan *et al.*, 2014). In recent years, zinc oxide (ZnO) nanomaterials have attracted much consciousness from scientific researchers owing to their low cost, easy fabrication, photocatalytic activity, wide band-gap semiconductor (Manikandan *et al.*, 2015, Manikandan *et al.*, 2014, Zhu *et al.*, 2006, Selvam *et al.*, 2013, Shah *et al.*, 2013), unique optical, magnetic, and electronic properties, etc. (Kennedy *et al.*, 2016, Manikandan *et al.*, 2015, Kennedy *et al.*, 2008) ZnO materials are very versatile, translucent piezoelectric as well as electro conductive materials. In addition, ZnO materials act as an admirable ultraviolet absorber and antibacterial agent (Manikandan *et al.*, 2015). ZnO materials possess band gap energy of 3.37 eV and great excitation binding energy of 60 meV at room temperature (RT), which provides more efficient excitonic emission even at high temperatures (Murmu *et al.*, 2012). ZnO materials have been synthesized through numerous methods, which include chemical precipitation, sol-gel, microwave radiation, and hydrothermal methods, and is a very versatile compound (Kennedy *et al.*, 2013).

Amid numerous host luminescent materials, zinc silicate ( $\text{Zn}_2\text{SiO}_4$ ) is



recognized as a suitable host matrix to integrate with rare earth (RE) ions and transition metal ions developing in a first luminescence region in blue, green, and red spectra (Reddy *et al.*, 2014). RE ions are nowadays considered better dopants than transition metal ions for light activators. In addition to this, RE ions are an efficient ion substitute used in optical materials because of their large number of emission and absorption bands emitted due to transition within different energy levels. Given these factors, many scientists focused their interest on trivalent samarium ions ( $\text{Sm}^{3+}$ ) as a luminescence center in deep red emission arising from conduction band  $^4\text{G}_{5/2} \rightarrow ^6\text{H}_{9/6}$  transition (Sanchez *et al.*, 2014). Optical amplifiers, lasers, and electroluminescent devices mostly use  $\text{Sm}^{3+}$  ions doped phosphors and as such  $\text{Sm}^{3+}$  ions have become the most attractive and valuable RE ion dopant. Various methods have been grown to prepare  $\text{Zn}_2\text{SiO}_4:\text{Sm}^{3+}$  such as sol-gel synthesis, spray pyrolysis, co-precipitation synthesis, conventional solid-state reaction, and hydrothermal method (Auwalul *et al.*, 2018). Though the stable states technique provides better clarity than sol-gel method it uses an expensive  $\text{SiO}_2$  source for synthesizing zinc silicate.

It can be used in many applications such as solar cells, electrodes, sensors, etc. (Bhujel *et al.*, 2019). The possible doping of rare earths (La, Ce, Pr, Er, and Yb) has been shown by Cerrato *et al.* Similarly, John *et al.*, showed the ZnO doped with  $\text{Er}^{3+}$  using a solid-state reaction. The electrical conductivity was also increased due to the doping of rare earth (RE) (John *et al.*, 2012). Alam *et al.*, demonstrated the degradation of dyes due to RE metal doping (La, Nd, Sm, and Dy) for photocatalytic activity using the sol-gel method (Alam *et al.*, 2018). Campos *et al.*, reported the green emission from the borosilicate glass with Sm doping synthesized using the sol-gel route and can be used in many applications such as color displays, undersea communication, and optical storage (Campos-Zuniga *et al.*, 2019). Zhang *et al.* showed the concentration and thermal quenching of Phosphors of  $\text{Sm}^{3+}$  doped  $\text{Bi}_2\text{ZnB}_2\text{O}_7$  (Wheeler *et al.*, 2013). In the study of Novotny *et al.*, the doping of ZnO in Sm showed luminescence enhancement in the near band edge emission (Novotny *et al.*, 2016). Nagabushana *et al.* prepared the Sm-doped ZnO nanoparticles using low temperature combustion method. The optical properties of Sm-doped ZnO showed that this can be used in photo-catalytic and optoelectronic applications (Vishwas *et al.*, 2022). The enhancement in dielectric properties and the band gap

tuning was performed by Mirda *et al.* (Nath *et al.*, 2022). They doped  $\text{Sm}^{3+}$  in  $\text{Na}_2\text{O-ZnO-TeO}_2$  glass materials using the melt-quenching method. Badreddine *et al.*, also reported the mechanical and dielectric properties of Sm-doped ZnO nanoparticles (Badreddine *et al.*, 2020). Sm doping affects mechanical properties also. The increase in dopant concentration of Sm affects Zinc Silicate. It also tuned the band gap as well (Auwalu *et al.*, 2018). The doping of  $\text{Sm}^{3+}$  influenced the ZnO thin film on photocatalytic activity. The efficiency of the ZnO thin film decreased when reused many times, but with the doping of  $\text{Sm}^{3+}$ , the efficiency was improved (Nivaldo *et al.*, 2019). Similarly, Faraj *et al.* also reported the improvement in photocatalytic activity and recyclability of ZnO nanoparticles with the Sm doping (Hanifehpour *et al.*, 2016). Sm doping on ZnS improved the decolourization efficiency (Hanifehpour *et al.*, 2016). Mondal *et al.* reported the effect of Sm doping on the structural, thermal, linear, and non-linear optical properties of  $\text{ZnO-TeO}_2\text{-P}_2\text{O}_5$  (ZnO-modified phosphor-tellurite glass) (Mondal *et al.*, 2020). Pal *et al.* have examined the spectroscopic nature of  $\text{Sm}^{3+}$  doped Zn bismuth silicate glasses. Doping has influenced the Judd-Ofelt parameters, which depend upon the content of the host (Pal *et al.*, 2013).

This novel material has been synthesized and characterized because of the quest for the bright luminescent material. It is very stable even in harsh chemical and environmental situations, this property has led to the ideal selection of sol-gel derived zinc silicate ( $\text{ZnO-SiO}_2$ ) matrix as a host of the  $\text{Sm}^{3+}$  (Nguyen *et al.*, 2020). It is compatible with other materials which is advantageous to integrate for the assimilation of other organic and nanoparticles as a hybrid system with better control of particle size, uniform morphology, and high homogeneity (Gugu *et al.*, 2011, Kajihara *et al.*, 2013). The enhancement of UV absorption is suitable for developing applications associated with UV protection (Kumar *et al.*, 2017). The refractive index (Hiena *et al.*, 2019), electrical conductivity, and mechanical strength (Kozuka *et al.*, 2005) can be tuned through the adjustment of ZnO to  $\text{SiO}_2$  ratio whereas these materials have high transparency. The phase of zinc-silicate hosts is transformed from amorphous to crystalline nature at elevated annealing temperatures (Hiena *et al.*, 2019). In both the amorphous and crystalline structures, the chemical and thermal stability is being possible due to silicon dioxide ( $\text{SiO}_2$ ). It also exhibits both

hydrophobic and hydrophilic properties, thus it has photo-catalytic utility (Xiaoqi *et al.*, 2014) against anti-soiling which is desirable in different photonic appliances. The introduction of the network modifier (e.g.  $\text{TiO}_2$  (Halin *et al.*, 2017),  $\text{ZnO}$  (Agustin *et al.*, 2018),  $\text{SnO}_2$  (Tran *et al.*, 2017),  $\text{MgF}_2$  (Sun *et al.*, 2020), etc.) in silica host is intended to promote lower phonon energy and lower symmetry. The formation of non-bridging oxygen (NBO) offers an efficient absorption (Lee *et al.*, 2017), and luminescence of RE ion. Xiao *et al.*, prepared a  $\text{ZnO-SiO}_2\text{:Yb}^{3+}$  composite by admixing stabilized-ZnO solution to the acid-catalyzed TEOS solution to complete the hydrolysis and condensation process where the formation of ZnO quantum dot helps in the transfer of energy to RE ion (Xiao *et al.*, 2012). Hien *et al.* prepared  $\text{ZnO-SiO}_2\text{:Er}^{3+}$  crystalline thin film on a Si substrate using the sol-gel process where tri-ethanolamine stabilized ZnO solution was mixed with acid-catalyzed silica precursor to obtain an enhanced luminescence of  $\text{Er}^{3+}$  ion (Hien *et al.*, 2019). The sol-gel process can be adapted for obtaining modified zinc-silicate host with possible symmetry (Nguyen *et al.*, 2020).

#### 3.4.2. Experimental Details

$\text{Sm}^{3+}$  (2 mol%) co-doped ZnO (X mol%; X = 0.0, 0.5, 1.5, 2.5 mol%) in silicate glass were prepared with sol-gel methods. Analytical-grade reagents were used. The procedures were as follows: zinc acetate dehydrate ( $\text{Zn}(\text{CH}_3\text{COO})_2 \cdot 2\text{H}_2\text{O}$ ) was used as the starting material and Samarium (III) nitrate hexahydrate ( $\text{Sm}(\text{NO}_3)_3 \cdot 6\text{H}_2\text{O}$ ) as the dopant source while ethanol and nitric acid as solvent. A fixed amount of  $\text{Sm}(\text{NO}_3)_3 \cdot 6\text{H}_2\text{O}$  was initially dissolved in nitric acid that yielded a transparent solution with a pH value of 6–7, and  $\text{Zn}(\text{CH}_3\text{COO})_2 \cdot 2\text{H}_2\text{O}$  was similarly dissolved in ethanol. TEOS was added to the mixture drop-by-drop and stirred for an additional 50 minutes. These two solutions were then thoroughly mixed and immediately stirred at 60 °C for 3 h to form sol. This sol was then poured into a plastic container with a lid and left for some time to turn into stiff gels. For slow evaporation, small holes were punctured in the lid of the plastic container and kept as such for 2-3 weeks. This was followed by gradual drying of the gels up to 80 °C and then annealed in an electric furnace at a heating rate of 1 °C/min up to 1030 °C. The product was allowed to gradually cool down to room temperature (RT) and hence

Sm<sup>3+</sup>-doped ZnO nanoparticles were successfully produced.

### 3.4.3. Result and discussions

#### 3.4.3.1. Physical properties

Certain physical properties have been estimated from the measured glass densities and refractive index for fixed Sm<sup>3+</sup> ions doped with (2.5 mol%) ZnO NPs in sol-gel silicate dense glass-ceramic. These values are presented in Table 3.4.1. The values are estimated based on the procedure reported by (Dihingia *et al.*, 2020).

**Table 3.4.1**

The physical characteristics of fixed Sm<sup>3+</sup> ions doped with (2.5 mol%) ZnO NPs in sol-gel silicate dense glass-ceramic annealed at 1030 °C.

Physical properties	ZnO
Refractive Index ( $n_i$ )	2.37
Density ( $\rho$ ) (g/cm <sup>3</sup> )	2.89
Thickness ( $Z_t$ )	0.23
Average Molecular Weight $M_T$ (g)	66.37
Sm <sup>3+</sup> ion Concentration ( $N_i \times 10^{20}$ )	5.24
Dielectric constant ( $\epsilon_d$ )	5.617
Optical Dielectric Constant ( $\epsilon_d-1$ )	4.617
Molar Volume ( $V_m$ )(cm <sup>3</sup> /mol)	22.97
Reflection Losses ( $R_L$ )	0.916
Molar Refractivity ( $R_m$ )	13.94
Energy gap ( $E_g$ )	3.08
Polaron Radius ( $R_p \times 10^{-7}$ )(Å)	1.997
Inter-ionic Distance ( $R_i \times 10^{-7}$ ) (Å)	0.636
Electronic Polarizability ( $\alpha_e \times 10^{-25}$ )	2.404
Field Strength ( $F_s \times 10^{13}$ )	5.693
Optical basicity	0.925
Molar electronic Polarizability ( $\alpha_m$ )	5.532
Oxygen packing density (OPD)	87.08
Metallization criterion ( $M_C$ )	0.677

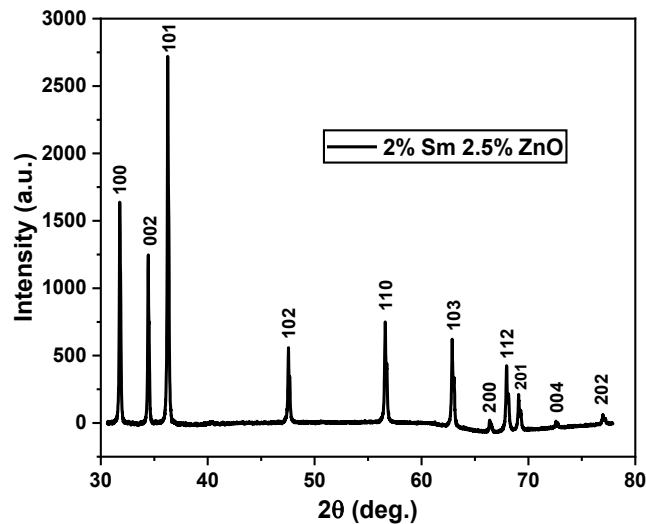
### 3.4.3.2. XRD Analysis

Fig. 3.4.1 show the XRD graph of fixed  $\text{Sm}^{3+}$  doped (2.5 mol%)ZnO NPs in the glass sample synthesized by the sol-gel method. The  $2\theta$  range was taken over 30–80°. The wurtzite phase of ZnO NPs is confirmed with this XRD pattern and no characteristic peaks were observed other than ZnO NPs. The average crystallite size of the nanoparticles is calculated after appropriate background correction from X-ray line broadening using Debye Scherrer's formula (Kumara *et al.*, 2013).

$$D = \frac{0.9\lambda}{\beta \cos \theta_B} \quad (3.6)$$

Where D is the crystallite size,  $\lambda$  is the wavelength of the X-ray source,  $\beta$  is the full width at half maximum (FWHM) of the peaks at the diffracting angle  $\theta$  (Fu *et al.*, 2003).

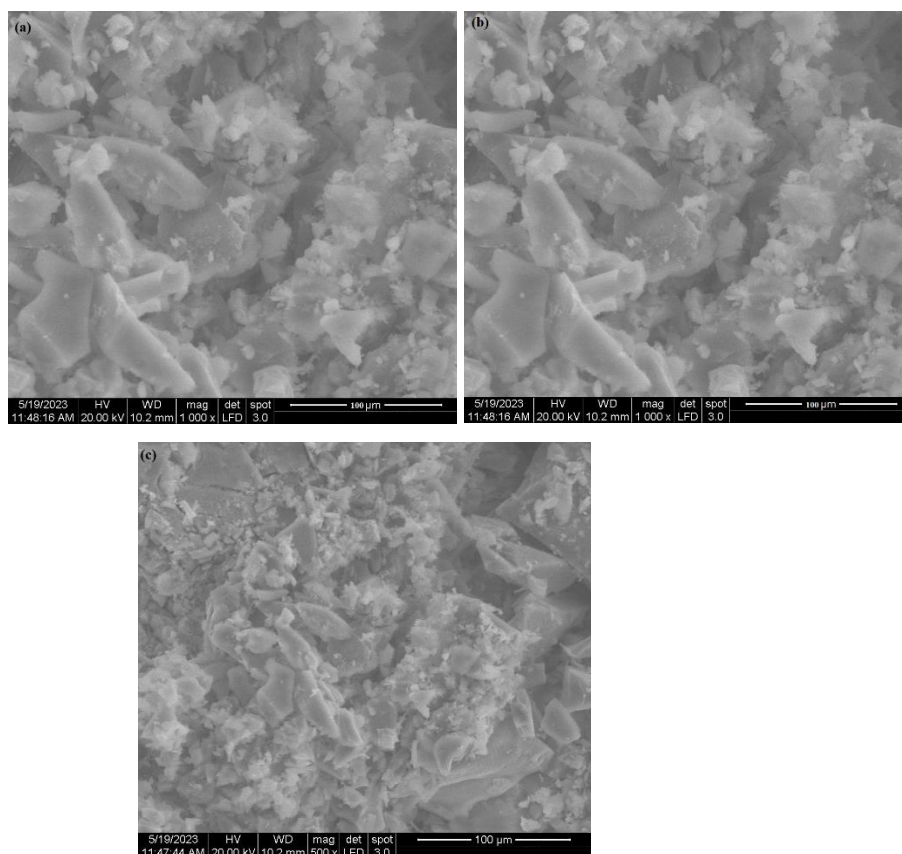
The high crystallinity and the polycrystalline nature of the ZnO NPs are confirmed by the intense peaks depicted in the graph. The peaks were at 31.74°, 34.48°, 36.26°, 47.58°, 56.62°, 62.91°, 66.37°, 68.21°, 69.18°, 72.66° and 77.12° and were indexed to the (100), (002), (101), (102), (110), (103), (200), (112), (201), (004) and (202) planes of the ZnO crystal. It can be observed from the crystallite size of  $\text{Sm}^{3+}$ -doped ZnO NPs of the glass sample is 18 nm.



**Fig. 3.4.1:** XRD pattern of  $\text{Sm}^{3+}$  doped ZnO NPs in the glass sample annealed at 900 °C.

### 3.4.3.3. SEM Analysis

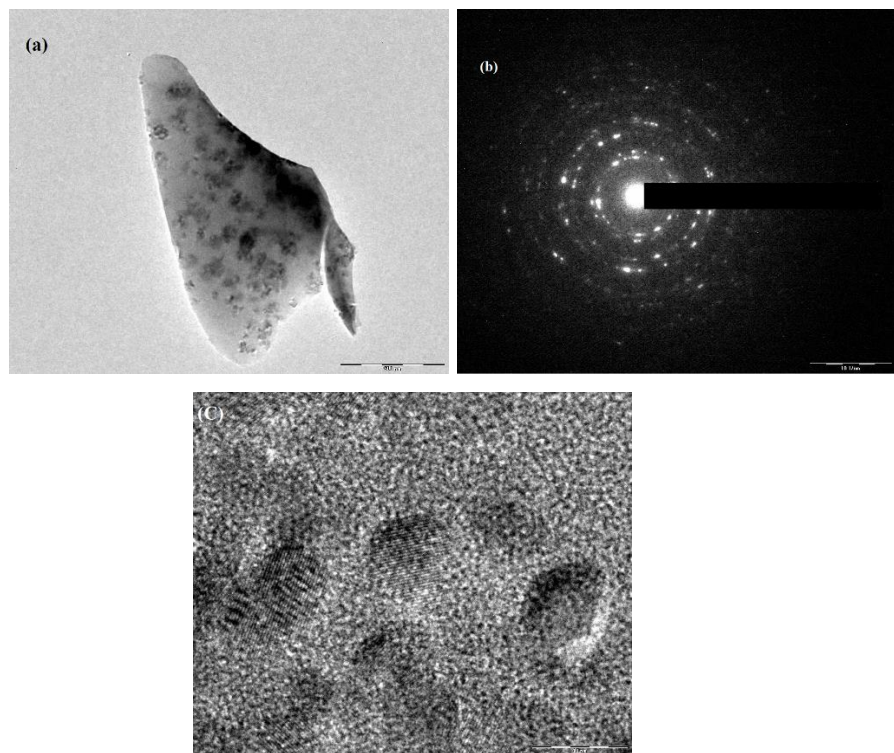
The data from SEM indicates the particle size to be approximately 16 nm, 18 nm and 21 nm for the Fig. 3.4.2((a) 0.5 mol%, 3.4.2(b) 1.5 mol% and 3.4.2(c) 2.5 mol%) ZnO NPs. Fig. 2(a), 2(b) and 2(c) consist of monodispersed and spherical shaped nanoparticles. As the concentrations of ZnO NPs the size of the particles increases and the shape is changed as the concentrations of ZnO NPs is increased. Rod like morphology of the particle is observed. Upon further increasing the concentrations of ZnO NPs, polygonal shaped micron sized particles are formed. The SEM micrographs of ZnO NPs were taken at various magnifications. The high-resolution SEM images confirms the presence of NPs. The SEM images show the agglomeration of the particles with narrow particle size distributions (Shamhari *et al.*, 2018, Talam *et al.*, 2012).



**Fig. 3.4.2.** SEM image of fixed Sm<sup>3+</sup>-doped ((a) 0.5, (b) 1.5 and (c) 2.5 mol%) ZnO NPs annealed at 900 °C.

#### 3.4.3.4. TEM Analysis

The TEM micrographs of fixed  $\text{Sm}^{3+}$  doped (2.5 mol%)ZnO NPs sample were obtained to visualize in detail the morphology of dense glass-ceramic which confirms the agglomeration of composite along with the presence of ZnO nano-crystallite in Silica matrix as can be seen in Fig. 3.4.3(a–c). The SAED pattern of fixed  $\text{Sm}^{3+}$  doped ZnO NPs in the sample can be observed with the growth of the ZnO crystallites in Fig. 3(b). The HRTEM image reveals the interplanar spacing of 0.27 nm in ZnO nano-crystallites in Fig. 3(c) (Nguyen *et al.*, 2020). The TEM images of  $\text{Sm}^{3+}$ -doped ZnO NPs shown in Fig. 4a, shows wurtzite-type structures with particle size 18 nm as seen from the spectrum which is in agreement with the XRD results.

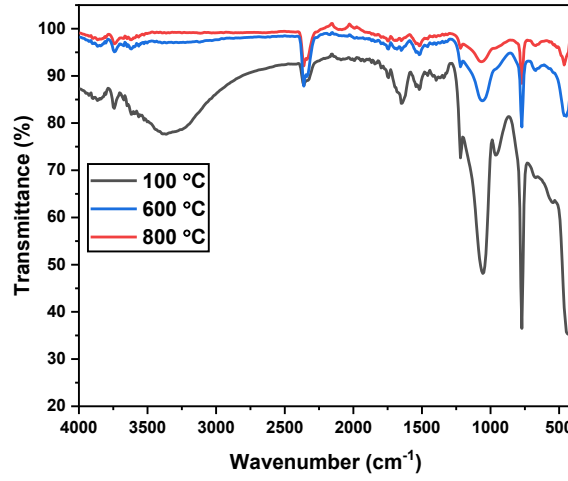


**Fig. 3.4.3:** (a) TEM image (b) SAED pattern (c) HRTEM of fixed  $\text{Sm}^{3+}$  doped ZnO(2.5 mol%) in sol-gel silicate glass annealed at 900 °C.

### 3.4.3.5. FTIR Analysis

The FTIR spectra of fixed  $\text{Sm}^{3+}$  ions doped  $\text{ZnO}$ (2.5 mol%) in sol-gel silicate glasses at various temperatures, (100 °C, 600 °C, and 800 °C) as shown in Fig. 3.4.4. The generated glass samples' FTIR spectra have been recorded at 250–4000  $\text{cm}^{-1}$ . It is observed various peaks at approximately 421, 432, 448, 473, 548, 672, 779, 957, 1049, 1342, 1652, 2360 and 3387  $\text{cm}^{-1}$ . In silicate glass, the energy phonons that originate from the Si-O-Si stretching vibration range from 1049  $\text{cm}^{-1}$  (Dihingia *et al.*, 2020). In the figure, we can also see that the peaks at 2360 and 3387  $\text{cm}^{-1}$ , which correspond to residual hydroxyls and the strength reduction with higher temperature treatment respectively (Puia *et al.*, 2023), significantly decrease in the glass with hosting at various temperatures. The FTIR can be used to identify the presence of various organic compounds in the samples. As a network modifier, the aluminium ion breaks up the silica structure to create a non-bridging Zn-O group (for example, Si-O-Zn), which can also be coordinated with  $\text{Sm}^{3+}$  ions (Nivaldo *et al.*, 2019). The band is observed around 479-548  $\text{cm}^{-1}$  due to Si-O-RE (non-bridging oxygen's (NBO)) doping in the glass host (Nivaldo *et al.*, 2019, Faraz *et al.*, 2018). A strong sharp band around 780  $\text{cm}^{-1}$  is assigned to the symmetrical stretching of the Si-O bond (Puia *et al.*, 2023). The bands at 1342  $\text{cm}^{-1}$  and 1049  $\text{cm}^{-1}$  are allocated to the polymerization of Si-OH groups leading to Si-O-Si bands (Dihingia *et al.*, 2020). The peak at 1653  $\text{cm}^{-1}$  was caused by the –OH bending vibration mode of water showing decreased and shifted to 1521  $\text{cm}^{-1}$  at high temperatures (Puia *et al.*, 2023). The varied bands in various wave number regions may be seen in the FTIR spectra of the glass samples. The corresponding wavenumbers were used to identify these stretching bands ( $\text{cm}^{-1}$ ).





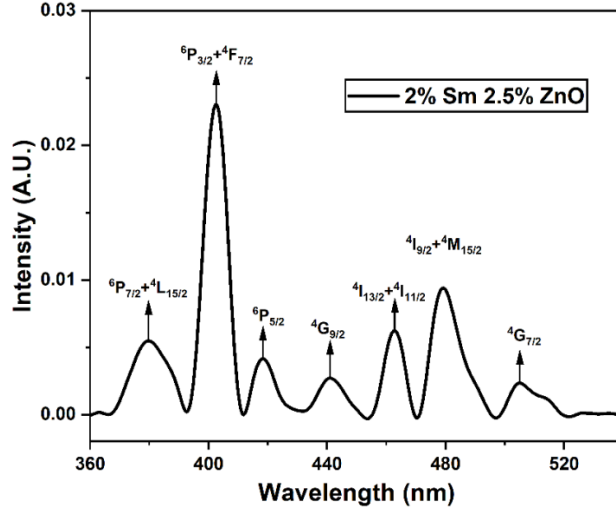
**Fig. 3.4.4:** FTIR spectrum of fixed  $\text{Sm}^{3+}$  ions doped with (2.5 mol%)ZnO NPs in sol-gel silicate glasses at various temperatures.

#### 3.4.3.6. Absorption Spectra

As shown in Fig. 3.4.5, the visible [350–550] regions of the absorption spectra of fixed  $\text{Sm}^{3+}$  ions doped with (2.5 mol%) ZnO NPs in sol-gel silicate dense glass-ceramic annealed at 1030 °C were recorded. These absorption bands are recorded at 377, 403, 417, 439, 464, 477 and 508 nm and are assigned as  $^6\text{H}_{5/2} \rightarrow ^6\text{P}_{7/2} + ^4\text{L}_{15/2}$ ,  $^6\text{H}_{5/2} \rightarrow ^4\text{F}_{7/2} + ^6\text{P}_{3/2}$ ;  $^6\text{P}_{5/2}$ ;  $^4\text{M}_{17/2}$ ;  $^4\text{I}_{13/2} + ^4\text{I}_{11/2}$ ;  $^4\text{I}_{9/2} + ^4\text{M}_{15/2}$  and  $^4\text{G}_{7/2}$  transitions respectively, originating from the ground state  $^6\text{H}_{5/2}$ . The oscillator strengths were estimated using data from  $\text{Sm}^{3+}$  ions absorption in sol-gel silicate dense glass-ceramic samples, and J-O intensity parameters were calculated for various transitions from the  $^6\text{H}_{5/2}$  ground state (Nivaldo *et al.*, 2019, Dawngliana *et al.*, 2023). The outcomes of these J-O intensity parameters are useful to understand the local configuration as well as bonding in the neighbour of the RE ions (Talam *et al.*, 2012).

The most intense  $^6\text{H}_{5/2} \rightarrow ^4\text{F}_{7/2} + ^6\text{P}_{3/2}$  transition is observed for the prepared sample among all the absorption bands (Faraz *et al.*, 2018). The ratio of intensities between electric dipole (ED) and magnetic dipole (MD) transitions determines the symmetry of the local neighbourhood surrounding the  $\text{RE}^{3+}$  ions (Mondal *et al.*,

2020). Here, the increased intensity of the ED transition denotes a larger degree of ion-environment asymmetry.

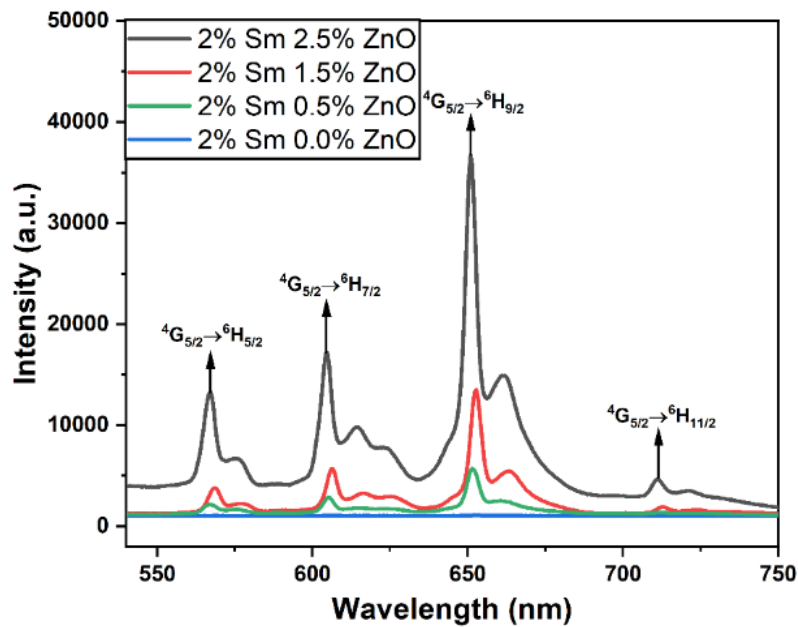


**Fig. 3.4.5:** Absorption spectra fixed  $\text{Sm}^{3+}$ -doped (2.5 mol%) ZnO NPs in sol-gel silicate dense glass-ceramic annealed at 1030 °C.

### 3.4.3.7. PL Spectra

The PL spectra of fixed  $\text{Sm}^{3+}$  ions doped with different concentrations of (0.0-2.5 mol%) ZnO NPs in sol-gel silicate glasses as shown in Fig. 3.4.6. The PL spectra of fixed  $\text{Sm}^{3+}$  ions doped with different concentrations of ZnO NPs in sol-gel silicate dense glass-ceramic have been recorded by the excitation wavelength ( $\lambda_{\text{ex}} = 450 \text{ nm}$ ) also within the spectral range of 530-750 nm as shown in Fig. 6 and the four emission bands at wavelengths of 567 nm (green), 606 nm (orange), 653 nm (red), and 708 nm (deep red) that are associated with the electronic transitions  ${}^4G_{5/2} \rightarrow {}^6H_{(2j+1)/2}$ , where  $j = 2, 3$ , and  $5$  (i.e.,  ${}^6H_{5/2}$ ,  ${}^6H_{7/2}$ ,  ${}^6H_{9/2}$  and  ${}^6H_{11/2}$ ), respectively (Nguyen *et al.*, 2020). When compared to the other three transitions, the transition  ${}^4G_{5/2} \rightarrow {}^6H_{9/2}$  (653 nm) is the most intense of the four. Due to the partial magnetic dipole and electric dipole that is allowed with the  $\Delta J = \pm 2$  selection rule, the transition  ${}^4G_{5/2} \rightarrow {}^6H_{9/2}$  is significant (Talam *et al.*, 2012). This makes it appropriate for laser emission. The transition  ${}^4G_{5/2} \rightarrow {}^6H_{5/2}$  (567 nm) is a forbidden magnetic dipole transition ( $\Delta J = 0$  i.e.,  $J \neq 0 \leftrightarrow 0$  values), the transition  ${}^4G_{5/2} \rightarrow {}^6H_{7/2}$  (606 nm)

is a forbidden electric dipole transition with a  $\Delta J = \pm 1$  having a respectable intensity, and the transition  $^4G_{5/2} \rightarrow ^6H_{11/2}$  (708 nm) is forbidden with a  $\Delta J = \pm 3$  having a faint intensity (Hanifehpour *et al.*, 2016, Mondal *et al.*, 2020). Additionally, Fig. 4 shows that when the concentration of ZnO ions rises, the hues of green, orange, red, and deep red become more intense. The highest and least intense transitions in the current investigation are from states  $^4G_{5/2} \rightarrow ^6H_{9/2}$  (653 nm) and  $^4G_{5/2} \rightarrow ^6H_{11/2}$  (708 nm), respectively (Pal *et al.*, 2013). In the present study of fixed  $\text{Sm}^{3+}$  ions doped with different concentration of ZnO in sol-gel silicate glasses annealed at 1030 °C.



**Fig. 3.4.6:** PL spectra of fixed  $\text{Sm}^{3+}$  doped with different concentrations of ZnO in sol-gel silicate glasses annealed at 1030 °C.

#### 3.4.3.8. Judd-Ofelt and Radiative parameters

The J-O theory determines the oscillator strength of several 4f–4f transitions in  $\text{RE}^{3+}$ . A study of the J-O parameter (Judd, 1962 Ofelt, 1962) is performed on the absorption spectra of the synthesized materials (Fig. 3.4.5) to extract valuable data about the optical properties as well as the neighborhood of  $\text{Sm}^{3+}$  ions in the host matrix. Table 3.4.2 lists the experimentally determined ( $f_{\text{exp}}$ ) and estimated oscillator strengths ( $f_{\text{cal}}$ ) of fixed  $\text{Sm}^{3+}$  doped with (2.5 mol%) ZnO NPs in sol-gel silicate

dense glass-ceramic as well as three distinct J-O intensity parameters ( $\Omega_\lambda$ ) (Dehingia *et al.*, 2020). The increase in the  $\Omega_2$  parameter along with the concentration of ZnO in the present samples indicates an enhanced asymmetry around the  $\text{Sm}^{3+}$  ions for this silica matrix which further confirms the role of ZnO NPs as an effective modifier in the studied network (Dehingia *et al.*, 2020). The result is very significant as the transition probability for emission from tri-positive lanthanide ions is expected to increase with the increase in asymmetry and covalency around the RE ions (Dehingia *et al.*, 2020). The remaining two parameters,  $\Omega_4$  and  $\Omega_6$ , are affected by the vibronic transition of the  $\text{Sm}^{3+}$  ions attaching to the ligand atoms as well as the bulk characteristics of the medium, such as viscosity and dielectric (Nguyen *et al.*, 2020). The spectroscopic quality ( $\Omega_4/\Omega_6$ ) of the laser active medium, which may also be determined from J-O parameters, has a considerable impact on forecasting the stimulated emission (Dihingia *et al.*, 2020). Table 3.4.3 shows comparative J-O intensity parameters between the present sample and other glass hosts. The present sample has a higher  $\Omega_2$  value indicative of higher asymmetry and an improved covalent environment around the  $\text{Sm}^{3+}$  ions (Nguyen *et al.*, 2020).

The radiative properties of the produced glass sample's  $^4\text{G}_{5/2}$  fluorescence level are approximated using the J-O parameter calculated from absorption data and photoluminescence spectra (Dihingia *et al.*, 2020). Table 3.4.4 tabulates the radiative characteristics of fixed  $\text{Sm}^{3+}$  ions doped with different concentrations of (0.0-2.5 mol%) ZnO NPs in sol-gel silicate dense glass-ceramic annealed at 1030 °C.

**Table 3.4.2**

The calculated ( $f_{\text{cal}}$ ) and experimental ( $f_{\text{exp}}$ ) oscillator strengths with esteem to the relative absorption peak for fixed  $\text{Sm}^{3+}$  doped with (2.5 mol%)ZnO NPs in sol-gel silicate dense glass-ceramic annealed at 1030 °C.

Transitions	Energy ( $\text{cm}^{-1}$ )	Wavelength (nm)	$f_{\text{exp}}$ ( $\times 10^{-6}$ )	$f_{\text{cal}}$ ( $\times 10^{-6}$ )
${}^6\text{H}_{5/2} \rightarrow {}^4\text{G}_{7/2}$	19685	508	0.06	1.07
${}^4\text{I}_{9/2} + {}^4\text{M}_{15/2}$	20964	477	0.62	0.36
${}^4\text{I}_{13/2} + {}^4\text{I}_{11/2}$	21552	464	0.07	0.19
${}^4\text{G}_{9/2}$	22779	439	0.04	0.54
${}^6\text{P}_{5/2}$	23981	417	0.42	0.31
${}^4\text{F}_{7/2} + {}^6\text{P}_{3/2}$	24814	403	1.06	0.35
${}^6\text{P}_{7/2} + {}^4\text{L}_{15/2}$	26525	377	0.09	0.03
	$\Omega_2=33.063\pm0.027$ ( $\times 10^{-20} \text{ cm}^2$ )	$\Omega_4= 3.806\pm0.021$ ( $\times 10^{-20} \text{ cm}^2$ )	$\Omega_6=2.037\pm0.032$ ( $\times 10^{-20} \text{ cm}^2$ )	
	$\Omega_4/\Omega_6=1.868\pm0.039$ ( $\times 10^{-20}$ )			

**Table 3.4.3**

Comparison of spectroscopic quality factors and J-O intensity characteristics for  $\text{Sm}^{3+}$  across many well-known hosts.

Hosts	$\Omega_2 (10^{-20} \text{ cm}^2)$	$\Omega_4 (10^{-20} \text{ cm}^2)$	$\Omega_6 (10^{-20} \text{ cm}^2)$	$\Omega_4/\Omega_6$	Reference
ZnO co-doped $\text{SiO}_2$	$33.063 \pm 0.027$	$3.806 \pm 0.021$	$2.037 \pm 0.032$	$1.868 \pm 0.039$	Present work
$\text{TiO}_2$ co-doped $\text{SiO}_2$	$6.179 \pm 0.023$	$0.215 \pm 0.016$	$0.208 \pm 0.045$	$1.034 \pm 0.299$	[48]
ZBSS1	3.17	1.32	1.25	1.05	[35]
ZBSS2	2.75	1.61	1.38	1.16	[35]
ZBSS5	1.56	2.19	1.77	1.23	[35]
Al- $\text{SiO}_2$	$0.47 \pm 0.016$	$0.24 \pm 0.009$	$2.28 \pm 0.038$	$0.105 \pm 0.006$	[53]
Ag- $\text{SiO}_2$	$31.93 (\pm 0.93)$	$23.96 (\pm 0.34)$	$18.26 (\pm 0.07)$	1.31	[54]

**Table 3.4.4**

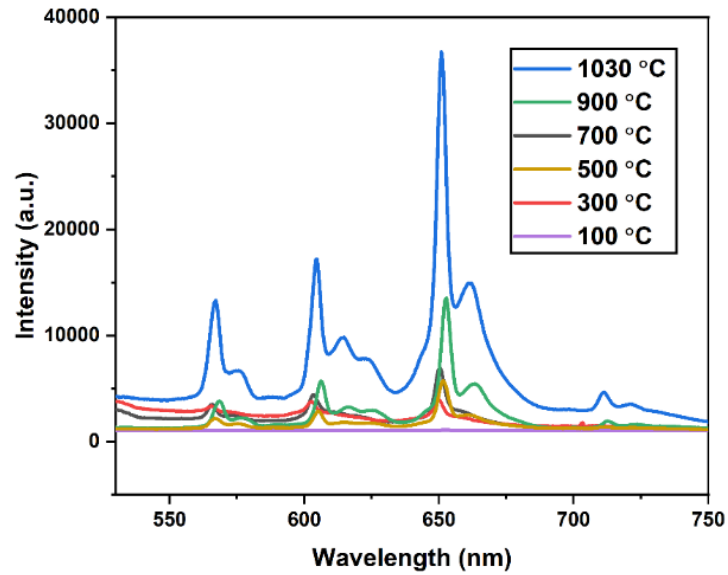
Estimated radiative characteristics of fabricated glass samples.

Transitions	Wavelength( $\lambda_p$ ) (nm)	$A_{ed}(s^{-1})$	$\beta_r$ (%)	$\lambda_{eff}$ (nm)	$\sigma_P$ ( $\times 10^{-22}$ $cm^2$ )
<b>Sm<sup>3+</sup>:ZnO(0.5%)</b>					
$^4G_{5/2} \rightarrow ^6H_{5/2}$	567	10.87	13.16	6.43	0.398
$^6H_{7/2}$	606	35.96	43.54	6.92	1.634
$^6H_{9/2}$	653	29.49	35.71	7.32	1.709
$^6H_{11/2}$	708	6.27	7.59	9.38	0.392
	$A_T (s^{-1}) =$	82.59			
	$\tau_R(\mu s) =$	12121.2			
<b>Sm<sup>3+</sup>:ZnO(1.5%)</b>					
$^4G_{5/2} \rightarrow ^6H_{5/2}$	567	14.08	14.95	8.53	0.389
$^6H_{7/2}$	606	39.21	41.62	8.97	1.374
$^6H_{9/2}$	653	32.74	34.76	9.71	1.407
$^6H_{11/2}$	708	8.25	8.75	11.36	0.426
	$A_T (s^{-1}) =$	94.2			
	$\tau_R(\mu s) =$	10615.7			
<b>Sm<sup>3+</sup>:ZnO(2.5%)</b>					
$^4G_{5/2} \rightarrow ^6H_{5/2}$	567	58.06	18.73	11.36	1.204
$^6H_{7/2}$	606	97.62	31.39	14.09	2.179
$^6H_{9/2}$	653	132.14	42.50	18.65	3.011
$^6H_{11/2}$	708	23.08	7.42	22.89	0.592
	$A_T (s^{-1}) =$	310.9			
	$\tau_R(\mu s) =$	3216.5			

#### 3.4.3.9. Effect of annealing PL spectrum

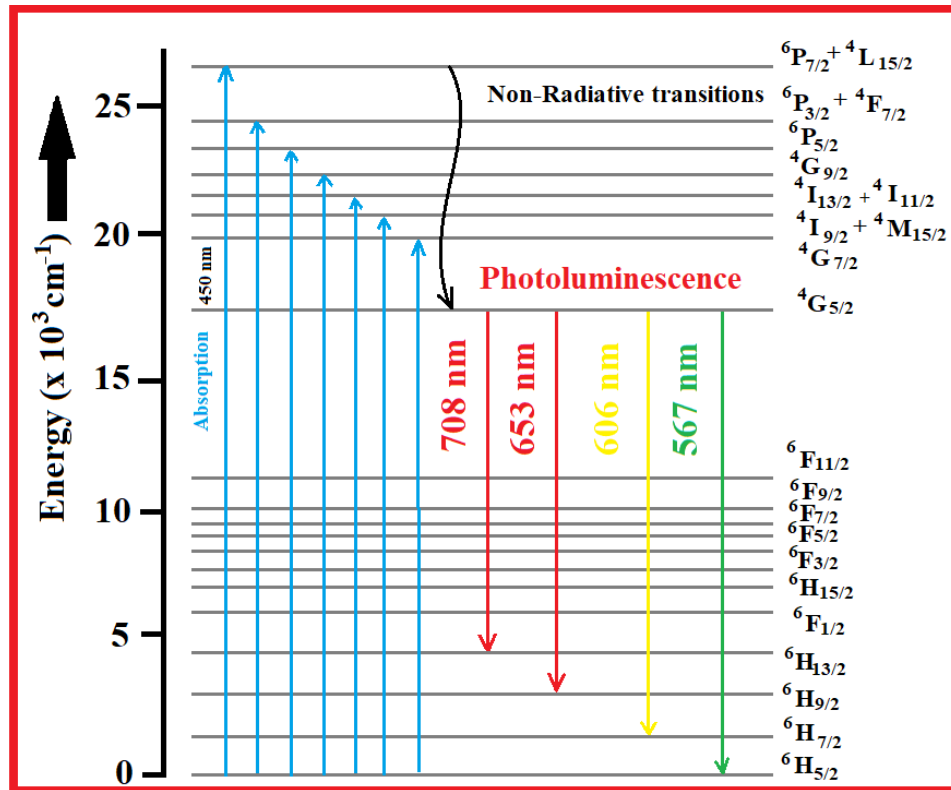
The excitation wavelength ( $\lambda_{\text{ex}} = 450 \text{ nm}$ ) was used to record the PL spectra of sol-gel silicate glasses co-doped with fixed  $\text{Sm}^{3+}$  and ZnO (2.5 mol%) at various annealing temperatures, as shown in Fig. 3.4.7. Effect of annealing temperature is plotted for fixed  $\text{Sm}^{3+}$  ions doped with ZnO NPs in sol-gel silicate glasses as in Fig. 3.4.8. Weak emissions from samples that were annealed at lower temperatures suggest intense hydroxyl quenching. The hydroxyls are removed during annealing, which significantly improves luminescence. The samples' weight loss after annealing made it clear that the hydroxyls had been removed. It has been found that PL peak intensity increases when annealing temperatures increase by 100–1030 °C.

In the Fig. 3.4.8 showing a possible absorption and photoluminescence mechanism. The schematic diagram of fixed  $\text{Sm}^{3+}$  ion and different concentrations of ZnO (0.0-2.5 mol%) co-doped in sol-gel silicate glass annealed at 1030 °C with PL (solid line) and possible non-radiative relaxation (solid line) transitions as in Fig. 3.4.8.



**Fig. 3.4.7:** *Effect of annealing temperature on PL intensity of fixed  $\text{Sm}^{3+}$  ions doped (2.5 mol%) ZnO NPs in sol-gel silicate glasses.*

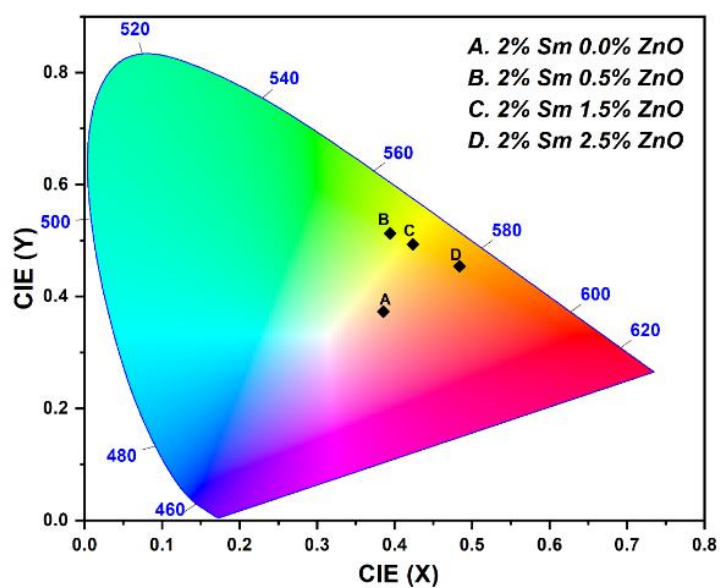




**Fig. 3.4.8:** Energy level diagram of  $\text{Sm}^{3+}$  doped ZnO NPs in sol-gel silicate glasses.

#### 3.4.3.10. Color tunability

The CIE X, Y color chromaticity coordinates of the  $\text{Sm}^{3+}$  doped with ZnO in sol-gel glasses have been determined and presented in Table 3.4.5 along with the X, Y color chromaticity coordinates of the reported  $\text{Sm}^{3+}$  doped glasses. PL color is tuned from the pink region without ZnO concentration as shown in Fig. 3.4.9. PL color is tuned from greenish-yellow to orange regions with the increase in ZnO concentrations as in Fig. 3.4.9. Among all the four glasses, fixed  $\text{Sm}^{3+}$  doped ZnO(2.5 mol%) glass (0.484, 0.454) is having brightest orange emission



**Fig. 3.4.9:** CIE chromaticity diagram of fixed  $\text{Sm}^{3+}$  ions doped with different concentrations of ZnO NPs in sol-gel silicate glasses.

**Table 3.4.5**

CIE Chromaticity coordinates of fixed  $\text{Sm}^{3+}$ -doped with different concentrations of ZnO NPs in sol-gel silicate dense glass-ceramic.

Color	0.0% ZnO	0.5% ZnO	1.5% ZnO	2.5% ZnO
<b>Coordinates</b>				
<b>X</b>	0.385	0.394	0.423	0.484
<b>Y</b>	0.373	0.513	0.493	0.454

### 3.4.3.11. Non-linear Properties

Certain non-linear properties can be estimated from optical parameters like the non-linear refractive index [ $n_2$ , susceptibility ( $\chi^{(3)}$ ), co-efficient ( $\gamma_{ce}$ )] and sensibly large Abbe number ( $v_{Ab}$ ) (which) indicate the good optical quality of the sol-gel SiO<sub>2</sub> glass (Dihingia *et al.*, 2020). These values are summarized in Table 3.4.6. These values are estimated using the approach outlined by (Dihingia *et al.*, 2012).

**Table 3.4.6**

Non-linear properties of fixed Sm<sup>3+</sup> ions doped (2.5 mol%) ZnO NPs in sol-gel silicate dense glass-ceramic annealed at 1030 °C.

$n_g$	$n_r$	$n_g - n_r$	$n_b$	$v_{Ab}$	$1/v_{Ab}$	$n_2$ (in $10^{-13}$ esu)	$\gamma_c$ (in $cm^2/W$ )	$\omega_o \times 10^{-13}$	$N \times 10^{-16}$	$\chi^{(3)} \times 10^{-6}$
1.5	1.5	0.0	1.5	50.7	0.020	3.121	0.869	108.47	1097.8	3.307
12	02	10	07					2	74	

### 3.4.4. Conclusions

This study provides a modified sol-gel synthesis method of obtaining optically active Sm<sup>3+</sup> (2 mol%) doped with different concentrations ZnO (0.0, 0.5, 1.5, 2.5 mol%) in silicate dense glass-ceramic materials. XRD, FTIR, SEM, and TEM spectra are used to analyze the prepared sample's structural characteristics. The oxide phase (e.g. Zn-O-Zn, Si-O-Si, Zn-O-Si) was successfully formed (Gugu *et al.*, 2011). The OH<sup>-</sup> molecule was absent indicating advantages against hydroxyl quenching of RE<sup>3+</sup> ion. The experimental absorption and PL spectra evaluated the J-O intensity parameters and other radiative parameters. These studied samples showed a trend of  $\Omega_2 > \Omega_4 > \Omega_6$  in the J-O intensity parameters. Compared to other popular hosts higher value of the  $\Omega_2$  parameter was noted in the present matrix which indicates higher asymmetry around the Sm<sup>3+</sup> ions in the ZnO NPs co-doped SiO<sub>2</sub> matrix. Enhancement in the  $\Omega_2$  parameter along with the concentration of ZnO NPs

reveals the network modifying role of the ZnO NPs (Gugu *et al.*, 2011). An improvement in the radiative characteristics of each of the three PL bands was seen upon the addition of ZnO NPs. The emission transition  $^4G_{5/2} \rightarrow ^6H_{9/2}$  of  $Sm^{3+}$  corresponding to the red color observed at 653 nm showed maximum peak intensity, highest branching ratio, and spontaneous emission probability (Dawngliana *et al.*, 2023). It is clear from the CIE chromaticity diagram that the color of emission can be changed with ZnO varying. Non-linear properties have been estimated from optical parameters like the non-linear refractive index [ $n_2$ , susceptibility ( $\chi^{(3)}$ ), co-efficient ( $\gamma_{ce}$ )] and large Abbe number ( $\mathfrak{A}_{Ab}$ ), calculations are used to determine the good optical quality of the sol-gel silicate glasses. Conclusively, the acquired results confirm that the present glass samples are generally an excellent possibility for various photonic applications, including temperature sensors, photovoltaic solar cells, bio-sensing, and display devices, etc.

## Reference

- A. Chiasera, C. Meroni, F. Scotognella, Y.G. Boucher, G. Galzerano, A. Lukowiak (2019), Coherent emission from fully  $\text{Er}^{3+}$  doped monolithic 1-D dielectric micro-cavity fabricated by rf-sputtering, *Opt. Mater.* **87**: 107–111
- A. Manikandan, M. Durka, K. Seevakan, S. Arul Antony (2015), A novel one-pot combustion synthesis and opto-magnetic properties of magnetically separable spinel  $\text{Mn}_x\text{Mg}_{1-x}\text{Fe}_2\text{O}_4$  ( $0.0 \leq x \leq 0.5$ ) Nano-photocatalysts, *J. Supercond. Nov. Magn.* **28**: 1405-1416.
- A. Manikandan, M. Durka, S. Arul Antony (2014), A novel synthesis, structural, morphological, and opto-magnetic characterizations of magnetically separable spinel  $\text{Co}_x\text{Mn}_{1-x}\text{Fe}_2\text{O}_4$  ( $0 \leq x \leq 1$ ) nano-catalysts, *J. Supercond. Nov. Magn.* **27**: 2841-2857.
- A.H. Shah, E. Manikandan, M.B. Ahmed (2013), Enhanced bioactivity of Ag/ZnO nanorods-a comparative antibacterial study, *J. Nanomed. Nanotech.* **4**: 6.
- B. Meenatchi, V. Sathiya Lakshmi, A. Manikandan, V. Renuga, A. Sharmila, K. R. Nandhine Deve & Saravana Kumar Jaganathan (2017), Protic ionic liquid assisted synthesis and characterization of ferromagnetic cobalt oxide nanocatalyst, *J. Inorg. Organomet. Polym.* **27**: 446–454.
- B.R. Judd (1962), Optical absorption intensities of rare-earth ions, *Phys. Rev.* **127**: 750.
- C. Agustín-Saenz, J.A. Sanchez-Garcia, M. Machado, M. Brizuela, O. Zubillaga, A. Tercjak (2018), Broadband antireflective coating stack based on mesoporous silica by acid-catalyzed sol-gel method for concentrated photovoltaic application, *Sol. Energy Mater. Sol. Cells*, **186**: 154–164.
- C.P. Reddy, V. Naresh, and B.C. Babu (2014), Photoluminescence and Energy Transfer Process in  $\text{Bi}^{3+}/\text{Sm}^{3+}$  Co-Doped Phosphate Zinc Lithium Glasses, *Advances in Materials Physics and Chemistry*, **4** 165–171.
- C.S. Lee, K.A. Matori, S.H. Ab Aziz, H.M. Kamari, I. Ismail, M.H.M. Zaid (2017), Fabrication and characterization of glass and glass-ceramic from rice husk ash as a potent material for optoelectronic applications, *J. Mater. Sci. Mater. Electron*, **28**: 17611–17621.
- D.A. Wheeler and J.Z. Zhang (2013), Exciton dynamics in semiconductor

- nanocrystals, *Advanced Materials*, **25** 2878–2896.
- N. Dehingia, S. Rai (2012), Synthesis of TiO<sub>2</sub> nanoparticles and spectroscopic upconversion luminescence of Nd<sup>3+</sup>-doped TiO<sub>2</sub>–SiO<sub>2</sub> composite glass, *J. Lumin.* **132**: 1243-1251.
- Lalruat Puia, KMS Dawngliana, A L Fanai and S. Rai (2023), Effect of ZnS nanoparticles in photoluminescence properties of Tb<sup>3+</sup> ion doped silica glass for photonic applications, *Applied Physics A*, **129**: 751
- D.S.C. Halin, M.M.A.B. Abdullah, N. Mahmed, S.N.A. Abdul Malek, P. Vizureanu, A.W. Azhari (2017), Synthesis and characterization of TiO<sub>2</sub>/SiO<sub>2</sub> thin film via sol-gel method, *IOP Conf. Ser. Mater. Sci. Eng.* **209**: 87-96.
- E. Manikandan, J. Kennedy, G. Kavitha, K. Kaviyarasu, M. Maaza, B.K. Panigrahi, U. Kamachi Mudali (2015), “Hybrid Nanostructured Thin-Films by PLD for Enhanced Field Emission Performance for Radiation Micro-Nano Dosimetry Applications, *J. Alloys & Comps*, **647**: 141-145.
- E. Manikandan, M. K. Moodley, S. S. Ray, B. K. Panigrahi, R. Krishnan, K. G. M. Nair, A.K. Tyagi (2010), Zinc oxide epitaxial thin-film deposited over carbon on various substrates by PLD technique, *J. Nanosci. Nanotech.* **10**: 5601-5611.
- E.E. Campos-Zuniga, I.L. Alonso-Lemus, V. Agarwal, and J. Escorcía-García (2019), Sol-gel synthesis for stable green emission in samarium doped borosilicate glasses, *Ceram In.* **45**: 24052–24059.
- F. Xiao (2012), Efficient energy transfer and enhanced infrared emission in Er-doped ZnO–SiO<sub>2</sub> composites, *J. Phys. Chem. C*, **116(24)**: 13458–13462.
- G.S. Ofelt (1962), Intensities of crystal spectra of rare-earth ion, *J. Chem. Phys.* **37**: 511.
- H. Kozuka, Handbook of Sol-Gel Science and Technology: Processing, Characterization, and Applications, Kluwer Academic Publisher, New York, 2005.
- H. Takahashi (2011), High performance planar light wave circuit devices for large capacity transmission, *Optic Express*, **19**: 173–180.
- I. Pal, A. Agarwal, S. Sanghi, and M. P. Aggarwal (2013), Investigation of spectroscopic properties, structure and luminescence spectra of Sm<sup>3+</sup> doped

zinc bismuth silicate glasses, *Spectro. Acta A. Mol Bio. Spectrosc.* **101**: 74–81.

I.A. Auwalu, M.A.Y. Hotoro, U.H. Jamo, and D.G. Diso (2018), Effect of Samarium Oxide on Structural and Optical Properties of Zinc Silicate Glass Ceramics from Waste Material, *Nano Hybrids and Composites*, **22**: 35–46.

I.A. Auwalu<sup>1</sup>, M.A.Y. Hotoro, U.H. Jamo, D.G. Diso (2018), Effect of Samarium Oxide on Structural and Optical Properties of Zinc Silicate Glass Ceramics from Waste Material, *Nano Hybrids and Composites*, **22**: 35-46.

J. Kennedy, B. Sundrakannan, R.S. Katiyar, A. Markwitz, Z. Li, W. Gao (2008), Raman scattering investigation of hydrogen and nitrogen ion implanted ZnO thin films, *Current Applied Physics*, **8**: 291-294.

J. Kennedy, G.V.M. Williams, P.P. Murmu, B.J. Ruck (2013), Intrinsic magnetic order and inhomogeneous transport in Gd-implanted zinc oxide, *Physical Review B*, **88**: 214423.

J. Kennedy, P.P. Murmu, J. Leveneur, A. Markwitz, J. Futter (2016), Controlling preferred orientation and electrical conductivity of zinc oxide thin films by post growth annealing treatment, *Applied Surface Science*, **367**: 52-58.

J. Nath Mirda, S. Mukhopadhyay, K. Ranjan Sahu, M. Nanda Goswami, and C. Author (2022), Enhancement of optical properties and dielectric nature of Sm<sup>3+</sup> doped Na<sub>2</sub>O-ZnO-TeO<sub>2</sub> Glass materials, *Journal of physics and chemistry solids*, **167**: 110776.

J.F. Sanchez-Royo, G. Munoz-Matutano, M. Brotons-Gisbert, J.P. Martínez-Pastor, A. Segura, A. Cantarero, R. Mata, J. Canet-Ferrer, G. Tobias, E. Canadell, J. Marqués-Hueso, and B. D. Gerardot (2014), Electronic structure, optical properties, and lattice dynamics in atomically thin indium selenide flakes, *Nano Research*, **7**: 1556–1568.

J.F. Zhu and Y.J. Zhu (2006), Microwave-assisted one-step synthesis of polyacrylamide-metal (M = Ag, Pt, Cu) nanocomposites in ethylene glycol, *J. Phys. Chem. B*, **110**: 8593-8597.

K. Badreddine, A. Srour, R. Awad, and A.I. Abou-Aly (2020), The investigation of mechanical and dielectric properties of Samarium doped ZnO nanoparticles,” *Mater. Res. Express*, **7**: 78-85.

- K. Bhujel, S. S. Ningthoujam, L. R. Singh, and S. Rai (2019), Effect of solution aging on properties of spin coated zinc oxide thin films, *Mater Today Proce.* **46**: 56-61.
- K. Kajihara (2013), Recent advances in sol-gel synthesis of monolithic silica and silica-based glasses, *Journal of Asian Ceram. Soc.* **1**: 121–133.
- Kumara Raja Kandula, Anirban Sarkar, and B N Shivakiran Bhaktha (2013), Sol-gel fabrication and characterization of ZnO and Zn<sub>2</sub>SiO<sub>4</sub> nanoparticles embedded silica glass-ceramic waveguides, *Optical Materials Express*, **3**: 2078-2085.
- L.T.T. Hiena, N. Van Dub, N.N. Hab, N.D. Hoab, T.N. Khiemb, N.D. Chiena (2019), Optical Materials Photoluminescence enhancement OF Er<sup>3+</sup>-doped ZnO/SiO<sub>2</sub> nanocomposites fabricated through two-step synthesis, *Opt. Mater.* **92**: 262–266.
- M. Faraz, F.K. Naqvi, M. Shakir, and N. Khare (2018), Synthesis of samarium-doped zinc oxide nanoparticles with improved photocatalytic performance and recyclability under visible light irradiation, *New Journal of Chemistry*, **42**: 2295–2305.
- M. Gugu Hlengiwe, Luminescence Investigation of Trivalent Rare Earth Ions in Sol-Gel Derived SiO<sub>2</sub> and ZnO co-doped SiO<sub>2</sub>:Pr<sup>3+</sup>, University of Free State, 2011.
- M. Novotny, E. Maresova, P. Fitl, J. Vlcek, M. Bergmann, M. Vondracek,, R. Yatskiv, J. Bulr, P. Hubk, P. Hruska, Drahokoupil, N. Abdellaoui, M. Vrnata, J. Lancok (2016), The properties of samarium-doped zinc oxide/phthalocyanine structure for optoelectronics prepared by pulsed laser deposition and organic molecular evaporation, *App. Phys A*, **122**: 1–8.
- M. Vishwas, B.R. Nagabushana, D. Joseph, K.V.A. Gowda, and S.B. Gandla (2022), Low temperature combustion synthesis and characterization of undoped and samarium doped zinc oxide nanoparticles, *J. Adv. Sci. Res*, **13**: 37–40.
- M. Xiaoqi, L. Lianqiang, Z. Kaishun, L. Juncheng (2014), The effect of SiO<sub>2</sub> on TiO<sub>2</sub> up-conversion photoluminescence film, *Opt. Mater.* **37**: 367–370.
- N. Dehingia, P. Gogoi, D. Kakoti, N. Rajkonwar, A. Boruah, P. Dutta (2020), Effect of Ag nanoparticles on the Judd–Ofelt and radiative parameters of Sm<sup>3+</sup> ions



- in sol–gel silica matrix, *Journal of Luminescence*, **226**: 117414.
- N.C.S. Selvam, A. Manikandan, L. John Kennedy, and J. Judith Vijaya (2013), Comparative investigation of zirconium oxide ( $\text{ZrO}_2$ ) nano and microstructures for structural, optical and photocatalytic properties, *J. Colloid Inter. Sci.* **389**: 91-98.
- N.M. Shamhari, B.S. Wee, S.F. Chin, K.Y. Kok (2018), Synthesis and characterization of zinc oxide nanoparticles with small particle size distribution. *Acta Chim. Slov.* **65** 578–585.
- N.Q. Vinh, N.N. Ha, T. Gregorkiewicz (2009), Photonic properties of Er-doped crystalline silicon, *Proc. IEEE*, **97**: 1269–1282.
- Nguyen Minh Ty, Dacheng Zhou, Jianbei Qiu, Ho Kim Dan (2020), Broadband flat near/mid-infrared emissions of  $\text{Tm}^{3+}$ – $\text{Ho}^{3+}$  co-doped, and  $\text{Tm}^{3+}$ – $\text{Ho}^{3+}$ – $\text{Yb}^{3+}$  tri-doped zinc silicate glasses under 808 and 980 nm laser diode excitations, *Infrared Physics & Technology*, **111**: 103483.
- Nivaldo Freire de Andrade Neto, Raquel Guilherme de Carvalho, Laurenia Martins Pereira Garcia, Rubens Maribondo Nascimento, Carlos Alberto Paskocimas, Elson Longo, Mauricio Roberto Bomio Delmonte, Fabiana Villela da Motta (2019), Influence of doping with  $\text{Sm}^{3+}$  on photocatalytic reuse of ZnO thin films obtained by spin coating, *Revista Mater.* **24**: 678-684.
- P.P. Murmu, J. Kennedy, G.V.M. Williams, B.J. Ruck, S. Granville, S.V. Chong (2012), Observation of magnetism, low resistivity, and magnetoresistance in the near-surface region of Gd implanted ZnO, *Applied Physics Letters*, **101**: 082408.
- R. John and R. Rajakumari (2012), Synthesis and characterization of rare earth ion doped nano ZnO, *Nanomicro Lett*, **4**: 65–72.
- Rittwick Mondal, Dipankar Biswas, Anindya Sundar Das, R.K. Nanao Ningthemcha, Debalina Deb, Subhratanu Bhattacharya, Soumyajyoti Kabi (2020), Influence of samarium content on structural, thermal, linear and non-linear optical properties of  $\text{ZnO}$ – $\text{TeO}_2$ – $\text{P}_2\text{O}_5$  glasses, *Mater Chem. Phys.* **255**: 932-938.
- S. Berneschi, A. Chiappini, M. Ferrari, S. Pelli, G.C. Righini (2011), Erbium doped

- silica-hafnia glass ceramic waveguides, *Phys. Status Solid*, **8**: 2875–2879.
- S. Talam, S.R. Karumuri, N. Gunnam (2012), Synthesis, Characterization, and Spectroscopic Properties of ZnO Nanoparticles, *ISRN Nanotech.* **2012**: 1–6.
- T. Kakkar, N. Bamiedakis, T.T. Fernandez, Z. Zhao, M. Irannejad, P. Steenson, A. Jha, R. Penty, I. White, G. Jose (2014), Glass–polymer super lattice for integrated optics, *Opt. Eng.* **53**: 071818.
- T.T.V. Tran, T.M.D. Cao, Q.V. Lam, V.H. Le (2017), Emission of  $\text{Eu}^{3+}$  in  $\text{SiO}_2\text{-ZnO}$  glass and  $\text{SiO}_2\text{-SnO}_2$  glass-ceramic: correlation between structure and optical properties of  $\text{Eu}^{3+}$  ions, *J. Non Cryst. Solids*, **459**: 57–62.
- U. Alam, A. Khan, D. Ali, D. Bahnemann, and M. Muneer (2018), Comparative photocatalytic activity of sol-gel derived rare earth metal (La, Nd, Sm and Dy)-doped ZnO photocatalysts for degradation of dyes, *RSC Adv.* **8**: 17582–17594.
- V. Kumar, O.M. Ntwaeaborwa, T. Soga, V. Dutta, H.C. Swart (2017), Rare earth doped zinc oxide nanophosphor powder: a future material for solid state lighting and solar cells, *ACS Photonics*, **4**: 2613–2637.
- X. Sun (2020), Preparation of  $\text{MgF}_2/\text{SiO}_2$  coating with broadband antireflective coating by using sol–gel combined with electron beam evaporation, *Opt. Mater.* **101**: 2–10.
- Y. Hanifehpour, B. Soltani, A. R. Amani-Ghadim, B. Hedayati, B. Khomami, and S. W. Joo (2016), Synthesis and characterization of samarium-doped ZnS nanoparticles: A novel visible light responsive photocatalyst, *Mater Res Bull.* **76**: 411–421.
- Z. Fu, B. Yang, L. Li, W. Dong, C. Jia, and W. Wu (2003), An intense ultraviolet photoluminescence in sol–gel ZnO– $\text{SiO}_2$  nanocomposites, *J. Phys. Condens. Matter*, **15(17)**: 2867–2873.

## CHAPTER 4

### INVESTIGATION ON $\text{Eu}^{3+}$ DOPED ( $\text{Al}_2\text{O}_3$ and $\text{TiO}_2$ ) IN SILICATE MATRIX

---

#### **4.1. Structural and Spectroscopic properties of $\text{Eu}^{3+}$ ions in alumino-silicate glass**

##### **Overview**

The structural, and optical properties of the  $\text{Eu}^{3+}$  ion in alumino-silicate  $35\text{Al}(\text{NO}_3)_3$ : (65-x)  $\text{SiO}_2$  glass (x = 0.75, 2.0, and 4.0 mol%) were investigated. X-ray diffraction proved that the present glasses are amorphous. FTIR spectral analysis was used to determine which functional groups were present at specific annealing temperatures. The PL spectra with different  $\text{Eu}^{3+}$  concentrations are recorded with excitation wavelength 370 nm have been recorded at room temperature (RT). The PL spectra showed the ( $^5\text{D}_0 \rightarrow ^7\text{F}_J$ ;  $J = 0, \dots, 4$ ) transitions of  $\text{Eu}^{3+}$  in the prepared glasses. The rise in  $\text{Eu}^{3+}$  ions in the host matrix was the explanation for the concentration quenching behaviour that was also seen. To ensure the dominant emission of the present glasses, the PL spectra were characterized using the CIE 1931 chromaticity diagram, and the results were discussed and reported in detail.

##### **4.1.1. Introduction**

Glasses are ideal systems for photonic devices the study of their optical properties is an essential part of photonic devices. Rare-Earth (RE) ions doped in various host materials have been extensively studied over the years due to their potential in optoelectronics, bio-photonics, optical memory, and other fields (Arai *et al.*, 1986, Wang *et al.*, 1993). There are many advantages to silica glass as a host for RE ions, these application-oriented studies of materials need optimized performance, which is hindered by the quenching mechanism. To avoid this quenching mechanism, effective dispersion of RE ions in the host is necessary. This dispersion of RE ions in silicate glass hosts is possible through the codoping of different metals and semiconductors such as  $\text{Al}_2\text{O}_3$ , etc. in the host lattice (Lochhead *et al.*, 1995, Stone *et al.*, 1996, Tanabe *et al.*, 1996, Chiasera *et al.*, 2003). The formation of NBO (such as Al–O–RE (Monteil *et al.*, 2004, etc.) helps partition RE ions rather than

clustering and forming RE–O–RE bonds (Alombert *et al.*, 2005). The optical and physical properties of  $\text{Eu}^{3+}$ -doped silica glass by the sol-gel method have been extensively studied to study optical and physical properties in various hosts such as glass, powders, crystals, and so on (Hench *et al.*, 1990, Brinker *et al.*, 1990, Collings *et al.*, 1994, Hreniak *et al.*, 2002). Among these hosts, glass has gained lucrative interest due to its immediate device applicability (Rai *et al.*, 2015). The spectroscopic properties of RE ions are host independent due to their outermost shielding, although the phonon energy of a host is regarded as a deciding factor for optical performance (Fan *et al.*, 1996). The sol-gel technique is one of the preferable methods to prepare inorganic oxides and glasses of high purity and homogeneity for various optoelectronic and photonic applications due to its advantages of low-temperature processing, homogeneity, and low cost (Martinez *et al.*, 2011). Theoretical and experimental work has been done on the spectroscopic properties of  $\text{Eu}^{3+}$  ions in the glass system (Swapna *et al.*, 2014). The  $\text{Eu}^{3+}$  ion has the ground state  $J = 0$ , which induces a special restriction on the induced electric-dipole (ED) transitions originating from the ground state (Wong *et al.*, 2014) and also has quite different luminescent intensities depending upon different symmetry sites (Lee *et al.*, 2007). Eu is widely utilized in commercial red luminous phosphors and is doped in silica glass. The electrons at the  $^5\text{D}_0 \rightarrow ^7\text{F}_2$  level's electric dipole transitions are what give the color red. It is hypersensitive to a local symmetry, in other words, lattice plays an important role in its PL, thus making  $\text{Eu}^{3+}$  an ideal candidate to investigate the dependence of glass compositions on luminescence characteristics.

#### 4.1.2. Experimental Details

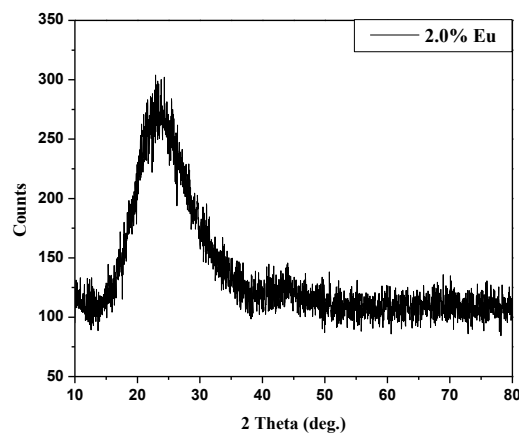
The glasses containing  $\text{Eu}^{3+}$  in  $(65-x) \text{SiO}_2:35\text{Al}(\text{NO}_3)_3:x\text{Eu}_2\text{O}_3$  (where  $x = 0.75, 2.0, \text{ or } 4.0 \text{ mol\%}$ ) were made using a sol-gel technique. Methanol is used as a solvent, Nitric acid ( $\text{HNO}_3$ ) as the catalyst, and Tetraethylorthosilicate (TEOS) is used as the main precursor.  $\text{Eu}_2\text{O}_3$  is used as the source for  $\text{Eu}^{3+}$  ions. The dopant is mixed with banana trunk sap, methanol, and nitric acid. The solution is stirred for 40 min. To this solution, TEOS is added and further stirred for 2 hours using a magnetic stirrer to form a sol. The molar ratio of TEOS, nitric acid, banana trunk sap, and

methanol is 16:4:10:70. The resulting sol is then poured into a plastic container, sealed, and kept from evaporating. Pinholes are made in the lid of a plastic container to allow for slow evaporation after the sol has solidified into a gel after being sealed at room temperature for 24 days. The container is then left for a few weeks. The gels are further dried by slowly heating to 50 °C and then annealing up to 1050 °C at a heating rate of 1 °C/min in an electric muffle furnace to create dense glass samples in the form of discs. The Abbe refractometer method was used to calculate the refractive index.

### 4.1.3. Results and discussion

#### 4.1.3.1. XRD spectra

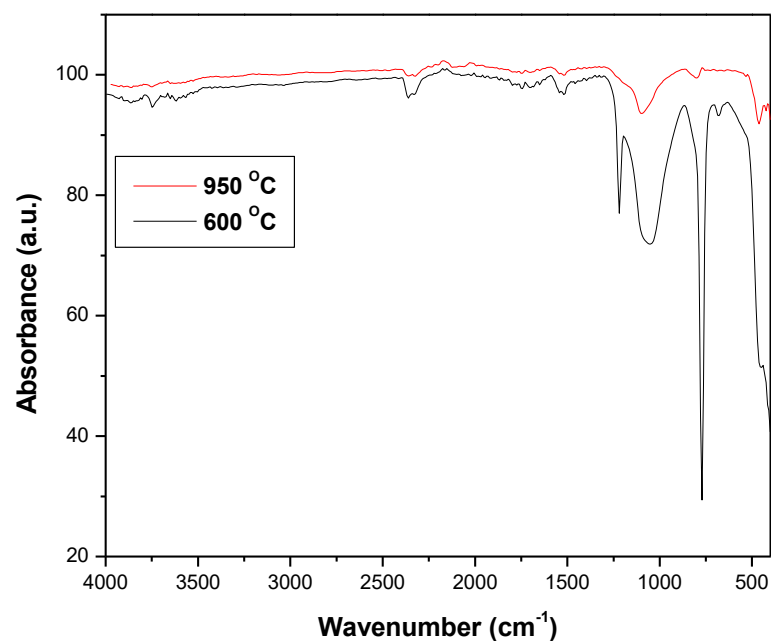
Fig. 4.1.1 shows the (2.0 mol%)Eu<sup>3+</sup> ions co-doped alumino-silicate glass' powdered XRD spectrum after being annealed at 900 °C. The distinct broad hollow peaks around  $2\theta = 22^\circ$  are observed rather than intense crystalline peaks with a crystallinity index of more than 39%, which established the glassy amorphous nature of the prepared sample (Wang *et al.*, 1997).



**Fig. 4.1.1:** XRD spectra of (2.0 mol%)Eu<sup>3+</sup>-doped Al in silicate glass annealed at 900 °C.

#### 4.1.3.2. FTIR spectra

Fig. 4.1.2 shows the FTIR spectra of the co-doped (2.0 mol%)Eu<sup>3+</sup> ions in aluminum-silicate glass that were annealed at 600 °C and 950 °C, respectively. These spectra were recorded in the 400–4000 cm<sup>-1</sup> range. The various peak positions and vibrations assigned are shown in Table 1. The samples in the gel stage have a lot of H<sub>2</sub>O and other organics. The slow heating of the prepared sample in an electric muffle furnace leads to the gradual reduction of various compounds from the gel matrix and contributes to the formation of a rigid glassy network. Due to the polymerization process of symmetric stretching of Si-O-Si or vibrational modes of the ring structure, respectively, a weak band at around 772 cm<sup>-1</sup> is observed for the gel annealed at 600 °C. A sensitive peak around 1215 cm<sup>-1</sup> is owing to vibrations of TEOS, an ethoxy group. The Eu<sup>3+</sup> ions doped in the glass matrix contribute to the peaks at around 1042–1093 cm<sup>-1</sup>. The vibrations due to the deformation of the bonds of the H<sub>2</sub>O molecules are related to the peaks around 2365 cm<sup>-1</sup>. Si-O-Si bending modes are ascribed to the peaks about 678 cm<sup>-1</sup>. Then, the bending mode of H<sub>2</sub>O molecules is assigned to the other weak bands at about 3700–3748 cm<sup>-1</sup>. Thus, FTIR spectra of Eu<sup>3+</sup> doped in alumino-silicate glass confirm the invariance of the silica matrix structure with Eu<sup>3+</sup> doping and annealing temperature.



**Fig. 4.1.2:** FTIR spectra of glass co-doped with  $\text{Eu}^{3+}$  ions (2.0 mol%) at various annealing temperatures.

**Table 4.1.1**

The glass sample's FTIR peak positions and various assignments.

Wavenumber ( $\text{cm}^{-1}$ )	Assignment	Observed intensity	Change in intensity during heating
444-452	Vibrations of asymmetric stretching in Si-O, O-Si-O stretching (Yan <i>et al.</i> , 2021)	Minor	A minor peak arises at 600 °C, Intense peak arises at 950 °C.

<b>686</b>	Vibration of asymmetric Si-O-Al bending with NBO (non-bridging oxygen) (Naveen et al., 2015)	Intense peak	At 600 °C, intense peaks appear, and they disappear at 950 °C.
<b>763-791</b>	Si-OH stretching (Yan <i>et al.</i> , 2021)	Strong	Decrease when the temperature rises
<b>1042-1093</b>	Si-O-Al, asymmetric stretching (Yan <i>et al.</i> , 2021)	Strong	Redshift, decrease in intensity
<b>1215</b>	C-O-C stretching vibration (Driss <i>et al.</i> , 2019)	Minor peak	Remove in T > 950 °C
<b>1525</b>	–OH bending vibration mode of water	Strong	At increasing temperatures peak will be decreased
<b>2365</b>	Deformation of the water molecules' bonds through vibrations (Umar <i>et al.</i> , 2017)	Minor peak	Decrease with increasing temperature
<b>3700-3748</b>	O-H stretching (Yan <i>et al.</i> , 2021)	Broad	In T > 950 °C, it is fully removed.



#### 4.1.3.3. Physical properties of Eu<sup>3+</sup> doped in Al-Si glass

Certain physical properties have been estimated from the measured glass densities, refractive index for all this Eu<sup>3+</sup> doped glasses. These values are presented in Table 4.1.2. These values are estimated using the approach outlined by (Dihingia *et al.*, 2012).

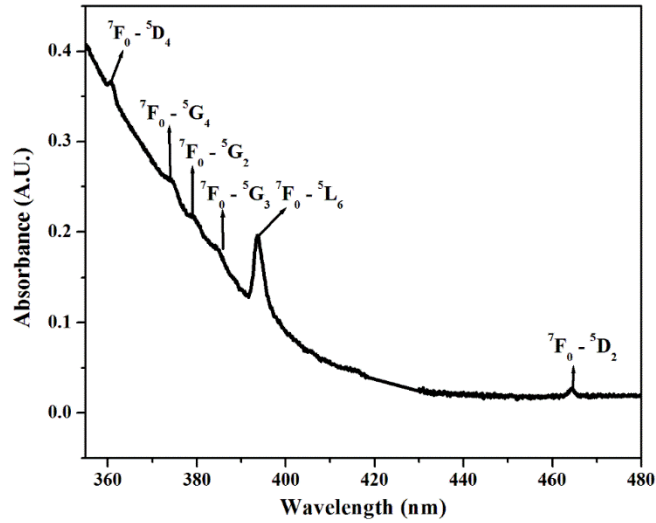
**Table 4.1.2**

Certain physical properties of Eu<sup>3+</sup> co-doped with Al in sol-gel SiO<sub>2</sub> glasses.

Physical properties	Eu (0.75%)	Eu (2.0%)	Eu (4.0%)
Refractive index (n)	1.643	1.647	1.649
Density ( $\rho$ ) (gcm <sup>-3</sup> )	2.102	2.204	2.301
Thickness (Z)	0.215	0.219	0.227
Average molecular weight M <sub>T</sub> (g)	75.82	77.66	80.58
Eu <sup>3+</sup> ions concentration (N <sub>i</sub> ) (x 10 <sup>20</sup> )	1.252	2.903	6.876
Dielectric constant ( $\epsilon$ )	2.699	2.713	2.719
Optical dielectric constant (P dt/dp)	1.699	1.713	1.719
Molar volume (V <sub>m</sub> ) (cm <sup>3</sup> /mol)	36.07	35.24	35.02
Reflection loss (R <sub>L</sub> )	0.059	0.060	0.060
Molar refraction (R <sub>M</sub> )	13.042	12.808	12.757
Energy gap (E <sub>g</sub> )	8.14	8.12	8.08
Polaron radius r <sub>p</sub> (Å)	8.05	6.09	4.57
Inter nuclear distance (r <sub>i</sub> ) (x10 <sup>-7</sup> cm <sup>-3</sup> )	2.93	2.21	1.66
Electronic polarizability ( $\alpha_e$ ) (x 10 <sup>21</sup> )	1.43	1.44	1.45
Field strength (F) (x 10 <sup>13</sup> cm <sup>-2</sup> )	3.318	5.905	10.869
Molar polarizability ( $\alpha_m$ )	5.175	5.083	5.062
Oxygen packing density (OPD)	36.151	35.782	33.561
Metallization criterion (M)	0.638	0.637	0.636

#### 4.1.3.4. Absorption spectra

Fig. 4.1.3 shows the absorption spectra of  $\text{Eu}^{3+}$  ions in  $\text{SiO}_2$  sol-gel glass with fixed aluminium. In the UV-VIS range (355-480 nm), absorption bands resolved correspond to the transitions  $^7\text{F}_0 \rightarrow ^5\text{D}_4$  (362 nm),  $^7\text{F}_0 \rightarrow ^5\text{G}_4$  (375 nm),  $^7\text{F}_0 \rightarrow ^5\text{G}_2$  (379 nm),  $^7\text{F}_0 \rightarrow ^5\text{G}_3$  (385 nm),  $^7\text{F}_0 \rightarrow ^5\text{L}_6$  (394 nm), and  $^7\text{F}_0 \rightarrow ^5\text{D}_2$  (465 nm). The data of Carnal *et al.*, is used to assign all above peaks (Carnall *et al.*, 1968). The  $^7\text{F}_0 \rightarrow ^5\text{D}_2$  induced electric-dipole transition is hypersensitive in nature and is known to exhibit wide variation in its band intensity (Hazarika *et al.*, 2004). The strongest absorption band in the glass is the transition band between  $^7\text{F}_0 \rightarrow ^5\text{L}_6$ . The transition ( $^7\text{F}_0 \rightarrow ^5\text{L}_6$ ) is allowed by the  $\Delta J$  rule even if it is prohibited by the  $\Delta S$  and  $\Delta L$  selection rules.

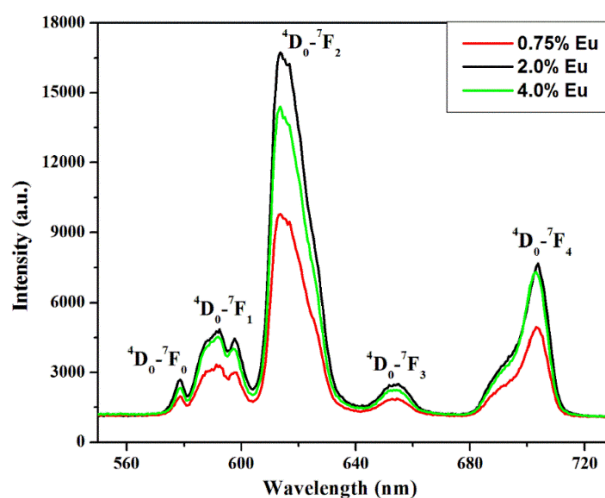


**Fig. 4.1.3:** Absorption spectra of (2.0 mol%) $\text{Eu}^{3+}$  ions co-doped with Al sol-gel silica glasses.

#### 4.1.3.5. Photoluminescence spectra

The PL spectra of the  $\text{Eu}^{3+}$  (0.75, 2.0, and 4.0 mol%) ions co-doped with a fixed aluminium concentration in sol-gel silica glasses are shown in Fig. 4.1.4. A 370 nm source is used to excite the  $\text{Eu}^{3+}$  ions from their ground state of  $^7\text{F}_0$  to their excited state of  $^5\text{D}_2$ . The emission spectra consist of five groups of emission bands at around 578, 592, 614, 654, and 703 nm, which result from the transitions  $^5\text{D}_0 \rightarrow ^7\text{F}_J$  ( $J = 0, 1, 2, 3$ , and  $4$ ), respectively (You *et al.*, 2004). Fluorescence intensity varies with concentrations of  $\text{Eu}^{3+}$ , the fluorescence intensity is maximum for 2 mol% of  $\text{Eu}^{3+}$ . But it decreases at high concentration 4 mol%. It indicates that the formation of clusters at higher concentrations of  $\text{Eu}^{3+}$ , due to which fluorescence quenching occurs.

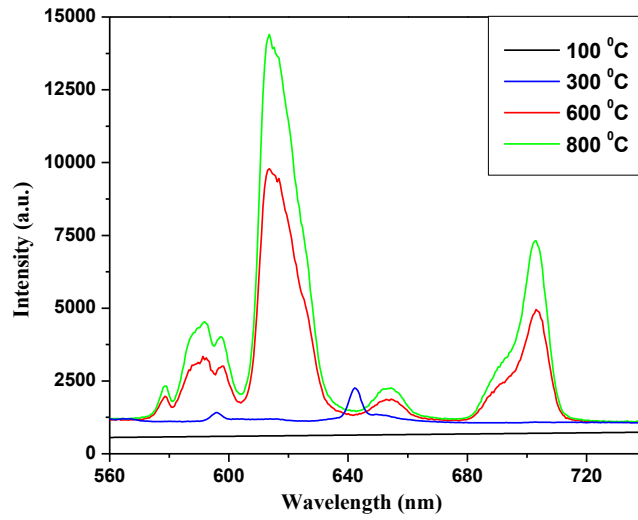
The line emissions in the spectra correspond to  $^5\text{D}_0 \rightarrow ^7\text{F}_0$  (578 nm),  $^5\text{D}_0 \rightarrow ^7\text{F}_1$  (592 nm),  $^5\text{D}_0 \rightarrow ^7\text{F}_2$  (614 nm),  $^5\text{D}_0 \rightarrow ^7\text{F}_3$  (654 nm) and  $^5\text{D}_0 \rightarrow ^7\text{F}_4$  (703 nm) transitions of  $\text{Eu}^{3+}$  ions (You *et al.*, 2004, Manju *et al.*, 2020, Binnemans *et al.*, 2015). Because there is no crystal field splitting at the  $^5\text{D}_0$  and  $^5\text{F}_0$  levels, the  $^5\text{D}_0 \rightarrow ^7\text{F}_0$  transition is also useful for determining the bonding environment of the  $\text{Eu}^{3+}$  ions. All of the glass samples with various amounts of  $\text{Eu}^{3+}$  had a relatively low peak at 578 nm. The  $^5\text{D}_0 \rightarrow ^7\text{F}_2$  is an electric dipole allowed transition and its intensity is hypersensitive to the variation of the bonding environment of the  $\text{Eu}^{3+}$  ions, while  $^5\text{D}_0 \rightarrow ^7\text{F}_1$  is a magnetic dipole allowed transition and its intensity hardly varies with the bonding environment of the  $\text{Eu}^{3+}$  ions (Chang *et al.*, 2017, Irena *et al.*, 2018). The strong emission peak at 614 nm is shown in Fig. 4, which can be attributed to the hypersensitive ED transition. It is established that the  $\text{Eu}^{3+}$  ion is located at low-symmetry sites because the intensity of emission of the ED transition is significantly higher than intensity of the MD transition. With the increase in  $\text{Eu}^{3+}$  ions concentrations, a relative change in the intensities of the emission peaks is also seen.



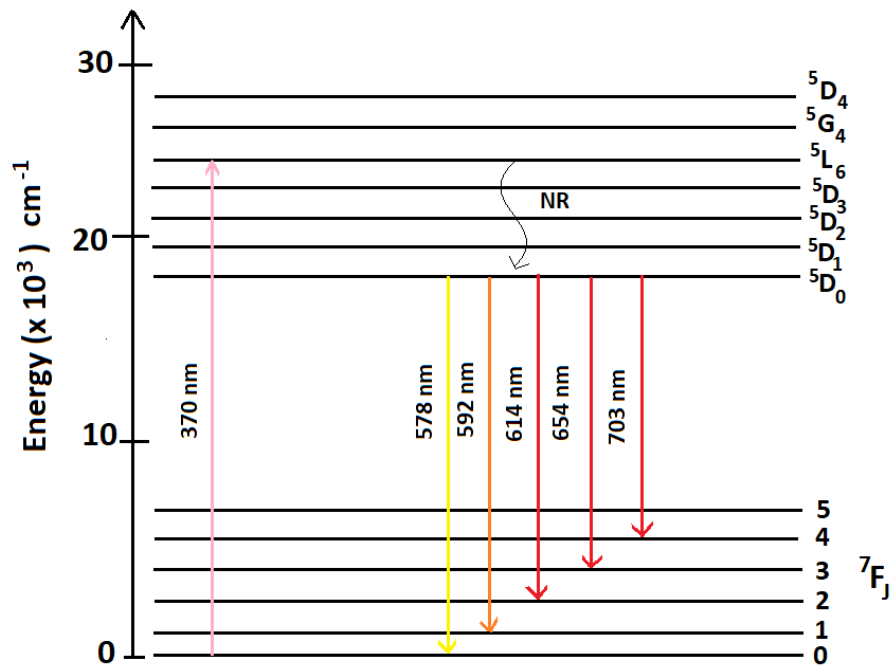
**Fig. 4.1.4:** PL spectra of  $\text{Eu}^{3+}$  ions co-doped with Al sol-gel silica glasses.

#### 4.1.3.6. Annealing temperature's effect on PL spectrum

The PL spectra of  $\text{Eu}^{3+}$  (2.0 mol %) ions co-doped with a fixed aluminium concentration in sol-gel silica glasses were annealed at different annealing temperatures (100, 300, 600, and 800 °C) as shown in Fig. 4.1.5. The sample quenched by the hydroxyl (OH) group exhibits very little intensity after being annealed at 100–300 °C. The PL of  $\text{Eu}^{3+}$  ions has been quenched by the high phonon energy of the OH group. In silica xerogel, energy release and transfer to the  $\text{Eu}^{3+}$  ions is suppressed by the generation of electrons and holes from the recombination of defects. For higher temperatures were used to anneal the sample, the rise of asymmetry caused by the growth of NBO (Si-O-Al), which has a lower phonon energy than the vibration of the Si-O-Si bond, contributes to PL enhancement. This is already confirmed from recorded FTIR spectra. Thus, the PL intensity increases for dense glasses that are annealed at higher temperatures after the OH group is removed (Fig. 4.1.5). As a result, PL enhancement is successfully accomplished by asymmetry in the host matrix and OH group removal at a high annealing temperature.



**Fig. 4.1.5:** Effect of annealing temperature on PL intensity. (Note: PL intensities of samples annealed to 100 °C and 300 °C are magnified to 100 and 10 times for clarification).



**Fig. 4.1.6:** Energy diagram of co-doped Eu<sup>3+</sup> and Al ions in a silica host schematic.

#### 4.1.3.7. Judd-Ofelt and Radiative parameters

According to the Judd-Ofelt theory [Judd, 1962, Ofelt, 1962], the radiative transitions belonging to the  $4f^2$  configuration of  $\text{Eu}^{3+}$  can be analyzed based on the absorption spectra of  $\text{Eu}^{3+}$  (Fig. 4.1.3). The Judd-Ofelt intensity parameters  $\Omega_t$  ( $t = 2, 4$ , and  $6$ ) for (2.0 mol%) $\text{Eu}^{3+}$ -doped with fixed aluminium in sol-gel silicate glass sample are derived by a least square fitting of oscillator strength derived from experiment ( $f_{\text{exp}}$ ) and calculation ( $f_{\text{cal}}$ ) oscillator strength using as obtained squared matrix elements (Table 4.1.3) (Carnal *et al.*, 1968, Carnall *et al.*, 1978). The large value of  $\Omega_4$  reasonably specifies the existence of covalent bonding among  $\text{Eu}^{3+}$  ions and other two metals in host [Eu-O, Eu-Al] (Dejneka *et al.*, 1995, Hazarika *et al.*, 2002). Here  $\Omega_2$  is extremely structure sensitive and association with the symmetry and covalency of the  $\text{Eu}^{3+}$  ions neighborhood (Vijayakumar *et al.*, 2015). The values of  $\Omega_4$  and  $\Omega_6$  are decided by the viscosity and dielectric properties of the media (glass) and induce vibronic transition due to the bond between  $\text{Eu}^{3+}$  ions and the ligand atoms (Khan *et al.*, 2018). The spectroscopic quality ( $\Omega_4/\Omega_6$ ) is significant in foreseeing the stimulation of emission for the laser active host (Agarwal *et al.*, 2009). Table 4.1.4 shows the comparisons of the JO intensity parameters of  $\text{Eu}^{3+}$  doped glasses. The estimation of radiative properties such as spontaneous emission probabilities ( $A_{\text{rad}}$ ), luminescence branching ratios ( $\beta$ ), and radiative lifetime ( $\tau_{\text{rad}}$ ) for the optical transitions of (2.0 mol%) $\text{Eu}^{3+}$ -doped with fixed aluminium in sol-gel silicate glass, have been estimated using J-O intensity parameters in Table 4.1.5 (Babu *et al.*, 2000).

**Table 4.1.3**Judd-Ofelt intensity parameters and oscillator strengths of  $\text{Eu}^{3+}$  ion.

Transitions	Energy (in $\text{cm}^{-1}$ )	Wavelength (in nm)	$f_{\text{exp}}$ ( $\times 10^{-6}$ )	$f_{\text{cal}}$ ( $\times 10^{-6}$ )
${}^7\text{F}_0 \rightarrow {}^5\text{D}_4$	27624	362	0.121	0.183
${}^7\text{F}_0 \rightarrow {}^5\text{G}_4$	26667	375	0.214	0.113
${}^7\text{F}_0 \rightarrow {}^5\text{G}_2$	26385	379	0.087	0.093
${}^7\text{F}_0 \rightarrow {}^5\text{G}_3$	25974	385	0.072	0
${}^7\text{F}_0 \rightarrow {}^5\text{L}_6$	25381	394	1.173	1.173
${}^7\text{F}_0 \rightarrow {}^5\text{D}_2$	21505	465	0.107	0.101
$\Omega_2 = 3.346 \pm 0.031$ ( $\times 10^{-20} \text{ cm}^2$ )				
$\Omega_4 = 3.428 \pm 0.01$ ( $\times 10^{-20} \text{ cm}^2$ )				
$\Omega_6 = 1.695 \pm 0.046$ ( $\times 10^{-20} \text{ cm}^2$ )				
$\Omega_4 / \Omega_6 = 2.022 \pm 0.063$ ( $\times 10^{-20}$ )				

**Table 4.1.4**

Comparison of calculated Judd-Ofelt intensity parameters.

$\Omega_2$	$\Omega_4$	$\Omega_6$	$\Omega_4/\Omega_6$	References
3.346	3.428	1.695	2.022	Present work
0.64	4.87	2.84	1.71	ZBLA (Dejneka <i>et al.</i> , 1995)
5.44	4.44	5.38	0.83	L5FBE (Babu <i>et al.</i> , 2000)
11.62	-	2.82	-	L4BE (Babu <i>et al.</i> , 2000)
5.61	3.47	2.91	1.19	Al(NO <sub>3</sub> ) <sub>3</sub> -SiO <sub>2</sub> (Rai <i>et al.</i> , 2004)
6.36	3.94	0.51	7.73	KMgSi (Nageno <i>et al.</i> , 1994)
5.47	1.55	1.07	1.45	BaO (Tripathi <i>et al.</i> , 2006)

**Table 4.1.5**

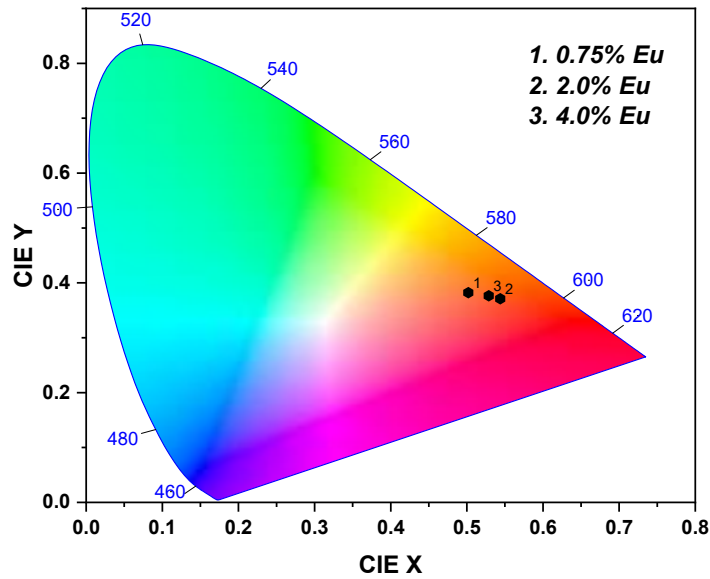
Radiative properties of Eu<sup>3+</sup> (2.0 mol%) co-doped with fixed aluminium in sol-gel SiO<sub>2</sub> glasses.

Transitions	Energy (in cm <sup>-1</sup> )	A <sub>ed</sub> (in s <sup>-1</sup> )	β <sub>r</sub> (in %)	λ <sub>eff</sub> (nm)	σ <sub>P</sub> (x 10 <sup>-22</sup> cm <sup>2</sup> )
<sup>5</sup> D <sub>0</sub> → <sup>7</sup> F <sub>0</sub>	17301.038	0	0	2.075	0
<sup>5</sup> D <sub>0</sub> → <sup>7</sup> F <sub>1</sub>	16891.892	63.732	14.609	12.605	2.702
<sup>5</sup> D <sub>0</sub> → <sup>7</sup> F <sub>2</sub>	16286.645	271.157	62.156	14.410	11.638
<sup>5</sup> D <sub>0</sub> → <sup>7</sup> F <sub>3</sub>	15290.520	0	0	10.761	0
<sup>5</sup> D <sub>0</sub> → <sup>7</sup> F <sub>4</sub>	14244.751	101.362	23.235	13.085	8.233
		A <sub>T</sub> (s <sup>-1</sup> ) =	τ <sub>R</sub> = 2.292		
		436.251	(ms)		



#### 4.1.3.8. CIE Chromaticity

The sample's estimated color chromaticity coordinates, CIE X and CIE Y, are listed in Table 4.1.6. Color tunability of PL spectra from Orange to Red is evident with  $\text{Eu}^{3+}$  concentrations quenching occurs as shown in Fig. 4.1.7.



**Fig. 4.1.7:** CIE chromaticity diagram.

**Table 4.1.6**

CIE chromaticity coordinates of (0.75, 2.0, 4.0 mol%) $\text{Eu}^{3+}$ -doped Al in sol-gel silicate glasses.

Color	Eu (0.75 mol%)	Eu (2.0 mol%)	Eu (4.0 mol%)
Coordinates			
X	0.502	0.544	0.529
Y	0.382	0.371	0.377

#### 4.1.3.9. Non-Linear Properties of Eu<sup>3+</sup> doped in Al-Si glass

Certain non-linear properties have been estimated from optical parameters like the non-linear refractive index ( $n_2$ ), non-linear refractive index susceptibility ( $\chi^{e(3)}$ ), co-efficient ( $\gamma_{ce}$ ), and reasonably high Abbe number ( $v_{Ab}$ ) indicate the good optical quality of the sol-gel SiO<sub>2</sub> glass. These values are presented in Table 4.1.7. The values are estimated based on the procedure reported by (Dihingia *et al.*, 2012).

**Table 4.1.7**

Sol-gel alumino-silicate glass was doped with different nonlinear levels of Eu<sup>3+</sup> (2.0 mol%) and annealed at 950 °C.

$n_F$	$n_r$	$n_F - n_r$	$n_b$	$v_{Ab}$	$1/v_{Ab}$	$n_2$ (in $10^{-13}$ esu)	$\gamma_{ce}$ (in $cm^2/W$ )	$\omega_o \times 10^{-13}$	$N \times 10^{-16}$	$\chi^{e(3)} \times 10^{-6}$
1.628	1.616	0.012	1.622	51.833	0.019	1.834	0.473	113.238	1085.966	2.396

#### 4.1.4. CONCLUSION

The Sol-Gel method was used to successfully synthesis the Eu<sup>3+</sup> (0.75, 2.0, and 4.0 mol%) doped in the alumino-silicate glass. The transparent glass samples are of good optical quality. The XRD spectra confirmed that the glass samples were amorphous. The FTIR spectra analysis confirms the removal of the OH-group along with the formation of NBO. The PL spectral is confirmation of the utility of prepared materials in optoelectronic devices. The chromaticity diagram is evidence of color tunability at different Eu<sup>3+</sup> ion concentrations. Additionally, the high optical quality of the glass as well as its excellent third-order non-linear behaviour are confirmed by the physical and non-linear properties, such as the relatively high Abbe number ( $v_{Ab}$ ), low non-linear refractive index ( $n_2$ ), co-efficient ( $\gamma_{ce}$ ) and susceptibility ( $\chi^{e(3)}$ ) values

## Reference

- A. Agarwal, I. Pal, S. Sanghi, M.P. Aggarwal (2009), Judd–Ofelt parameters and radiative properties of  $\text{Sm}^{3+}$  ions doped zinc bismuth borate glasses, *Optical Materials*, **32**: 339–344.
- A. Chiasera, M. Montagna, R. Rolli (2003),  $\text{Er}^{3+}/\text{Yb}^{3+}$  Co-Activated Silica-Alumina Monolithic Xerogels, *J. Sol–Gel Sci. Technol.* **26**: 943–946.
- A. Monteil, S. Chaussedent, G.S. Alombert (2004), Clustering of rare earth in glasses, aluminum effect: experiments and modeling, *J. Non-Cryst. Solids*, **348**: 44–50.
- B.C. Collings and A.J. Silversmith (1994), Avalanche up-conversion in  $\text{LaF}_3$ :  $\text{Tm}^{3+}$ . *J. Lumin.* **62**: 271–279.
- B.R. Judd (1962), Optical absorption intensities of rare-earth ions, *Phys. Rev.* **127**: 750.
- B.T. Stone, K.L. Bray (1996), Fluorescence properties of  $\text{Er}^{3+}$ -doped sol-gel glasses, *J. Non-Cryst. Solids*, **197**: 136–144.
- N. Dehingia, S. Rai (2012), Synthesis of  $\text{TiO}_2$  nanoparticles and spectroscopic upconversion luminescence of  $\text{Nd}^{3+}$ -doped  $\text{TiO}_2$ – $\text{SiO}_2$  composite glass, *J. Lumin.* **132**: 1243–1251.
- C.J. Brinker and G.W. Scherer (1990), *Sol-Gel Science: The Physics and Chemistry of Sol-Gel Processing*. Academic Press, New York.
- D. Hreniak, M. Jasierski, K. Maruszewski, L. Kepinski, L. Krajczyk, J. Misiewicz and W. Strek (2002), Nature and optical behavior of heavily Europium-doped silica glasses obtained by sol-gel method, *J. Non-Cryst. Solids*, **298**: 146–152.

- G. Tripathi G, V. K. Rai, and S. B. Rai (2006), Spectroscopic studies of  $\text{Eu}^{3+}$  doped calibo glass: Effect of the addition of barium carbonate, energy transfer in the presence of  $\text{Sm}^{3+}$ . *Optics Communications*, **264**: 116–122.
- G.G. Alombert, N. Gaumer, J. Obriot, and A. Rammal (2005), Aluminum effect on photoluminescence properties of sol–gel-derived  $\text{Eu}^{3+}$ -activated silicate glasses. *J. Non-Cryst. Sol.* **351**: 1754–1758.
- G.S. Ofelt (1962), Intensities of crystal spectra of rare-earth ions, *J. Chem. Phys.* **37**: 511.
- H. You and M. Nogam (2004), Optical properties and local structure of  $\text{Eu}^{3+}$  ions in sol-gel  $\text{TiO}_2\text{-SiO}_2$  glasses, *J. Phys. Chem. B*, **108**: 12003-12008.
- Irena Kostova, Georgi Patronov (2018), Dan Tonchev, Luminescent Properties of Rare Earthdoped $\text{ZnO-B}_2\text{O}_3\text{-P}_2\text{O}_5$  Glasses. *Journal of Chemical Technology and Metallurgy*, **53(6)**: 1087-1094.
- J. Wang, W.S. Brocklesby, J.R. Lincoln, J.E. Townsend, and D.N. Payne (1993), Local structures of rare-earth ions in glasses: the ‘crystal-chemistry’ approach, *J. Non-Cryst. Solids*, **163**: 261-267.
- J.R. Martinez, E. Erika (2011), Effect of Aging in the Structure of Silica Xerogels with Incorporation of Extract’s Leaves. *New J. of Glass and Ceram.* **1**: 7-12.
- K. Arai, H. Namikawa, K. Kumata, T. Honda, Y. Ishii, T. Handa (1986), Aluminum or phosphorus co-doping effects on the fluorescence and structural properties of neodymium-doped silica glass, *J. Appl. Phys.* **59**: 3430.
- K. Binnemans (2015), Interpretation of europium (III) spectra. Co-ord. *Chem. Rev.* **295**: 1–45.
- K. Swapna, S.K. Mahamuda (2014), Visible luminescence characteristics of  $\text{Sm}^{3+}$  doped Zinc Alumino Bismuth Borate glasses, *J. Lumin.* **146**: 288–294.
- K.V. Naveen, L. Vijayalakshmi, Y.C. Ratnakaram (2015), Energy transfer based

photoluminescence properties of ( $\text{Sm}^{3+}+\text{Eu}^{3+}$ ): PEO + PVP polymer films for Red luminescent display device applications, *Optical Materials*, **45**: 148–155.

L.L. Hench, J.K. West (1990), The sol-gel process. *Chem. Rev.* **90**: 33-72.

Lahcene Driss, Asmaa Behilil, Brahim Zahraoui (2019), Physicochemical characterization of new natural clay from south west of Algeria: Application to the elimination of malachite green dye, *Environmental Progress & Sustainable Energy*, **38(4)**: 1-5.

M. Chang, Y. Son, Y. Sheng, J. Chen and H. Zou (2017), Understanding the Remarkable Luminescence Enhancement: Via  $\text{SiO}_2$  Coating on  $\text{TiO}_2:\text{Eu}^{3+}$  Nanofibers, *Phys. Chem. Chem. Phys.* **19(26)**: 17063–17074.

M. Dejneka, E. Snitzer, R.E. Riman (1995), Blue, green and red fluorescence and energy transfer of  $\text{Eu}^{3+}$  fluoride in glasses, *J. Lumin.* **65**: 227.

M. Vijayakumar, K. Marimuthu, V. Sudarsan (2015), Concentration dependent spectroscopic behavior of  $\text{Sm}^{3+}$  doped leadfluoro-borophosphate glasses for laser and LED applications, *J. Alloys and Comp*, **647**: 209-220.

M.J. Lochhead, K.L. Bray (1995), Rare-Earth Clustering and Aluminum Co-doping in Sol-Gel Silica: Investigation Using Europium (III) Fluorescence Spectroscopy, *Chem. Mater.* **7**: 572-577.

P. Babu, C.K. Jayasankar (2000), Optical spectroscopy of  $\text{Eu}^{3+}$  ions in lithium borate and lithium fluoroborate glasses *Physic. B*, **279**: 262.

P.S. Wong, M.H. Wan (2014), Structural and luminescence studies of Europium ions in lithium aluminium borophosphate glasses, *J. Rare Earths*, **32**: 585-592.

R.J. ManjuGopinath, S. Gopi, S.M. Simon, A.C. Saritha, P.R. Biju, Cyriac Joseph and N.V. Unnikrishnan (2020), Spectroscopic analysis of  $\text{Eu}^{3+}$  doped silica–titania polydimethylsiloxane hybrid ORMOSILs. *RSC Adv.* **10**: 20057-20066.

S. Hazarika and S. Rai (2004), Structural, optical and non-linear investigation of  $\text{Eu}^{3+}$  ions in sol-gel silicate glass, *Optical Materials*, **27**: 173-179.

- S. Hazarika, S. Rai (2002), In: Proc. of Sixth International Conference on Optoelectronics, *Fibre Optics and Photonics*, **4**: 16–18.
- S. Hazarika, S. Rai (2004), Structural, optical and non-linear investigation of  $\text{Eu}^{3+}$  ions in sol–gel silicate glass, *Optical Materials*, **27**: 173–179.
- S. Rai and A.L. Fanai (2015), Optical spectroscopic properties of  $\text{Nd}^{3+}$  ions in aluminum glass matrix. National Laser Symposium (NLS-24), RRCAT, Indore.
- S.A. Umar, M.K. Halimah, K.T. Chan, A.A. Latif (2017), Polarizability, optical basicity and electric susceptibility of  $\text{Er}^{3+}$  doped silicate borotellurite glasses, *J. Cryst. Solids*, **471**: 101-109.
- S.H. Lee, P. Du, L.K. Bharat and J.S. Yu (2017), Ultraviolet radiation excited strong red-emitting  $\text{LaAlO}_3:\text{Eu}^{3+}$  nanophosphors: synthesis and luminescent properties. *Ceramics International*, **43**: 4599-4605.
- S.S. Wang, Y. Zhou, Y.L. Lam, C.H. Kam, Y.C. Chan, X. Tao (1997), Fabrication and characterization of neodymium-doped silica glass by sol-gel process, *Mat Res Innovat*, **1**: 92-96.
- Tanabe S, Hanada T (1996), Local structure and 1.5  $\mu\text{m}$  quantum efficiency of erbium doped glasses for optical amplifiers, *J. Non-Cryst. Solids*, **196**: 101-105.
- Uzair Khan, A.L. Fanai, S. Rai (2018), Optical properties of holmium-doped in sol-gel silica glass, *Advances in Engineering Research*, **178**: 194-197.
- W.T. Carnal, P.R. Fields, K. Rajnak (1968), Electronic Energy Levels of the Trivalent Lanthanide Aquo Ions. IV.  $\text{Eu}^{3+}$ , *J. Chem. Phys.* **49**: 4450–4455.
- W.T. Carnall, H. Crosswhite and H.M. Crosswhite (1978), Energy level structure and transition probabilities in the spectra of the trivalent lanthanides in  $\text{LaF}_3$ , Argonne National Laboratory, Report no. ANL-78-XX-95.
- W.T. Carnall, P.R. Fields and K.J. Rajnak (1968), Electronic Energy Levels in the Trivalent Lanthanide Aquo Ions. I.  $\text{Pr}^{3+}$ ,  $\text{Nd}^{3+}$ ,  $\text{Pm}^{3+}$ ,  $\text{Sm}^{3+}$ ,  $\text{Dy}^{3+}$ ,  $\text{Ho}^{3+}$ ,  $\text{Er}^{3+}$ , and  $\text{Tm}^{3+}$ , *Chem. Phys.* **59**: 4424-4432.
- X. Fan, M. Wang and G. Xiong (1996), Spectroscopic studies of RE ions in silica

glasses prepared by the sol-gel process, *Materials Letter*, **27**: 177-181.

Y. Nageno, H. Takebe, K. Morinaga, T. Inzumi (1994), Effect of modifier ions on fluorescence and absorption of  $\text{Eu}^{3+}$  in alkali and alkaline earth silicate glasses, *J. Non-Cryst. Solids*, **169**: 288.

Yan Jiao, Mengting Guo, Renle Wang, Chongyun Shao, and Lili Hu (2021), Influence of Al/Er ratio on the optical properties and structures of  $\text{Er}^{3+}/\text{Al}^{3+}$  co-doped silica glasses, *J. Appl. Phys.* **129**: 053104.

## **4.2. Structural and Spectroscopic properties of Eu<sup>3+</sup> doped SiO<sub>2</sub>-TiO<sub>2</sub> nanoparticles for photonic applications**

### **Overview**

The Eu<sup>3+</sup>-doped TiO<sub>2</sub> nanoparticles in sol gel silicate glasses of composition (80-x)SiO<sub>2</sub> + 20TiO<sub>2</sub> + 0.5xEu<sub>2</sub>O<sub>3</sub>, (SiTiEu) where x = 0.0, 0.5, 1.5, 2.5 and 3.5 mol%, have been prepared by sol-gel technique. The glass samples were investigated by thermogravimetric analysis (TGA/DTA), ATR-FTIR, XRD, SEM, TEM, EDX, optical absorption and photoluminescence emission spectroscopy at room temperature (RT). The absorption wavelength of TiO<sub>2</sub> doped sol-gel silicate glass were red shifted due to a reduction in band gap energy with increasing annealing temperatures. According to the TEM images, all of the particles were spherical and had an average diameter is around 10 nm. The visible spectra of the Eu<sup>3+</sup> doped TiO<sub>2</sub> nanoparticles in sol-gel silicate glasses displayed characteristic PL emission <sup>5</sup>D<sub>0</sub>→<sup>7</sup>F<sub>J</sub> (J=0, 1, 2, 3, 4, 5) transitions of Eu<sup>3+</sup> ions at 370 nm excitation. The anatase TiO<sub>2</sub>:1.5Eu<sup>3+</sup> nanocomposite showed high photoluminescence emission at 370 nm excitation, which was attributed to the f-f transitions of Eu<sup>3+</sup>. The hypersensitive <sup>5</sup>D<sub>0</sub>→<sup>7</sup>F<sub>2</sub> transition was responsible for the major red emission. From the recorded spectra, radiative parameters and Judd-Ofelt (JO) intensity parameters were computed. The Eu<sup>3+</sup> co-doped TiO<sub>2</sub> nanoparticles in sol-gel silicate glasses displayed emissions mostly in the red regions realized from a CIE chromaticity diagram. The results suggested that materials may be used as an optical material of technological importance such as display devices and also for optical amplifier.



#### 4.2.1. Introduction

In current technological quests, sol-gel process is extensively used to process material for optical device due to the benefits such as low temperature of processing, homogeneity of higher order and opportunity of manufacturing material with desired refractive indices. Silica based glasses activated by Rare-earth (RE) ions has seen a renaissance in the study for their possible application in the photonic devices, colors displays and optical communication fields. Among the RE,  $\text{Eu}^{3+}$  is one of the efficient ions (Carnall *et al.*, 1968). The host materials are considered as a very important factor during the development of RE ion doped optical device. In the last decade, an extensive investigation of optical properties of RE ions in various nano-structured materials has been performed. There has been a great significance in the study of size related effects pertaining to intensity of emission in different materials (Wrzyszczyk *et al.*, 2002). The sol-gel syntheses of novel materials have been extensively explored (Brinker *et al.*, 1990, Matsuura *et al.*, 2002) and is found to be effective technique to prepare luminophores as solids matrices of silica, titania and silica-titania oxides. It is convenient to dope rare-earth ions in such materials via the sol-gel method (Gaponenko *et al.*, 2001).

In last decade, the optical properties of RE ions doped in sol-gel glasses have induced a sizable importance due to the prospective implications arena of field sensor and laser, along with the role of amplifiers for fiber-optic communication, high frequency domain optical memory (Biswas *et al.*, 2003, Stone *et al.*, 1997, Nagami *et al.*, 2002). Among the various metal oxides, titania ( $\text{TiO}_2$ ) is rated to be one of the most lucrative materials due to its non-toxicity, long-term stability and low-cost. In the case of RE ion incorporated in titania nanocrystals, a unique optical properties could be tailored through size controlling as well as band-gap engineering, which is incredibly impressive in fabrication of a nano-device with technological utilities. A reasonably simple structure of  $\text{Eu}^{3+}$  energy level permits the absorption and emission spectra in the range of visible photons (You *et al.*, 2004).  $\text{Eu}^{3+}$  doped hosts are universally used in commercial luminescent phosphors of red color. This red color is initiated from the electric dipole (ED) transitions of an electron to the  $^7\text{F}_2$  level from the  $^5\text{D}_0$  level. It is hypersensitive to local symmetry (Anjaiah *et al.*, 2014). In other words, an important role is played by host in its photoluminescence, thus

making  $\text{Eu}^{3+}$  perfect contender to explore luminescent characteristics phosphor on glass composition.  $\text{Eu}^{3+}$  doped in variety of glasses like borate, phosphate, tellurite etc., have been studied over the years (Anjaiah *et al.*, 2014, Hegde *et al.*, 2017, Soltys *et al.*, 2015, Maheshvaran *et al.*, 2012), most of which are prepared by melt quenching. Silica glasses have some structural and chemical advantages but have extremely high melting point (Yamane *et al.*, 2001). Sol-gel technique (Bokatial *et al.*, 2012) allows the synthesis at relatively lower temperature with great control over the composition of the glass.

#### **4.2.2. Experimental Details**

The  $\text{Eu}^{3+}$ -doped  $\text{TiO}_2$  nanoparticles in sol gel silicate glasses of composition  $(80-x)\text{SiO}_2 + 20\text{TiO}_2 + 0.5x\text{Eu}_2\text{O}_3$ , ( $\text{SiTiEu}$ ) where  $x = 0.0, 0.5, 1.5, 2.5$  and  $3.5$  mol%, have been prepared by sol-gel technique. Tetraethyl orthosilicate (TEOS) in appropriate quantity was first dissolved in methanol, in presence of banana trunk sap (as an agent of hydrolysis instead of water) and dimethylformamide (DMF) under continuous stirring for 50 minutes by magnetic force stirrer. Small amount of nitric acid (conc.) was added as a catalyst. After that calculated volume of titanium isopropoxide (TIPO) was mixed to the solution of partially hydrolyzed TEOS and kept stirring for another 1 hour at room temperature under vigorous stirring. Finally, required quantity of Europium chloride hexahydrate was added to this solution mixture and stirring was continued for another half an hour and then transferred into a plastic container where they were kept to gel formation at RT. The time of gelation differed from 3 to 5 weeks depending on the composition. After gelation, the container's cover has a few pinholes made to allow for slow, controlled evaporation. The gels are then gradually dried up to  $80\text{ }^\circ\text{C}$  before being annealed in an electric muffle furnace at a rate of  $1\text{ }^\circ\text{C}$  per minute up to  $1050\text{ }^\circ\text{C}$  (Dihingia *et al.*, 2012).

### 4.2.3. Results and discussion

#### 4.2.3.1. Various Physical Properties

Physical properties of the prepared samples were obtained by methods and techniques reported elsewhere (Boiling *et al.*, 1978). The Archimedes principle was used to determine the density of  $\text{Eu}^{3+}$  ions doped with  $\text{TiO}_2$  in silica glass-ceramic using the sol-gel method. In this instance, distilled water is used as the immersion fluid. The Abbe Refractometer technique was used to determine the refractive index of glass. Using the appropriate expressions, additional associated properties such as molecular electronic polarizability ( $\alpha_e$ ), average molecular weight ( $M_T$ ), molar refractivity ( $R_M$ ), the concentration of  $\text{Eu}^{3+}$  ion ( $N$ ), dielectric constant ( $\epsilon$ ), optical dielectric constant ( $\epsilon-1$ ), reflection losses ( $R_L$ ), molar refraction ( $R_m$ ), polaron radius ( $R_p$ ), and interatomic distance ( $R_i$ ) have been computed from the practically computed densities and refractive index and listed in Table 4.2.1. Electronic polarizability is regarded as an important feature that determines the non-linear behavior of materials. The strong light that strikes the material causes electrical polarization, which leads to optical nonlinearity. The refractive index ( $n$ ) and polarizability ( $\alpha_e$ ), according to theoretical formulations by Volf and Lorentz-Lorentz (Praveen *et al.*, 2014), are estimated as follows:

$$\frac{(n^2-1)}{(n^2+1)} V_m = \frac{4}{3\pi} N\alpha_e \quad (4.1)$$

**Table 4.2.1**

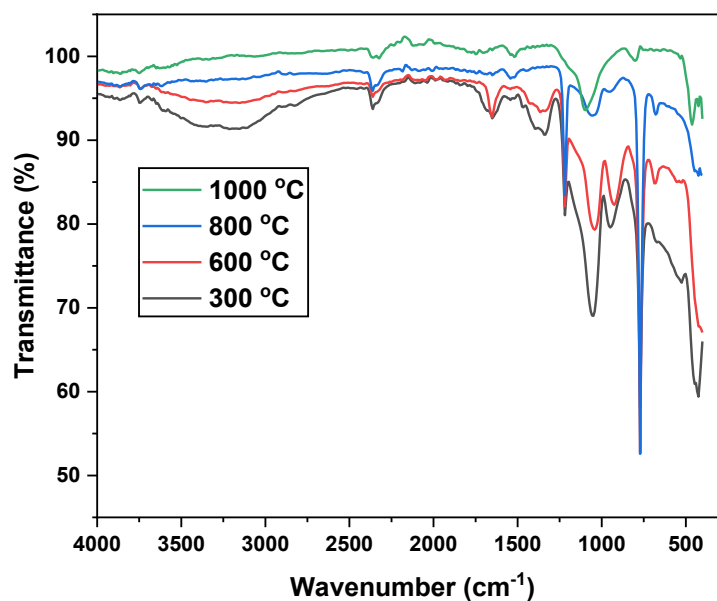
Various physical properties of 1.5%Eu<sup>3+</sup> ions doped with 20%TiO<sub>2</sub>–80%SiO<sub>2</sub> binary glass-ceramic derived by sol-gel process.

Physical properties	Value
Refractive index ( $n$ )	2.135
Density ( $\rho$ ) ( $gm/cm^3$ )	2.015
Thickness ( $Z$ )	0.127
Average molecular weight ( $M_T$ ) ( $g$ )	72.093
Reflection losses ( $R_L$ ) (%)	0.131
Molar refractivity ( $R_m$ ) ( $cm^3$ )	19.411
Energy gap ( $E_g$ )	4.1
Molar electronic polarizability ( $\alpha_m$ )	7.703
Dielectric constant ( $\epsilon$ )	4.558
Optical dielectric constant ( $\epsilon - 1$ )	3.558
Electronic polarizability ( $\alpha_e$ ) ( $\times 10^{-21}$ )	2.152
Eu <sup>3+</sup> ion concentration ( $N$ ) ( $\times 10^{20} ions/cm^3$ )	2.525
Molar volume ( $V_m$ ) ( $cm^3/mol$ )	35.778
Polaron radius ( $R_p$ ) ( $\times 10^{-8}$ )	3.95
Inter-ionic distance ( $R_i$ ) ( $\times 10^{-7}$ )	1.32
Field strength ( $F$ ) ( $\times 10^{-16} cm^{-2}$ )	7.29
Metallization criterion ( $M$ )	0.453

#### 4.2.3.2. ATR–FTIR Analysis

The ATR-FTIR spectroscopy may be used as an active technique for analyzing the chemical and structural changes in the host source when it is doped with Eu<sup>3+</sup> (Boiling *et al.*, 1978). After annealing up to 1000 °C, the sol-gel sample was powdered for analysis. The Eu<sup>3+</sup> doped sample was measured from 400–4000 cm<sup>-1</sup>, as shown in Fig. 4.2.1. The stretching vibration of the Ti-O bonds in Ti-O-Ti is responsible for the absorption bands in the 400-556 cm<sup>-1</sup> range (Fozia *et al.*, 2017). According to reports, bands in the 900-1000 cm<sup>-1</sup> range are composite characteristics of Si-OH, Ti-OH, and Si-O-Ti, and our sample also displays bands in the 924-952

$\text{cm}^{-1}$  region, which is typical for  $\text{TiO}_2\text{-SiO}_2$  glass (Dihingia *et al.*, 2012). The band center at  $1000\text{ cm}^{-1}$  can be ascribed to the Si-O-Si bond stretching in the  $\text{SiO}_4$  tetrahedral unit of the silica sources (Yamane *et al.*, 2001). The band peak at  $2360\text{ cm}^{-1}$  is due to the stretching of  $\text{CH}_2$  in aspect (Dihingia *et al.*, 2012). The peak at  $924\text{-}952\text{ cm}^{-1}$  is clearly indicating the exclusive fluctuation arise from the Ti-O-Si bonds formation (Dihingia *et al.*, 2012). The peak at around  $3264\text{ cm}^{-1}$  can be ascribed to the stretching fluctuation of OH- of minor quantity of free surplus  $\text{H}_2\text{O}$  that may be commenced and the identical OH-curving fluctuation owing to chemically consumed  $\text{H}_2\text{O}$  (Dihingia *et al.*, 2012). The C = C fluctuation is ascribed around at  $1528\text{-}1654\text{ cm}^{-1}$  (Wang *et al.*, 1997). Table 4.2.2 shows the list of identified bands.



**Fig. 4.2.1:** ATR-FTIR spectra of SiTiEu1.5 glass annealed at different temperatures.

**Table 4.2.2**

The glass-ceramic samples' ATR-FTIR peak locations and their various assignments.

Wavenumber (cm <sup>-1</sup> )	Assignment	Observed Intensity	During heating, the intensity changes
400-463	The Ti-O bond stretching vibration in Ti-O-Ti (Fozia <i>et al.</i> , 2017)	Strong, broad	In six peaks arise 416, 424, 432, 439, 447, 463 at annealing temperature
524-556	The vibration of the O-Ti-O bond (Praveen <i>et al.</i> , 2014)	No peak	An intense peak arises at 300 °C and slightly decreases 600 °C and remove in 800 °C & 1000 °C
671-679	Si-O of SiO <sub>4</sub> symmetric bending (Yamane <i>et al.</i> , 2001)	Minor peaks	A slight peak occurs at 800 °C and decreases as temperature rises.
772	Si-OH stretching (Boiling <i>et al.</i> , 1978)	Strong	Decrease with increasing temperature
924-952	The vibration of the Si-O-Ti bond (Dihingia <i>et al.</i> , 2012).	Sharp peaks	Decrease in higher temperatures
1041-1058	Si-O-Si, asymmetric stretching (Boiling <i>et al.</i> , 1978)	Intense peak	Reducing intensity and redshift

1219	Stretching vibration C-O-C (Dihingia <i>et al.</i> , 2012)	Minor peak	Remove in T > 1000 °C
1328	Si-O-Si	Diffuse	Remove in T > 800 °C and 1000 °C
1528-1654	C = C stretching (Praveen <i>et al.</i> , 2014)	Minor peak	Shifted when annealed at 800 °C and 1000 °C
2360	CH <sub>2</sub> stretching vibrations (Praveen <i>et al.</i> , 2014)	Minor peak	Decrease with increasing temperature
3500-3700	O-H stretching (Boiling <i>et al.</i> , 1978)	Broad, strong	Slightly decreases at 1000 °C

---

#### 4.2.3.3. X-Ray Diffraction (XRD) Analysis

The study of the XRD pattern showed the crystallinity and grain size of the synthesized TiO<sub>2</sub> nanoparticles (NPs), as well as the phases contained in them. Fig. 4.2.2 displays the XRD pattern of chemically and greenly synthesized TiO<sub>2</sub> nanoparticles. The XRD pattern shows that strong and sharp peaks indicate that the material's crystalline structure. The XRD pattern of the two samples shows peaks at 2 $\theta$  values 25.5, 37.8, 48.2, 54.1, 55.3, 62.7, 69.1, 70.5, and 75.1 corresponding to the (101), (004), (200), (105), (211), (204), (116), (220) and (215) planes of anatase phase (You *et al.*, 2004). Three additional peaks are seen in the sample (a) 20%TiO<sub>2</sub>-80%SiO<sub>2</sub>, which corresponds to the rutile phase's lattice planes (110), (101) and (111), respectively, at 2 $\theta$  values 27.4, 36.2, and 41.4.

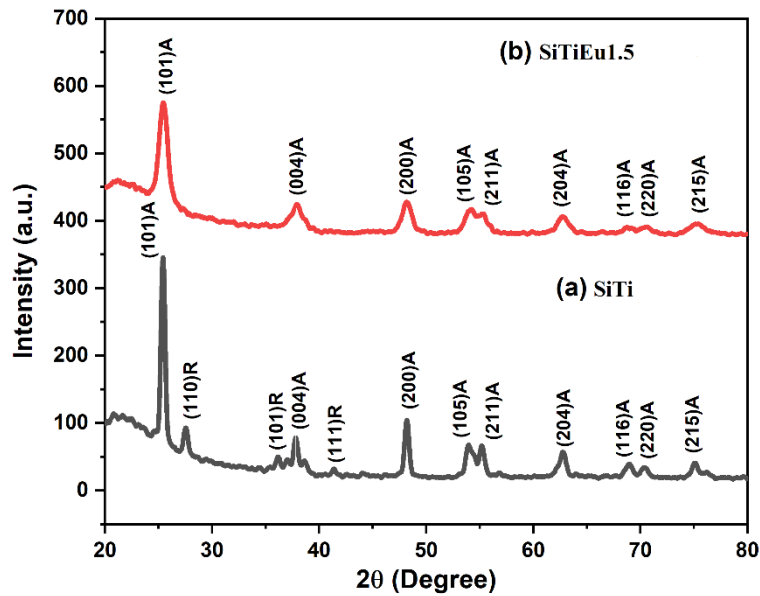
The crystallite size ( $D$ ), of TiO<sub>2</sub> NPs can be estimated from the width of peak using the Scherrer's formula (Yan *et al.*, 2012),

$$D = \frac{0.9\lambda}{\beta \cos \theta_B} \quad (4.2)$$

where D is the average crystallite size or grain size, X-ray wavelength is represented by  $\lambda$ , angle of diffraction is represented by  $\theta_B$ , and full width at half maximum (FWHM) of the diffraction peak is represented by  $\beta$ .

But one should remember that nanoparticles frequently form twinned structures, therefore the Scherrer formula can provide a value that differs from the genuine particle size (Fozia *et al.*, 2017, Gregory *et al.*, 1957). Additionally, X-ray diffraction generally requires an important amount of powder and only provides aggregate information on particle sizes.

The Debye-Scherrer formula was used to determine the size of the TiO<sub>2</sub> crystals (Birks *et al.*, 1946). The calculated average crystallite size for (a) SiTi and (b) SiTiEu1.5 glasses are 9.6 and 10.4 nm.



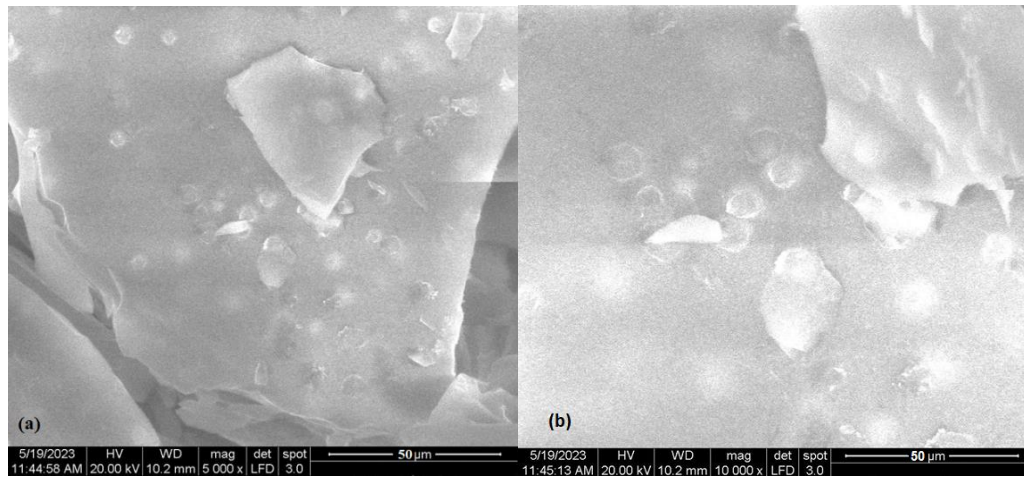
**Fig. 4.2.2:** XRD diffractogram of (a) SiTi and (b) SiTiEu1.5 glasses annealed up to 700 °C.



#### 4.2.3.4. SEM analysis

Morphology of the representative samples of SEM image of SiTi and SiTiEu1.5 binary glasses obtained through Pechini-type polymerized complex route is shown in Fig. 4.2.3: (a) and (b). The micrograph provided by SEM analysis, indicated that SiTi and SiTiEu1.5 glasses formed wholly of smaller particles. This figure shows the  $\text{TiO}_2$  nanoparticles are in spherical shape with agglomerate nanoparticles. According to the SEM images, all of the particles were spherical and had an average diameter of between 13 and 15 nm.

The surface morphology of prepared glass-ceramic samples of  $\text{TiO}_2$  NPs in sol-gel silicate was characterized by SEM analysis as shown in Fig. 4.2.3: (a) and (b). The synthesized particles are well dispersed and have a spherical form. Less agglomeration of nanoparticles also appeared, this may be due to aggregation of primary  $\text{TiO}_2$  particles at high calcination temperature which is necessary to accelerate the crystal growth of titanium dioxide (Tong *et al.*, 2020).

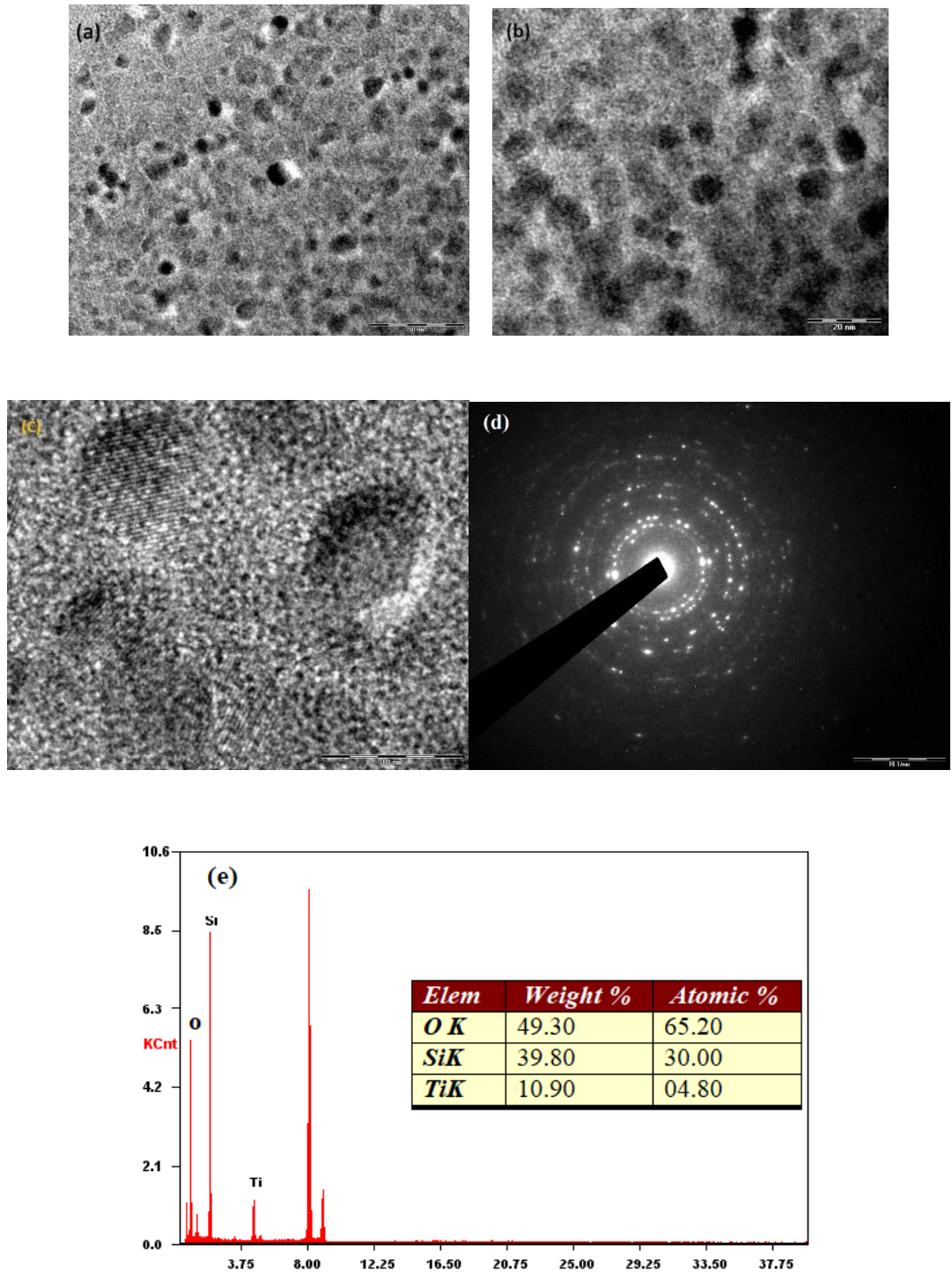


**Fig. 4.2.3:** (a) SEM image of SiTi (b) SEM image of SiTiEu1.5 binary glasses annealed up to 700 °C.

#### 4.2.3.5. Transmission Electron Microscopy (TEM) and Energy Dispersive X-Ray Spectroscopy (EDX) Study

The TEM image with selective area electron diffraction (SAED) is shown in Fig. 4.2.4: (a), (b) and (d) respectively. The average particle size, as indicated by the TEM image, is around 10 nm, which is comparable to the crystallite sizes determined by the Scherrer equation. The HRTEM image further confirms the 0.35 nm (101) anatase interplanar spacing in TiO<sub>2</sub> nano-crystallites, as seen in the fig. 4.2.4(c). It is possible to determine a region's crystal characteristics using an SAED pattern, such as whether the substance is singly-crystalline, polycrystalline, polycrystalline with texture, or amorphous (Fozia *et al.*, 2017). While polycrystalline materials have ring pattern shape, single-crystalline materials' SAED patterns are merely spot patterns. The SAED pattern shows a ring-like pattern, which means the prepared TiO<sub>2</sub> nanoparticles doped with glass samples is a polycrystalline material (Ciric *et al.*, 2018).

The EDX spectra of TiO<sub>2</sub> doped SiO<sub>2</sub> in sol-gel glass sample is found to be consistent with the elements (Si, O, Ti) supposed to be present in the sample as in Fig. 4.2.4(e), which is also true for other as-synthesized samples (Fozia *et al.*, 2017). The peaks at 8.04 keV and 8.9 keV are due to the K-alpha and K-beta lines of the copper grid used in the measurements.



**Fig. 4.2.4:** (a) TEM image of SiTi, (b) TEM image of SiTiEu1.5, (c) HR-TEM, (d) SAED pattern of SiTiEu1.5, and (e) EDX spectrum of SiTi of the binary glasses annealed up to 700 °C.

#### 4.2.3.6. Absorption spectra

The absorption spectra of SiTiEu1.5 glass as shown in Fig. 4.2.5. From the absorption spectrum, it is clear that 5 absorption bands have been observed in the UV region. These absorption bands correspond to the transitions  ${}^7F_0 \rightarrow {}^5D_4$  (361 nm),  ${}^7F_0 \rightarrow {}^5G_4$  (374 nm),  ${}^7F_0 \rightarrow {}^5G_2$  (380 nm),  ${}^7F_0 \rightarrow {}^5G_3$  (386 nm) and  ${}^7F_0 \rightarrow {}^5L_6$  (395 nm). The data of Carnall et al. (Carnall *et al.*, 1968) is used to assign all the above peaks. The  ${}^7F_0 \rightarrow {}^5L_6$  transition located at 395 nm (violet) is forbidden by  $\Delta S$  and  $\Delta L$  selection rules but allowed by  $\Delta J$  selection rule and is more intense than the other transitions (Hazarika *et al.*, 2004).

The UV-Vis absorption spectra for the doped TiO<sub>2</sub> nanoparticles samples in sol-gel silicate glass-ceramic are presented in Fig. 4.2.6(a). The absorption wavelength of TiO<sub>2</sub> doped sol-gel silicate glass-ceramic were red shifted from 280 nm to 325 nm with increasing various temperatures, indicating the decrease of the optical bandgap. The bandgap energy was calculated using following Tauc's relation:

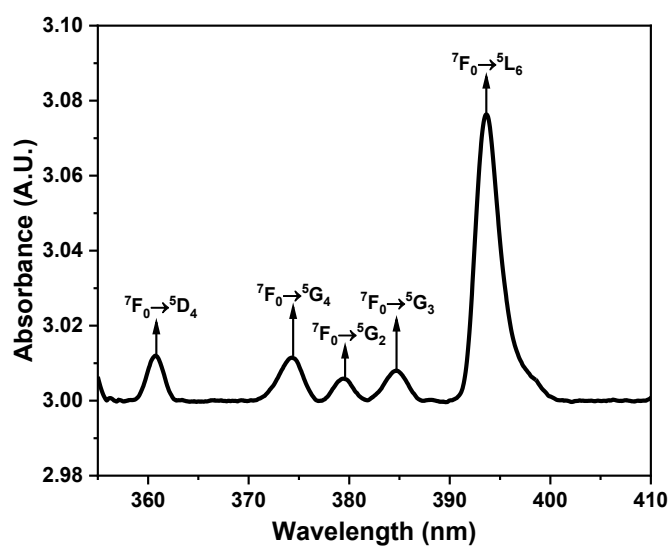
$$E_g = \frac{1240}{\lambda_{ab}} eV \quad (4.3)$$

Using Tauc's relation, the optical bandgap is calculated.

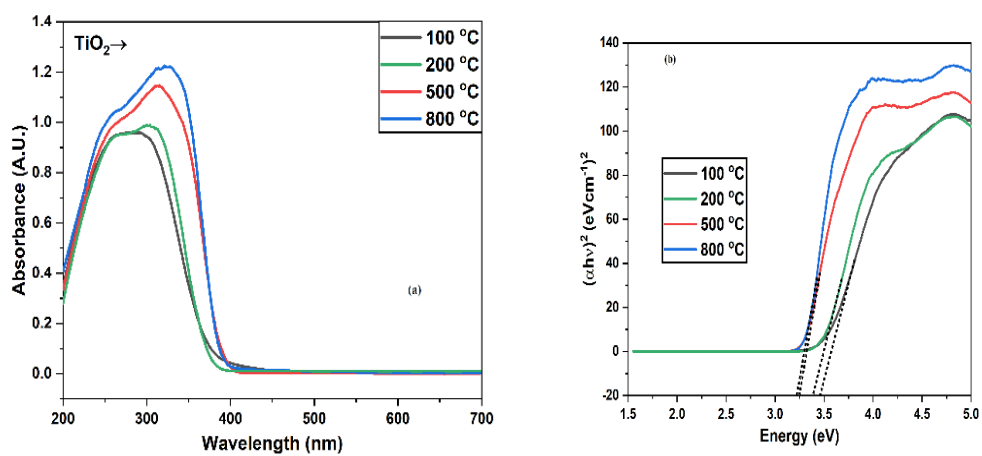
$$\alpha h\nu = A(h\nu - E_g)^r \quad (4.4)$$

where  $r$  is an index with values of 1/2 and 2 for permissible direct and indirect transitions, respectively, and  $A$  is a parameter that depends on transition probability and  $E_g$  stands for bandgap energy (Ciric *et al.*, 2018). By estimating the straight portion of the plot between  $(\alpha h\nu)^2$  versus  $h\nu$ , one may determine the band gap values. As shown in Fig. 4.2.6(b), the best linear fit was achieved for  $n = 2$ , showing that a direct allowed transition between the valence and conduction bands is possible (Ciric *et al.*, 2018). As clearly shown in Fig. 4.2.6(b) and Table 4.2.3, it is evident that an increase in annealing temperature leads to a decrease in optical bandgaps.

The effect of annealing temperatures of SiTi glass results in different optical bandgaps. At annealing temperatures treatment of 100, 200, 500 and 800 °C resulted in the optical bandgap of 3.469, 3.386, 3.249 and 3.221 eV.



**Fig. 4.2.5:** Absorption spectrum of SiTiEu1.5 glass annealed up to 700 °C.



**Fig. 4.2.6:** (a) UV-vis absorption spectra of SiTi glass. (b) Kubelka-Munk plots and bandgap energy estimation of SiTi glass.

**Table 4.2.3**

The values of bandgap energy of SiTi glass at different annealing temperatures

Sample (TiO <sub>2</sub> )	100 °C	200 °C	500 °C	800 °C
Energy bandgap (eV)	3.469	3.386	3.249	3.221

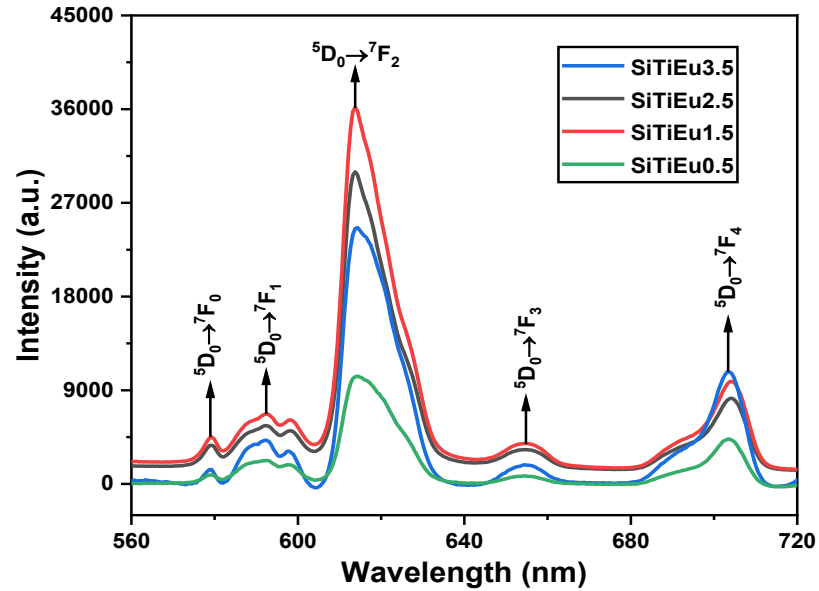
#### 4.2.3.7. PL spectra

Fig. 4.2.7 represents the PL spectra of SiTiEu0.5, SiTiEu1.5, SiTiEu2.5 and SiTiEu3.5 glasses annealed at 700 °C is recorded in 560–720 nm range. From the emission spectra, five distinct emission peaks were observed corresponding to the transitions from  $^5D_0 \rightarrow ^7F_0$ ,  $^7F_1$ ,  $^7F_2$ ,  $^7F_3$ ,  $^7F_4$  (579 nm, 593 nm, 614 nm, 654 nm and 704 nm). According to the PL spectra, all transitions' peak intensities gradually rise with  $Eu^{3+}$  ions concentration up to 1.5 mol% of  $Eu^{3+}$  ions and beyond, when concentration quenching causes the decrease shown in Fig. 4.2.7. Beyond 1.5 mol%, the interaction between the host glass matrix and  $Eu^{3+}$  ion is strong. This is explained by the fact that when concentration increases further, emission intensity decreases. The strongest and sharp red emission peak located at 614 nm corresponds to the electric-dipole (ED) allowed transition  $^5D_0 \rightarrow ^7F_2$  ( $\Delta J = \pm 2$ ) and is so called “hypersensitive” transition, which means that its intensity is extremely sensitive to the local environment of  $Eu^{3+}$  ions (Binnemans *et al.*, 2015), while the intensity of the peak at 593 nm corresponds to magnetic-dipole (MD) allowed  $^5D_0 \rightarrow ^7F_1$  ( $\Delta J = \pm 1$ ) transition is hardly varies with the crystal field strength about  $Eu^{3+}$  ions (Ciric *et al.*, 2018, Linganna *et al.*, 2012). The relative intensity ratio of electric-dipole (ED) transition ( $^5D_0 \rightarrow ^7F_2$ ) to magnetic-dipole (MD) transition ( $^5D_0 \rightarrow ^7F_1$ ) has been calculated to identify the lattice symmetry and coordination of  $Eu^{3+}$  ions in the  $TiO_2$  lattice (Linganna *et al.*, 2012). The R/O ratio also known as the asymmetric ratio used to compute the distortion from inversion symmetry of the local environment around the  $Eu^{3+}$  ions in the  $TiO_2$  host matrix (Nogami *et al.*, 1998). For the glasses SiTiEu0.5, SiTiEu1.5, SiTiEu2.5 and SiTiEu3.5, the values of asymmetric ratio (R/O) for the current study are determined to be 2.87, 5.73, 4.20 and 3.69, respectively. The asymmetric ratio varying with amount of Eu-doping, demonstrates that the degree of symmetry of  $Eu^{3+}$  ions decreases (Nogami *et al.*, 1998) and strong Eu-O covalence band forms. Generally,  $^5D_0 \rightarrow ^7F_J$  ( $J=0, 2$ ) ED transitions are extremely sensitive to bonds in the vicinity of  $Eu^{3+}$  ion, i.e., the enhanced emission intensities indicate the bond between the europium and oxygen become strong covalent (Mohapatra *et al.*, 2011). In ideal case is to have one emission weakly dependent on temperature to serve as an internal reference (Lojpur *et al.*, 2016). In this case, the hypersensitive transition  $^5D_0 \rightarrow ^7F_1$  is chosen as an internal reference

since the peak at ca. 593 nm has almost constant intensity over the temperature range of measurements (Dhiren *et al.*, 2012). The other, also hypersensitive, transition chosen to measure luminescence intensity ratio,  $^5D_0 \rightarrow ^7F_2$ , dominates the spectrum in host matrices with low symmetries and with no inversion center (such is the case of  $Eu^{3+}$  doped titanium dioxide) (Dhiren *et al.*, 2012, Mohapatra *et al.*, 2011). Within the crystal volume they are  $Ti^{4+}$  while surface Ti atoms adjust their coordination environment, favoring the formation of  $Ti^{3+}$  (Antic *et al.*, 2012).  $Ti^{4+}$  ions have 6-fold ligand coordination number and are at the center of the  $D_{2d}$  distorted octahedron (Liu *et al.*, 2006). In anatase titanium dioxide there are three possible sites that can incorporate  $Eu^{3+}$  ion: two sites are reduced from the original  $D_{2d}$  symmetry to  $D_2$  when  $Eu^{3+}$  substitutes  $Ti^{4+}$  and to  $C_{2v}$  when it substitutes a vacancy, and the third site is with  $C_1$  symmetry at the surface, which occurs when  $Ti^{3+}$  is replaced by  $Eu^{3+}$  (Dawngliana *et al.*, 2023, Mohapatra *et al.*, 2011). Emission spectra shown in Fig. 4.2.7 resemble emission of  $Eu^{3+}$  in sites of the lowest symmetry  $C_1$  which are located near nanoparticles' surface or defects and which are, therefore, the most abundant and exist in both anatase and rutile forms of  $TiO_2$  (Antic *et al.*, 2012, Aleksandar *et al.*, 2018). For this reason, it is impossible to exclude solely from emission spectra emission contribution of  $Eu^{3+}$  incorporated in rutile phase; however, this situation doesn't affect thermometry measurements and derived conclusions (Antic *et al.*, 2012). In general the forbidden  $^5D_0 \rightarrow ^7F_0$  and  $^5D_0 \rightarrow ^7F_3$  ED transitions are very weak in intensity compared to other transitions. The observation of the strictly forbidden  $^5D_0 \rightarrow ^7F_0$  ED transition at 579 nm suggest that the  $Eu^{3+}$  ions are located at site symmetry of  $C_{nv}$ ,  $C_n$  or  $C_s$  (Binnemans *et al.*, 2015, Ciric *et al.*, 2018). One should note that from Fig. 4.2.7 that in contrast to, the  $^5D_0 \rightarrow ^7F_2$  transition, is highly dependent on  $Eu^{3+}$  concentrations, and its intensity drops rapidly with the concentrations increase. It implies that fluorescence quenching occurs as a result of cluster formation at higher  $Eu^{3+}$  concentrations (Reisfeld *et al.*, 2002, Boiling *et al.*, 1978).

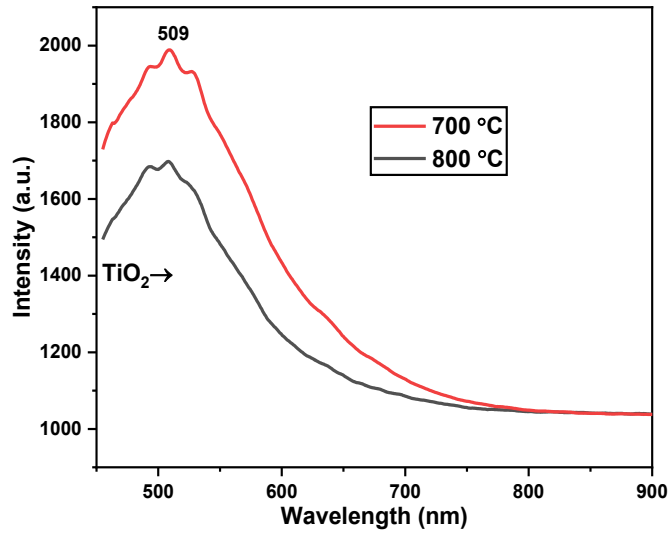
The PL spectra were measured on  $TiO_2$ - $SiO_2$  in sol-gel glass sample at different temperatures (700 °C and 800 °C) as shown in Fig. 4.2.8. The PL spectra of SiTi glass- samples show the peaks at 509 nm, respectively. Luminescence features also depend on other crucial factors which includes solvent, atmosphere, starting

materials, etc. and is attributed to different processing conditions during synthesis process (Haque *et al.*, 2013, Roy *et al.*, 2015, Roy *et al.*, 2015, Jia *et al.*, 2013). The results shows that the formation of resolved manifold lines implies that positive ions were located on the well-defined lattices site in the TiO<sub>2</sub> spherical structures (Haque *et al.*, 2013, Durgam *et al.*, 2019). Fig. 4.2.9 shown that, SiTi glass sample annealed at 700 °C and 800 °C, the emission intensities has been showing sharp peaks due to the agglomerated lattice sites. The result indicated that, the PL intensity was slightly reduced with increasing the temperatures (Roy *et al.*, 2015).



**Fig. 4.2.7:** PL spectra of SiTiEu glasses ( $\lambda_{\text{ex}}=370$  nm).





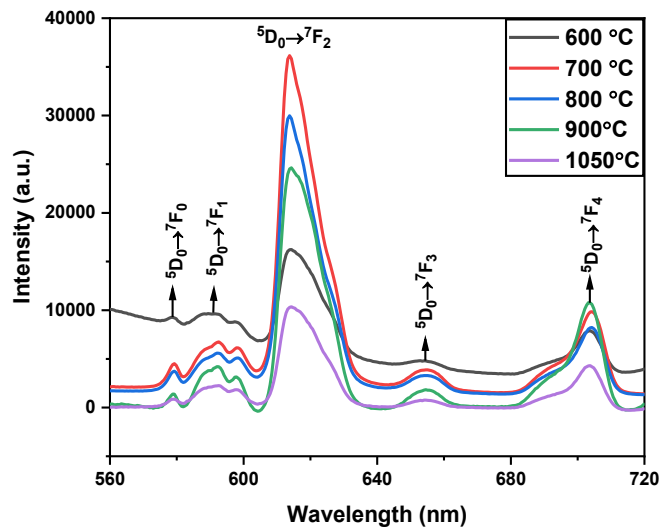
**Fig. 4.2.8:** PL spectra of SiTi glasses ( $\lambda_{\text{ex}}=370$  nm).

#### 4.2.3.8. Effect of annealing temperatures of PL Spectra

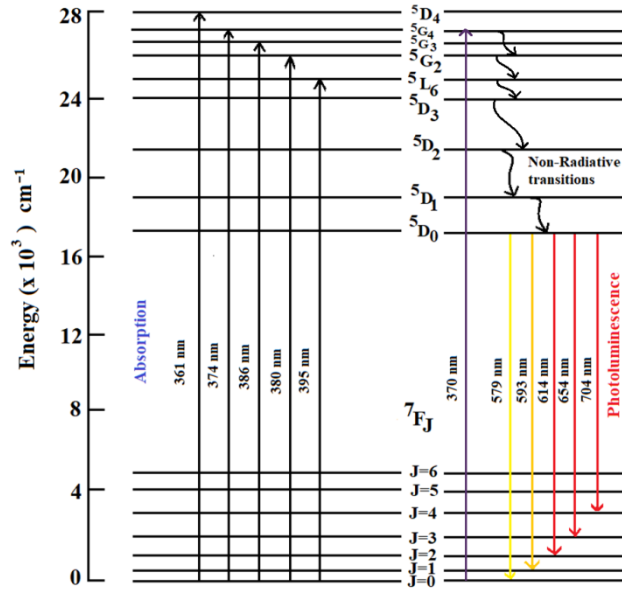
As shown in Fig. 4.2.9, the PL spectra of SiTiEu1.5 glasses were annealed at various temperatures (600, 700, 800, 900, and 1050 °C). The intensity of  $\text{Eu}^{3+}:\text{TiO}_2$  emission also rises with annealing temperature, reaches a maximum at 700 °C, and then falls as annealing temperature rises (Rai *et al.*, 2011). This result can be explained as follows. Additionally, during the annealing process, numerous defect centers were created by the hydrolysis and condensation of alkoxysilane precursor, resulting in a reduction in the concentration of hydroxyl groups (OH) that are present in the glass throughout the heat treatment process (Lojpur *et al.*, 2016). On the one hand, the emission was caused by a strong electron-photon interaction. As the  $\text{TiO}_2$  particles are in nanometer size, we cannot ignore the existence of the electron or hole-trapped surface level on  $\text{TiO}_2$  particles (Rai *et al.*, 2011). Because most of the ions of the nanoparticles are located on the surface and they are non-saturated in coordination, electrons or holes may be excited easily and escape from the ions (Mohan *et al.*, 2013). The energy released from the electron and hole produced by defect recombination was transferred to the  $\text{Eu}^{3+}$  ions that were embedded in the network of silica xerogel, improving the environment for the  $\text{Eu}^{3+}:\text{TiO}_2$  ions (Dhiren *et al.*,

2012). On the other hand, the influence of high energy vibration of the hydroxyl group on the emission of  $\text{Eu}^{3+}$  ions was reduced (Mohan *et al.*, 2013). Because of this, a more effective luminescent center is formed, and the intensity of the emission rises with the annealing temperature (Lojpur *et al.*, 2016). Further raising the annealing temperature may cause the formation of a  $\text{Eu}^{3+}$  cluster or may reduce the defect concentration in the silica xerogel network, blocking the energy transfer between the defects and  $\text{Eu}^{3+}$  ions (Rai *et al.*, 2011). As a result, the emission intensity may decrease. Fig. 4.2.9 shows that, in contrast to the  $^5\text{D}_0 \rightarrow ^7\text{F}_2$  transition, which is strongly temperature sensitive and rapidly decreases in intensity as temperature rises.

Fig. 4.2.10 shows the transitions involved for the observed spectra reported in this work. The  $\text{Eu}^{3+}$  ions, after excitation by the 370 nm source relax non-radiatively to the  $^5\text{D}_0$  state from which we observe radiative relaxation to the  $^7\text{F}_J$  states. Emission from the higher states are not observed, which is expected due to the smaller energy gaps that can be easily bridged by the non-radiative multi-phonon relaxation.



**Fig. 4.2.9:** Effect of annealing temperatures of PL emission spectra.



**Fig. 4.2.10:** Schematics energy diagram of SiTiEu glasses.

#### 4.2.3.9. Judd-Ofelt and Radiative parameters

According to the Judd–Ofelt theory (Judd, 1962, Ofelt, 1962), the radiative transitions belonging to the  $4f^2$  configuration of  $\text{Eu}^{3+}$  can be analyzed based on the absorption spectra of  $\text{Eu}^{3+}$  (Fig. 4.2.5). The Judd–Ofelt intensity parameters  $\Omega_\lambda$  ( $\lambda = 2, 4$ , and  $6$ ) for  $\text{Eu}^{3+}$  in the SiTiEu1.5 sample are derived by a least square fitting of oscillator strength derived from experiment ( $f_{\text{exp}}$ ) and calculation ( $f_{\text{cal}}$ ) oscillator strength using as obtained squared matrix elements as shown in Table 4.2.4 (Carnall *et al.*, 1978). The huge value  $\Omega_2$  explains the covalent bonding between  $\text{Eu}^{3+}$  ions and the other two metals in the host  $[\text{Eu-O}, \text{Eu-TiO}_2]$  appropriately (Iwdsona *et al.*, 2007, Rai *et al.*, 2014, Vijayaakumar *et al.*, 2015). The JO intensity parameters give an insight into the local structure and bonding in vicinity of the RE ions (Khan *et al.*, 2018). The environment sensitive parameter ( $\Omega_2$ ) indicates the amount of covalent bonding and the vibronic dependent parameter ( $\Omega_6$ ) is related to the rigidity of the material (Agarwal *et al.*, 2009, Garima *et al.*, 2006). The ratio  $\Omega_4/\Omega_6$  determines the spectroscopic of the material, more the ratio, less is the rigidity and better is the spectroscopic quality of the material (Agarwal *et al.*, 2009). The comparison of J-O parameters of  $\text{Eu}^{3+}$  ion is tabulated in Table 4.2.5. The estimation of radiative parameters such as stimulated emission cross-sections ( $\sigma_p \times 10^{-22} \text{ cm}^2$ ), effective bandwidths ( $\lambda_{\text{eff}}$ ), radiative transition probabilities ( $A_{\text{ed}}$ ), and branching ratios for the

optical transitions of  $\text{Eu}^{3+}$  in the SiTiEu1.5 have been estimated using J-O intensity parameters in Table 4.2.6 (Marimuthu *et al.*, 2009).

**Table 4.2.4**

The following absorption spectra were calculated ( $f_{\text{cal}}$ ) and experimentally ( $f_{\text{exp}}$ ) for SiTiEu1.5 glass during annealing at 700 °C.

Transitions	Energy (in $\text{cm}^{-1}$ )	Wavelength (in nm)	$f_{\text{exp}}$ ( $\times 10^{-6}$ )	$f_{\text{cal}}$ ( $\times 10^{-6}$ )
${}^7\text{F}_0 \rightarrow {}^5\text{D}_4$	27700.83	361	0.124	0.195
${}^7\text{F}_0 \rightarrow {}^5\text{G}_4$	26737.97	374	0.218	0.123
${}^7\text{F}_0 \rightarrow {}^5\text{G}_2$	26315.79	380	0.089	0.096
${}^7\text{F}_0 \rightarrow {}^5\text{G}_3$	25906.74	386	0.077	0
${}^7\text{F}_0 \rightarrow {}^5\text{L}_6$	25316.46	395	1.204	1.205
$\Omega_2 = 3.279$ ( $\times 10^{-20} \text{ cm}^2$ )	$\Omega_4 = 2.928$ ( $\times 10^{-20} \text{ cm}^2$ )	$\Omega_6 = 1.742$ ( $\times 10^{-20} \text{ cm}^2$ )		
$\Omega_4 / \Omega_6 = 1.681$				

**Table 4.2.5**

Judd Ofelt intensity measurements for  $\text{Eu}^{3+}$  doped in various hosts were compared.

$\Omega_2$	$\Omega_4$	$\Omega_6$	$\Omega_4/\Omega_6$	References
3.279	2.928	1.742	1.681	Present work
5.61	3.47	2.91	1.19	$\text{Al}(\text{NO}_3)_3\text{-SiO}_2$ (Hazarika <i>et al.</i> , 2004)
4.13	1.13	0.82	1.38	BaO (Garima <i>et al.</i> , 2006)
5.72	2.45	-	-	BLNE (Marimuthu <i>et al.</i> , 2009)
26.59	5.75	-	-	$\text{SrAl}_2\text{O}_4$ (Santos <i>et al.</i> , 2012)
5.90	1.4	-	-	$\text{Sr}(\text{PO}_3)_2$ (Reisfeld <i>et al.</i> , 1983)
6.91	5.01	-	-	Phosphate glasses (Zaccaria <i>et al.</i> , 1998)

**Table 4.2.6**

Radiative parameters

Transitions	$\lambda_p$ (nm)	Energy (in $\text{cm}^{-1}$ )	$A_{ed}$ (in $\text{s}^{-1}$ )	$\beta_r$ (in %)	$\lambda_{eff}$ (nm)	$\sigma_p$ ( $\times 10^{-22}\text{cm}^2$ )
$^5\text{D}_0 \rightarrow ^7\text{F}_0$	579	17271	0	0	3.81	0
$^5\text{D}_0 \rightarrow ^7\text{F}_1$	593	16863	65.41	13.39	11.93	3.08
$^5\text{D}_0 \rightarrow ^7\text{F}_2$	614	16286	275.27	61.39	16.37	12.31
$^5\text{D}_0 \rightarrow ^7\text{F}_3$	654	15290	0	0	9.85	0
$^5\text{D}_0 \rightarrow ^7\text{F}_4$	704	14204	107.71	24.02	15.28	9.53
		$A_T (\text{s}^{-1}) =$ 448.39	$\tau_R = 2.23$ (ms)			

#### 4.2.3.10. Non-Linear Properties

The non-linear refractive index ( $n_2$ ), non-linear refractive index susceptibility ( $\chi^{(3)}$ ), co-efficient ( $\gamma_{ce}$ ), and relatively high Abbe number ( $v_{Ab}$ ) show that the sol-gel SiO<sub>2</sub> glass has good optical quality as shown by certain non-linear qualities that have been determined from optical parameters (Dihingia *et al.*, 2012). These values are presented in Table 4.2.7. We estimate these values following the procedure described by (Dihingia *et al.*, 2012).

**Table 4.2.7**

Non-linear parameters (e.g.  $\vartheta_d$ ,  $1/\vartheta_d$ ,  $n_2$ ,  $\gamma_c$  and  $\chi$ ) of SiTiEu1.5 binary glass

$n_f$	$n_e$	$n_f - n_e$	$n_d$	$\vartheta_d$	$1/\vartheta_d$	$n_2$ ( $10^{-13}$ esu)	$\gamma_c$ ( $\text{cm}^2/\text{W}$ )	$\omega_o$ (* $10^{-13}$ )	$N$ $\times 10^{-16}$	$\chi$ $\times 10^{-7}$
1.504	1.495	0.009	1.500	55.6	0.018	1.378	0.385	126.13	816.296	8.69

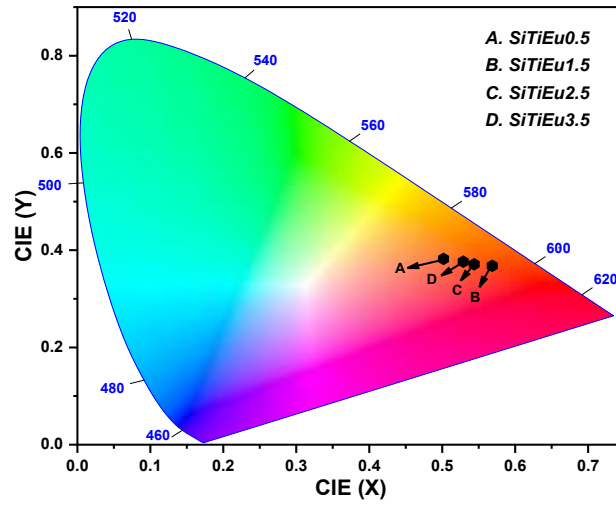
#### 4.2.3.11. CIE Chromaticity

Fig. 4.2.11 is a graphic from the Commission International de'Eclairage (CIE) 1931 that shows the exact color of the current Eu<sup>3+</sup> doped SiTi glasses' emission. From Fig. 4.2.11, it can be seen that irrespective of the Eu<sup>3+</sup> ion concentration the color coordinates measured for all the glasses falls in the red region (Fig. 4.2.11) (Monisha *et al.*, 2023). It was advantageous to use the SiTiEu1.5 nano phosphor in solid-state lighting applications such as developing the red regions of WLEDs.

**Table 4.2.8**

CIE chromaticity coordinates of SiTiEu glasses.

Glass code	X	Y	CCT	Color Purity
SiTiEu0.5	0.382	0.502	12731	78
SiTiEu1.5	0.368	0.569	11349	84
SiTiEu2.5	0.371	0.544	7384	86
SiTiEu3.5	0.376	0.529	6391	87



**Fig. 4.2.11:** CIE 1931 chromaticity diagram of SiTiEu glasses.

#### 4.2.4. Conclusion

Different concentrations of  $\text{Eu}^{3+}$  ions doped with Titania-Silicate (SiTi) glasses were using sol-gel technique. Using spectroscopic methods like absorption and photoluminescence to evaluate their usefulness for applications involving visible red emission. Very limited absorption bands observed for the titled glasses constrained us to calculate J–O parameters needed to evaluate the radiative properties (Dihingia *et al.*, 2012). The emission spectra recorded for all these glasses give five emission bands at 579, 593, 614, 654 and 704 nm related to the  $^5\text{D}_0 \rightarrow ^7\text{F}_J$  ( $J=0,1,2,3,4$ ) transitions, respectively. Red to orange luminescence intensity (R/O) ratio increases with  $\text{Eu}^{3+}$  ion concentration in these glasses indicates that the symmetry of  $\text{Eu}^{3+}$  decreases whereas the covalency increases (Marimuthu *et al.*, 2009). From  $\Omega_2$  parameter proves hypersensitive behavior of  $^5\text{D}_0 \rightarrow ^7\text{F}_2$  transition, confirms  $\text{Eu}^{3+}$  ions are situated in a deeply polarizable chemical domain. The high luminescence intensity ratio R specifies lower symmetry around Eu ions and higher Eu-O covalence. The values of  $A_{\text{ed}}$ ,  $\sigma_{\text{P}}$ ,  $\beta_{\text{r}}$  indicates the  $^5\text{D}_0 \rightarrow ^7\text{F}_2$  emission line is best for the development of color display devices and visible red laser. The SiTiEu1.5 glasses observed radiative characteristics also indicate that these glasses are best suited for strong red emission at greater  $\text{Eu}^{3+}$  ion concentrations. The removal of the

OH group and evolution of NBO on the low phonon energy side for the sample annealed at higher temperatures are both verified by ATR-FTIR spectra (Dawngliana *et al.*, 2023). In TiO<sub>2</sub> nanocrystals in the rutile and anatase phases were found in our glass-ceramic sample, according to the XRD, SEM, and HR-TEM studies. Additional confirmation of TiO<sub>2</sub> crystallite formation in silica host has been obtained by TEM monograph. EDX spectra resolve the elemental purity of the as-synthesized material. In context of physical properties the comparatively high Abbe number ( $\mathcal{V}_d$ ), low non-linear refractive index ( $n_2$ ) and the non-linear susceptibility ( $\chi^{e(3)}$ ) value authenticates the high optical quality of the sample and a very good non-linear nanomaterials (Dihingia *et al.*, 2012). CIE chromaticity co-ordinates, it was concluded that SiTiEu1.5 glass is quite suitable for visible red emission applications. From above results, the europium doped SiTi glass system is best for photonic applications.



## Reference

- A. Biswas, G.S. Maciel, R. Kapoor, C. S. Friend and P. N. Prasad (2003), Er<sup>3+</sup>-doped multicomponent sol-gel-processes silica glass for optical signal amplification at 1.5 $\mu$ m, *Appl. Phys. Lett.* **82**: 2389.
- B.T. Stone, V.C. Costa and K.L. Bray (1997), In situ dehydroxylation in Eu<sup>3+</sup>-doped sol-gel silica, *Chem. Mater.* **9**: 2592-2598.
- C.J. Brinker and G.W. Scherer (1990), Sol–Gel Science, The physics and chemistry of sol–gel processing, *Academic Press Inc. San Diego*, **8**: 391-392.
- H. You and M. Nogami (2004), Optical properties and local structure of Eu<sup>3+</sup> ions in sol-gel TiO<sub>2</sub>-SiO<sub>2</sub> glasses, *J. Phys. Chem.* **108**: 12003-12008.
- J. Anjaiah, C. Laxmikanth and N. Veeraiah (2014), Spectroscopic properties and luminescence behaviour of europium doped lithium borate glasses, *Phys. B: Condens. Matter.* **454**: 148.
- J. Wrzyszczyk, W. Mista, D. Hreniak, W. Strek, M. Zawadzki and H. Grabowska (2002), Preparation and optical properties of nanostructured europium-doped  $\gamma$ -Al<sub>2</sub>O<sub>3</sub>, *J. Alloys Compd.* **341**: 358-361.
- K. Maheshvaran and K. Marimuthu (2012), Concentration dependent Eu<sup>3+</sup> doped boro-tellurite glasses structural and optical investigations, *J. Lumin.* **132**: 2259-2267.
- L. Bokatiyal and S. Rai (2012), Photoluminescence and energy transfer study of Eu<sup>3+</sup> codoped with CdS nanoparticles in silica glass, *J. Fluor.* **22**: 505-510.
- M. Nagami and K. Suzuki 2002, Fast spectral hole burning in Sm<sup>2+</sup>-doped Al<sub>2</sub>O<sub>3</sub>–SiO<sub>2</sub> glasses, *Adv. Mater.* **14**: 923-926.
- M. Soltys, J. Janek, L. Zur, J. Pisarska and W.A. Pisarski (2015), Compositional-dependent europium-doped lead phosphate glasses and their spectroscopic properties, *Mater.* **40**: 91-96.
- M. Yamane and Y. Asahara (2001), Glasses for Photonics, *Laser and particle beams*, **19**: 667-667.
- N.L. Boling, A.J. Glass and A. Owyong (1978), Empirical relationships for predicting non-linear refractive index changes in optical solids, *J. Quantum*

*Electron*, **14**: 601-608.

- N.W. Gaponenko, O.V. Sergeev, E.A. Stepanova, M.V. Parkun, A.V. Mudryi, H. Gnaser, J. Misiewicz, R. Heiderhoff, L.J. Balk and G.E. Thompson (2001), Optical and structural characterization of erbium doped TiO<sub>2</sub> xerogel films on porous processed anodic alumina, *J. Electro. chem. Soc.* **148**: 13.
- P. Praveen, G. Viruthagiri, S. Mugundan, N. Shanmugam (2014), Structural, optical and morphological analyses of pristine titanium dioxide nanoparticles – Synthesized via sol–gel route, *Spec. Acta Part A: Molecular and Bimolecular spectroscopy*, **117**: 622-629.
- V. Hegde, C.S. Dwaraka Viswanath, V. Upadhyaya, K.K. Mahato and Sudha D. Kamath (2017), Red light emission from europium doped zinc sodium bismuth borate glasses, *Phys. B: Condens. Matter.* **527**: 35-43.
- W.T. Carnall, P.R. Fields and K. Rajnak (1968), Electronic energy levels of the trivalent lanthanide aquo ions. IV. Eu<sup>3+</sup>, *J. Chem. Phys.* **49**: 4450
- Y. Matsuura, K. Matsukawa, R. Kawabata, N. Higashi, M. Niwa and H. Inoue (2002), Synthesis of polysilane-acrylamide copolymers by photopolymerization and their application to polysilane-silica hybrid thin films, *Polymer*, **43**: 1549-1553.
- P.J. Dihingia and S. Rai (2012), Synthesis of TiO<sub>2</sub> nanoparticles and spectroscopic upconversion luminescence of Nd<sup>3+</sup>-doped TiO<sub>2</sub>-SiO<sub>2</sub> composite glass. *J. Luminescence*, **132(5)**: 1243–1251.
- S. S. Wang, Y. Zhou, Y.L. Lam, C.H. Kam, Y.C. Chan and X. Yao (1997), Fabrication and characterisation of neodymium-doped silica glass by sol-gel process, *Materials Research Innovations*, **1(2)**: 92–96.
- Z. H Fozia, N. Ruchi and Purnima Singh (2017), Evaluating photo-degradation properties of anatase and rutile TiO<sub>2</sub> nanoparticles for organic compounds, *Optik.* **128**: 191–200.
- Yan Yu, Jian Wang and J.F. Parr (2012), Preparation and properties of TiO<sub>2</sub>/fumed silica composite photo-catalytic materials, *Procedia Engineering*, **27**: 448-456.
- A. Agarwal, I. Pal, S. Sanghi, M.P. Aggarwal (2009), Judd–Ofelt parameters and

- radiative properties of  $\text{Sm}^{3+}$  ions doped zinc bismuth borate glasses, *Optical Materials*, **32**: 339–344.
- A. Ciric, S. Stojadinovic, M.D. Dramicanin (2018), Luminescence Intensity Ratio thermometry and Judd-Ofelt analysis of  $\text{TiO}_2\text{:Eu}^{3+}$ , *Opt. Mater.* **85**: 261–266.
- Aleksandar Ciric, Stevan Stojadinovica, Miroslav D. Dramicanin (2018), Luminescence Intensity Ratio thermometry and Judd-Ofelt analysis of  $\text{TiO}_2\text{:Eu}^{3+}$ , *Optical Materials*, **85**: 261–266.
- B.F. Dos Santos, M.V. Dos Santos Rezende, P.J.R. Montes, R.M. Araujo, M.A.C. Dos Santos, M.E.G. Valerio (2012), Spectroscopy study of  $\text{SrAl}_2\text{O}_4\text{:Eu}^{3+}$ , *J. Lumin.* **132**: 1015.
- B.R. Judd (1962), Optical absorption intensities of rare-earth ions, *Phys. Rev.* **127**: 750.
- C. Jia, Y. Cao, P. Yang (2013),  $\text{TiO}_2$  HOLLOW SPHERES: ONE-POT SYNTHESIS AND ENHANCED PHOTOCATALYSIS, *Fun. Mater. Lett.* **6**: 1350025.
- C. Liu, J. Liu, K. Dou (2006), Judd–Ofelt intensity parameters and spectral properties of  $\text{Gd}_2\text{O}_3\text{:Eu}^{3+}$  nanocrystals, *J. Phys. Chem. B*, **110**: 20277–20281.
- Durgam Komaraiaha, Eppa Radha, Jemmy James, Nandakumar Kalarikkal, J. Sivakumar, M.V. Ramana Reddy, R. Sayanna (2019), Effect of particle size and dopant concentration on the Raman and the photoluminescence spectra of  $\text{TiO}_2\text{:Eu}^{3+}$  nanophosphor thin films, *Journal of Luminescence*, **211**: 320–333.
- F.Z. Haque, N. Singh, P. Pandey, M.R. Parra (2013), Study of zinc oxide nano/micro rods grown on ITO and glass substrates, *Optik*, **124(20)**: 4167–4171.
- G.S. Ofelt (1962), Intensities of crystal spectra of rare-earth ions, *J. Chm. Phys.* **37**: 511–520.
- Garima Tripathi, Vineet Kumar Rai, S.B. Rai (2006), Spectroscopic studies of  $\text{Eu}^{3+}$  doped calibo glass: Effect of the addition of barium carbonate, energy transfer in the presence of  $\text{Sm}^{3+}$ , *Optics Communications*, **264**: 116–122

- Iwdsona Zareba-Grodz, Robert Pazik, Włodzimierz Tylus, Witold Mielcarek, Krzysztof Hermanowicz, Wiesław Strek and Krzysztof Maruszewski (2007), Europium-doped silica–titania thin films obtained by the sol–gel method, *Optical Materials*, **29**: 1103–1106.
- J.S. Roy, T. Pal-Majumder (2015), Optical behaviour of cadmium sulphide nanorods suspended in different dispersive media with varying refractive index, *Indian J. Phys.* **89**: 485
- J.S. Roy, T. Pal-Majumder, R. Dabrowski, A. Dey, P.P. Ray (2015), Tuning photoluminescence of liquid crystals doped ZnS nanoflakes, *Opt. Mater.* **46**: 467
- J.S. Roy, T. Pal-Majumder, R. Dabrowski, B.K. Mahato, A. Barman (2015), Optical behaviour of CdS nanorods dispersed in liquid crystal, *Adv. Mater. Lett.* **6**: 47.
- K. Binnemans (2015), Interpretation of europium(III) spectra, *Coo. Chem. Rev.* **295**: 1–45.
- K. Linganna, C.K. Jayasankar (2012), Optical properties of  $\text{Eu}^{3+}$  ions in phosphate glass, *Spectrochim. Acta Mol. Biomol. Spectrosc.* **97**: 788–797.
- K. Marimuthu, R.T. Karunakaran, S. SurendraBabu, G. Muralidharan, S. Arumugam and C.K. Jayasankar (2009), Structural and spectroscopic investigations on  $\text{Eu}^{3+}$ -doped alkali fluoroborate glasses, *Solid State Sciences*, **11**: 1297-1302.
- L.S. Birks and H. Friedman (1946), Particle size determination from X-ray line broadening, *Journal of Applied Physics*, **17**: 687.
- M. Mohapatra, Y.P. Naik, V. Natarajan, T.K. Seshagiri, S.V. Godbole (2011), Photoluminescence properties of  $\text{Eu}^{3+}$  in lithium titanate, *Phys. B Condens. Matter*, **406**: 1977–1982.
- M. Nogami, N. Umehara, T. Hayakawa (1998), Effect of hydroxyl bonds on persistent spectral hole burning in  $\text{Eu}^{3+}$ -doped  $\text{BaO-P}_2\text{O}_5$  glasses, *Phys. Rev. B*, **58**: 6166.
- M. Vijayakumar, K. Marimuthu and V. Sudarsan (2015), Concentration dependent spectroscopic behavior of  $\text{Sm}^{3+}$  doped leadfluoro-borophosphate glasses for laser and LED applications, *Journal of Alloys and Compounds*, **647**: 209-220.

- M. Monisha, M.S. Murari, M.I. Sayyed, Karunakara Naregundi, Nuha AlHarbi, D. K amath (2023), Judd-Ofelt analysis and luminescence characteristics of  $\text{Eu}^{3+}$  doped Nepheline ( $\text{NaAlSiO}_4$ )-based glass ceramics for solid-state lighting applications, *Journal of Non-Crystalline Solids*, **599**: 121971.
- Mohan Chandra Mathpal, Anand Kumar Tripathi, Manish Kumar Singh, S.P. Gairola, S.N. Pandey, Arvind Agarwal (2013), Effect of annealing temperature on Raman spectra of  $\text{TiO}_2$  nanoparticles, *Chemical Physics Letters*, **555**: 182-186.
- N.L. Boling and A.J. Glass (1978), Empirical relationships for predicting nonlinear refractive index changes in optical solids, *J. Quantum Electron.* **14**: 601-608.
- N.W. Gregory (1957), Elements of X-ray diffraction, *J. Am. Chem. Soc.* **79**: 1773-1774.
- R. Reisfeld (2002), Rare-earth complexes in sol gel glasses, *Mat. Sci.* **20**: 5-8.
- R. Reisfeld, E. Greenberg, R.N. Brown, M.G. Drexhage, C.K. Jorgensen (1983). Fluorescence of europium(III) in a fluoride glass containing zirconium, *Chem. Phys. Lett.* **95**: 91.
- S. Dhiren Meetei, S. Dorendrajit Singh, N. Shanta Singh, V. Sudarsan, R.S. Ningthoujam, M. Tyagi, S.C. Gadkari, R. Tewari, R.K. Vatsa (2012), Crystal structure and photoluminescence correlations in white emitting nanocrystalline  $\text{ZrO}_2\text{:Eu}^{3+}$  phosphor: effect of doping and annealing, *J. Lumin.* **132**: 537–544.
- S. Hazarika and S. Rai (2004), Structural, optical and non-linear investigation of  $\text{Eu}^{3+}$  ions in sol–gel silicate glass, *Optical Materials*, **27**: 173–179.
- S. Rai and L. Bokatial (2011), Effect of CdS nanoparticles on photoluminescence spectra of  $\text{Tb}^{3+}$  in sol–gel-derived silica glasses, *Bull. Mater. Sci.* **34**: 227–231.
- S. Rai and P.J. Dishingia (2014), Photoluminescence of  $\text{Eu}^{3+}$  doped  $\text{TiO}_2\text{-SiO}_2$  glass derived by sol-gel method, *BRNS National Laser Symposium*, **22**: 1-4.
- S. Zaccaria, M. Casarin, A. Speghini, D. Ajo, M. Bettinelli (1998), Optical spectroscopy of trivalent lanthanide ions in strontium metaphosphate

glasses, *Spectro. Acta, Part A*, **55**: 171.

- Tong Wu, Jingyao Li, Meiqi Chang, Yanhua Song, Qi Sun, Fangke Wang, Haifeng Zou and Zhan Shi (2020), Photoluminescence properties and photocatalytic activities of  $\text{SiO}_2@\text{TiO}_2\text{:Sm}^{3+}$  nanomaterials, *Journal of Physics and Chemistry of Solids*, **149**: 109775.
- Uzair Khan, A.L. Fanai and S. Rai (2018), Optical properties of holmium-doped in sol-gel silica glass, *Advances in Engineering Research*, **178**: 194-197.
- V. Lojpur, S. Culubrk, M. Medic, M. Dramicanin (2016), Luminescence thermometry with  $\text{Eu}^{3+}$  doped  $\text{GdAlO}_3$ , *J. Lumin.* **170**: 467–471.
- W. T. Carnall, P. R. Fields and K. Rajnak (1968), Spectral Intensities of the Trivalent Lanthanides and Actinides in Solution. II.  $\text{Pm}^{3+}$ ,  $\text{Sm}^{3+}$ ,  $\text{Eu}^{3+}$ ,  $\text{Gd}^{3+}$ ,  $\text{Tb}^{3+}$ ,  $\text{Dy}^{3+}$ , and  $\text{Ho}^{3+}$ , *J. Chem. Phys.* **49**: 4412–4423.
- W.T. Carnall, P.R. Fields and K.J. Rajnak (1968), Electronic Energy Levels in the Trivalent Lanthanide Aquo Ions. I.  $\text{Pr}^{3+}$ ,  $\text{Nd}^{3+}$ ,  $\text{Pm}^{3+}$ ,  $\text{Sm}^{3+}$ ,  $\text{Dy}^{3+}$ ,  $\text{Ho}^{3+}$ ,  $\text{Er}^{3+}$ , and  $\text{Tm}^{3+}$ , *Chem. Phys.* **59**: 4424-4432.
- Z. Antic, R. Krsmanovic, M.G. Nikolic, M. Marinovic-Cincovic, M. Mitric, S. Polizzi, M.D. Dramicanin (2012), Multisite luminescence of rare earth doped  $\text{TiO}_2$  anatase nanoparticles, *Mater. Chem. Phys.* **135**: 1064–1069.

## CHAPTER 5

### Effect of Al on photoluminescence properties of Nd<sup>3+</sup> in silicate glass-ceramic prepared by in-situ sol-gel method

---

#### Overview

Structural and spectroscopic properties of Nd<sup>3+</sup> co-doped alumino-silicate glass prepared by an in-situ sol-gel method. Structural characterization was carried out using X-ray powder diffraction (XRD), Fourier-transform infrared spectroscopy (FTIR) and scanning electron microscopy (SEM) techniques. The XRD analysis reveals that the material is still amorphous even after being heated to 900 °C. FTIR analysis was used to identify the functional groups of the produced sol-gel silicate glass. The optical absorption spectra from the ground state <sup>4</sup>I<sub>9/2</sub> show seven peaks in the UV-VIS and NIR regions. The optical absorption spectrum of Nd<sup>3+</sup> co-doped alumino-silicate glass-ceramic was used to determine the Judd-Ofelt (JO) intensity parameters ( $\Omega_2$ ,  $\Omega_4$  and  $\Omega_6$ ). The photoluminescence (PL) spectrum was recorded with a 2W diode laser source of 808 nm excitations. From the larger stimulated emission cross-section ( $3.80 \times 10^{-20} \text{ cm}^2$ ) of the <sup>4</sup>F<sub>3/2</sub> → <sup>4</sup>I<sub>11/2</sub> transition, it is concluded that the SiNdAl glasses could be highly useful for the development of solid state laser materials. From the observed refractive indices at three different wavelengths, non-linear parameters for the glass, such as the Abbe number ( $v_{Ab}$ ) and non-linear refractive index ( $n_2$ ), are derived.

#### 5.1. Introduction

Recently, the study of rare earth (RE) ions doped amorphous or crystalline solids materials have attracted much attention because of their attractive optical characteristics, high transition temperature, and low thermal expansion coefficients (Hazarika *et al.*, 2007, Azam *et al.*, 2018, Hajer *et al.*, 2019). These materials hold promise for diverse applications such as optical communications, biosensors, optical amplifiers, and light-emitting diodes (LEDs) (Soltys *et al.*, 2018, Caldino *et al.*, 2018). Rare earth-doped materials are essential components for low-cost integrated laser sources, integrated optical amplifiers, 3D display devices, sensors, up-

conversion fibers, and low-loss components (Kashif *et al.*, 2014, Pisarski *et al.*, 2020, Ramesh *et al.*, 2018), among other current optical technology products (Ramesh *et al.*, 2018, Venkateswarlu *et al.*, 2015), because of their fluorescence in the near IR region at 1.06  $\mu\text{m}$  after the introduction of the first glass laser by Snitzer (Snitzer *et al.*, 1961). The choice of a suitable glass matrix as a host for the development of efficient optical devices doped with lanthanide ions is an active area of research. Even hosts with higher phonon energies can exhibit fluorescence spectra effectively due to the relatively large energy gap in the transition from the lanthanide ion's  $^4\text{F}_{3/2}$  level to the next lower  $^4\text{I}_{15/2}$  level (Venkateswarlu *et al.*, 2015).  $\text{SiO}_2$  glass is an excellent host for lanthanide ions because of its low cost, high optical transmission, low thermal expansion, excellent chemical and thermal stability, good mechanical strength and good moisture resistance (Yamane *et al.*, 2000). However, the exceptional thermal stability of  $\text{SiO}_2$  glass poses challenges in conventional synthesis methods, as silica typically required processing temperatures above 2000  $^{\circ}\text{C}$  (Silversmith *et al.*, 2006). Such doped silica glasses can be created using the sol-gel process at significantly lower temperatures. Additionally, while still preserving an amorphous character, it allows the incorporation of larger dopant concentrations than traditional melt glasses (Bouzidi *et al.*, 2016, Dabboussi *et al.*, 2009). However, a variety of factors prevent them from being used as effective optical materials. In the sol-gel glass hosts, lanthanide ions tend to cluster, which causes concentration quenching (Almeida *et al.*, 1998). Additionally, there is quenching brought on by hydroxyl (-OH) groups that were left over from the initial preparation procedure. Prolonged heat treatment can lower the hydroxyl concentration. Heating affects the physical parameters of the system, such as density, refractive index, and other structural aspects, in addition to removing hydroxyls (Brinker *et al.*, 1985, Ferrari *et al.*, 1994). Vibrations within the host glass provide a non-radiative relaxation path for excited ions, resulting in energy loss via phonon in the glass network (Ferrari *et al.*, 1992).  $\text{SiO}_2$  glass has a rather high maximum phonon energy (1100  $\text{cm}^{-1}$ ) and energy loss occurs via multi-phonon relaxation (Ligang *et al.*, 2010). Hence, photoluminescence (PL) is typically only observed from excited states with significant energy gaps. Additionally, the energy level structure of the lanthanide ions makes it susceptible to cross-relaxation as concentration increases, which tends



to result in  $\text{Nd}^{3+}$  clustering. It has been demonstrated that co-doping aluminum with lanthanide ions in doped sol-gel glasses increases fluorescence output (Arai *et al.*, 1986, Zhong *et al.*, 1999). Non-bridging oxygen's (NBOs) are believed to be introduced into the matrix by aluminum doping (Alombert *et al.*, 2005). With silicon or aluminum, the NBOs only form one bond, leaving another open to form a bond with the lanthanide ions. Al species surround each lanthanide ions in this way, separating them from one another. Hence, cross-relaxation is decreased and PL efficiency is raised.

The highly efficient  $^4\text{F}_{3/2} \rightarrow ^4\text{I}_{11/2}$  lasing transition occurring at 1058 nm positions  $\text{Nd}^{3+}$  as one of the most extensively studied  $\text{RE}^{3+}$  ions when combined with various hosts, particularly for its application in solid-state lasers. The presence of absorption bands across the UV-VIS-NIR spectrum further enhance its suitability, facilitating the pumping of the Nd-laser systems through either broad-band sources such as xenon lamps or diode lasers (Snitzer *et al.*, 1961, Arai *et al.*, 1986). Laser efficiency primarily relies upon factors like emission cross-section and luminescence decay rates, which are significantly influenced by non-radiative decays within the system, including multi-phonon relaxation processes (Venkateswarlu *et al.*, 2015, Snitzer *et al.*, 1961). In hosts derived from sol-gel techniques, the phenomenon of dopant clustering where luminescent species aggregate through oxygen linkage can lead to a reduction in luminescence intensity due to cross-relaxation and energy transfer processes (Arai *et al.*, 1986). However, these limitation can be mitigated to a considerable extent by incorporating small quantities of co-dopant like Al,  $\text{TiO}_2$ , borate and tellurite (Hazarika *et al.*, 2007, Azam *et al.*, 2018, Kashif *et al.*, 2014, Venkateswarlu *et al.*, 2015), as well as utilizing organic salts as glass precursors instead of mineral acid salts, in addition to optimizing the concentrations of  $\text{RE}^{3+}$  ions and hosts.

## 5.2. Experimental Details

The composition of the bulk glasses (in mol%)  $(99-x)\text{SiO}_2 + 1\text{NdF}_3 + x\text{Al}_2\text{O}_3$  (here  $x = 0.0, 1.2, 2.0$  and  $3.0$  mol%) were prepared by using a sol-gel technique with Tetraethylorthosilicate (TEOS) as the main precursor, Ethanol as the solvent, Nitric acid ( $\text{HNO}_3$ ) as the catalyst,  $\text{Al}(\text{NO}_3)_3 \cdot 9\text{H}_2\text{O}$  and  $\text{NdF}_3$  as the source. The dopant is mixed with  $\text{CH}_3\text{OH}$ ,  $\text{HNO}_3$ , and banana trunk sap and stirred for 45 minutes. A sol is created by adding TEOS to this solution and stirring it for a further two hours using a magnetic stirrer. The final solutions of TEOS, banana trunk sap, EtOH, and  $\text{HNO}_3$  are in the following molar ratios: 1: 5.5; 3.5; 0.1. The last sol is then transferred to a plastic cap sealed to prevent evaporation. After the sol has gelled and been sealed at room temperature for 26 days, and also some pinholes are made in a plastic container's lid to allow for slow evaporation. After that, the container is left for a few weeks. To make dense glass samples in the shape of discs, the gels are further dried in an electric muffle furnace by gradually heating to  $40^\circ\text{C}$  and then annealing up to  $1060^\circ\text{C}$  at a heating rate of  $1^\circ\text{Cmin}^{-1}$ .

## 5.3. Result and discussions

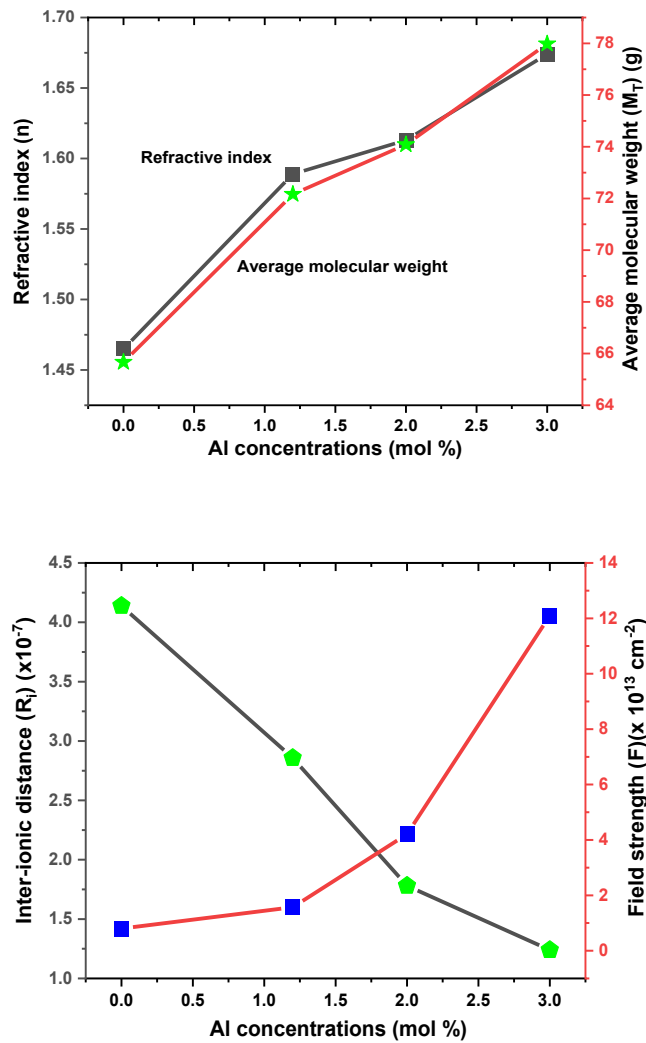
### 5.3.1. Various Physical Properties

The measured glass densities, refractive indices for all of these  $\text{SiNdAl0}$ ,  $\text{SiNdAl1.2}$ ,  $\text{SiNdAl2}$ , and  $\text{SiNdAl3}$  in sol-gel glasses, and other physical characteristics have all been estimated. These values are shown in Table 5.1. These values are estimated using the approach outlined by (Bokatial *et al.*, 2012)

**Table 5.1**

Various physical properties of SiNdAl0, SiNdAl1.2, SiNdAl2 and SiNdAl3 in sol–gel glasses annealed at 1060 °C were observed.

Physical properties	SiNdAl0	SiNdAl1.2	SiNdAl2	SiNdAl3
Refractive index ( $n$ )	1.465	1.589	1.613	1.674
Density ( $\rho$ ) ( $gm/cm^3$ )	1.92	2.06	2.11	2.20
Thickness ( $Z$ )	0.179	0.179	0.179	0.179
Average molecular weight ( $M_T$ ) ( $g$ )	65.665	72.163	74.085	77.982
Reflection losses ( $R_L$ ) (%)	0.036	0.052	0.055	0.064
Molar refractivity ( $R_m$ ) ( $cm^3$ )	9.449	11.806	12.223	13.302
Energy gap ( $E_g$ )	10.48	8.78	8.5	7.82
Molar electronic polarizability ( $\alpha_m$ )	3.676	4.685	4.694	5.006
Dielectric constant ( $\epsilon$ )	2.146	2.525	2.602	2.802
Optical dielectric constant( $\epsilon-1$ )	1.146	1.525	1.602	1.802
Electronic polarizability ( $\alpha_e$ ) ( $\times 10^{-25}$ )	1.096	1.337	1.381	1.488
Nd <sup>3+</sup> ion concentration ( $N$ )( $\times 10^{22}$ ions/ $cm^3$ )	0.141	0.429	1.771	5.258
Molar volume ( $V_m$ ) ( $cm^3/mol$ )	34.183	35.031	35.111	35.446
Polaron radius( $R_p$ )( $\times 10^{-8}$ )Å	14.92	11.51	7.18	4.35
Inter-ionic distance ( $R_i$ ) ( $\times 10^{-7}$ )Å	4.139	2.857	1.781	1.239
Field strength ( $F$ )( $\times 10^{13}$ $cm^{-2}$ )	0.804	1.570	4.209	12.102
Metallization criterion ( $M$ )	0.724	0.663	0.652	0.625



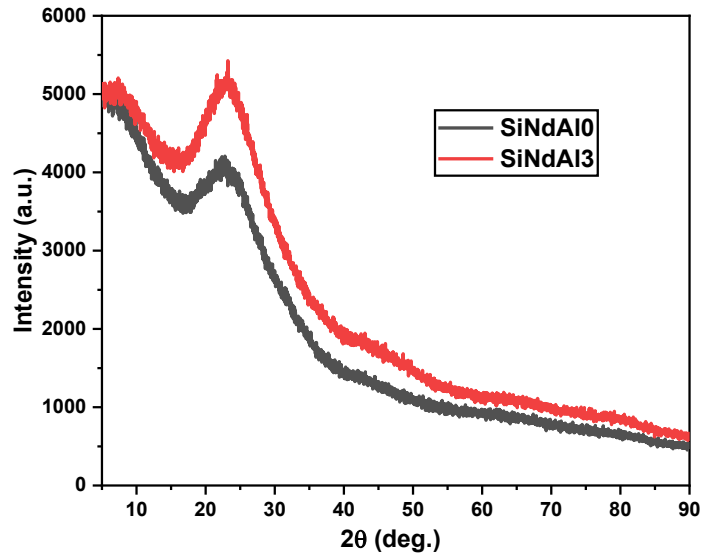
**Fig. 5.1(a):** The variations in the refractive index and average molecular weight (g) characteristics in sol-gel glasses for SiNdAl0, SiNdAl.2, SiNdAl2, and SiNdAl3. **5.1(b):** Inter ionic distance ( $10^{-7}$ ) and field strength ( $10^{13} \text{ cm}^{-2}$ ) parameter variations in sol-gel glasses as a function of SiNdAl0, SiNdAl.2, SiNdAl2, and SiNdAl3.

The variations in the sol-gel glasses' density ( $\text{g/cm}^3$ ), refractive index, average molecular weight ( $M_T$ ), inter ionic distance ( $R_i$ ), and field strength ( $\times 10^{13} \text{ cm}^{-2}$ ) as a function of SiNdAl are shown in Figs. 5.1a and 5.1b (Dihingia *et al.*, 2012). This is further verified by Figs. 5.1a and 5.1b, which demonstrate that the average molecular weight increased and the interionic distance decreased as the concentration of  $\text{Al}^{3+}$  ions increased. The tendency of decreasing inter ionic distance

in these glasses shows that the atoms are becoming more densely packed as the  $\text{Al}^{3+}$  ion concentration in these glasses increases (Bokatial *et al.*, 2012). Fig. 5.1a shows that the refractive index of SiNdAl in sol-gel glasses rises as the concentration of dopant ions increases. As the density of the SiNdAl in sol-gel glasses rises along with the concentration of the dopant ions, the medium's refractive index will rise as well. It is also evident from Fig. 5.1b that the field strength values rise as the concentration of  $\text{Al}^{3+}$  ions does. This is clear from the fact that when the concentration of aluminium ions in glass rises, more ions will be made available per unit volume, increasing the field strength. The molecule electronic polarizability of these glasses is of the order  $10^{-25}$ , it is incredibly low (Dawngliana *et al.*, 2022), as shown in Table 5.1. As a result, the present samples of SiNdAl in sol-gel glasses are considered to be more stable.

### 5.3.2. X-ray powder diffraction studies

The powdered X-ray diffraction spectrum of SiNdAl0 and SiNdAl3 in sol-gel glasses after annealing at 900 °C is shown in Fig. 5.2. Instead of sharp crystalline peaks with crystallinity indices more than 38%, distinct broad peaks are seen, confirming the glass samples' glassy amorphous nature. The amorphous nature of silica glass is thought to be responsible for the broad peak at  $2\theta = 22$  (Swapna *et al.*, 2014).

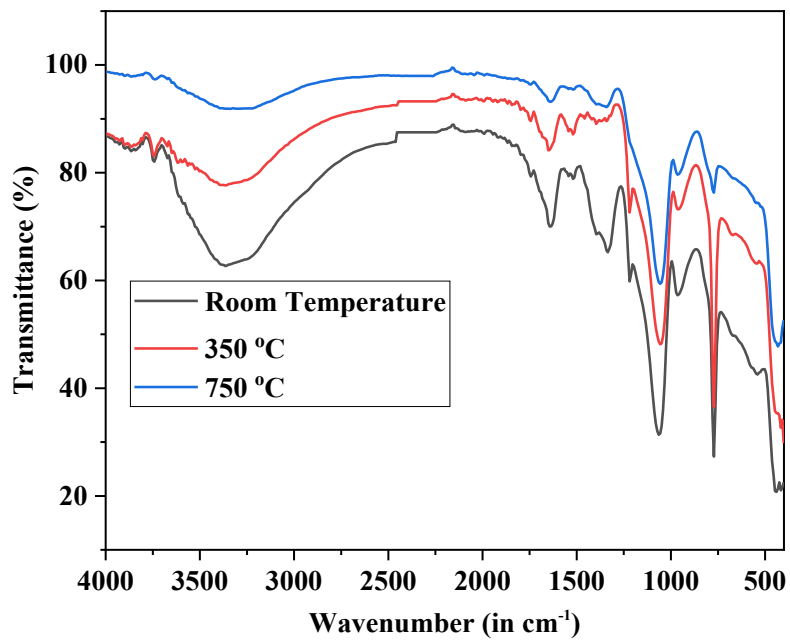


**Fig. 5.2:** XRD spectrum of SiNdAl0 and SiNdAl3 in sol-gel glasses.

### 5.3.3. FTIR Analysis

FTIR spectra of SiNdAl3 in sol-gel glasses is annealed at different temperatures (room temperature, 350, and 750 °C), as shown in Fig. 5.3, the FTIR spectra obtained from the vibration of different bonds present are captured in the 400–4000  $\text{cm}^{-1}$  wavenumber range. A number of peaks can clearly be seen at about 417, 441, 471, 588, 671, 771, 964, 1065, 1219, 1335, 1397, and 3363  $\text{cm}^{-1}$ . To create a 3-D silica network, TEOS is hydrolyzed and condensed with the help of water and alcohol. This process also yields Si-OH groups. The gel stage of the sol-gel glass is mostly made up of water and other organic species. As the sintering temperature is increased, the broad peak between 3363 and 3723  $\text{cm}^{-1}$  vanishes as a result of the removal of OH- and water molecules ( $\text{H}_2\text{O}$ ), which are responsible for the sample's O-H stretching vibration (Osman *et al.*, 2022). The band's intensity is greatest for glass at room temperature and gradually decreases as the temperature rises. As temperatures increased, the peak brought on by the stretching of Si-OH bands and the appearance of absorbed water became less intense, according to the FTIR spectra (Osman *et al.*, 2022). The peak's broadening and shift to the low frequency side indicate a decrease in phonon energy. The aluminium ion modifies the network by

dissolving the SiO<sub>2</sub> structure to create a non-bridging Al-O group, such as Si-O-Al, which can also coordinate with lanthanide ions (Bokatial *et al.*, 2012). When the Si-O-Si bond breaks, the NBO of Nd-O-Si may also arise ions (Bokatial *et al.*, 2012). Al-O in the octahedral coordination state is attributed to the bending mode of the peak around 487-548 cm<sup>-1</sup>. Si-OH group polymerization results in Si-O-Si bands with frequencies of 1335–1397 cm<sup>-1</sup> and 1057–1065 cm<sup>-1</sup>, respectively (Hussein *et al.*, 2018). The presence of a widened Si-O free peak at 964 cm<sup>-1</sup> in gels that were annealed at room temperature has been noted. Hence, annealing of the glass sample leads the components to gradually vanish from the glass host matrix, leading to the development of a stiff glassy network, which is evident from the FTIR spectra. Table 5.2 displays the bands' assignments.



**Fig. 5.3:** The Fourier Transmission Infrared spectra of SiNdAl<sub>3</sub> in the glass samples after being annealed at various temperatures.

**Table 5.2**

The various assignments of the glass samples' FTIR peak positions.

Wavenumber (cm <sup>-1</sup> )	Assignment	Observed intensity	Change in intensity during heating
417-441	Si-O and O-Si-O vibrations caused by asymmetric stretching (Hussein <i>et al.</i> , 2018)	Broad	In room temperature and 350 °C, there is two peaks arise 417, 439. At temperature 750 °C, peaks arise at 428.
487-548	Si-O-Al bending with an asymmetric NBO (Non-bridging oxygen) ions (Bokatial <i>et al.</i> , 2012)	Minor peak	Intense peak arise at room temperature, 350 °C and removed in 750 °C
673	Bending of the symmetric Si-O of SiO <sub>4</sub> ions (Bokatial <i>et al.</i> , 2012)	No peak	Minor peak at room temperature, 350 °C and remove with rising temperature
771	Si-OH stretching (Wang <i>et al.</i> , 1997)	Strong	Decrease with increasing temperature
964	Si-O-H stretch vibrational mode	Strong	Decrease with increasing temperature
1057-1065	Si-O-Al & Al-O-	Intense peak	Reduction in



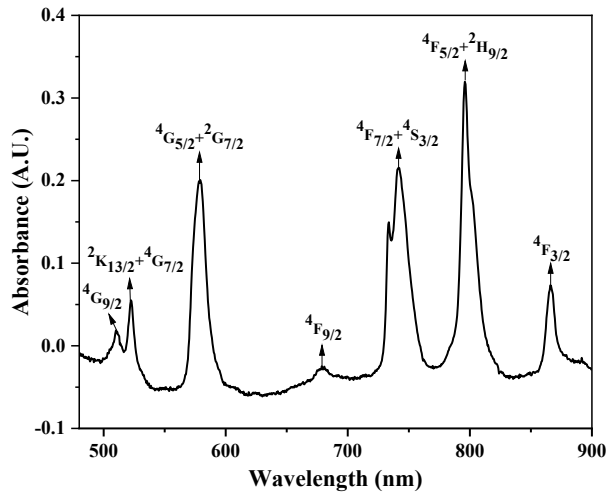
	Al asymmetric stretching ions (Bokatial <i>et al.</i> , 2012)		intensity and a red shift
1219	Stretching vibration C-O-C (Yan <i>et al.</i> , 2021)	Minor peak	The peak remove in $T > 750\text{ }^{\circ}\text{C}$
1335-1397	Si-O-Si	Broad	Decrease with increasing temperature
1519-1652	-OH bending vibration mode of water	Minor peak	Decrease when the temperature rises
3363-3723	O-H stretching (Naveen <i>et al.</i> , 2015)	Broad, strong	Decrease when the temperature rises

---

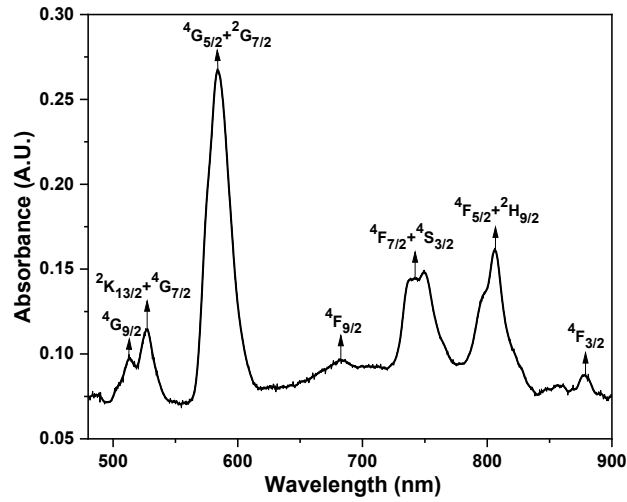
#### 5.3.4. Absorption Spectra

The absorption spectra of SiNdAl3 samples with sol-gel glass as shown in Figs. 5.4(a) and 5.4(b), respectively, in the porous gel stage and densified stage. The relative intensities of the various absorption peaks shift as the heat treatment is varied. Some physical characteristics of the material were changed by heating up to 1060 °C. The first case uses a sample that quickly reabsorbs atmospheric moisture because it is extremely porous, has a low density of about 1.34 g/cm<sup>3</sup>, and is exposed to the atmosphere. The sample loses the majority of its porosity after being annealed at 1060 °C and reaches a density of around 2.20 g/cm<sup>3</sup> that is comparable to melt glass. Figs. 5.4(a) & 5.4(b) show the spectral range 480–900 nm of SiNdAl3 glass samples in optical absorption spectrum at room temperature along with band assignments. As seen in the Figs. 5.4(a) & 5.4(b), there are 7 bands in the absorption spectra that correspond to the transition between the ground state (GS) <sup>4</sup>I<sub>9/2</sub> and the excited states (ES) of the 4f<sup>3</sup> configuration of lanthanide ions (Osman *et al.*, 2022).

The band positions at 512, 523, 579, 679, 742, 795, 870 nm are corresponding to the transitions  $^4I_{9/2} \rightarrow ^4G_{9/2}$ ,  $^2K_{13/2} + ^4G_{7/2}$ ,  $^4G_{5/2} + ^2G_{7/2}$ ,  $^4F_{9/2}$ ,  $^4F_{7/2} + ^4S_{3/2}$ ,  $^4F_{5/2} + ^2H_{9/2}$  and  $^4F_{3/2}$  respectively (Wang *et al.*, 1997). One transition in particular,  $^4I_{9/2} \rightarrow ^4G_{5/2} + ^2G_{7/2}$ , is more intense than others in the dense glass and has high oscillator strengths across all the glasses being studied (Wang *et al.*, 1997). The selection rules  $|\Delta J| \leq 2$ ;  $|\Delta L| \leq 2$  and  $|\Delta S| = 1$  are valid for this transition, which is also referred to as the hypersensitive transition (Wang *et al.*, 1997). As the material is heated to higher temperatures, the redshift in the absorption peaks that occurs is another interesting result. In Figs. 5.4(a) and 5.4(b), the major near-infrared peaks change from 795 nm and 871 nm to 806 nm and 879 nm (Rai *et al.*, 2016). The redshift seen after annealing is caused by the nephelauxetic effect, which occurs as the  $Nd^{3+}$  starts incorporating into the covalent glass network (Rai *et al.*, 2016).



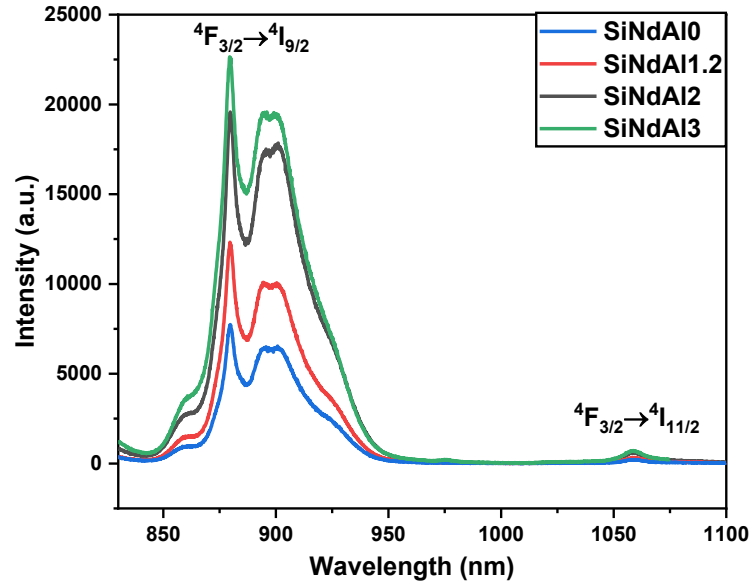
**Fig. 5.4(a):** Sol-gel glass at the porous gel stage (150 °C) absorption spectra with SiNdAl3.



**Fig. 5.4(b):** Sol-gel glass after densification (1060 °C) absorption spectra with SiNdAl3.

### 5.3.5. Photoluminescence Spectra

The photoluminescence spectra of SiNdAl0, SiNdAl1.2, SiNdAl2 and SiNdAl3 glasses annealed at 1060 °C, are recorded using the excitation wavelength  $\lambda_{\text{ex}} = 808$  nm in the 830-1100 nm range. The two broad, asymmetric bands in the emission spectra are located around 879 and 1058 nm. These emission bands correspond to the  $\text{RE}^{3+}$  ion transitions  $^4\text{F}_{3/2} \rightarrow ^4\text{I}_{9/2}$  and  $^4\text{F}_{3/2} \rightarrow ^4\text{I}_{11/2}$ , respectively. The emission line near 879 nm in Fig. 5.5 is the  $^4\text{F}_{3/2} \rightarrow ^4\text{I}_{9/2}$  transition. With increasing concentrations of aluminium ions and lessening the effects of concentration quenching, a peak that initially occurred at about 1058 nm and transformed into a minor from a broad one may be seen (Rai *et al.*, 2016). The most intense transition in the current studies has a peak at 879 nm. The increase in NBO changes the electronic structure of glasses, promoting transitions with lower energy, which are further confirmed by FTIR spectra (Bokatial *et al.*, 2012). The peaks are intense with increasing concentrations of aluminum (Zamratul *et al.*, 2016, Duhan *et al.*, 2008). In silicate sol-gel glasses, it has been reported that SiNdAl0, SiNdAl1.2, SiNdAl2 and SiNdAl3 results in PL spectra with splitting (Stark splitting), which is consistent with the host being altered by the presence of Al (Table 5.6) (Zhang *et al.*, 2014).



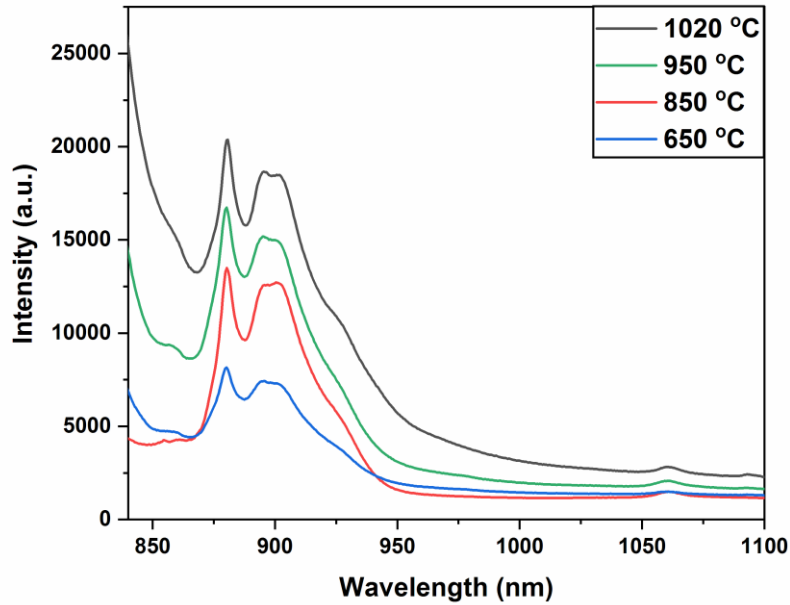
**Fig. 5.5:** PL spectra of SiNdAl0, SiNdAl1.2, SiNdAl2 and SiNdAl3 in sol–gel glasses annealed at 1060 °C.

### 5.3.6. Effect of annealing temperature of PL intensity

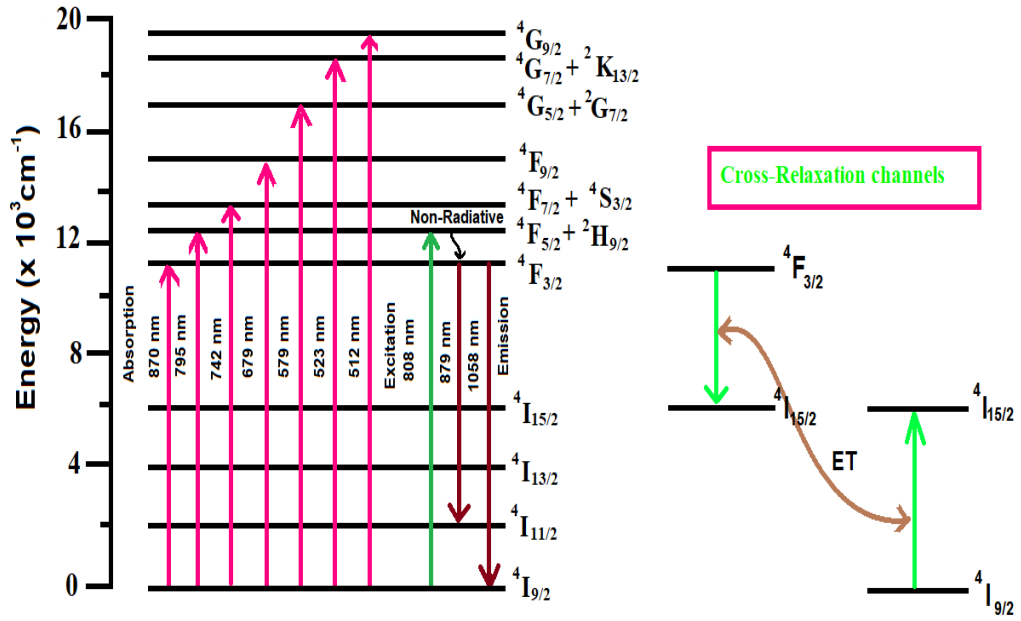
Using the excitation ( $\lambda_{\text{ex}} = 808 \text{ nm}$ ), the photoluminescence spectra of SiNdAl3 sol-gel glasses was measured at various annealing temperatures. NBO (Si-O-Al), whose phonon energy is lower than the vibration of the Si-O-Si bond, is formed and causes asymmetry (Bokatial *et al.*, 2012). This is confirmed by the observed FTIR spectra. The sample quenched by the hydroxyl (OH) group after being annealed at 650 °C exhibits very little intensity. The high phonon energy OH group quenches the PL of  $\text{Nd}^{3+}$  ions (Zamratul *et al.*, 2016). Energy transfer to the  $\text{Nd}^{3+}$  ions in silica xerogel is slowed down by the creation of electrons and holes through defect recombination. As a result, the elimination of the OH group increases the PL intensity for dense glasses that are annealed at higher temperatures (Fig. 5.6) (Zamratul *et al.*, 2016, Dawngliana *et al.*, 2023). As a result, PL enhancement is due to host matrix asymmetry and OH group elimination at high annealing temperatures. Stark splitting at transitions  $^4\text{I}_{9/2}$  in  $\text{Nd}^{3+}$  in silicate glass is observed in photoluminescence spectra for SiNdAl0, SiNdAl1.2, SiNdAl2 and SiNdAl3 (Table 5.6), which is consistent with the host being modified at the higher temperature

(1060 °C) (Yan *et al.*, 2021). Compare the stark-split energy levels of  $\text{Nd}^{3+}$  in various crystalline lattices as well (Table 5.7).

For the cross-relaxation of two ions that are close to one another, the energy level structure of  $\text{Nd}^{3+}$  provides a very effective approach (Bokatia *et al.*, 2012). With increasing concentration, the possibility of cross-relaxation increases because  $\text{Nd}^{3+}$  clusters are more likely to form. Both  $\text{Nd}^{3+}$  ions may occupy the intermediate state  $^4\text{I}_{15/2}$  before relaxing non-radiatively to the ground state as a result of one RE ion in the excited  $^4\text{F}_{3/2}$  state losing some of its energy to the neighboring ion in the ground state (Fig. 5.7) (Rai *et al.*, 2016).



**Fig. 5.6:** Effect of the PL spectrum of SiNdAl3 glass samples at annealing temperatures.



**Fig. 5.7:** Schematics diagram of energy level of SiNdAl0, SiNdAl1.2, SiNdAl2 and SiNdAl3 in sol-gel glasses.

### 5.3.7. Judd-Ofelt/ Radiative parameters

According to the Judd–Ofelt (J-O) theory (Judd, 1962, Ofelt, 1962), the radiative transitions belonging to the  $4f^2$  configuration of  $\text{Nd}^{3+}$  can be analyzed based on the absorption spectra of  $\text{Nd}^{3+}$  ion (Fig. 5.4(a) & 5.4(b)). The J–O intensity parameters  $\Omega_\lambda$  ( $\lambda = 2, 4$ , and  $6$ ) for  $\text{Nd}^{3+}$  in the SiNdAl3 sample are derived by the least square fitting of oscillator strength derived from experiment ( $f_{\text{exp}}$ ) and calculation ( $f_{\text{cal}}$ ) oscillator strength using as obtained squared matrix elements (Carnall *et al.*, 1978, Bhatia *et al.*, 2015, Carnall *et al.*, 1968). The large number of  $\Omega_6$  reasonably indicates that the hosts [Nd-O, Nd-Al] (Chimalawong *et al.*, 2010, Hazarika *et al.*, 2007, Sontakke *et al.*, 2013) and  $\text{Nd}^{3+}$  ions have covalent bonds with the other two metals. The  $\Omega_2$  value in the present study increases from  $2.12 \times 10^{-20} \text{ cm}^2$  in lower temperature treated to  $4.93 \times 10^{-20} \text{ cm}^2$  with annealing while the  $\Omega_6$  value decreases from  $3.32 \times 10^{-20} \text{ cm}^2$  to  $2.21 \times 10^{-20} \text{ cm}^2$ . This might be because as the temperature rises, more  $\text{Nd}^{3+}$  ions are incorporated into the strong covalent glass network and hydroxyl ions are removed. A reduced centrosymmetric coordination

environment around  $\text{Nd}^{3+}$  ions in the silica host is also suggested by the large value of  $\Omega_2$ . Although the Judd Ofelt analysis and the  $\Omega_\lambda$  parameters (Binnemans *et al.*, 1998) have a significant inherent error, a pattern is seen where the  $\Omega_2$  value rises as the temperature rises (Table 5.3(a) & 5.3(b). Similar patterns were seen in the emission spectra of the  $\text{RE}^{3+}$  ion in sol-gel glass by Qiao *et al.* (Qiao *et al.*, 2007) and Reisfeld *et al.* (Reisfeld *et al.*, 1999), both of which showed that Al may reduce the site symmetry of the  $\text{RE}^{3+}$  ion. Due to the bond between the ligand atoms and  $\text{RE}^{3+}$  ions, the values of  $\Omega_4$  and  $\Omega_6$  produce vibronic transitions, which are dependent on the dielectric and viscosity characteristics of the medium (glass) (Syam *et al.*, 2018). Table 5.4 compares the spectroscopic quality factor ( $\Omega_4/\Omega_6$ ) and J-O intensity values in various hosts. The local structure and bonding around  $\text{Ln}^{3+}$  ions are revealed by the J-O parameter (Sontakke *et al.*, 2013). A significant value of  $\Omega_2$  indicates a strong covalency of the metal-ligand bonding, whereas a large value of  $\Omega_6$  indicates a high stiffness. The parameter  $\Omega_2$  is known to be structure/environment sensitive and to depend on the covalency and asymmetry of ion sites near  $\text{Ln}^{3+}$  ions, in contrast to  $\Omega_6$ , which is dependent on vibronic (Singh *et al.*, 2017). Due to the nephelauxetic effect, covalent bonding reduces the electronic levels of free ions and raises  $\Omega_2$  values. It is found that for hypersensitive transitions with  $|\Delta J| = 2$ ,  $\Omega_2$  becomes more significant (Hehlen *et al.*, 2013). The hosts' structural characteristics have a significant impact on the transitions' intensities. The comparison of J-O parameters of  $\text{Nd}^{3+}$  ion is tabulated in Table 2. The radiative properties such as the radiative lifetimes ( $\tau_R$ ), branching ratios ( $\beta_r$  (%)), total transition probabilities ( $A_{ed}$ ), and radiative transition probabilities ( $A_T$ ) for the optical transitions of  $\text{Nd}^{3+}$  in the  $\text{SiNdAl3}$  are estimated using J-O intensity parameters in Table 5.5.

**Table 5.3(a)**Oscillator strengths and  $\Omega_\lambda$  parameters for SiNdAl3 samples in the porous gel stage.

Transitions $^4I_{9/2} \rightarrow ES$	Energy ( $\text{cm}^{-1}$ )	Wavelength (nm)	$f_{\text{exp}}$ ( $\times 10^{-6}$ )	$f_{\text{cal}}$ ( $\times 10^{-6}$ )
$^4G_{9/2}$	19531	512	1.02	1.45
$^2K_{13/2} + ^4G_{7/2}$	19120	523	2.46	4.70
$^4G_{5/2} + ^2G_{7/2}$	17271	579	9.98	3.30
$^4F_{9/2}$	14728	679	2.68	0.37
$^4F_{7/2} + ^4S_{3/2}$	13477	742	5.42	11.39
$^4F_{5/2} + ^2H_{9/2}$	12579	795	4.09	2.53
$^4F_{3/2}$	11494	870	1.56	0.66
	$\Omega_2 = 2.12$ ( $\times 10^{-20}$ $\text{cm}^2$ )	$\Omega_4 = 2.09$ ( $\times 10^{-20} \text{ cm}^2$ )	$\Omega_6 = 3.32$ ( $\times 10^{-20} \text{ cm}^2$ )	
		$\Omega_4 / \Omega_6 = 0.63$ ( $\times 10^{-20}$ )		



**Table 5.3(b)**

After densification, the oscillator strengths and  $\Omega_\lambda$  parameters for SiNdAl3 samples in the dense glass.

Transitions	Energy	Wavelength	$f_{\text{exp}}$	$f_{\text{cal}}$
$^4\text{I}_{9/2} \rightarrow \text{ES}$	( $\text{cm}^{-1}$ )	(nm)	( $\times 10^{-6}$ )	( $\times 10^{-6}$ )
$^4\text{G}_{9/2}$	19268	519	0.78	1.28
$^2\text{K}_{13/2} + ^4\text{G}_{7/2}$	18797	532	3.12	3.25
$^4\text{G}_{5/2} + ^2\text{G}_{7/2}$	17123	584	18.96	11.95
$^4\text{F}_{9/2}$	14641	683	2.08	0.86
$^4\text{F}_{7/2} + ^4\text{S}_{3/2}$	13316	751	3.70	4.87
$^4\text{F}_{5/2} + ^2\text{H}_{9/2}$	12422	805	3.72	3.96
$^4\text{F}_{3/2}$	11390	878	1.60	0.95
	$\Omega_2 = 4.93$	$\Omega_4 = 3.01$	$\Omega_6 = 2.21$	
	( $\times 10^{-20} \text{ cm}^2$ )	( $\times 10^{-20} \text{ cm}^2$ )	( $\times 10^{-20} \text{ cm}^2$ )	
		$\Omega_4 / \Omega_6 = 1.36$		
		( $\times 10^{-20}$ )		

**Table 5.4**

Spectroscopic quality factor ( $X=\Omega_4/\Omega_6$ ) and JO parameters ( $\times 10^{-20} \text{ cm}^2$ ) comparison of the  $\text{Nd}^{3+}$  co-doped with aluminum in  $\text{SiO}_2$  glasses with previous published works.

$\Omega_2$	$\Omega_4$	$\Omega_6$	$\Omega_4/\Omega_6$	References
<b>2.12</b>	2.09	3.32	0.63	<b>Present work</b>
<b>4.93</b>	3.01	2.21	1.36	<b>Present work</b>
<b>7.16</b>	3.20	2.97	1.077	<b><math>\text{SiO}_2\text{-Al}^{3+}:\text{Nd}^{3+}</math> (Qiao <i>et al.</i>,</b>
<b>2.088</b>	2.260	2.884	0.795	<b><math>\text{NdCl}_3</math> in methanol (Mitra <i>et al.</i>,</b>
<b>1.790</b>	1.542	1.756	0.878	<b><math>\text{NdCl}_3</math> in butanol (Mitra <i>et al.</i>,</b>
<b>1.039</b>	1.531	3.209	0.447	<b><math>\text{NdCl}_3</math> in iso-propanol (Mitra</b>
<b>0.10</b>	3.58	2.87	1.24	<b>Glass A (Nisha <i>et al.</i>, 2018)</b>
<b>0.09</b>	3.68	2.94	1.25	<b>Glass B (Nisha <i>et al.</i>, 2018)</b>
<b>2.14</b>	2.57	1.93	1.33	<b>BSGdCaNd0.5 (Lee <i>et al.</i>,</b>
<b>1.83</b>	4.73	4.19	1.09	<b>Fluorophosphates (Choi <i>et al.</i>,</b>
<b>4.81</b>	<b>1.97</b>	<b>3.94</b>	<b>0.50</b>	<b>SPB1 (Karthikeyan <i>et al.</i>,</b>

**Table 5.5**

Radiative parameters.

Transitions $^4F_{3/2} \rightarrow$	Energy (in $\text{cm}^{-1}$ )	$A_{\text{ed}}$ (in $\text{s}^{-1}$ )	$\beta_r$ (in %)	$\Delta\lambda_{\text{eff}}$ (nm)	$\sigma_p(\lambda_p)$ ( $\times 10^{-20} \text{ cm}^2$ )
$^4I_{9/2}$	11377	678.85	43.3	13.56	1.42
$^4I_{11/2}$	9452	738.54	47.1	19.32	3.80
$^4I_{13/2}$	7468	142.63	9.1	-	-
$^4I_{15/2}$	5324	6.89	0.5	-	-
$A_T (\text{s}^{-1})=1566.91\text{s}^{-1} \quad \tau_R= 638 (\mu\text{s})$					

**Table 5.6**

Stark splitting in the spectrum of SiNdAl0, SiNdAl1.2, SiNdAl2 and SiNdAl3 in sol-gel glasses.

Transitions $^4G_{5/2} \rightarrow$	Wavelength ( $\lambda_p$ ) (nm)	Energy ( $\text{cm}^{-1}$ )	Assignment
$^4I_{9/2}$	879	11376	0
	894	11185	191
	901	11098	278
	926	10799	577

**Table 5.7**

Compare stark-split energy levels of  $\text{Nd}^{3+}$  in various crystalline lattices.

Transitions ${}^4\text{G}_{5/2} \rightarrow$	$\text{Nd}^{3+}$ in YAG [60]	$\text{Nd}^{3+}$ in $\text{Nd}_2\text{O}_3$ [61]	Present work
${}^4\text{I}_{9/2}$	0	0	0
	133	115	191
	199	123	278
	310	238	577
	859	249	-

### 5.3.8. Non-Linear Properties

The sol-gel  $\text{SiO}_2$  glass's good optical quality is reflected in the non-linear refractive index ( $n_2$ ), non-linear refractive index susceptibility ( $\chi^{(3)}$ ), coefficient ( $\gamma_{\text{ce}}$ ), and suitably high Abbe number ( $\nu_{\text{Ab}}$ ) (Dihingia *et al.*, 2012). These non-linear qualities have been determined from optical parameters. These values are shown in Table 5.8. The values are estimated based on the procedure reported by (Dihingia *et al.*, 2012).

**Table 5.8**

Non-linear parameters of co-doped with  $\text{SiNdAl3}$  in sol-gel glasses annealing at  $1060^\circ\text{C}$ , such as  $\eta_d$ ,  $1/\eta_d$ ,  $n_2$ ,  $\gamma$  and  $\chi$ .

$n_f$	$n_e$	$n_f - n_e$	$n_d$	$\nu_{\text{Ab}}$	$1/\nu_{\text{Ab}}$	$n_2$ ( $10^{-13}\text{esu}$ )	$\gamma$ ( $\text{cm}^2/\text{W}$ )	$\omega_o$ (* $10^{-13}$ )	$N$ $\times 10^{-16}$	$\chi$ $\times 10^{-7}$
1.504	1.495	0.009	1.500	55.6	0.018	1.378	0.385	126.13	816.296	8.69

#### 5.4. Conclusions

Al co-doping and the annealing process can be attributed for the increased PL intensity of  $\text{Nd}^{3+}$ .  $\text{RE}^{3+}$  ions are subjected to a modified vibrational coupling,  $\text{RE}^{3+}$  clustering is prevented by Al co-doping, and  $\text{RE}^{3+}$  are found in the aluminum-rich regions that have greater non-bridging Al-O groups available for coordination. The phonon energy of Al-O-Si bonds is lower than that of Si-O-Si bonds. In XRD confirmed that the present glass sample is amorphous nature. FTIR spectra show that the sample annealed at higher temperatures removed the OH group and evolved NBO on the low phonon energy side. The interesting candidates for laser host materials in ultrahigh peak power laser systems of Nd–alumina–silicate glasses. The JO intensities parameters are also estimated. The greater value of  $\Omega_2$  indicate of higher degree of covalency of the Nd–O bond and asymmetry of the  $\text{Nd}^{3+}$  sites in the Nd–alumina–silicate glass, according to the calculation of the J–O intensity parameters. Additionally, the observed nephelauxetic effect and the considerable change in the  $\Omega_2$  value both demonstrate it. The results indicate that an increase in Al concentrations strongly effects the improvement of PL property. Physical characteristics such as the relatively high Abbe number ( $\mathfrak{g}_d$ ), low non-linear refractive index ( $n_2$ ), and non-linear susceptibility ( $\chi^{e(3)}$ ) value confirm to the sample's strong optical quality (Dihingia *et al.*, 2012) and its superiority as a non-linear amorphous material.

## Reference

- A.D. Sontakke, K. Annapurna (2013), Spectroscopic properties and concentration effects on luminescence behavior of Nd<sup>3+</sup> doped Zinc-Boro-Bismuthate glasses, *Mat. Chem. Phys.* **137**: 916-921.
- A.J. Silversmith, D.M. Boye, K.S. Brewer, C.E. Gillespie, Y. Lu, D.L. Campbell (2006), <sup>5</sup>D<sub>3</sub>→<sup>7</sup>F<sub>J</sub> emission in terbium-doped sol–gel glasses, *J. Lumin.* **121**: 14-20.
- B. Bhatia, S.L. Meena, V. Parihar, M. Poonia (2015), Optical basicity and polarizability of Nd<sup>3+</sup> doped bismuth borate glasses, *New J. Glass and Cere.* **5**: 44-52.
- B. Karthikeyan, R. Philip, S. Mohan (2005), Optical and non-linear optical properties of Nd<sup>3+</sup> doped heavy metal borate glasses, *Opt. Com.* **246**: 153-162.
- B.R. Judd (1962), Optical absorption intensities of rare-earth ions, *Phys. Rev.* **127**: 750.
- C. Bouzidi, M. Ferhi, H. Elhouichet and M. Ferid (2016), Structural and luminescence properties of (Ba<sub>1-x</sub>Eu<sub>x</sub>)MoO<sub>4</sub> powders, *J. Lum.* **179**: 230-235.
- C.J. Brinker, G.W. Scherer, E.P. Roth (1985), Sol → gel → glass: II. Physical and structural evolution during constant heating rate experiments, *J. Non-Cryst Sol.* **72**: 345-368.
- C.R. Kesavulu, H.J. Kim, S.W. Lee, J. Kaewkhao, N. Wantana, E. Kaewnuam, S. Kothan, S. Kaewjaeng (2017), Spectroscopic investigations of Nd<sup>3+</sup> doped gadolinium calcium silica borate glasses for the NIR emission at 1059 nm, *J. Alloys Comp.* **695**: 590-598.
- E. Snitzer (1961), Optical Maser Action of Nd<sup>3+</sup> in a Barium Crown Glass, *Phys. Rev. Lett.* **7**: 444.
- G. Alombert-Goget, N. Gaumer, J. Obriot, A. Rammal, S. Chaussedent, A. Monteil, H. Portales, A. Chiasera, M. Ferrari (2005), Aluminum effect on photoluminescence properties of sol–gel-derived Eu<sup>3+</sup>-activated silicate glasses, *J. Non-Cryst Sol.* **351**: 1754-1758.
- G. Singh, R. Selvamani (2017), Spectroscopic investigations of Nd<sup>3+</sup> doped PLZT ceramics on the basis of Judd-Ofelt theory, *J. Lum.* **192**: 1084–1088.

- G.S. Ofelt (1962), Intensities of crystal spectra of rare-earth ions, *J. Chem. Phys.* **37**: 511.
- H. Zhong, W. Cai, L. Zhang (1999), Fluorescence properties of Tb<sup>3+</sup> ions in SiO<sub>2</sub> glass co-doped with Al<sup>3+</sup>, *Mat. Res. Bul.* **34**: 233.
- Hajer Said, Refka Oueslati Omrani, Laura Ruiz Arana, Dhouha El Bahri, Slim Boussen, Chaker Bouzidi, Huayna Terraschke, Ahmed Hichem Hamzaoui and Adel M'nif (2019), The effect of silica additive on the structural and luminescence properties of Eu<sup>3+</sup>/Tb<sup>3+</sup> co-doped metaphosphate glasses, *J. Mol. Struct.* **1192**: 42–48.
- Hussein Fneich, Nathalie Gaumer, Nathalie Gaumer, Wilfried Blanc and Ahmad Mehdi (2018), Europium-Doped Sol-Gel SiO<sub>2</sub>-Based Glasses: Effect of the Europium Source and Content, Magnesium Addition and Thermal Treatment on Their Photoluminescence Properties, *Molecules*, **23**: 1768.
- I. Kashif, A. Abd El-Maboud, A. Ratep (2014), Effect of Nd<sub>2</sub>O<sub>3</sub> addition on structure and characterization of lead bismuth borate glass, *Results Phys.* **4**: 1-5.
- J.H. Choi, A. Margaryan, A. Margaryan, F.G. Shi (2005), Judd Ofelt analysis of spectroscopic properties of Nd<sup>3+</sup>-doped novel fluorophosphates glass, *J. Lumin.* **114**: 167-177.
- K. Arai, H. Namikawa, K. Kumata, T. Honda, Y. Ishii, T. Handa (1986), Aluminum or phosphorus co-doping effects on the fluorescence and structural properties of neodymium-doped silica glass, *J. App. Phys.* **59**: 3430.
- K. Binnemans, C. Gorller-Walrand (1998), Are the Judd - Ofelt intensity parameters sensitive enough to reflect small compositional changes in lanthanide-doped glasses, *J. Phys. Con. Mat.* **10**: 167-170.
- K. Swapna, S.K. Mahamuda (2014), Visible luminescence characteristics of Sm<sup>3+</sup> doped Zinc Alumino Bismuth Borate glasses, *J. Lum.* **146**: 288–294.
- K.Naveen Kumar, L. Vijayalakshmi, Y.C. Ratnakaram (2015), Energy transfer based photoluminescence properties of (Sm<sup>3+</sup> +Eu<sup>3+</sup>):PEO + PVP polymer films for Red luminescent display device applications, *Opt. Mat.* **45**: 148–155.

- L. Bokatial, S. Rai (2012), Optical properties of  $\text{Sm}^{3+}$  ions in sol-gel derived alumino-silicate glasses, *J. Opt.* **41(2)**: 94-103.
- Ligang Zhu, Chenggang Zuo (2010), Photoluminescence of  $\text{Dy}^{3+}$  and  $\text{Sm}^{3+}$ :  $\text{SiO}_2$ – $\text{Al}_2\text{O}_3$ – $\text{LiF}$ – $\text{CaF}_2$  glasses, *Physica B: Condens. Mat.* **405(21)**: 4401–4406.
- M. Ferrari, R. Campostrini, G. Carturan, M. Montagna (1992), Spectroscopy of trivalent europium in gel-derived silica glasses, *Philos. Mag. B*, **65**: 251-260.
- M. Ferrari, A. Piazza, M. Montagna, G. Carturan & R. Campostrini (1994), Site selection spectroscopy of  $\text{SiO}_2\text{:Eu}^{3+}$  gels, *J. Sol-Gel Sci. Tech.* **2**: 783–786.
- M. Sołtys, J. Pisarska, M. Lesniak, M. Sitarz, W.A. Pisarski (2018), Structural and spectroscopic properties of lead phosphate glasses doubly doped with  $\text{Tb}^{3+}$  and  $\text{Eu}^{3+}$  ions, *J. Mol. Struct.* **1163**: 418-427.
- M. Venkateswarlu, Sk. Mahamuda, K. Swapna, M.V.V.K.S. Prasad, A. Srinivasa Rao, A. Mohan Babu, Suman Shakya and G. Vijaya Prakash (2015), Spectroscopic studies of  $\text{Nd}^{3+}$  doped lead tungsten tellurite glasses for the NIR emission at 1062 nm, *Optical Mater.* **39**: 8-15.
- M. Yamane, Y. Asahara (2000), Glasses for Photonics, first ed., Cambridge University Press, UK.
- M.I.M. Zamratul, A.W. Zaidan, A.M. Khamirul, M. Nurzilla, S.A. Halim (2016), Formation, structural and optical characterization of neodymium doped-zinc soda lime silica based glass, *Results in Phys.* **6**: 295–298.
- M.P. Hehlen, M.G. Brik, K.W. Kramer (2013), 50th anniversary of the Judd–Ofelt theory: An experimentalist's view of the formalism and its application, *J. Lum.* **136**: 221-239.
- Mohd Azam and V. K. Rai (2018), Study of Visible Luminescence Spectra from  $\text{Nd}^{3+}$  Doped TPO Glass upon 808 nm Excitation, *AIP Conference Procee.* **1953**: 090048.
- N. F. Osman (2022), Electrical and optical properties of Neodymium ions doped  $\text{P}_2\text{O}_5$ – $\text{ZnO}$ – $\text{Na}_2\text{O}$ – $\text{Li}_2\text{O}$  glasses, *The International Journal for Engineering and Modern Science*, **1**: 22006.



- Nisha Deopa, A.S. Rao, Mohini Gupta, G. Vijaya Prakash (2018), Spectroscopic investigations of  $\text{Nd}^{3+}$  doped Lithium Lead Alumino Borate glasses for 1.06  $\mu\text{m}$  laser applications, *Opt. Mat.* **75**: 127-134.
- P Ramesh, G Jagannath, B Eraiah and M K Kokila (2018), Optical and Physical Investigations of Lanthanum Bismuth Borate glasses doped with  $\text{Ho}_2\text{O}_3$ , *Mater Sci. Eng.* **310**: 012032.
- P. Chimalawong, J. Kaewkhao, C. Kedkaew and P. Limsuwan (2010), Optical and electronic polarizability investigation of  $\text{Nd}^{3+}$ -doped soda-lime silicate glasses, *J. Phys. Chem. Sol.* **71**: 965-970.
- P. Syam Prasad and P. Venkateswara Rao (2018), Structural and Luminescence Properties of Tellurite Glasses for Laser Application, *Mat. Spr. Cham.* **45**: 66.
- R. Reisfeld, G. Panczer, A. Patra, M. Gaft (1999), Time-resolved spectroscopy of  $\text{Sm}^{3+}$  in silica and silica–Al sol–gel glasses, *Mater. Lett.* **38**: 413-417.
- R.M. Almeida, H.C. Vasconcelos, M.C. Goncalves, L.F. Santos (1998), XPS and NEXAFS studies of rare-earth doped amorphous sol–gel films, *J. Non-Cryst Sol.* **232–234**: 65-71.
- R.R. Jacobs, M.J. Weber (1976), Dependence of the  $^4\text{F}_{3/2} \rightarrow ^4\text{I}_{11/2}$  induced-emission cross section for  $\text{Nd}^{3+}$  on glass composition, *IEEE J. Qua. Elec.* **12**: 102.
- S. Dabboussi, H. Elhouichet, C. Bouzidi, G.K. Maliarevich, N.V. Gaponenko and M. Oueslati (2009), Excitation and emission processes of  $\text{Tb}^{3+}$  in porous anodic alumina, *J. Appl. Surface Sci.* **255**: 4255–4258.
- S. Duhan, P. Aghamkar (2008), Synthesis and Characterization of Neodymium Oxide in Silica Matrix by Sol-gel Protocol Method, *Res. Lett. Phys.* **237023**: 1-4.
- S. Hazarika and S. Rai (2007), Characteristics of  $\text{Nd}^{3+}$  ions in sol-gel derived silicate glass in presence of  $\text{Al}(\text{NO}_3)_3$  and the  $^4\text{F}_{3/2} \rightarrow ^4\text{I}_{11/2}$  transition, *Opt. Mater.* **30**: 462-467.
- S. Hazarika, S. Rai (2007), Characteristics of  $\text{Nd}^{3+}$  ions in sol–gel derived silicate

glass in presence of  $\text{Al}(\text{NO}_3)_3$  and the  $^4\text{F}_{3/2} \rightarrow ^4\text{I}_{11/2}$  transition, *Opt. Mat.* **30**: 462–467.

- PJ Dihingia, S Rai (2012), Synthesis of  $\text{TiO}_2$  nanoparticles and spectroscopic upconversion luminescence of  $\text{Nd}^{3+}$ -doped  $\text{TiO}_2\text{--SiO}_2$  composite glass, *Journal of luminescence*, 132: 1243-1251.
- S. Mitra & Samar Jana (2015), Properties of the Energy Bands, Judd-Ofelt Parameters and the Fluorescence of Neodymium Chloride ( $\text{NdCl}_3$ ) in Methanol, Iso-propanol and Butanol Solvents, *J. Flu.* **25**: 541–549.
- S. Rai and A. L. Fanai (2016), Effect of the annealing and dopants concentration on the optical properties of  $\text{Nd}^{3+}:\text{Al}^{3+}$  co doped sol-gel silica glass, *J. Lum.* **170**: 325-329.
- S.S. Wang, Y. Zhou, Y.L. Lam, C.H. Kam, Y.C. Chan, X. Tao (1997), Fabrication and characterization of neodymium-doped silica glass by sol-gel process, *Mat. Res. Inn.* **1**: 92-96.
- U. Caldino, A. Lira, A.N. Meza-Rocha, I. Camarillo, R. Lozada-Morales (2018), Development of sodium-zinc phosphate glasses doped with  $\text{Dy}^{3+}$ ,  $\text{Eu}^{3+}$  and  $\text{Dy}^{3+}/\text{Eu}^{3+}$  for yellow laser medium, reddish-orange and white phosphor applications, *J. Lumin.* **194**: 231-239.
- W.A. Pisarski, Karolina Kowalska, Marta Kuwik, Justyna Polak, Ewa Pietrasik, Tomasz Goryczka and Joanna Pisarska (2020), Novel Multicomponent Titanate-Germanate Glasses: Synthesis, Structure, Properties, Transition Metal and Rare Earth Doping, *Mater.* **13(19)**: 54-62.
- W.T. Carnall, H. Crosswhite and H.M. Crosswhite (1978), Energy level structure and transition probabilities in the spectra of the trivalent lanthanides in  $\text{LaF}_3$ . Argonne National Laboratory, Report no. ANL-78-XX-95.
- W.T. Carnall, P.R. Fields and K.J. Rajnak (1968), Electronic Energy Levels in the Trivalent Lanthanide Aquo Ions, I.  $\text{Pr}^{3+}$ ,  $\text{Nd}^{3+}$ ,  $\text{Pm}^{3+}$ ,  $\text{Sm}^{3+}$ ,  $\text{Dy}^{3+}$ ,  $\text{Ho}^{3+}$ ,  $\text{Er}^{3+}$ , and  $\text{Tm}^{3+}$ , *Chem. Phys.* **59**: 4424.
- Y. Qiao, N. Da, D. Chen, Q. Zhou, J. Qiu, T. Akai (2007), Spectroscopic properties of neodymium doped high silica glass and aluminum codoping effects on

the enhancement of fluorescence emission, *App. Phys. B*, **87**: 717-722.

Yan Jiao, Mengting Guo, Renle Wang, Chongyun Shao, and Lili Hu (2021), Influence of Al/Er ratio on the optical properties and structures of  $\text{Er}^{3+}/\text{Al}^{3+}$  co-doped silica glasses, *J. App. Phys.* **129**: 053104.

Yu Zhang, P. Shan, Z. Zhang and S. Chen, Growth (2014), Structure, Thermal Properties and Spectroscopic Characteristics of Nd-Doped  $\text{KGdP}_4\text{O}_{12}$  Crystal, *Pl. One.* **9(6)**: 1-10.

## CHAPTER 6

### SUMMARY AND CONCLUSION

---

#### 6.1. Introduction

Nowadays, glass has become an essential material in various compositions and preferred forms, such as lenses, screens, prisms, and optical communication fibers, all of which are in high demand in everyday life. Rare earth (RE) doped glasses are of great interest due to their versatile applications in fabricating optical, storage, and fiber amplifier devices. RE ions, known for their radiative transitions, are excellent probes for understanding the local environment of the host matrix. The host glass plays a crucial and intriguing role in developing RE-doped optical devices. Given the wide range of applications, extensive research is needed to identify new host materials doped with RE ions. The theoretical background has been given to draw the interest of potential readers in chapter 1. The preparation technique is discussed in detail with briefly describes different scientific equipment's and techniques used in the collection of experimental data in chapter 2. In chapter 3 present the investigation of luminescence properties of  $\text{Sm}^{3+}$ -doped with  $\text{Al}_2\text{O}_3/\text{TiO}_2/\text{ZnS}/\text{ZnO}$  in silicate glasses. In chapter 4 present the investigation of luminescence properties of  $\text{Eu}^{3+}$ -doped in alumino-silicate and titania-silicate glasses. In chapter 5 present the investigation of luminescence properties of  $\text{Nd}^{3+}$ -doped in alumino-silicate glasses. This chapter provides a comprehensive analysis of the results obtained, comparing them with similar ion-doped materials to identify similarities, differences, and challenges in designing  $\text{RE}^{3+}$ -based optical glass devices. It also outlines future research directions to improve the luminescence efficiency of  $\text{Al}_2\text{O}_3$ ,  $\text{TiO}_2$ ,  $\text{ZnS}$ , and  $\text{ZnO}$  in silicate glasses by optimizing co-dopant rare earth ions in these glass systems. In this investigation, the electronic structure of RE ions in the glasses was determined from the optical absorption spectra using Judd-Ofelt (JO) theory. The intensity parameters and transition probabilities of the excited states in  $\text{RE}^{3+}$ -doped systems have been evaluated.

## 6.2 Summary and conclusions

### 6.2.1 Salient features of results on $\text{Sm}^{3+}$ doped with (i.e. $\text{Al}_2\text{O}_3/\text{TiO}_2/\text{ZnS}/\text{ZnO}$ ) in silicate glasses

- ❖ In XRD studies of  $\text{Sm}^{3+}$  doped alumino-silicate glasses is confirm that the amorphous nature of the glass samples. But in  $\text{Sm}^{3+}$  doped  $\text{TiO}_2/\text{ZnS}/\text{ZnO}$  in silicate glasses is confirm that the crystalline nature of the glass samples.
- ❖ The density of each glass series is found to increase with addition of rare-earth oxides at the expense of modifiers ( $\text{Al}_2\text{O}_3/\text{TiO}_2/\text{ZnS}/\text{ZnO}$ ), which is quite obvious due to large molecular weight of rare-earth oxides as compared to that of modifiers ( $\text{Al}_2\text{O}_3/\text{TiO}_2/\text{ZnS}/\text{ZnO}$ ).
- ❖ FTIR spectra reveal that the sample annealed at higher temperatures experiences the evolution of NBO on the low phonon energy side along with the elimination of the OH group. Furthermore, the presence of rare-earth cations at their network sites has also been observed.
- ❖ The absorption spectra of all the  $\text{Sm}^{3+}$  doped  $\text{Al}_2\text{O}_3/\text{TiO}_2/\text{ZnS}/\text{ZnO}$  glasses have been traced in the visible and near-infrared region to evaluate Judd-Ofelt intensity parameters.
- ❖  $\text{Sm}^{3+}$  doped  $\text{Al}_2\text{O}_3/\text{TiO}_2/\text{ZnS}/\text{ZnO}$  in sol-gel silicate glass is also studies with ultraviolet and laser irradiation. The absorption spectra shows the characteristic nature of  $\text{Sm}^{3+}$  ions in both UV and NIR regions. Absorption spectra and Emission spectra reveals that these glasses emits the light radiation in orange red color in the current glasses. Therefore these glasses are useful in preparing red emitting materials. So, the present work shows a new path to prepare and fabricate the materials which are useful for various kinds of optical and light applications.
- ❖ The J-O parameters were further used to evaluate the certain radiative properties
- ❖ In conclusion,  $\text{Sm}^{3+}$ -doped  $\text{Al}_2\text{O}_3/\text{TiO}_2/\text{ZnS}/\text{ZnO}$  glass exhibits significant potential for lasing action in the orange spectral region. This material is

particularly promising for the development of visible lasers and display devices, featuring a prominent emission around 650 nm.

- ❖ The Energy Dispersive X-ray (EDX) analysis, integrated with the SEM and TEM system, was primarily utilized to confirm the presence of rare earth ions.

### **6.2.2 Salient features of results on $\text{Eu}^{3+}$ doped with alumino-silicate and titania-silicate glasses**

- ❖ The XRD spectra of  $\text{Eu}^{3+}$  doped alumino-silicate glasses has broadened diffuse scattered peaks confirms the amorphous nature. But in  $\text{Eu}^{3+}$  doped  $\text{TiO}_2\text{-SiO}_2$  glasses is confirm that the crystalline nature of the glass samples.
- ❖ From the FTIR studies, various functional groups exist in the network has been identified.
- ❖ The absorption spectra has been recorded for the  $\text{Eu}^{3+}$  doped  $\text{Al}_2\text{O}_3/\text{TiO}_2$  in silicate glasses absorption bands resolved correspond to the transitions  $^7\text{F}_0 \rightarrow ^5\text{D}_4$  (362 nm),  $^7\text{F}_0 \rightarrow ^5\text{G}_4$  (375 nm),  $^7\text{F}_0 \rightarrow ^5\text{G}_2$  (379 nm),  $^7\text{F}_0 \rightarrow ^5\text{G}_3$  (385 nm),  $^7\text{F}_0 \rightarrow ^5\text{L}_6$  (394 nm), and  $^7\text{F}_0 \rightarrow ^5\text{D}_2$  (465 nm). The  $f_{\text{exp}}$  and  $f_{\text{cal}}$  are calculated for the  $\text{Eu}^{3+}$  doped  $\text{Al}_2\text{O}_3/\text{TiO}_2$  glass. They are further used to evaluate JO intensity parameters. The optical absorption spectra of the prepared glasses were used to calculate the Judd-Ofelt parameter ( $\Omega_2$ ). In this work, a high  $\Omega_2$  value indicates stronger Eu-O covalence and lower symmetry around the trivalent europium-doped ions in the glasses.
- ❖ From photoluminescence studies, the certain radiative and laser characteristic parameters of the  $^5\text{D}_0$  excited for the  $\text{Eu}^{3+}$  doped  $\text{Al}_2\text{O}_3/\text{TiO}_2$  in silicate glasses level are computed.
- ❖ The values of  $\sigma_e$  and  $\beta_R$  obtained for  $^5\text{D}_0 \rightarrow ^7\text{F}_2$  transition revealed that,  $\text{Eu}^{3+}$  doped  $\text{Al}_2\text{O}_3/\text{TiO}_2$  in silicate glasses are suitable for good laser action in the visible region.
- ❖ The  $\text{Eu}^{3+}$ -doped  $\text{Al}_2\text{O}_3/\text{TiO}_2$  in silicate glass that was prepared and studied exhibits higher stimulated emission cross-section and branching ratio values.

These properties suggest its suitability for laser action at 614 nm, corresponding to the  $^5D_0 \rightarrow ^7F_2$  transition.

- ❖ The Energy Dispersive X-ray (EDX) analysis, integrated with both SEM and TEM systems, was primarily used to confirm the presence of rare earth ions.

### 6.2.3 Salient features of results on $Nd^{3+}$ doped with aluminosilicate glasses

- ❖ XRD studies confirm that the glass samples exhibit an amorphous nature.
- ❖ The density of each glass series is found to increase with addition of rare-earth oxides at the expense of aluminium, which is quite obvious due to large molecular weight of rare-earth oxides as compared to that of aluminium. A corresponding decrease in molar volume shows the expected harmony between these two parameters.

The density of the sample  $(99-x)SiO_2 + 1NdF_3 + xAl_2O_3$  (here  $x = 0.0, 1.2, 2.0$  and  $3.0$  mol%)(i.e. SiNdAl0, SiNdAl1.2, SiNdAl2 and SiNdAl3) is found to be the highest among all the prepared glass samples which is due to maximum concentration of neodymium fluoride.

- ❖ The FTIR spectra confirm that non-bridging oxygen's (NBO) on the low phonon energy side increase for the sample annealed at higher temperatures, along with the removal of OH groups.  $RE^{3+}$  ions are subjected to a modified vibrational coupling,  $RE^{3+}$  clustering is prevented by Al co-doping, and  $RE^{3+}$  are found in the aluminum-rich regions that have greater non-bridging Al-O groups available for coordination. The phonon energy of Al-O-Si bonds is lower than that of Si-O-Si bonds.
- ❖ The absorption spectra reveal a total of seven absorption bands (i.e. porous gel stage and densification) originated from  $^4I_{9/2}$  to various excited states of  $Nd^{3+}$  ion and their intensities increase with increase in various temperatures. Judd-Ofelt intensity parameters follow the trend  $\Omega_6 > \Omega_2 > \Omega_4$  (porous gel stage) and  $\Omega_2 > \Omega_4 > \Omega_6$  (dense glass) for the SiNdAl3 glass at various temperatures. According to J-O intensity parameters, the greater value of

$\Omega_2$  indicate of higher degree of covalency of the Nd–O bond and asymmetry of the  $\text{Nd}^{3+}$  sites in the Nd–alumina–silicate glass.  $\Omega_6$  decreased with annealing indicating the strong covalency and asymmetry of the RE ion site as well as increased rigidity of the host with annealing.

- ❖ The value of  $\Omega_4$  and  $\Omega_6$  are used to estimate the spectroscopic quality factor  $\chi = \Omega_4/\Omega_6$  is observed to increase with increase in different temperatures in the glass matrix which infers the increase in luminescence efficiency of the host matrix with increase in different temperatures. The value of  $\chi$  greater than one is observed only for glass sample which suggests this glass sample will have higher luminescence efficiency.
- ❖ It has been reported that SiNdAl0, SiNdAl1.2, SiNdAl2 and SiNdAl3 results in PL spectra with splitting (Stark splitting), which is consistent with the host being altered by the presence of Al. The results indicate that an increase in Al concentrations strongly effects the improvement of PL property. Cross-relaxation was found to be a major quenching mechanism for  $^4\text{F}_{3/2}$  emissions of  $\text{Nd}^{3+}$ .

So, there is a lot of scope to work on this host composition with different intermediates and also with different Rare earth ions for not only lighting applications but also optical windows, fiber amplifiers and sensors etc.



### **Scope of the Future Work**

Recently, rare-earth (RE) ion-doped glass systems have been extensively studied for developing UV-visible lasers. These lasers have significant applications in storage sensors, optoelectronics, and underwater communications. Based on the conclusions drawn from this investigation, future work can extend to co-doping europium, neodymium, and samarium oxides with other suitable rare earth oxides. This would involve analyzing their physical, structural and optical properties for further photonic applications. In this thesis, novel glass systems were investigated by maintaining a constant RE ion concentration while varying the composition of modifiers. Future research will focus on enhancing the luminescence efficiency of these glasses by either fixing the composition or varying the dopant ion concentration or by doping with double or triple RE ions. Additionally, these compositions can be used to form glass/glass ceramics, and their behavior can be studied for applications in photonics.

In this study, due to limited facilities, fluorescence decay and lifetime could not be experimentally measured. Recording and measuring these parameters would enable the calculation of quantum efficiency by comparing experimental and theoretical radiative lifetimes. This would also provide valuable insights and a better understanding of quenching and energy transfer between the RE ions.

### **BIO DATA**

**Name** : K.M.S. Dawngliana  
**Father's Name** : K. Thankima (L)  
**Date of Birth** : 13.04.1996  
**Address** : H-54, Bualpui 'N' Kolasib,  
Mizoram; India-796009

**Educational Qualifications** :

▪ HSLC	2011	MBSE
▪ HSSLC	2013	MBSE
▪ B. Sc (Physics)	2018	Mizoram University
▪ M. Sc (Physics)	2020	Mizoram University

### **Research Experience:**

- Registered Ph.D researcher in Dept. of Physics. Mizoram University under the supervision of Prof. S. Rai since 2020.

### List of Publications

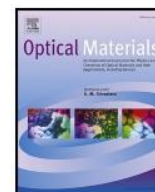
1. KMS Dawngliana, S. Rai, Linear and nonlinear and optical properties of  $\text{Sm}^{3+}$  co-doped alumino-silicate glass prepared by sol-gel method, *Journal of Non-Crystalline Solids*, **598** (2022), 121929.
2. KMS Dawngliana, A.L. Fanai, S. Rai, Structural and optical studies of  $\text{Sm}^{3+}$ -doped silica glass along with  $\text{TiO}_2$  nanoparticles for photonic applications, *Journal of Non-Crystalline Solids*, **607** (2023) 122226.
3. KMS Dawngliana, A.L. Fanai & S. Rai, Structural and Spectroscopic Properties of  $\text{Eu}^{3+}$  ions in Alumino-Silicate Glass, *Indian Journal of Pure & Applied Physics*, **61** (2023) 182-189.
4. KMS Dawngliana, Lalruatpuia, Lalrempuia Ralte, S. Rai, Effect of ZnS nanoparticles on the optical properties of  $\text{Sm}^{3+}$  ions in silicate matrix, *Journal of Non-Crystalline Solids*, **632** (2024) 122871.
5. KMS Dawngliana, Kamal Bhujel, S Rai, Effect of ZnO nanoparticles on the Judd–Ofelt and radiative parameters of  $\text{Sm}^{3+}$  ions in sol–gel silica matrix, *Applied Physics A*, **130** (2024) 1-13.
6. KMS Dawngliana, AL Fanai, S Rai, Structural and Spectroscopic properties of  $\text{Eu}^{3+}$  doped  $\text{SiO}_2\text{--TiO}_2$  nanoparticles for photonic applications, *Optical Materials*, **152** (2024) 115470.
7. KMS Dawngliana, Lalruat Puia, Lalrempuia Ralte, A.L. Fanai, S. Rai, Effect of Al on photoluminescence properties of  $\text{Nd}^{3+}$  in silicate glass-ceramic prepared by in-situ sol-gel method, *Journal of Sol-Gel Science and Technology*, **24** (2024) 1-12.
8. KMS Dawngliana, S. Rai, Physical and Optical Properties of  $\text{Nd}^{3+}$  co-doped Al in sol-gel silicate glass, *Indian Journal of Physics*, **16** (2024) 65-69.
9. KMS Dawngliana, S. Rai, Nanoarchitectonics and spectroscopic studies of  $\text{Pr}^{3+}$  doped ZnS nanoparticles glasses for visible reddish orange luminescent device applications, *Applied Physics A*, **130** (2024) 523.
10. Lalruatpuia, Uzair Khan, KMS Dawngliana S Rai, Synthesis and Spectral Characteristics of RhB and Rh6G Dyes and their Mixture in Solid Matrix, *Indian Journal of Pure & Applied Physics (IJPAP)*, **60** (2022) 883-891.

11. KMS Dawngliana, Lalruat Puia, A.L. Fanai, S. Rai, Spectroscopic properties of  $\text{Pr}^{3+}$ -doped Titania-Silicate glass ceramic for photonic applications, *Optical Materials*, **155** (2024) 115841.
12. KMS Dawngliana & S. Rai, Effect of titania nano composite on structural and optical properties of  $\text{Ho}^{3+}$  doped silica glasses for green laser applications, *Applied Physics A*, **130** (2024) 476.
13. KMS Dawngliana and S. Rai, Effect of ZnS nanoparticles on the Judd-Ofelt and radiative parameters of  $\text{Ho}^{3+}$  ions in sol-gel silicate matrix, *Applied Physics A*, **130** (2024) 715.
14. Lalruatpuia, KMS Dawngliana, AL Fanai, S. Rai, Effect of ZnS nanoparticles in photoluminescence properties of  $\text{Tb}^{3+}$  ion doped silica glass for photonic applications, *Applied Physics A*, **129** (2023) 751.
15. Lalruatpuia, KMS Dawngliana & S Rai, Spectroscopic investigation of  $\text{Pr}^{3+}$  doped ZnS nanoparticle in silica glass matrix prepared by sol-gel method, *Applied Physics A*, **130**(11) (2024) 1-10.
16. KMS Dawngliana, Lalruat Puia, A.L. Fanai, S. Rai, Optical basicity and electronic polarizability of  $\text{Sm}^{3+}$ -doped silica glass prepared by sol-gel process, *Materials Today: Proceedings*, **65**(5) (2022) 2572-2577.
17. KMS Dawngliana, S. Rai, Nanoarchitectonic and spectroscopic properties of  $\text{Eu}^{3+}$  co-doped ZnS nanoparticles in silicate dense glass ceramic prepared by sol-gel method, *Ceramic International*, **51** (2025) 18428-18438.
18. C. Zothansanga, KMS Dawngliana, Beckham Zathang and S. Rai, Investigation of Judd-Ofelt parameters, luminescent properties and energy transfer analysis of  $\text{Eu}^{3+}$  doped Al in silica glass matrix synthesized via sol-gel technique, *Optical Material*, **159** (2025) 116598.
19. KMS Dawngliana, S. Rai, Spectroscopic properties and Judd-ofelt study of  $\text{Ho}^{3+}$  doped alumino-silicate glasses for green laser applications, *Applied Physics A*, **131** (2025) 1-12.
20. KMS Dawngliana, and S. Rai, Luminescence characterization of  $\text{Eu}^{3+}$  doped ZnO nanoparticles in sol-gel silicate glasses for visible red emission applications, *Optical materials* (Communicated).

21. KMS Dawngliana, S. Rai, Enhanced upconversion and temperature sensing study of  $\text{Ho}^{3+}$ - $\text{Yb}^{3+}$  co-doped ZnS nanoparticles in silicate matrix, *Ceramic International* (Communicated).
22. KMS Dawngliana, S. Rai, Structural and Spectroscopic properties of  $\text{Sm}^{3+}$  doped  $\text{SiO}_2$  glass synthesized by sol-gel method, *Journal of Optics*, (Communicated).
23. Lalruatpuia, KMS Dawngliana, Lalnunpuia Khiangte, Kham Suan Pauva & S Rai, Effect of  $\gamma$ -ray irradiation of the optical properties of  $\text{Sm}^{3+}$ -doped silicate glass, *Journal of Optics*, (Communicated).

### **Papers presented in Conferences/Seminars/Workshop attended**

1. Photoluminescence of  $\text{Eu}^{3+}$  doped  $\text{TiO}_2\text{-SiO}_2$  glass derived by sol-gel method, *International conference on “SMART MATERIALS CHEMISTRY” (CHEMSMAT-21)* on 29<sup>th</sup>, 30<sup>th</sup> and 31<sup>th</sup> July 2021 organized by Department of Chemistry, St. Joseph’s College, Tiruchirappalli, Tamil Nadu, India.
2. *International Virtual Conference on Light Applications in Science & Engineering Research (LASER-2021)* conducted on 14<sup>th</sup> September 2021 at SAIF-SPIHER, Avadi, Chennai.
3. Optical basicity and electronic polarizability of  $\text{Sm}^{3+}$ -doped silica glass prepared by sol-gel process, *Biennial National Conference of Physics Academy of North East (PANE 2021)*, 15<sup>th</sup> – 17<sup>th</sup> December, 2021 organized by Department of Physics, Tripura University.
4. *Workshop on Software in Mathematics and Statistics” (WSMS–2021)* on 02 – 06 August 2021, organized by the Department of Mathematics, National Institute of Technology Tiruchirappalli.
5. Structural and optical studies of  $\text{Sm}^{3+}$ -doped silica glass along with  $\text{TiO}_2$  nanoparticles for photonic application, *“International conference on current trends in advanced materials and their applications for societal development” (ICTAMASD-2022)* March 8<sup>th</sup> -10<sup>th</sup> 2022 organized by the Department of Physics, Dr. Harisingh Gour Vishwavidyalaya Sagar (MP).
6. Physical, Structural and non-linear investigation of  $\text{Eu}^{3+}$  doped silica glass prepared by sol-gel process, *“International virtual conference on materials science and technology (ICMAST-2022)* organized by Department of Physics, Kandaswami Kandar’s College, Velur, Namakkal in collaboration with Indian Spectrophysics Association (ISPA) between 15 and 16 March 2022.
- 7 *Participated in Two-Day International Symposium on the History of Astronomy of the Mizo People*, 18<sup>th</sup> -19<sup>th</sup> May, 2023 organized by Department of Physics, Mizoram University and Mizoram Science Centre.



## Research Article

Structural and Spectroscopic properties of  $\text{Eu}^{3+}$  doped  $\text{SiO}_2\text{--TiO}_2$  nanoparticles for photonic applicationsK.M.S. Dawngliana<sup>a,\*</sup>, A.L. Fanai<sup>b</sup>, S. Rai<sup>a</sup><sup>a</sup> Laser and Photonics Laboratory, Department of Physics, Mizoram University, Aizawl, 796004, India<sup>b</sup> Physics Section, Mahila Mahavidyalaya, Banaras Hindu University, Varanasi, 221005, India

## ARTICLE INFO

## Keywords:

$\text{TiO}_2$  nanoparticle  
Europium ions  
Sol-gel  
Luminescence  
Judd-Ofelt analysis  
CIE chromaticity

## ABSTRACT

The  $\text{Eu}^{3+}$ -doped  $\text{TiO}_2$  nanoparticles in sol gel silicate glasses of composition  $(80-x)\text{SiO}_2 + 20\text{TiO}_2 + 0.5x\text{Eu}_2\text{O}_3$ , ( $\text{SiTiEu}$ ) where  $x = 0.0, 0.5, 1.5, 2.5$  and  $3.5$  mol%, have been prepared by sol-gel technique. The glass samples were investigated by thermogravimetric analysis (TGA/DTA), ATR-FTIR, XRD, SEM, TEM, EDX, optical absorption and photoluminescence emission spectroscopy at room temperature (RT). The absorption wavelength of  $\text{TiO}_2$  doped sol-gel silicate glass were red shifted due to a reduction in band gap energy with increasing annealing temperatures. According to the TEM images, all of the particles were spherical and had an average diameter is around 10 nm. The visible spectra of the  $\text{Eu}^{3+}$  doped  $\text{TiO}_2$  nanoparticles in sol-gel silicate glasses displayed characteristic PL emission  $^5\text{D}_0 \rightarrow ^7\text{F}_J$  ( $J = 0, 1, 2, 3, 4, 5$ ) transitions of  $\text{Eu}^{3+}$  ions at 370 nm excitation. The anatase  $\text{TiO}_2:1.5\text{Eu}^{3+}$  nanocomposite showed high photoluminescence emission at 370 nm excitation, which was attributed to the f-f transitions of  $\text{Eu}^{3+}$ . The hypersensitive  $^5\text{D}_0 \rightarrow ^7\text{F}_2$  transition was responsible for the major red emission. From the recorded spectra, radiative parameters and Judd-Ofelt (JO) intensity parameters were computed. The  $\text{Eu}^{3+}$  co-doped  $\text{TiO}_2$  nanoparticles in sol-gel silicate glasses displayed emissions mostly in the red regions realized from a CIE chromaticity diagram. The results suggested that materials may be used as an optical material of technological importance such as display devices and also for optical amplifier.

## 1. Introduction

In current technological quests, sol-gel process is extensively used to process material for optical device due to the benefits such as low temperature of processing, homogeneity of higher order and opportunity of manufacturing material with desired refractive indices. Silica based glasses activated by Rare-earth (RE) ions has seen a renaissance in the study for their possible application in the photonic devices, colors displays and optical communication fields. Among the RE,  $\text{Eu}^{3+}$  is one of the efficient ions [1]. The host materials are considered as a very important factor during the development of RE ion doped optical device. In the last decade, an extensive investigation of optical properties of RE ions in various nano-structured materials has been performed. There has been a great significance in the study of size related effects pertaining to intensity of emission in different materials [2]. The sol-gel syntheses of novel materials have been extensively explored [3,4] and is found to be effective technique to prepare luminophores as solids matrices of silica, titania and silica-titania oxides. It is convenient to dope rare-earth ions in such materials via the sol-gel method [5].

In last decade, the optical properties of RE ions doped in sol-gel glasses have induced a sizable importance due to the prospective implications arena of field sensor and laser, along with the role of amplifiers for fiber-optic communication, high frequency domain optical memory [6–8]. Among the various metal oxides, titania ( $\text{TiO}_2$ ) is rated to be one of the most lucrative materials due to its non-toxicity, long-term stability and low-cost. In the case of RE ion incorporated in titania nanocrystals, a unique optical properties could be tailored through size controlling as well as band-gap engineering, which is incredibly impressive in fabrication of a nano-device with technological utilities. A reasonably simple structure of  $\text{Eu}^{3+}$  energy level permits the absorption and emission spectra in the range of visible photons [9].  $\text{Eu}^{3+}$  doped hosts are universally used in commercial luminescent phosphors of red color. This red color is initiated from the electric dipole (ED) transitions of an electron to the  $^7\text{F}_2$  level from the  $^5\text{D}_0$  level. It is hypersensitive to local symmetry [10]. In other words, an important role is played by host in its photoluminescence, thus making  $\text{Eu}^{3+}$  perfect contender to explore luminescent characteristics phosphor on glass composition.  $\text{Eu}^{3+}$  doped in variety of glasses like borate, phosphate, tellurite etc., have been

\* Corresponding author.

E-mail address: [jerrykms0000@gmail.com](mailto:jerrykms0000@gmail.com) (K.M.S. Dawngliana).





# Effect of ZnS nanoparticles on the optical properties of $\text{Sm}^{3+}$ ions in silicate matrix

KMS Dawngliana<sup>a,\*</sup>, Lalruatpuia<sup>a</sup>, Lalrempuia Ralte<sup>b</sup>, S. Rai<sup>a</sup>

<sup>a</sup> Laser and Photonics Laboratory, Department of Physics, Mizoram University, Aizawl, 796004, India

<sup>b</sup> Department of Chemistry, Mizoram University, Aizawl, 796004, India

## ARTICLE INFO

### Keywords:

Samarium, Sol-gel  
Dense glass-ceramic  
ZnS nanoparticles  
Judd-Ofelt  
Radiative properties and CIE Chromaticity

## ABSTRACT

ZnS and  $\text{Sm}^{3+}$ -doped ZnS nanoparticles (NPs) in silicate glasses were prepared by sol-gel technique. X-ray diffractometer (XRD), scanning electron microscopy (SEM), transmission electron microscopy (TEM), and photoluminescence (PL) emission spectra were used to analyze the sample's morphology and crystal structure. UV-visible absorption spectra and PL emission spectra were used to look at the sample's optical characteristics. The formation of NBO and the elimination of the OH-group are confirmed by the FTIR spectra analysis. The XRD, SEM and TEM measurements confirmed that our glass sample is a nano-crystal. Optical absorption spectra have been used to evaluate three phenomenological Judd-Ofelt (JO) parameters  $\Omega_\lambda$  ( $\lambda = 2, 4, 6$ ) to determine the local structure and bonding surrounding  $\text{Sm}^{3+}$  ions. Glasses containing SSZ5 are found to have the highest parameter  $\Omega_2$ , which shows the covalency of the Sm-O bond, followed in decreasing order by glasses containing SSZ3 and SSZ1. This result implies that the coordination environment surrounding the  $\text{Sm}^{3+}$  ions site is less centrosymmetric and more asymmetric in glass containing ZnS. For the glasses under investigation, the covalent character of the Sm-O bond is shown by the positive values of the bonding parameter  $\delta$ . Four emission bands were seen in the PL spectra obtained at an excitation wavelength of 450 nm. Glass samples containing SSZ5 are shown to have greater radiative characteristics, such as branching ratio ( $\beta_R$ ) and stimulated emission cross-section ( $\sigma$ ), as well as potential emission band intensity. However all other prepared glasses, however, have been shown to be efficient lasing materials, indicating their appropriateness for the development of photonic materials that emit radiations in the range of blue to white regions. The Figure of Merit (FOM) results suggest that the prepared glasses might be used as optical amplifiers.

## 1. Introduction

Glasses doped with rare earth (RE) are particularly interesting because of their outstanding optical, spectroscopic, and luminescence characteristics [1,2]. These many potential applications are made possible by the versatility of RE-doped glasses as well as their broader emission and absorption spectra [3–6]. They have been found to have potential applications in the fields of solid-state lasers, optoelectronic and photonic devices, sensors, solid-state lighting systems, light emitting diodes, optical amplifiers, energy up-converters, optical data storage devices, and high-power laser gain medium, among others [6–9]. They are also crucial to the development of a number of technologically significant devices [1–12]. A thorough analysis of several rare earth doped glass compositions has been provided by Gorller-Walrand and Binnemans [13]. The host matrix's composition has a highly sensitive

effect on how rare earth ion optical and spectroscopic characteristics are altered. Glass has shown to be an excellent host for rare earth doping due to its random network structure and capacity to accept a broad variety of dopants. It also offers a substantial amount of space for active functioning [7–9]. We may transfer a passive glass into a laser glass, a non-linear optical glass, a magneto-optic glass, etc. by properly doping it [14].

Samarium ion ( $\text{Sm}^{3+}$ ), one of the several rare earth ions, has drawn a lot of interest as it may be found in many different applications such as memory devices, phosphor materials, display panels, UV sensors, and visible lasers [15–21]. The transitions  $^4\text{G}_{5/2} \rightarrow ^6\text{H}_J$  ( $J = 5/2, 7/2, 9/2, 11/2$ ) of  $\text{Sm}^{3+}$ , an essential activator ion, create bright luminescence in the visible range [16]. Numerous hosts, including borate [15], bismuth borate [16], lithium borate and lithium fluoroborate [17], lithium aluminoborate [18], lead fluoro-borophosphate [19], oxyfluorosilicate

\* Corresponding author.

E-mail address: [jerrykms0000@gmail.com](mailto:jerrykms0000@gmail.com) (K. Dawngliana).

<https://doi.org/10.1016/j.jnoncrysol.2024.122871>

Received 22 November 2023; Received in revised form 1 February 2024; Accepted 6 February 2024  
0022-3093/© 2024 Elsevier B.V. All rights reserved.




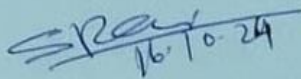


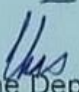
Mizoram University, Aizwal

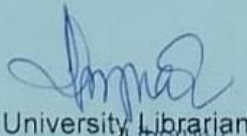
Certificate of Plagiarism Check for Thesis

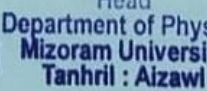
Author Name	K.M.S. Dawngliana
Course of Study	Ph.D
Name of Guide	Prof. Suman Rai
Department	Physics
Acceptable Maximum Limit	10% (Core)
Submitted By	lib.mzu@gmail.com
Paper Title	Optical Studies of Some Rare-Earth Doped Nano-Composites for Photonic Applications
Similarity	5%
Paper ID	2411675
Total Pages	134
Submission Date	2024-10-14 12:04:46

  
Signature of Student

  
Signature of Guide

  
Head of the Department  
Head  
Department of Physics  
Mizoram University  
Tanhrii : Aizawl

  
University Librarian  
Central Library  
Mizoram University  
Aizawl : Mizoram

  
Director of Post Graduate Studies

\* This report has been generated by DrillBit Anti-Plagiarism Software



Mizoram University, Aizawl

Certificate of Plagiarism Check for Thesis

Author Name	K M S Dawngliana
Course of Study	Ph.D
Name of Guide	Prof. Suman Rai
Department	Physics.
Acceptable Maximum Limit	10% (Non-Core)
Submitted By	lib.mzu@gmail.com
Paper Title	Optical Studies of Some Rare-Earth Doped Nano-Composites for Photonic Applications
Similarity	5%
Paper ID	2412482
Total Pages	33
Submission Date	2024-10-14 14:55:16

Signature of Student

Signature of Guide

Head of the Department  
Head  
Department of Physics  
Mizoram University  
Tanhri : Aizawl

University Librarian  
Central Librarian  
Mizoram University  
Aizawl : Mizoram

Director of Post Graduate Studies

This report has been generated by DrillBit Anti-Plagiarism Software

## ANNEXURE-I

## MIZORAM UNIVERSITY (A Central University)

## Ph.D. Thesis/M.Phil. Dissertation Certificate on Plagiarism Check

Name of Research Scholar/Student	K M S Dawngliana	
Ph.D./M.Phil. Registration Number	MZU/Ph.D/1525 of 21.10.2020	
Title of PhD thesis/MPhil dissertation	Optical Studies of Some Rare-Earth Doped Nano-composite for Photonics Applications	
Name & Institutional Address of the Supervisor/Joint Supervisor	Prof. Suman Rai, MZU	
Name of the Department and School	Physics / School of Physical Science MZU	
Date of submission	16.10.2024	
Date of plagiarism check	14.10.2024	
Name of the software used	Dui11Bit - Anti-Plagiarism Software	
Percentage of similarity detected by the <del>URKUND</del> software	Core Areas	5%
	Non-Core areas	5%
Percentage of similarity permissible under MZU regulations	Core Areas	a common knowledge or coincidental terms and/or up to fourteen (14) consecutive words, if option is available in the software.
	Non-Core areas	Up to 10%

Dui11Bit

I hereby declare/certify that the Ph.D. Thesis/M.Phil. Dissertation submitted by me is complete in all respect, as per the guidelines of the Mizoram University (MZU) for this purpose. I also certify that the Thesis/Dissertation (soft copy and print version) has been checked for plagiarism using ~~URKUND~~ similarity check software. Copy of the Report generated by the ~~URKUND~~ software is also enclosed.

Dui11Bit

Place : (Name &amp; Signature of the Scholar):

K M S Dawngliana

Date :

4/10/2024

Name & Signature of the Supervisor:  
with seal

Prof. Suman Rai

Professor

Department of Physics  
Mizoram University  
Tanhri : AizawlName & Signature of the Joint Supervisor (if any):  
with sealName & Signature of the DRC Chairperson/Head:  
with sealProf. Znithanzuwa Pichneu  
4/10/2024Head  
Department of Physics  
Mizoram University  
Tanhri : Aizawl



Annexure-II

**Plagiarism Verification Certificate**

(This certificate should be submitted to the Examination Department at the time of submission of the Thesis/Dissertation)

This is to certify that the plagiarism check has been performed for Ph.D. Thesis /M. Phil.

Dissertation: Optical studies of some Rare Earth Doped Nano-composite for photonic Applications submitted by **Mr./Ms**

K M S Dawaythang, under the Supervision of  
Prof. Guman Rai Department of Physics, School of Physical Science.

Mizoram University. The check performed by the Scholar/Student is found correct/adheres to

MZU regulations and authentic software URKIND has been used for the similarity check.

Onillogit

Name, Signature & Seal of the Dean of the School:

Prof. Guman Rai  
[Signature]  
Dean  
4.10.24  
School of Physical Sciences  
Mizoram University

## **PARTICULARS OF THE CANDIDATE**

Name : **K.M.S. DAWNGLIANA**  
Degree : Ph.D.  
Department : Physcis  
Title of Thesis : OPTICAL STUDIES OF SOME RARE-  
EARTH DOPED NANO-COMPOSITES  
FOR PHOTONICS APPLICATIONS  
Date of admission : 21.10.2020  
Approval of research proposal  
DRC : 20.04.2021  
BOS : 30.04.2021  
SCHOOL BOARD : 17.05.2021  
MZU Registration No : 1502661  
Ph.D. Registration No & Date : MZU/Ph.D./1525 of 21.10.2020  
Extension : NIL

  
(Prof. ZAITHANZA UVA PACHUAU)

**Head**

**Department of Physics**

Head  
Department of Physics  
Mizoram University  
Tanhril : Aizawl

# **ABSTRACT**

## **OPTICAL STUDIES OF SOME RARE - EARTH DOPED NANO-COMPOSITES FOR PHOTONIC APPLICATIONS**

**AN ABSTRACT SUBMITTED IN PARTIAL FULFILLMENT  
OF THE REQUIREMENTS FOR THE DEGREE OF DOCTOR  
OF PHILOSOPHY**

**K.M.S. DAWNGLIANA**

**MZU REGISTRATION NO.: 1502661**

**Ph.D. REGISTRATION NO.: MZU/Ph.D./1525 OF 21.10.2020**



**DEPARTMENT OF PHYSICS**

**SCHOOL OF PHYSICAL SCIENCES**

**OCTOBER, 2024**

**OPTICAL STUDIES OF SOME RARE - EARTH DOPED NANO-  
COMPOSITES FOR PHOTONIC APPLICATIONS**

**By**

**K.M.S. DAWNGLIANA**

**Department of physics**

**Supervisor**

**Prof. SUMAN RAI**

**Submitted**

**In partial fulfillment of the requirement of the degree of Doctor of  
Philosophy in Physics in Mizoram University, Aiza**

# THESIS TITLE: OPTICAL STUDIES OF SOME RARE-EARTH DOPED NANO-COMPOSITES FOR PHOTONIC APPLICATIONS

## Introduction

The rare earth (RE) ions are an extraordinary source of sharp and stable visible and infrared emissions that originate from transitions between partially filled 4f-electronic shells. Their photoluminescence (PL) emissions have been vastly exploited in the fabrication and development of optoelectronic and photonic devices, like lasers, optical amplifiers, light emitting diodes, sensors, phosphors, display devices etc. Although, in free ion state, the 4f transitions of RE ions are forbidden by Laporte's selection rule (for allowed transitions  $\pm 1$ ), when incorporated in a host, the electric field of the host modifies the RE energy level structures and allows admixing of high energy opposite parity levels and makes the f-f transitions possible. These induced dipole transitions make the RE doped in different hosts suitable for diverse optical applications. However, the absorption cross-section of the 4f transitions is very small which results in low PL efficiency. Hence, various methods are being utilized for the enhancement in PL efficiency of RE ions in different hosts. Among different techniques, co-doping with metal nanoparticles (NPs) with the RE ions is a potential technique to achieve this goal. Therefore, the primary motivation of the present thesis work was to study the effect of metal NPs on the spectroscopic behaviour of RE ions in sol-gel derived silica matrices and harness the Localized Surface Plasmon (LSPR), network modification, and energy transfer (ET) effect of metal NPs for the enhancement in radiative efficiencies of the RE ions. Silica glass is a highly attractive host of RE ions for optical applications due to its favorable mechanical, thermal and chemical properties. For the present thesis work, three RE ions, namely Samarium ( $\text{Sm}^{3+}$ ), Europium ( $\text{Eu}^{3+}$ ) and Neodymium ( $\text{Nd}^{3+}$ ) were selected.  $\text{Al}_2\text{O}_3$ ,  $\text{TiO}_2$ ,  $\text{ZnS}$ ,  $\text{ZnO}$  were chosen as the metal NP co-dopants. The study was carried out both for methanol medium and for silica matrices. The structural characterizations were done with the help of X-ray diffraction (XRD), Fourier Transform Infrared (FTIR), Scanning electron microscope (SEM-EDAX) and Transmission Electron Microscope (TEM). Spectroscopic characterizations of the fabricated samples were carried out through optical absorption (UV to NIR



regions) and Photoluminescence (PL) spectroscopic techniques. The observations were quantified with the aid of famous and well accepted Judd Ofelt (J. O.) theory. The results were compared with earlier reported works. The thesis is presented in the form of six chapters as discussed below:

**Chapter I** gives a general introduction to the whole thesis work. The chapter emphasizes about the RE ions, their transitions, Judd-Ofelt parameters, important radiative parameters, sol-gel method and the motivation behind the thesis work.

**Chapter II** deals the methods of preparation (chemical sol-gel method) of the RE<sup>3+</sup> doped Al<sub>2</sub>O<sub>3</sub>, TiO<sub>2</sub>, ZnS and ZnO in silicate matrix. Various characteristic techniques used in this work and the procedures followed are given.

**Chapter III** deals the synthesis and characterization of Sm<sup>3+</sup> doped Al<sub>2</sub>O<sub>3</sub>, TiO<sub>2</sub>, ZnS and ZnO nanoparticles were presented characterized through X-ray diffraction (XRD), Scanning electron microscope (SEM-EDAX). High resolution transmission electron microscopy (HR-TEM), Fourier transform infrared spectroscopy (FTIR), UV-visible spectroscopy (UV-vis), Photoluminescence spectroscopy (PL), Non-linear properties and CIE Chromaticity. The obtained results are presented and discussed in this chapter.

**Chapter IV** deals the synthesis and characterization of Eu<sup>3+</sup> doped Al<sub>2</sub>O<sub>3</sub> and TiO<sub>2</sub> nanoparticles were presented characterized through X-ray diffraction (XRD), Scanning electron microscope (SEM-EDAX). High resolution transmission electron microscopy (HR-TEM), Fourier transform infrared spectroscopy (FTIR), UV-visible spectroscopy (UV-vis), Photoluminescence spectroscopy (PL), Non-linear properties and CIE Chromaticity. The obtained results are presented and discussed in this chapter.

**Chapter V** deals the effect of Al on photoluminescence properties of Nd<sup>3+</sup> in silicate glass on the physical, structural and optical properties. The obtained results are presented and discussed in this chapter.

Finally, a summary providing the conclusions of the present work along with the future plan of research is given in **Chapter VI**.